Syntheseoptimierung und Formgebung von Metall-organischen Gerüstverbindungen für die Anwendung in adsorptionsgetriebenen Kältemaschinen

Dissertation

zur Erlangung des Doktorgrades

Dr. rer. nat.

der Mathematisch-Naturwissenschaftlichen Fakultät

der Heinrich-Heine-Universität Düsseldorf

vorgelegt von

Serkan Gökpinar

aus Mönchengladbach

Düsseldorf, Oktober 2019

aus dem Institut für Anorganische Chemie und Strukturchemie I
der Heinrich-Heine-Universität Düsseldorf

Gedruckt mit der Genehmigung der
Mathematisch-Naturwissenschaftlichen Fakultät der
Heinrich-Heine-Universität Düsseldorf

Referent: Prof. Dr. Christoph Janiak
Korreferent: Prof. Dr. Christian Ganter

Tag der mündlichen Prüfung: 12.11.2019

Die folgende Dissertation wurde im Rahmen des Projekts „Optimierung von neuartigen Materialien für zyklische Adsorptionsprozesse“ (kurz OPTIMAT-Projekt) angefertigt. Teilnehmende Verbundprojektpartner waren das Fraunhofer-Institut für Solare Energiesysteme (ISE), DencoHappel GmbH (später FläktGroup) und die Heinrich-Heine-Universität Düsseldorf (HHU Düsseldorf). Ziel des Projekts OPTIMAT ist die Entwicklung neuer, hydrothermal stabiler, mikroporöser Materialien und Komposite für den Einsatz in thermisch angetriebenen Wärmepumpen und Klimaanlagen. Die vorliegende Arbeit wurde in der Zeit von Oktober 2016 bis September 2019 an der Heinrich-Heine-Universität Düsseldorf im Institut für Anorganische Chemie und Strukturchemie I im Arbeitskreis von Prof. Dr. Christoph Janiak angefertigt. Im Februar 2018 wurde ein Teil der praktischen Arbeiten an der Universität Hasselt (Belgien) in der Arbeitsgruppe von Prof. Dr. ir. Wim Deferme durchgeführt.

Eidesstattliche Erklärung

Ich versichere an Eides statt, dass die Dissertation von mir selbstständig und ohne unzulässige fremde Hilfe unter der Beachtung der „Grundsätze zur Sicherung guter wissenschaftlicher Praxis“ an der Heinrich-Heine-Universität Düsseldorf erstellt worden ist. Die aus fremden Quellen direkt oder indirekt übernommenen Gedanken sind als solche kenntlich gemacht. Die Arbeit wurde bisher weder im Inland noch im Ausland in gleicher oder ähnlicher Form einer anderen Prüfungsbehörde vorgelegt. Es wurden zuvor keine erfolglosen Promotionsversuche unternommen.

……. …….

Ort, Datum Unterschrift

Publikationsliste

Erstautor:

S. Gökpinar, T. Diment and C. Janiak, Environmentally benign dry-gel conversions of Zr-based UiO metal–organic frameworks with high yield and the possibility of solvent re-use, *Dalton Trans.*, 2017, **46**, 9895–9900.

N. Tannert,‡ S. Gökpinar,‡ E. Hastürk, S. Nießing und C. Janiak, Microwave-assisted dry-gel conversion-a new sustainable route for the rapid synthesis of metal–organic frameworks with solvent re-use, *Dalton Trans.*, 2018, **47**, 9850 – 9860.

‡ contributed equally to the paper

S. Gökpinar, S.-J. Ernst, E. Hastürk, M. Möllers, I. El Aita, R. Wiedey, N. Tannert, S. Nießing, S. Abdpour, A. Schmitz, J. Quodbach, G. Füldner, S. K. Henninger und C. Janiak, Engineering metal–organic frameworks in binder composites for water sorption driven chiller system, *submitted*, 2019.

Koautor:

T. J. Matemb Ma Ntep, H. Reinsch, B. Moll, E. Hastürk, S. Gökpinar, H. Breitzke, C. Schlüsener, L. Schmolke, G. Buntkowsky und C. Janiak, Realizing the Potential of Acetylenedicarboxylate by Functionalization to Halofumarate in ZrIV Metal–Organic Frameworks, *Inorg. Chem.*, 2019, **58**, 10965−10973.

S. Millan, B. Gil-Hernandez, E. Milles, S. Gökpinar, G. Makhloufi, A. Schmitz, C. Schlüsener und C. Janiak, rtl-M-MOFs (M = Cu, Zn) with a T-shaped bifunctional pyrazole-isophthalate ligand showing flexibility and S-shaped Type F-IV sorption isotherms with high saturation uptakes for M = Cu, *Dalton Trans.*, 2019, **48**, 8057–8067.

S. Menzel, S. Millan, S.-P. Höfert, S. Gökpinar und C. Janiak, *manuscript in preperation*.

Y. Sun, S. Gökpinar, R. Wiedey und C. Janiak, *manuscript in preperation*.

Danksagung

An erster Stelle möchte ich Herrn Prof. Dr. Christoph Janiak dafür danken, mir die Möglichkeit gegeben zu haben meine Dissertation in seinem Arbeitskreis durchführen zu können. Weiterhin bedanke ich mich bei ihm für die interessante Themenstellung, die netten Gespräche, die angenehme Zusammenarbeit und die Unterstützung bei der Erstellung der Publikationen.

Herrn Prof. Dr. Christian Ganter danke ich herzlich für die Übernahme des Korreferates.

Ein ganz besonderer Dank gilt meinen Bürokollegen Anna Goldman, Ülkü Kökcam-Demir, Simon Millan und Saskia Menzel. Desweiteren möchte ich mich ganz besonders bei Emrah Hastürk, Niels Tannert, Irina Gruber und Christian Jansen für die enge Zusammenarbeit danken. Auch gilt ein großer Dank den Koorperationspartnern insbesondere Sebastian-Johannes Ernst, Ilias el Aita, Raphael Wiedey und Julian Quodbach. Dem ganzen Arbeitskreis danke ich für eine besonders angenehme Atmosphäre.

Den fest angestellten Mitarbeitern Birgit Tommes, Annette Ricken und Marcell Demandt sowie dem Team der Analytik um Karsten Klauke und Ralf Bürgel gilt mein Dank für die schnelle Hilfe bei sämtlichen Problemen rund um die Messgeräte und die Durchführung von Messungen.

Abschließend danke ich meiner Familie, die mir viel Verständnis gezeigt und mich ständig unterstützt hat.

Inhaltsübersicht

In der vorliegenden Arbeit wurde das Ziel der Synthese hydrothermal stabiler, mikroporöser Materialien und deren Komposite für den Einsatz in thermisch getriebenen Kältemaschinen verfolgt.

Im ersten Teil der Arbeit wurden Syntheseoptimierungen bereits bekannter Plattform-MOFs durchführt. Zur Syntheseoptimierung von MOFs wurde sowohl die konventionelle als auch die mikrowellenassistierte Trockengelsynthese (engl.: *(Mircrowave-assisted) Dry-Gel Conversion;* kurz (MW-)DGC) genutzt. DGC ist eine nützliche und neuartige Methode, um MOFs optimiert zu synthetisieren, da hierbei prinzipiell die nahezu vollständige Lösungsmittelrückgewinnung sowie erhöhte Kristallinität und BET-Oberfläche möglich sind. Bei einer DGC wird eine vermahlene Mischung der festen Edukte auf einem Sieb in einen verschlossenen Autoklav eingebracht und im Dampfraum, anstatt wie üblich in Lösung, umgesetzt. Die Synthese von Zirkonium-basierten MOF-Systemen wie UiO-66, UiO-66-NH_2 und UiO-67 wurde in einer konventiellen Trockengelumwandlung durchführt. In einer weiteren Arbeit konnten UiO-66 und das Polymorph MIL-140A in einer mikrowellenassistierten Trockengelumwandlung mit deutlich verringerten Reaktionszeiten erfolgreich umgesetzt werden. In beiden Arbeiten konnte unter anderem die vollständige Wiederverwendung des Lösungsmittels über mehrere Zyklen nachgewiesen werden.

Im zweiten Teil der Arbeit wurde das Ziel der Formgebung von MOFs für die Anwendung in Kältemaschinen verfolgt. MOFs werden typischerweise nach der Synthese als mikrokristalline Pulver erhalten. Die Formgebung, welche mittels organischer Polymere durchgeführt werden kann, ist für die Anwendung essentiell. Bei der Herstellung von Polymer/MOF Kompositen für sorptionsgetriebenen Kältemaschinen wurde der Fokus auf Polyvinylalkohol (kurz PVA) gesetzt, da sowohl die Hydrophilie als auch die Porenzugänglichkeit des Polymers vielversprechend erschienen. Die Verwendung von PVA als Bindemittel führte reproduzierbar zu hochstabilen, gleichmäßig geformten PVA/MOF-Pellets mit einer MOF-Beladung von 80 wt%. Die Porosität der MOFs nach der Formgebung blieb im Wesentlichen unverändert. Des Weiteren wurden Al-Pellets in einen realen Festbett-Wärmeaustauscher angebracht, bei der die kommerziell verwendeten Kieselgele unter vergleichbaren Betriebsbedingungen übertroffen wurden. Auch der Betrieb bei einer sehr niedrigen Desorptionstemperatur von 60 °C wurde erfolgreich nachgewiesen.

Abstract

The aim of the present work was the synthesis of hydrothermally stable, microporous materials and their composites for use in thermally driven chillers.

In the first part of the thesis, synthesis optimizations of already known platform MOFs were carried out. For the synthesis optimization of MOFs both the conventional and the microwave-assisted dry gel conversion (short: (MW-)DGC) was used. DGC is a useful and novel method to synthesize MOFs in an optimized manner. The complete solvent recovery and increased crystallinity and BET surface area are possible advantages of this methode. In a DGC, a milled mixture of the solid reactants is placed on a sieve in a sealed autoclave and reacted in the vapor atmosphere, rather than in solution as usual. The synthesis of Zr-based MOF systems such as UiO-66, UiO-66-NH_2, and UiO-67 were performed in a conventional dry gel conversion successfully. In another work, UiO-66 and the polymorph MIL-140A were synthesized in a microwave-assisted dry gel conversion with significantly decreased reaction times. In both works, the possibility of solvent reuse of over several cycles could be proved.

In the second part of the work, shaping MOFs for use in chillers was pursued. MOFs are typically obtained as microcrystalline powders after synthesis. Shaping of MOFs is essential for the application, which can be carried out by using organic polymers. In the production of polymer/MOF composites for sorption-driven chillers, the focus was sete on poly(vinylalcohol) (short: PVA), as the hydrophilicity and the pore accessibility of the polymer appeared promising. The use of PVA as a binder reproducibly resulted in highly stable, uniformly shaped PVA/MOF pellets with a MOF-loading of 80 wt%. The porosity of the MOFs after shaping was given. Furthermore, Al-pellets were applied in a "full-scale" fixed-bed heat exchanger, outperforming commercially used silica gels under comparable operating conditions. The possibility of operation at very low desorption temperature of 60 °C was also confirmed.

Inhaltsverzeichnis

Abkürzungsverzeichnis

MOF	Metal-organic framework
SBU	Secondary Building Unit
UiO	Universitetet i Oslo
Zr-MOFs	Zirkonium-basierte MOFs
Al-MOFs	Aluminium-basierte MOFs
Zr-fum	Zr-Fumarat
Al-fum	Al-Fumarat
MIL	Matériaux de l'Institut Lavoisier
ZIF	Zeolitic imidazolate framework
HKUST	Hong Kong University of Science and Technology
IRMOF	Isoreticular Metal-organic framework
AHT	Adsorption Heat Transformation
COP 21	21st Conference of the Parties
SFG	Solvent-Free Grinding
LAG	Liquid-Assisted Grinding
ILAG	Ion-and-Liquid-Assisted Grinding
(MW-)DGC	(Microwave-assisted) Dry gel conversion
SC	Sample Container
TGA	Thermogravimetrische Analyse
PXRD	Röntgenpulverdiffraktometrie
BET	Brunauer, Emmett und Teller
$p\ p_0^{-1}$	Gasdruck Sättigungsdruck^{-1}
BDC	1,4-Benzoldicarboxylat; Terephthalat
BTC	1,3,5-Benzoltricarboxylat; Trimesat
FDC	2,5-Furandicarboxylat
TbaPy	1,3,6,8-tetrakis(p-benzoat)pyren
Bipy	4,4‘-Bipyridin
rH	relative Humidity; relative Luftfeuchtigkeit
HoA	Heat of Adsorption
STP	Standardbedingungen

DMF	N,N-Dimethylformamid
MeOH	Methanol
EtOH	Ethanol
PVA	Polyvinylalkohol
PEI	Polyethylenimine
^{1}H-NMR	^{1}H-Kernresonanzspektroskopie
^{13}C-NMR	^{13}C-Kernresonanzspektroskopie
TGA	Thermogravimetrische Analyse
REM	Rasterelektronenmikroskop
ATC	After 1000 ad- and desorption cycles
DSC	Differential Scanning Calorimetry
wt%	Gewichtsprozent
HX	Heat Exchanger; Wärmeübertrager

1. Einleitung

Poröse Materialien lassen sich in drei Klassen unterteilen: den organischen, den anorganischen und den hybriden Materialien. Zu den organischen Materialien (bzw. Kohlenstoffmaterialien) werden die Aktivkohlen und die „covalent organic frameworks“ (COFs) gezählt, welche ausschließlich aus den Elementen Wasserstoff, Bor, Kohlenstoff, Stickstoff und Sauerstoff bestehen. Zu den anorganischen Materialien zählen die weitverbreiteten Silicagele (Siliciumoxide) und Zeolithe (Alumosilicate). Die dritte Klasse sind die hybriden Materialien, auch Koordinationspolymere, denen die Metall-organische Gerüstverbindungen (engl.: *Metal-organic frameworks*; kurz MOFs) untergeordnet sind. Poröse Materialien werden typischerweise anhand ihrer Porengröße kategorisiert. Hierbei bezeichnet man Materialien mit einem Porendurchmesser größer 50 nm als makroporös, zwischen 2–50 nm als mesoporös und unterhalb 2 nm als mikroporös. Die meisten Zeolithe und Aktivkohlen sind mikroporösese Materialien, die Silicagele hingegen mesoporös. MOFs, die im Fokus der Arbeit sind, zählen typischerweise zu den mikroporösen Materialien, wobei je nach Größe des Liganden auch deutlich größere Poren entstehen können.[1]

1.1 Metall-organische Gerüstverbindungen

Metall-organische Gerüstverbindungen sind potentiell poröse Verbindungen, welche aus metallischen Baueinheiten (engl.: S*econdary Building Units*; kurz SBUs), und verbrückenden, organischen Liganden (engl.: *Linker*) ein-, zwei- oder dreidimensionale Strukturen ausbilden (vgl. Abbildung 1). MOFs werden der Gruppe der Koordinationsnetzwerke sowie der Obergruppe der Koordinationspolymere zugeordnet. Die Koordinationsnetzwerke werden dabei durch kovalente Metall-Ligand-Bindungen oder über Wasserstoffbrückenbindungen (H-Brückenbindungen) aufgebaut.[2]

MOFs definieren sich im speziellen über das Vorhandensein von „potenziellen Hohlräumen“ und dem Vorhandensein von organischen Liganden. Wichtig hierbei ist, dass viele Systeme dynamisch sind und flexible Rahmenstrukturen vorweisen. Die Struktur der Materialien ist dabei abhängig von Faktoren wie Temperatur und Druck und können Einfluss auf die Porosität nehmen. Auch können die Poren der MOFs durch Lösungsmittelmoleküle blockiert sein.[3]

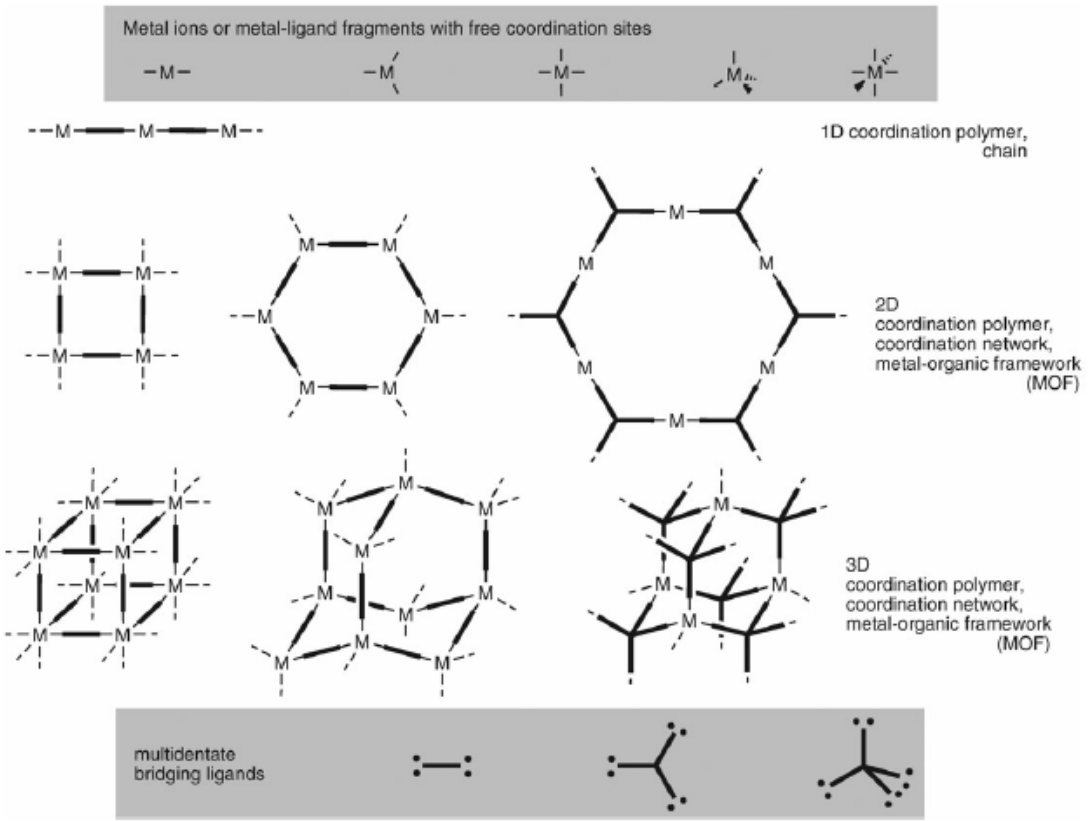

Abbildung 1: Schematische Darstellung des Aufbaus typischer Koordinationspolymere / MOFs aus molekularen Bausteinen. Nachgedruckt aus Lit. 4, mit Genehmung von der Centre National de la Recherche Scientifique (CNRS) und The Royal Society of Chemistry.

Der Begriff „MOF“ wurde im Jahr 1995 erstmals von Yaghi bei der Synthese eines mikroporösen Cu-Bipy- und Co-BTC-Komplexen mit reversiblen Gassorptionseigenschaften verwendet.[5,6] Nachfolgend präsentierten Kitagawa *et al*. und Yaghi *et al.* mikroporöse Verbindungen, bestehend aus M (M= Co, Ni, Zn) und Bipy bzw. Zn-BDC, an denen die Sorptionseigenschaften untersucht wurden und bildeten somit die Basis für die heutige MOF-Chemie.[7,8]

MOFs lassen sich entweder den mikro- oder dem unteren Bereich der mesoporösen Materialien zuordnen. Eine Besonderheit der MOFs ist, dass die Porengröße dieser Verbindungen unter Verwendung topologisch identischer, anorganischer Baueinheiten eingestellt werden kann. Dabei wird der verwendete organische Ligand variiert und der Abstand zwischen den SBUs verlängert oder verkürzt. Dieser Ansatz ist als isoretikulare Chemie bekannt und kann genutzt werden, um Materialien für bestimmte Anwendungen wie Gasseperation maßzuschneidern.[9]

Liganden sind mehrzähnige, verbrückende organische Moleküle. Um als verbrückender Ligand fungieren zu können, muss das Brückenelement mindestens zweizähnig sein. Höher koordinierende Liganden führen zu höheren Vernetzungsgraden. Typische organische Grundbausteine sind die anionischen Carboxylat-Liganden. Auch neutrale, heterozyklische Stickstoff-Liganden zählen zu den häufig eingesetzten Liganden wie das 4,4´-Bipyridin. Einige der prominentesten Liganden sind in Abbildung 2 dargestellt.

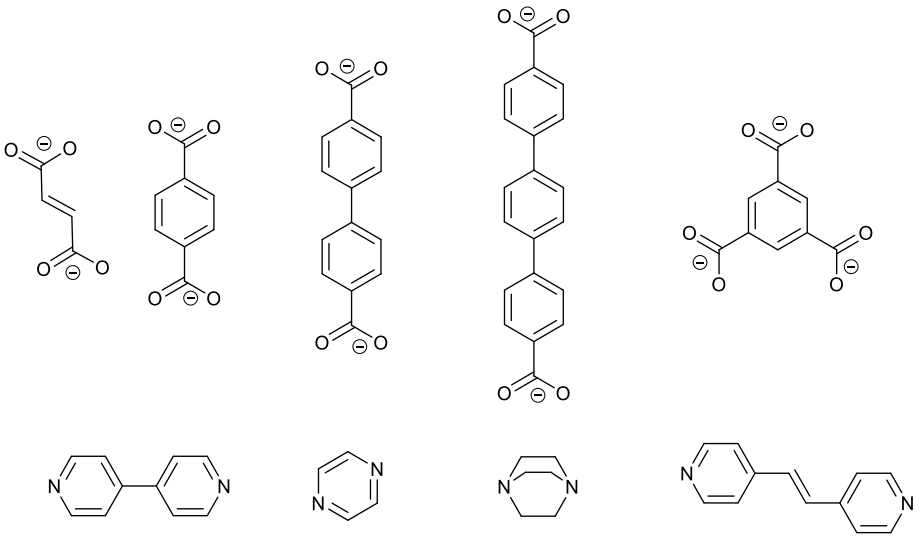

Abbildung 2: Beispiele für anionische Carboxylat-Liganden (oben) und neutrale, heterozyklische Stickstoff-Liganden (unten) in MOFs.

1.1.1 Zirkonium-MOFs

Zirkonium-basierte MOFs (kurz Zr-MOFs) gehören aufgrund ihrer hohen thermischen, chemischen und mechanischen Stabilität zu den attraktivsten Klassen der MOF-Materialien, welche aus der starken Carboxylat-Zr-Bindung und dem hohen Konnektivitätsgrad der Metallcluster resultiert. In den letzten zwei Jahrzehnten hat sich die retikulare Chemie zu einem wertvollen Werkzeug zum Designen und zur Synthese von porösen, kristallinen Materialien entwickelt. Die Entdeckung des hexanuklearen Zr-Clusters führte zur Entwicklung von einer hohen Anzahl von MOFs. Durch die Variation der Ligandenlänge, Anzahl an koordinierenden Carboxylat-Gruppen und durch das Einführen von funktionellen Gruppen an den Liganden können sämtliche MOFs erhalten werden. Die große Variabilität und Stabilität machen die Zr-MOFs zu einem einzigartigen Material, welches hohe Aufmerksamkeit in der Forschung auf sich zog. Ein weiterer, entscheidender Vorteil von Zr-MOFs beruht auch auf den einfachen und vielseitigen Synthesemöglichkeiten. Nach der ersten Solvothermalsynthese in N,N-Dimethylformamid (kurz DMF) wurden zahlreiche neue Lösungsmittel und Verfahren genutzt. Neben der Möglichkeit der hydrothermalen Synthese einiger Zr-MOFs, konnten auch mikrowellenunterstützte, mechanochemische oder kontinuierliche Synthesen erfolgreich durchgeführt werden. Das hexanukleare Cluster wird dabei unter unteschiedlichsten Reaktionsbedingungen in Zr-MOFs gebildet, während nur einige wenige Beispiele von anderen Zr-oxo Clustern bekannt sind, darunter die MIL-140-Reihe.[10]

Eine wichtige Serie der Zr-MOFs ist die UiO-Serie (*Universitetet i Oslo*), deren bekanntester Vertreter UiO-66 ist. UiOs sind Zr(IV)-basierte MOF-Systeme mit der Formel $Zr_6O_4(OH)_4(Linker)_6$.[11] Das erste MOF-System mit einem $[Zr_6(\mu_3\text{-}O)_4(\mu_3\text{-}OH)_4]^{12-}$-Cluster ist das UiO-66, welches durch den Terephthalat-Linker koordiniert wird. Dieser wurde von Cavka *et al.* im Jahr 2008 entdeckt.[21] Nachfolgend, wurde eine Reihe von isoretikulären Verbindungen veröffentlicht, darunter das UiO-67 $[Zr_6(\mu_3\text{-}O)_4(\mu_3\text{-}OH)_4(BPDC)_6]$ mit dem um eine Benzoleinheit verlängerten Biphenyldicarboxylat-Liganden und UiO-68 $[Zr_6(\mu_3\text{-}O)_4(\mu_3\text{-}OH)_4(TPDC)_6]$, welches um zwei Benzoleinheiten verlängert ist. Des Weiteren existieren das MOF-801 (auch bekannt als Zr-Fumarat) mit der Summenformel $[Zr_6(\mu_3\text{-}O)_4(\mu_3\text{-}OH)_4(fum)_6]$, welches einen verkürzten Liganden aufweist und das MOF-808 mit dem dreizähnigen Trimesat-Linker $[Zr_6(\mu_3\text{-}O)_4(\mu_3\text{-}OH)_4(HCOO)_6(BTC)_2]$. Diese und weitere Beispiele sind in der Abbildung 3 dargestellt.

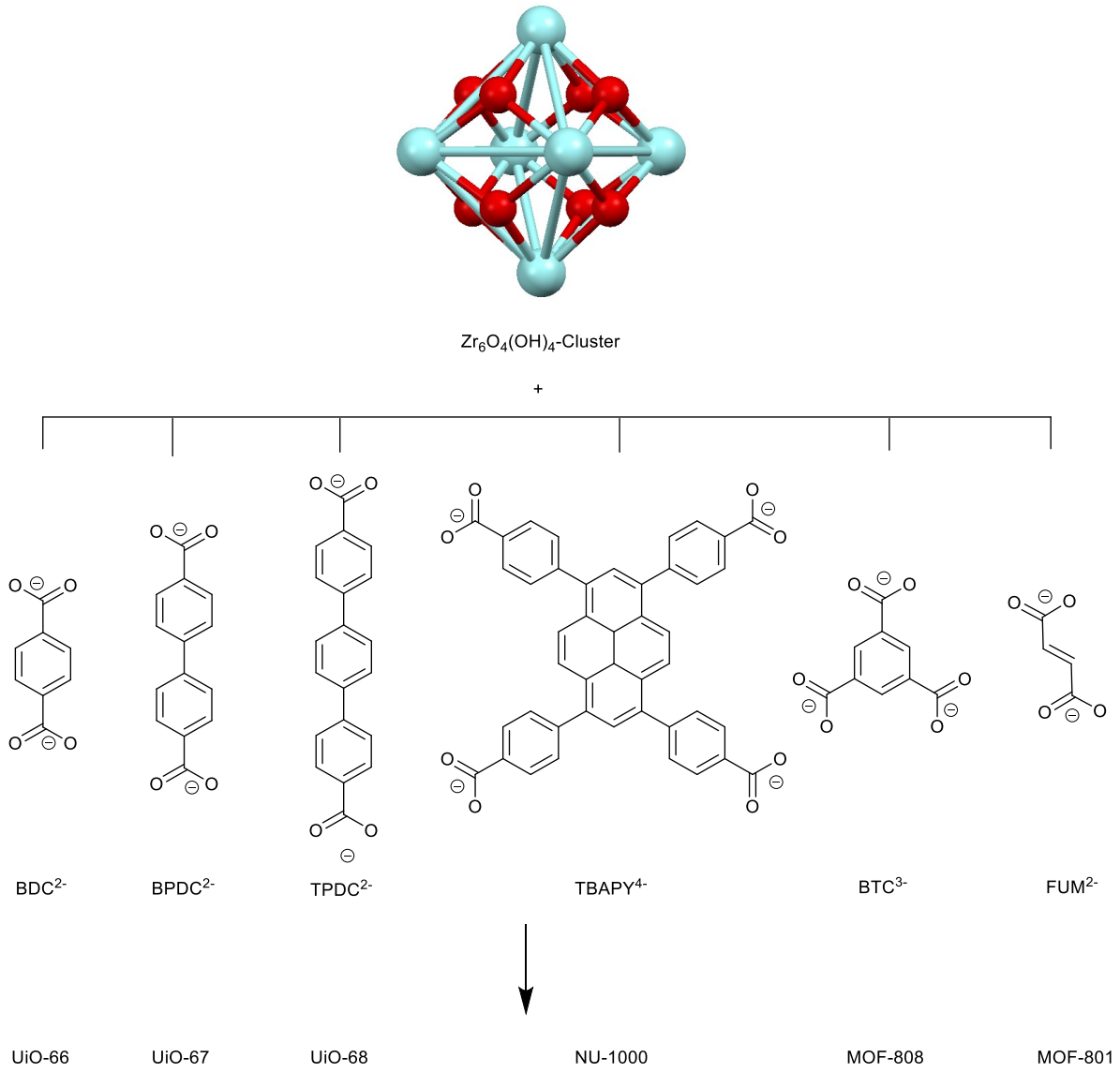

Abbildung 3: Beispiele für Kombinationen zwischen der $Zr_6O_4(OH)_4$-SBU und zwei-, drei- und vierzähnige Carboxylat-Liganden und die daraus entstehenden MOFs.

Eine wichtige Rolle bei der Synthese von Zr-MOFs spielen Defektstellen, welche erstmals im Jahr 2011 entdeckt wurden.[11] Vor der Entdeckung der Defektstellen in Zr-MOFs ging man davon aus, dass sich die Struktur von MOF-Gerüsten fehlerfrei ausbreiten. Das erste Indiz für Defektstellen lieferte die thermogravimetrische Analyse von UiO-66, da das Verhältnis zwischen dem Massenverlust für den Linker und der übrigbleibenden Masse für ZrO_2 nicht dem Verhältnis der idealen Kristallstruktur entsprach. Aus den Berechnungen ging hervor, dass jeder zwölfte Ligand fehlte.[11]

Aus dieser Erkenntnis heraus versuchte man anschließend gezielt durch den Einbau von Monocarbonsäuren als Modulator Defektstellen in MOFs zu erzeugen. Die Verwendung von Monocarbonsäuren oder auch anorganischen Säuren wie HCl entwickelte sich zu einem leistungsfähigen Werkzeug. Zu den verwendeten Monocarbonsäuren zählen die Ameisensäure, Benzoesäure, Essigsäure, Triflouressigsäure aber auch Aminosäuren wie L-Prolin. Monocarbonsäuren als Modulator, welche stöchiometrisch im deutlichen Überschuss eingesetzt werden, verbessern die Reproduzierbarkeit der Syntheseverfahren und ermöglichen die Erhöhung der Kristallinität des Produkts und in bestimmten Fällen die Kontrolle der Kristallgröße.[12] Diese verlangsamen dabei die Reaktion, da der vernetzende Linker in Konkurrenz um die Koordination an das Metall steht.[13] Anorganische Säuren wie HCl hingegen sind dafür bekannt die Reaktion zu beschleunigen.[14] Das Wasser der Säure beschleunigt dabei die Bildung des MOFs durch Hydrolyse des Zr-Vorläufers im Keimbildungsprozess.[13]

MOFs können dabei zwei Arten von Defekten, fehlende Linker und fehlende Cluster, ausbilden (siehe Abbildung 4). Die unbesetzten Stellen können durch terminale Liganden wie Hydroxygruppe,[14] Monocarboxylat,[15] Wasser[16] oder Chlorid[17] ausgeglichen werden.

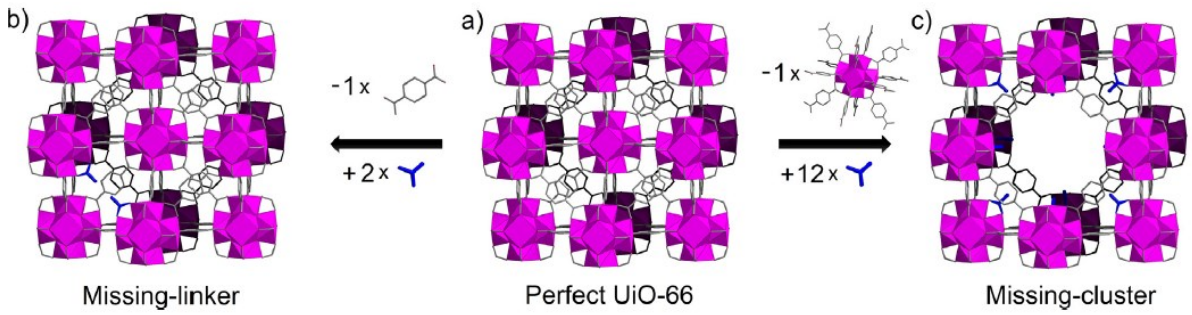

Abbildung 4: Idealisierter Prozess zur Erzeugung von Defekten in UiO-66 (a), ersetzen eines Linkers durch zwei Monocarbonsäuren (b) und Austausch einer $Zr_6O_6(BDC)_{12}$-Einheit durch zwölf Monocarbonsäuren (c). Nachdruck aus Lit. 13, © 2017, mit Genehmung von Elsevier.

Linkerdefekte entstehen, wenn ein organischer Linker aus der Struktur entfernt wird und die Koordinationslücken auf zwei benachbarten Metallclustern verbleiben (siehe Abbildung 4b). Clusterdefekte hingegen entstehen durch Entfernung eines $[Zr_6O_4(OH)_4]^{12+}$-Clusters einschließlich seiner zwölf organischen Linker (siehe Abbildung 4c). Zr-MOFs mit Clusterdefekten resultieren in einer reo-Topologie, statt der fcc-Topologie (face centred

cubic). Der qualitative Nachweis für Clusterdefekte kann mittels PXRD erfolgen, da im niedrigen Winkelbereich 2Θ ein verbreiterter Reflex auftaucht. Die Porengröße vergrößert sich im Fall von UiO-66 von 7 Å (tetraedischer Käfig) und 9 Å (oktaedrischer Käfig) auf 18 Å (oktaedrischer Käfig).[13] Die Defektstellen können somit einen signifikanten Einfluss auf die Porosität, die thermischen Eigenschaften und die mechanischen Eigenschaften des Materials nehmen (weitere Ausführung im Kapitel UiO-66).

Hinsichtlich des Fokus der Arbeit werden Adsorptionsmaterialien für die Wärmetransformation gesucht. Diese sollte eine Sorptionsisotherme mit S-Form (IUPAC-Klassifizierung Typ V) aufweisen, die einen steilen Anstieg der Wasseraufnahme im relativen Druckbereich von p p_0^{-1} ≈ 0,10–0,30 aufweist.[18,19] Die S-Form ist vorteilhaft, da sie einen großen Sorptionshub (bzw. Arbeitskapazität) innerhalb eines engen, relativen Druckbereichs (geringer Aufwand) bietet. Auch sollte Wasseraufnahme höher als 0,20 g g^{-1} gegeben sein.[19] Nachfolgend ist in Abbildung 5 eine Übersicht an Wassersorptionsisothermen ausgewählter Zr-MOFs bei 25 °C gegeben.

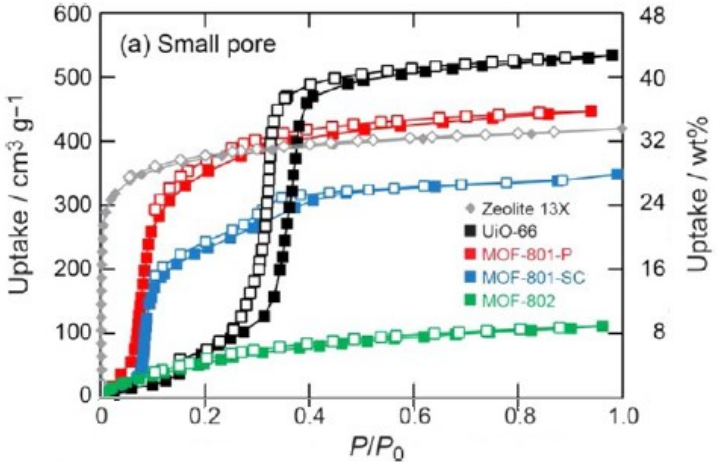

Abbildung 5: Wassersorptionsisothermen ausgewählter Zr-MOFs und Zeolith 13X bei 25 °C. Adaptiert aus Lit. 20, © 2014, mit Genehmigung von American Chemical Society.

Als potentiell ideale Materialien werden Zr-basierte MOFs wie UiO-66 und Zr-fum eingestuft. Nachfolgend sind beide MOFs näher beschrieben.

UiO-66

Das prominenteste Zr-basierte MOF System ist das UiO-66 mit der Formel $Zr_6O_4(OH)_4(BDC)_6$. Das entsprechende Netzwerk aus Zirkonium und Terephthalsäure wurde erstmals von Cavka *et. al.* beschrieben.[21] Als SBUs dienen Zr(IV)-Cluster, $Zr_6(\mu_3\text{-}O)_4(\mu_3\text{-}OH)_4^{12+}$, in denen sechs Zr(IV)-Ionen quadratisch-antiprismatisch von jeweils acht Sauerstoffatomen koordiniert sind. Die SBUs, die über zwölf BDC Liganden mit den benachbarten SBUs verbunden sind, bilden in der defektfreien Struktur eine kubisch dichteste Packung aus oktaedrischen und tetraedrischen Käfigen. Da die μ_3-OH Gruppen in der SBU nur schwach gebunden sind, können die SBUs reversibel dehydroxyliert werden. Die dadurch entstehenden SBUs der Formel $Zr_6(\mu_3\text{-}O)_6^{12+}$ besitzen somit freie Koordinationsstellen. Die unterschiedlichen Käfigstrukturen und die hydroxylierte und dedroxylierte Form des UiO-66 sind in Abbildung 6 dargestellt.[22]

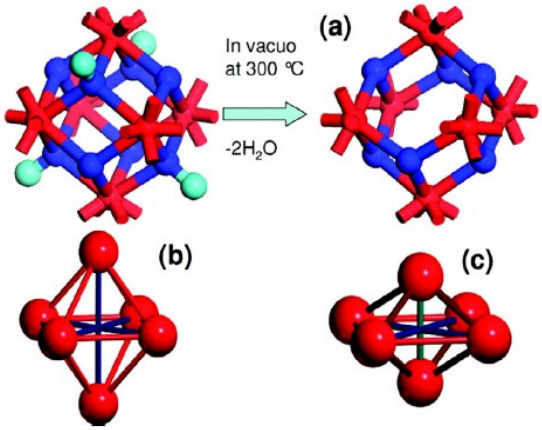

Abbildung 6: SBU von UiO-66: a) Abspaltung von zwei Wassermolekülen/ Umwandlung der hydroxylierten in die dehydroxylierte Form. Reduktion der Symmetrie von der perfekten (b) in die ‘‘squeezed” Form (c). Nachdruck aus Lit. 11, © 2011, mit Genehmigung von American Chemical Society.

Wie zuvor in Abbildung 4 dargestellt, weisen Zr-MOFs Defekte auf. Abhängig davon welche Art von Defekten auftreten, kann die BET-Oberfläche deutlich abweichen (siehe Abbildung 7). Clusterdefekte erzeugen im Vergleich zu Linkerdefekten eine deutlich erhöhte BET-Oberfläche. So konnten Wu *et al.* nachweisen, dass die BET-Oberfläche des UiO-66 defektstellenbedingt zwischen 1090 und 1617 $m^2\ g^{-1}$ schwankt.[15]

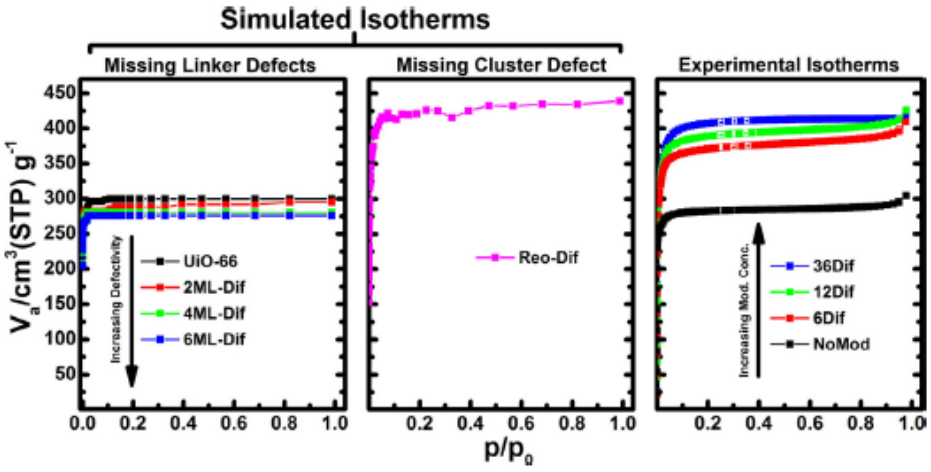

Abbildung 7: Simulierte N_2 Sorptionsisothermen für Linkerdefekte (links) und Clusterdefekte (mitte) und experimentelle N_2 Sorptionsisothermen (rechts) für Diflouressigsäure moduliertes UiO-66. Nachdruck aus Lit. 23, © 2016, mit Genehmigung von American Chemical Society.

Sehr hohe BET-Oberflächen des Zr-MOFs weisen dabei auf das Vorhandensein von Clusterdefekten hin. Da die Poren des MOFs durch Clusterdefekte deutlich vergrößert werden, kann mehr N_2 in die Poren eingelagert werden.[24]

Die Menge an Clusterdefekten kann durch eine Titration quantifiziert werden. Die Titrationskurve einer defekten Probe von UiO-66 zeigt drei scheinbare Wendepunkte bei pH (pKa-Werten) 5,44 (3,52), 7,56 (6,79) und 9,51 (8,30). Der niedrigste pKa-Wert wurde, übereinstimmend mit der für UiO-67 gemachten Beobachtung, den μ_3-OH-Gruppen zugeordnet. Die verbleibenden pKa-Werte wurden Zr-OH_2 (6,79) und Zr-OH (8,30) zugeordnet, die als Kompensationsspezies an defekten Stellen vorkommen.[25] Mit Hilfe dieser Methode können die Clusterdefekte quantifiziert werden.

Es besteht derzeit ein großes Interesse daran, zu verstehen, wie Defekte gezielt für Anwendungen genutzt werden können. Diese Anwendungen umfassen Gassorption,[26] Gastrennung,[27] heterogene Katalyse,[28] Wirkstoffabgabe[29] und vieles mehr.

Die thermische Stabilität der UiO-66 wird mittels thermogravimetrischer Analyse untersucht, wobei drei Gewichtssverluste beobachtet werden. Die erste Gewichtsabnahme erfolgt bei T < 150 °C, welche durch das Verdampfen des Lösungsmittels verursacht wird. Anschließend findet eine Dehydratisierung des Clusters von $[Zr_6O_4(OH)_4]^{12+}$ zu $[Zr_6O_6]^{12+}$ unter Abspaltung von zwei Wassermolekülen statt. Zuletzt wird der organische Linker zersetzt (T > 450 °C) und es bildet sich ZrO_2.[11,17]

Zr-fum

Zr-Fumarat (kurz Zr-fum) ist eine weitere, potentiell wasserstabile MOF-Struktur, die intensiv auf ihre vielversprechenden Wassersorptionseigenschaften untersucht wurde. Zr-fum ist ein Zr-basiertes MOF, welches in seiner defektfreien Struktur mit der Summenformel $Zr_6O_4(OH)_4(Fumarat)_6$ zu beschreiben ist.

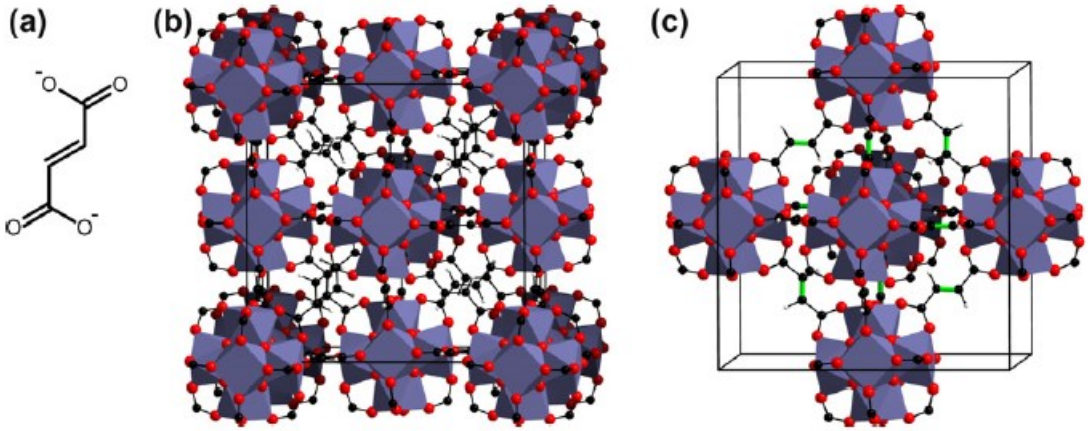

Abbildung 8: (a) Struktur des nichtlinearen Linkers Fumarat; (b) und (c): Strukturmodell für das Zr-fum-MOF. In (b) ist die kubische Einheitszelle gezeigt, (c) zeigt das zentrale Oktaeder einer Elementarzelle mit den grün dargestellten Doppelbindungen des Linkers. Nachdruck aus Lit. 12, © 2012, mit Genehmung von Elsevier.

Potentielle Anwendung findet das Zr-fum in der Gasspeicherung,[30] -seperation,[27] Wassersorption,[31,32] Katalyse und als Sensor.[33,34] Besondere Aufmerksamkeit bekam Zr-fum durch die Möglichkeit der Wassergewinnung aus der Luft, welches vollständig durch natürliches Sonnenlicht angetrieben werden kann. Yaghi *et al.* zeigten dabei, dass täglich 2,8 Liter Wasser pro Kilogramm MOF bei einer relativen Luftfeuchtigkeit von nur 20% gewonnen werden können.[35]

1.1.2 Aluminium-MOFs

In den letzten Jahren wurden eine Vielzahl an Al^{3+}-basierten, porösen MOFs synthetisiert.[36-39] Aluminium-MOFs (kurz Al-MOFs) haben aufgrund einer hohen Anzahl an möglichen Metallquellen, ihrer geringen Toxizität sowie ihrer hohen thermischen und chemischen Stabilität große Beachtung gefunden.[39,40,41] Neben der hohen Verfügbarkeit an Al^{3+}-Salzen, ist die Möglichkeit einer wasserbasierten Synthese für industrielle Anwendungen besonders interessant.[40] Auch das Einführen funktioneller Gruppen am Linker ermöglicht die gezielte Synthese eines anwendungsspezifischen MOFs.[42] Die SBUs in Al-MOFs führen in Kombination mit den vielen potentiellen, organischen Liganden zu verschiedenen Gerüststrukturen. Zu den prominentesten Al-MOFs zählen Al-Fumarat (auch Basolite A520 oder Al-fum),[43] MIL-160,[41] CAU-10-H,[42] CAU-23,[39] MIL-101(Al)-NH_2[44] und MIL-53(Al).[45]

Die Wassersorptionseigenschaften einiger Al-MOFs sind für die Anwendung in sorptionsgetriebenen Kältemaschinen interessant. Eine Voraussetzung für einen langfristigen Einsatz unter realen Bedingungen ist die hohe hydrothermale Stabilität, welche nur für wenige MOFs bekannt ist, darunter Al-fum, MIL-160, CAU-10-H und CAU-23. Des Weiteren sollten eine hohe Wasseraufnahme und ein hydrophiler Charakter für die Applikation gegeben sein. Die Wassersorption der relevantesten Al-MOFs sind in der nachfolgenden Abbildung 9 abgebildet.

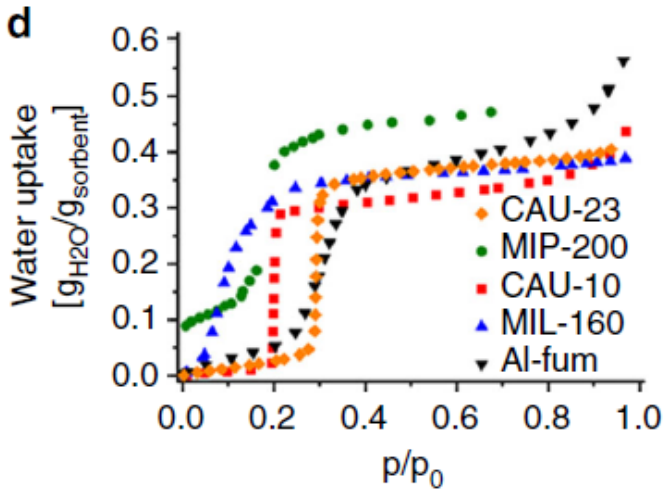

Abbildung 9: Wassersorptionsisothermen ausgewählter Al-MOFs bei 40 °C. Nachdruck aus Lit. 39, © 2019, mit Genehmung von Springer Nature.

In der Literatur sind einige, wenige Beispiele der MOFs zur Adsorptionswärmeumwandlung (engl.: *Adsorption Heat Transformation*; kurz AHT) wie MIL-160 mit einer Desorptionstemperatur von 90 °C, CAU-10-H mit 70 °C und Al-fum mit 90 °C vorhanden.[41,46,39,47,48] Das Ziel einer geringen Differenz zwischen Adsorptions- und Desorptionstemperatur wird in der Publikation „Engineering metal–organic frameworks in binder composites for water adsorption heat transformation systems“ unter Verwendung eines PVA/MOF Komposits verwirklicht (siehe 3.3).

MIL-160

Ein neuer und vielversprechender Kandidat zur Wärmetransformation ist das MIL-160 mit der Summenformel [Al(OH)(FDC)], welches kürzlich von Cadiau *et al.* veröffentlicht wurde.[41] Es besteht aus $AlO_4(OH)_2$-Oktaedern verbunden zu helikalen cis-Ketten, die durch den Linker 2,5-Furandicarboxylat verbunden sind und eindimensionale, quadratische sinusförmige Kanäle mit einem Durchmesser ≈5 Å bilden (siehe Abbildung 10). Die Sauerstoffatome des Oktaeders stammen aus vier Liganden und zwei Hydroxylgruppen. Die beiden OH-Gruppen befinden sich in cis-Position und überbrücken die Al-Zentren, um die Ketten zu bilden.

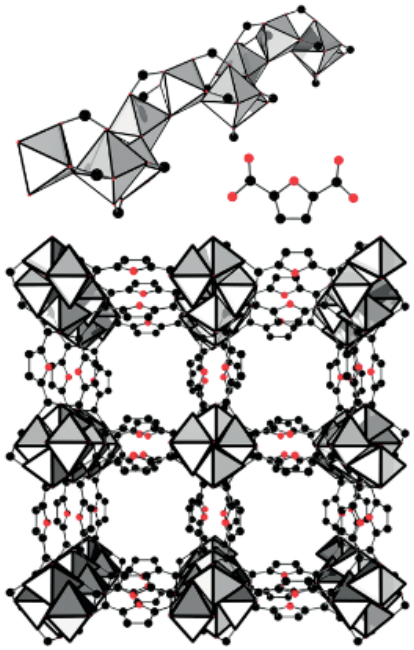

Abbildung 10: Helikale Kette aus AlO_6-Polyedern, Furandicarboxylat-Linker (oben) und das Netzwerk des MIL-160. Nachdruck aus Lit. 49, © 2018, mit Genehmung von John Wiley and Sons.

Beim Maßschneidern der MOF-Struktur wurde das Ziel einer gesteigertern Hydrophilie und einer guten Zugänglichkeit der Poren für Wassermoleküle verfolgt.[41] Zusätzlich soll die Löslichkeit des Linkers in Wasser gesteigert werden, sodass das Produkt über einen wasserbasierten, grünen Syntheseweg hergestellt werden kann. Das Produkt kann somit über eine Rückflusssynthese erhalten werden.

Al-fum/ Basolite A520

Das in der Patentliteratur beschriebene Al-Fumarat ist aufgrund seiner wasserbasierten Synthese, des kostengünstigen und umweltfreundlichen Metallkations und der hohen Stabilität eines der vielversprechendsten MOFs für adsorptionsgetriebene Wärmetransformation.[40] Das Gerüst mit der Summenformel $[Al(OH)(fum)\cdot nH_2O]m$ ist aus Al-OH-Al-Ketten aufgebaut, die durch Fumarat-Liganden verbunden sind und zu rautenförmigen 1D-Poren führen (siehe Abbildung 11).[50]

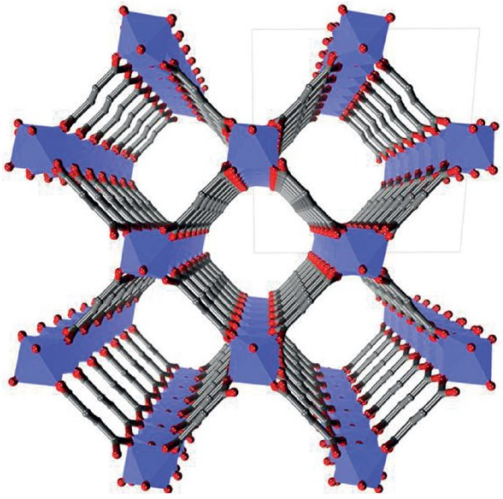

Abbildung 11: Kristallstruktur von Al-fum. Al-Oktaeder sind in blau, O-Atome in rot, C-Atome in grau dargestellt. Wasserstoffatome wurden zur besseren Übersichtlichkeit weggelassen. Nachdruck aus Lit. 50, © 2015, mit Genehmung von John Wiley and Sons.

1.2 Sorptionsgetriebene Kältemaschinen

Im Rahmenübereinkommen der UN-Klimakonferenz über Klimaänderungen im Jahr 2015 (engl.*: United Nations Framework Convention on Climate Change*, *21st Conference of the Parties,* kurz COP 21) haben sich die Nationen dazu verpflichtet ihre Treibhausgasemissionen erheblich zu senken. Gleichzeitig steigt der weltweite Energieverbrauch, wovon ein erheblicher Teil durch Heiz- und Kühlprozesse verursacht wird. Größtenteils werden dafür energieintensive Kompressionsklimaanlagen genutzt, die Kältemittel mit hohem Treibhauspotential nutzen und teilweise entflammbar, giftig und umweltschädlich sind.
Die Adsorptionswärmeumwandlung ist ein umweltfreundliches und energiesparendes Verfahren, dass zur Klimatisierung, Kühlen (einschließlich der Eisherstellung und -kühlung) und zum Heizen, eingesetzt wird. Als umweltfreundliches Arbeitsmedium wird typischerweise Wasser, alternativ aber auch Alkohole verwendet.[51] Die AHT basiert auf den zyklischen Adsorption- und Desorptionprozess eines Arbeitsmediums in einem porösen Material.

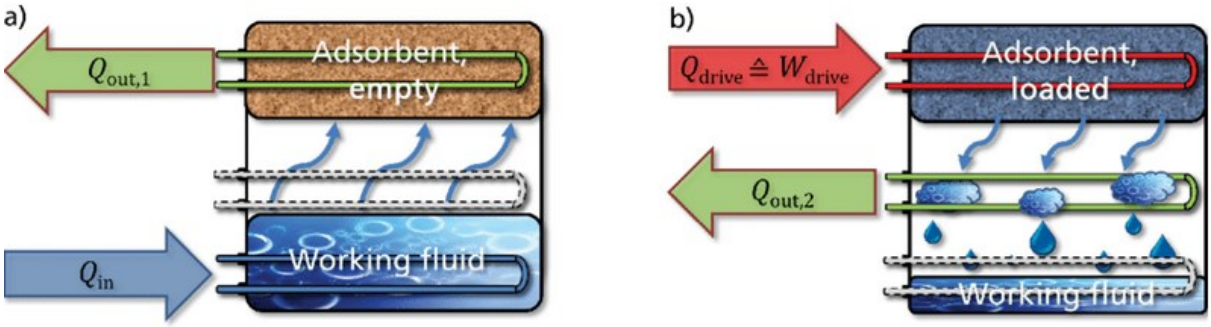

Abbildung 12: Arbeitsschema einer Sorptionswärmepumpe während der Adsorption (Arbeitsleistung) (a) und der Desorption (Regenerationsschritt) (b). Die Temperaturniveaus werden in verschiedenen Farben (kalt = blau, mittel = grün und heiß = rot) dargestellt. Nachdruck aus Lit. 52, mit Genehmigung von The Royal Society of Chemistry.

Eine AHT-Anlage besteht aus zwei wechselseitig arbeitenden Modulen. Während das eine Modul die gewünschte Arbeitsleistung erbringt, befindet sich das andere Modul in der Regenerationsphase, sodass eine permanente Kälte-/Wärmeleistung gewährleistet werden kann. Jedes Modul besteht aus zwei Kammern, in dem sich das poröse Material und das Arbeitsmedium befinden. Diese sind durch ein Ventil voneinander separiert. Ist das Sorptionsmaterial aktiviert und das Ventil zwischen beiden Kammern wird geöffnet, wird das

Arbeitsfluid durch das aktive, leere Sorptionsmaterial zur Verdampfung gebracht. Dabei wird die erforderliche Verdampfungswärme in thermisch getriebenen Adsorptionskältemaschinen zu einer nützlichen Kühlung umgewandelt (Abbildung 12, Q_{in}). Anschließend wird das Wasser aus dem porösen Material durch Erhöhung der Temperatur/ Antriebswärme (Abbildung 12, Q_{drive}) desorbiert, das Wasser kondensiert aus. Die Adsorptionswärme (engl.: *Heat of Adsortion*, kurz HoA) in dem Sorptionsmaterial und die Kondensationswärme des Arbeitsfluids können in Adsorptionswärmepumpen verwendet werden (Abbildung 12, $Q_{out,1}$ und $Q_{out,2}$).

Bislang kommen in handelsüblichen AHT-Anlagen Kieselgel und Zeolithe als Adsorbensmaterialien zum Einsatz. Diese haben vor allem den Vorteil der kostengünstigen Produktion. Nachteil hingegen ist die relativ niedrige Kälte-/Wärmeleistung die erbracht wird. Eine wichtige Rolle können hierbei die neue Materialklasse der MOFs spielen. MOFs ermöglichen die Nutzung bei Niedrigtemperatur-Antriebswärme (Q_{drive}) und übertrifft gleichzeitig die Adsorptionskapazität aktueller Werkstoffe. Sie haben daher das Potential die Adsorptionstechnologie voranzutreiben.

In der vorliegenden Arbeit wird eine Applikation des MOFs in einer Kältemaschine angestrebt, weshalb sich in den folgenden Abschnitten darauf beschränkt wird. Bei einem Arbeitszyklus in einer Kältemaschine spielen drei Temperaturniveaus eine wichtige Rolle:

T_{des}: Bei T_{des} handelt es sich um die Desorptionstemperatur bzw. Betriebstemperatur, welche eingestellt wird zur Regeneration des Sorptionsmaterials. Die Betriebstemperatur ist abhängig von der zur Verfügung stehenden Wärmequelle. Bei Verwendung von Sonnenkollektoren können Temperaturen von 70 °C über Flachkollektoren bis 130 °C über Vakuumröhrenkollektoren zur Verfügung gestellt werden. In dieser Arbeit wird das Ziel einer niedrigtemperaturgetriebenen Kältemaschine bei 60 °C und einer Standardtemperatur von 90 °C angestrebt. Der entsprechende Wasserdampfdruck liegt im Bereich von 199 bis 702 mbar.

T_{ads}: Die Adsorptionstemperatur ist die Temperatur der Adsorptions- und Kondensationswärme, welche an die Umwelt abgegeben wird. Die Adsorptionstemperatur liegt typischweise bei $25\ ^\circ C \leq T_{ads} \leq 35\ ^\circ C$ z. B. durch einen Außenluftwärmetauscher. Dies entspricht einem Wasserdampfdruck von 32 bis zu 56 mbar.

T_{evap}: Die Evaporationstemperatur ist die Nutzkälte, die der Kältemaschine zur Verfügung steht. Die Nutzkälte liegt typischerweise bei $T_{evap} \leq 10$ °C, welches ein typischer Wert für einen Haushaltswasserkühler ist. Wenn Wasser als Arbeitsmedium verwendet wird, entspricht dies einem Wasserdampfdruck von 12 mbar (siehe Tabelle 1).

Der ideale relative Druckbreich (relative Feuchte) für die Beladung des Materials lässt sich aus den Temperaturniveaus mittels folgender Formel ermitteln:

$$\text{p ads, rel} = \frac{\text{p H2O, evap.}}{\text{p H2O, adsorber } (Adsorption)} = \frac{6 \text{ bis } 12 \text{ mbar}}{32 \text{ bis } 56 \text{ mbar}} = 0{,}10 - 0{,}38$$

Die Bedingunen für den Regenerationszyklus hingegen ist erfüllt, wenn der stoffbezogene relative Desorptionsdampfdruck

$$\text{p des, rel} = \frac{\text{p H2O, kond.}}{\text{p H2O, adsorber } (Desorption)} = \frac{32 \text{ bis } 56 \text{ mbar}}{199 \text{ bis } 702 \text{ mbar}} = 0{,}05 - 0{,}28$$

beträgt. Die diesen Eigenschaften entsprechenden Adsorptionsisobaren sind in Abbildung 13 dargestellt.

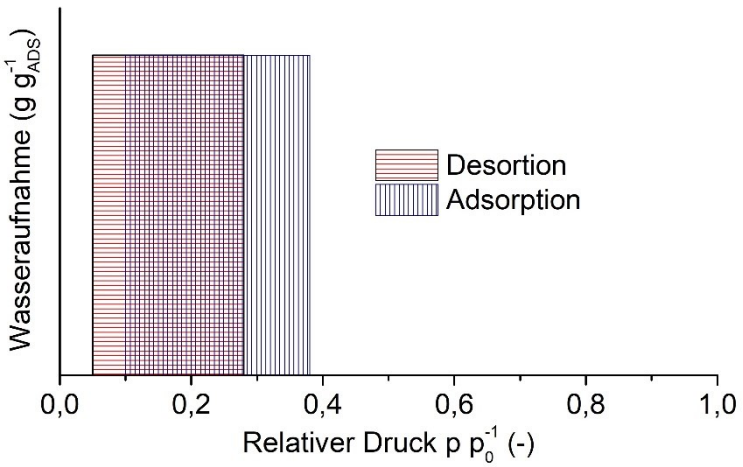

Abbildung 13: Gewünschte Wassersorptionseigenschaften eines Adsorbens in einer sorptionsgetriebenen Kältemaschine unter den angegebenen Bedingungen.

Tabelle 1: Wasserdampfdruck in Abhängigkeit von Temperatur.

Temp. (°C)	Wasserdampfdruck (mbar)	Temp. (°C)	Wasserdampfdruck (mbar)
0	6,11	10	12,28
20	23,39	25	31,70
30	42,47	35	56,29
60	199,46	70	312,01
80	474,14	90	701,82

1.3 Syntheseoptimierungen

Die Syntheseoptimierung von MOFs hat vor allem im letzten Jahrzehnt große Aufmerksamkeit auf sich gezogen, da eine Vielzahl von Strukturen erhalten werden konnte, welche für eine Reihe von potentiellen Anwendungen von großem Interesse sind. Das aus der konventionellen Synthese erhaltene MOF soll dabei auf eine einfache, schnelle, großskalige, kostengünstige und umweltfreundliche Route synthetisiert werden. Der Begriff konventionelle Synthese beschreibt die typische Solvothermalsynthese, welche häufig lösungsmittel-, zeit- und energieintensiv ist, jedoch bei Erstsynthesen bevorzugt wird.[53] Die Reaktionen findet dabei in geschlossenen Gefäßen unter autogenem Druck oberhalb des Siedepunktes der Lösungsmittel statt.[54] Die Reaktionstemperatur ist ein Hauptparameter bei der Synthese von MOFs. Während Solvothermalsynthesen oberhalb des Siepunkts des Lösungsmittels und erhöhtem Druck ablaufen, finden nicht-solvothermale Reaktionen unterhalb oder am Siedepunkt unter Umgebungsdruck statt, was die Syntheseanforderungen vereinfacht.[55]

Wird das Ziel einer industriellen Verwendung des MOFs verfolgt, werden alternative Syntheserouten wie elektrochemische Synthese, mechanochemische Synthese, sonochemische Synthese und mikrowellenunterstützte Synthese oftmals bevorzugt. Nachfolgend wird in Abbildung 14 eine Übersicht zu gängigen Synthesemethoden gegeben.

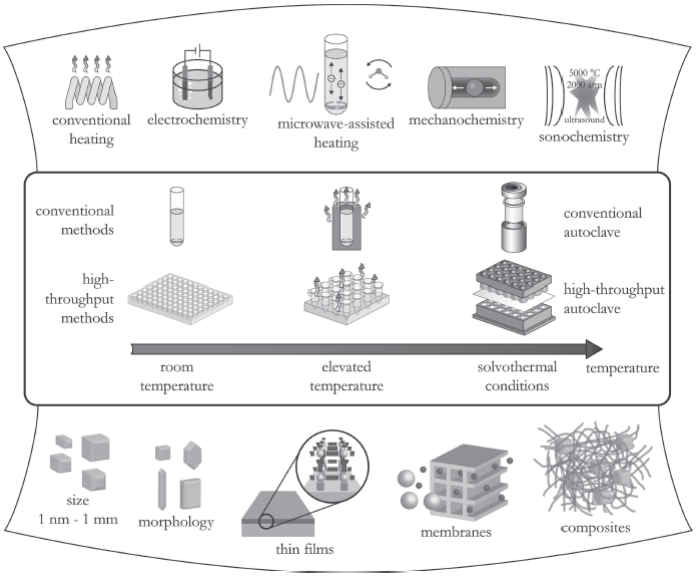

Abbildung 14: Übersicht zu gängigen Synthesemethoden. Nachdruck aus Lit. 55, © 2012, mit Genehmigung von American Chemical Society.

Die **elektrochemische Synthese** von MOFs wurde erstmals 2005 von Forschern der BASF für das HKUST-1 beschrieben.[56] Statt der Verwendung von Metallsalzen, werden Metallionen kontinuierlich durch anodische Auflösung in das Reaktionsmedium eingeführt und können anschließend mit dem zuvor gelösten Linker reagieren.[57] Diese Synthesemethode ermöglicht eine kontinuierliche Produktion und den Ausschluss von Anionen wie Nitrat, Perchlorat oder Chlorid während der Synthesen, was in einem industriellen Umfeld von großem Vorteil ist. Die Metallabscheidung auf der Kathode wird durch Verwendung protischer Lösungsmittel vermieden, wobei jedoch H_2 entsteht. Eine Alternative ist die Verwendung von Verbindungen wie Acrylnitril, Acrylsäure oder Maleinsäureestern, die bevorzugt reduziert werden. Bislang wurden allerdings nur einige, wenige Cu-, Zn- und Al-MOFs durch eine elektrochemische Synthese erfolgreich hergestellt.[55,58]

Mechanische Energie kann viele chemische Reaktionen auslösen.[59] Bei der **mechanochemischen Synthese** erfolgt der mechanische Bruch intramolekularer Bindungen, gefolgt von einer chemischen Umwandlung. Die mechanochemische MOF-Synthese hat den Vorteil, dass die Feststoff-Feststoff-Reaktion direkt zu pulverförmigen Produkten führt und die Materialien ohne zeitaufwändige Behandlungen wie Aufreinigungen für verschiedenste Anwendungen fertig stellt.[60] Kurze Reaktionszeiten (unter einem Tag), hohe Ausbeuten und kleine Partikel sind typische Merkmale für Produkte aus der mechanochemischen Synthese.[55] Es werden drei verschiedene mechanochemische Ansätze für die MOF-Herstellung unterschieden. Die einfachste Methode stellt das lösungsmittelfreie Mahlen (engl.: *Solvent-Free Grinding*; kurz SFG) dar. Das flüssigkeitsunterstützte Mahlen (engl.: *Liquid-Assisted Grinding*; kurz LAG) ist vielseitiger und schneller, da minimale Mengen an Flüssigkeit verwendet werden, welche Reaktion beschleunigen. Der dritte Ansatz ist Ionen- und Flüssigkeits-unterstützte Mahlen (engl.: *Ion-and-Liquid-Assisted Grinding*; kurz ILAG), bei dem sowohl minimale Mengen an Flüssigkeit als auch Spuren von Salzadditiven verwendet wird, um die MOF-Bildung zu beschleunigen.[61] Die mechanochemische Synthese wurde bereits für verschiedene MOFs wie HKUST-1, ZIF-8, Al-Fumarat, UiO-66 und weitere Zr-MOFs durchgeführt.[62,63]

Bei der **Sonochemie** hingegen wird die Reaktion mittels energiereichem Ultraschall durchgeführt. Ultraschall ist eine zyklische, mechanische Vibration mit einer Frequenz zwischen 20 kHz und 10 MHz.[55] Wechselwirkung zwischen Ultraschall und dem Lösungsmittel sorgen für zyklische Bereiche der Kompression (hoher Druck) und Verdünnung (niedriger

Druck). Im Niederdruckbereich fällt der Druck unter den Dampfdruck des Lösungsmittels und es bilden sich kleine Blässchen (Hohlräume), welche bis zur Instabilität wachsen und platzen. Dieser Prozess wird als Kavitation bezeichnet und führt zu einer raschen Energiefreisetzung mit Heiz- und Abkühlraten von > 1010 K s^{-1}, Temperaturen von ~ 5000 K und Drücken von ~1000 bar.[64] Sonochemische Methoden führen somit zu einer Verkürzung der Kristallisationszeit und zu einer deutlich geringeren Partikelgröße als bei der konventionellen Solvothermalsynthese. MOFs wie MOF-5 HKUST-1 Mg-MOF-74, PCN-6, IRMOF-9 und IRMOF-10 konnten bereits erfolgreich hergestellt werden.[65]

Die Einführung von Reaktionsenergie durch **Mikrowellenbestrahlung** ist eine etablierte Methode in der organischen Chemie, welche auch auf die Synthese anorganischer Materialien wie Zeolithen und MOFs übertragen wurde.[66,67,53] MW-unterstützte MOF-Synthesen bringen den Vorteil der Beschleunigung der Kristallisation und die Bildung von nanoskaligen Produkten.[55] Die Mikrowellenstrahlung sorgt aufgrund der schnellen Kinetik von Kristallkeimbildung und -wachstum für isolierte Produkte im Nanobereich. Auch ist eine Verbesserung der Produktreinheit und eine selektive Synthese von Polymorphen möglich.[68] Die erste Mikrowellensynthese von MOFs gelang an MIL-100(Cr), wobei bei gleicher Reaktionstemperatur die Synthesezeit von 96 h auf 4 h ohne Verluste in der Ausbeute reduziert wurde.[69]

(Microwave assisted-) Dry gel conversion

Die Trockengelumwandlung (engl.: *Dry gel conversion*, kurz DGC) ist ein alternatives Syntheseverfahren zur Herstellung von MOFs, welches von Zeolithen und Zeolithmembranen adaptiert wurde.[70,71] Hierbei erfolgt die Umsetzung eines Trockengels in der Dampfphase.

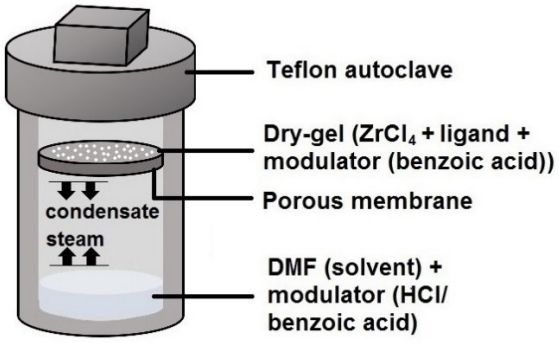

Abbildung 15: Übersicht zu Trockengelumwandlung am Beispiel der Synthese von UiO-MOFs. Nachdruck aus Lit. 72, mit Genehmigung von The Royal Society of Chemistry.

Am Boden eines Teflonbehälters wird eine kleine Menge an Lösungsmittel vorgelegt, die festen Ausgangsmaterialien hingegen werden auf einem Sieb angebracht. Daraus resultiert eine physikalische Trennung vom Lösungsmittel und dem Reaktantengemisch (siehe Abbildung 15). Die Vorteile der DGC-Methode liegen in der Minimierung der Abfallentsorgung, der Verringerung des Reaktionsvolumens und der vollständigen Umwandlung des Gels in einheitliche kristalline Materialien mit hoher Ausbeute.[65] Aus dieser Trennung resultiert einer der großen Vorteile von DGC, nämlich dass nach der Reaktion das Lösungsmittel weitgehend unkontaminiert zurückgewonnen werden kann. Kürzlich wurden einige MOFs und deren Komposite wie ZIF-8, ZIF-67, MIL-100(Fe), MIL-101(Cr) und HKUST-1/Fe_3O_4 Komposit mittels DGC hergestellt.[73-76] In der vorliegenden Arbeit konnte nachgewiesen werden, dass bei der erfolgreichen Synthese von UiO-MOFs das Lösungsmittel (DMF) über mindestens 5 Zyklen wiederverwendet werden kann (vgl. 3.1). Die Synthese von UiO-66, MIL-140A, MIL-100(Fe) und Al-Fumarat konnte zusätzlich in einer mikrowellenassistierter DGC erfolgreich hergestellt werden, wobei diese Methode zum ersten Mal an MOFs durchgeführt wurde (vgl. 3.2).

1.4 Formgebung von MOFs

Im Allgemeinen können poröse Materialien entweder in situ während der Synthese oder durch einen postsynthetischen Prozess in verschiedene Formen gebracht werden, beispielsweise durch in ein binderbasiertes Komposit.[77,78] Im ersten Fall werden die Kristallite direkt in der gewünschten Form beispielsweise als dünne Filme gebildet. Diese Art der Beschichtung wurde bereits bei der Syntese von Zeolithen vielmals angewendet.[77,79] Im zweiten Fall ist die Formgebung ein sekundärer Prozess, welcher nach Abschluss der Synthese erfolgt. Dabei werden Polymere als Bindemittel eingesetzt, welche applikationsspezifisch ausgewählt werden können. Typische Bindemittel sind Polyvinylalkohol, Polyetylenimin, Polyvinylpyrrolidon, Graphite, Celluloseester, Chitosan, ρ-alumina, Alginat und Silicophen.[78,80-84] Mittels der Binder können die porösen Materialien in verschiedenste Formen überführt werden. Die Wahl eines Formverfahrens kann von der spezifischen Anwendung abhängen darunter Granulate, Pellets, Monolithe, Schichten/ dünnen Filme, Schwämme und Papersheets (siehe Abbildung 16).[78,82,85]

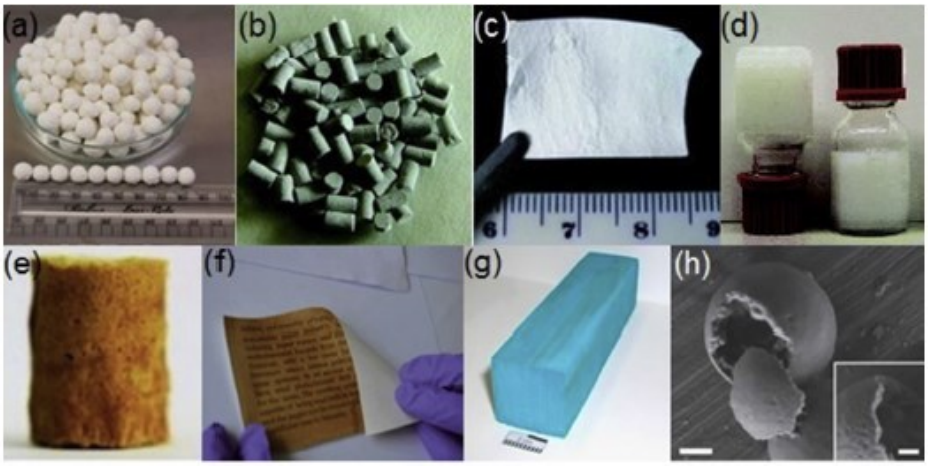

Abbildung 16: Übersicht über die möglichen Formen. Nachdruck aus Lit. 82, © 2018, mit Genehmung von Elsevier.

Die Eigenmerkmale des ursprünglichen porösen Materials spielen eine entscheidende Rolle bei der Formgebung. Die Kristallinität und Porenzugänglichkeit kann bei falscher Auswahl des Bindemittels reduziert und somit die gewünschten Eigenschaften des porösen Materials eingeschränkt oder sogar gänzlich verloren werden. Auch die mechanische und chemische Stabilität des hergestellten Körpers müssen gegeben sein.

1.4.1 Granulate/Tabletten

Die Granulierung ist ein Prozess der Agglomeration von pulverförmigen und festen Materialien, ohne deren chemische Identität zu ändern. Diese Formgebungsmethode ist in der chemischen und pharmazeutischen Industrie weit verbreitet, um Pulvermaterialien besser lagern und verarbeiten zu können. Typischerweise erreichen die Granulate eine Größe zwischen 0,2 und 4,0 mm. Bei Granulierungsprozessen unterscheidet man zwischen der Nass- und Trockengranulierung.[86]

Bei der Nassgranulierung wird ein flüchtiges Lösungsmittel verwendet, welches anschließend verdampft. Teilweise reichen jedoch die Kohäsionskräfte nicht aus, weshalb ein Bindemittel zur Erhöhung der mechanischen Stabilität eingesetzt wird. Einige typische Bindemittel sind in der Einleitung aufgelistet. Die Eigenschaften des gebildeten Granulats hängen stark vom porösen Material, der Oberflächenspannung und Viskosität des Bindemittels und den Wechselwirkungen zwischen ihnen ab.[82,84] Eine schematische Darstellung der Nassgranulierung ist in der Abbildung 17 gegeben.

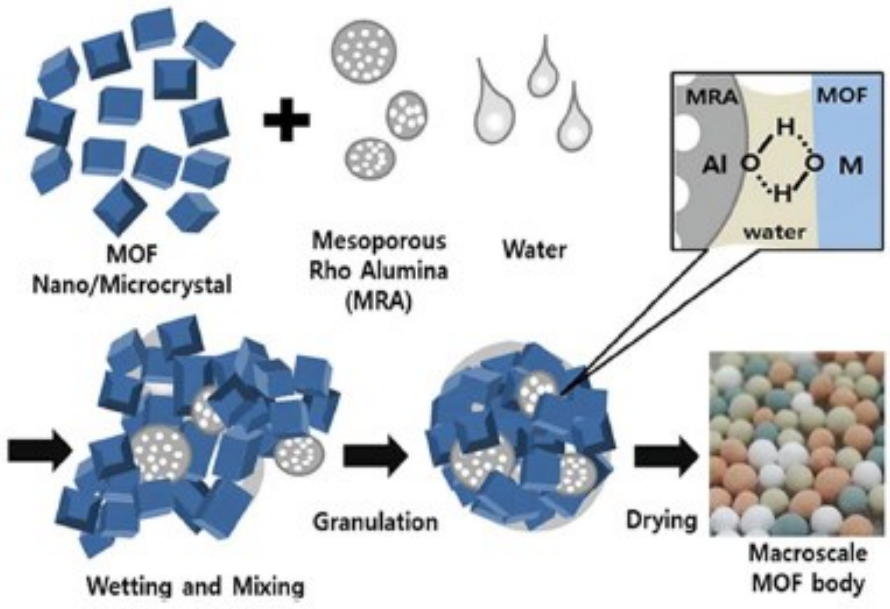

Abbildung 17: Schematische Darstellung der Nassgranulierung. Nachdruck aus Lit. 84, mit Genehmigung von The Royal Society of Chemistry.

Die Trockengranulierung hingegen wird verwendet, um Granulate ohne Einsatz eines Lösungsmittels zu bilden. Um ein Granulat ohne Feuchtigkeit bilden zu können, müssen die Pulver verdichtet werden. Bei diesem Verfahren wird das Pulver unter hohem Druck kompaktiert. Diese Methode findet Gebrauch, wenn das Produkt lösungsmittel- und hitzeempfindlich sein kann. Bei der Trockengranulierung werden entweder Tabletten in einer Tablettenpresse hergestellt (im Abschnitt 3.3 als large-scale product bezeichnet), oder das Pulver wird in einem Walzenkompaktor zwischen zwei Walzen in Blattform gepresst. Bei einer Tablettenpresse wird je nach Ausgangmaterial ein Additiv zugesetzt, um die Fließeigenschaften des Pulvers zu verbessern. Die größte Schwierigkeit bei der Granulierung, vor allem bei der Tablettierung, ist die Adsorptionskapazität/ Porösität des MOFs beizubehalten. Beispiele für die Trockengranulierung sind in der Arbeit Dhainaut *et al.* gegeben, darunter UiO-66, UiO-66-NH_2, UiO-67 und HKUST-1. Abhängig vom MOF-System und dem genutzten Druck während der Kompaktierung reduziert sich die BET-Oberfläche kaum, kann aber teilweise drastisch um 80% abnehmen.[87] Eine schematische Darstellung der Kompaktierung ist in der Abbildung 18 gegeben.

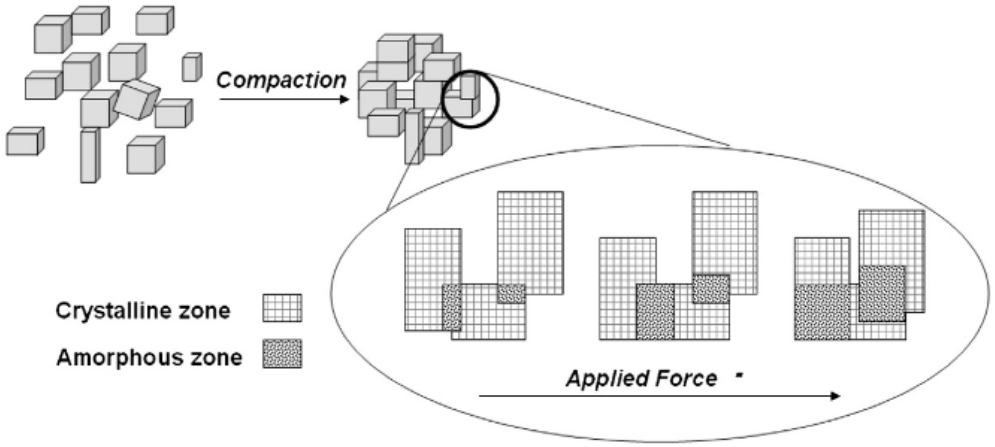

Abbildung 18: Schematische Darstellung der Kompaktierung. Nachdruck aus Lit. 88, © 2014, mit Genehmung von Elsevier.

Werden kristalline Materialien zu stark kompaktiert, kommt es zur Zerstörung der kristallinen Phase. Je höher dabei die angewendete Kraft ist, desto intensiver findet die Amorphisierung statt. Dieses Phänomen gilt sowohl für die Trockengranulierung als auch für –pelletierung, die im nächsten Abschnitt näher erläutert wird.

1.4.2 Pellets

Das Formen von Pellets ist die älteste und einfachste Formgebungsmethode für MOFs bei dem das Pulver, analog zur Granulierung, mit oder ohne Zugabe eines Bindemittels (nass oder trocken) durch Aufbringen von Druck zu Agglomeraten geformt wird. Die Pelletierung und Granulierung unterscheiden sich jedoch in der Form der resultierenden Agglomerate. Während Granulate kugelförmig sind, weisen Pellets eine zylindrische Form auf. In der Regel erfolgt bei der Pelletierung zur Steigerung der mechanischen Stabilität die Zugabe eines Binders. Wie zuvor erwähnt, kann die Zugabe auch einen negativen Einfluss auf die Porenzugänglichkeit des MOFs nehmen. Finsy *et al.* konnten durch Zugabe von 13 wt% Polyvinylalkohol als Bindemittel mechanisch stabile Pellets herstellen, während das zugängliche Porenvolumen um 32% abnahm.[89] Moreira *et al.* stellten Pellets in einer Tablettenpresse (Trockenpelletierung) mit 99 wt% MOF-Anteil (UiO-66) und 1 wt% Graphit her, bei denen die BET-Oberfläche des Materials um knapp 22 % abnahm.[90] Auch Bazer-Bachi *et al.* kompaktierten HKUST-1 mit einer BET-Oberfläche von 1897 $m^2\ g^{-1}$, welche je nach verwendetem Druck auf 1377 $m^2\ g^{-1}$ (0,3 kN) und 453 $m^2\ g^{-1}$ (5kN) verringert wurde.[88]
Auch die Extrusion ist eine beliebte und weitverbreitete Methode zur Herstellung von Pellets. Kürzlich publizierten Khabzina *et al.* die Herstellung von Silikonharz-basierten UiO-66-COOH Pellets (mit 1,5 mm Durchmesser und 3,0 mm Länge) zur Anwendung in NH_3-Filteranlagen.[91] Viele weitere MOFs darunter HKUST-1, ZIF-8, Al-Fumarat und weitere Zr-MOFs wurden ebenfalls für verschiedene Anwendungen im Extruder verarbeitet.[62,63] Die Pelletisierung der MOF-Kristalle wird dabei durch mechanisches oder hydraulisches Pressen durchgeführt.

1.5 Experimentelle Grundlagen zur Auswertung

Für die Untersuchung von porösen Materialien ist eine Charakterisierung hinsichtlich der Kristallinität und der Porenstruktur (Porengröße, Porenvolumen, spezifische Oberfläche, etc.) von besonderer Bedeutung. Dafür werden im Rahmen dieser Arbeit die Kristallinität mittels Pulver-Röntgenbeugung (engl.: Powder X-Ray Diffraction, kurz PXRD) und die Porenstruktur mittels Stickstoffsorption untersucht. Die PXRD und die Physisorption einschließlich der genutzten Auswertemethoden soll nachfolgend beschrieben werden.

1.5.1 Pulverröntgendiffraktometrie

Die Pulverröntgendiffraktometrie ist ein etabliertes Verfahren zur Strukturaufklärung von kristallinen Materialien. In der vorliegenden Arbeit wird diese als einfache und schnelle Methode zur Verifizierung einer erfolgreichen Synthese durch den Abgleich mit Referenzdiffraktogrammen genutzt. Die PXRD basiert auf der Beugung von Röntgenstrahlung an der Elektronenhülle der Atome. Die auftreffenden Wellen können je nach Atomabstand konstruktiv oder destruktiv miteinander interferieren. Konstruktive Interferenz, resultierend in einem Reflex, tritt nur bei bestimmten Winkeln auf, die nach der Bragg-Gleichung in Beziehung zum Netzebenabstand des Kristalls steht:

$$n \cdot \lambda = 2 \cdot d \cdot sin(\Theta)$$

n = Beugungsgrad; λ = Wellenlänge; d = Abstand der Gitterebenen; θ = Einfallswinkel

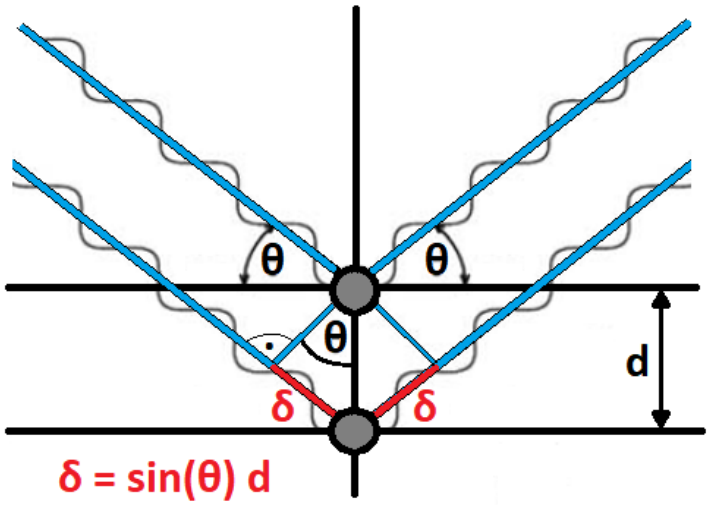

Abbildung 19: Strahlengang an einer Oberfläche mit den Parametern für die Bragg-Gleichung.

Die Bedingung für die konstruktive Interferenz ist somit erfüllt, wenn der Gangunterschied 2dsin(θ) ein ganzzahliges Vielfaches der Wellenlänge nλ beträgt. Somit kommt es zu einer Überlappung (bzw. Verstärkung) der Wellenmaxima (vgl. Abbildung 19). Kommt es hingegen zu einer Verschiebung der Wellenmaxima, resultiert eine Auslöschung (bzw. Aufhebung) der Wellen, bezeichnet als destruktive Interferenz. Es resultiert kein Reflex.

1.5.2 Physisorption

Die Bestimmung der Oberflächengröße und der Porosität eines Materials wird mittels Physisorption inerter Gase durchgeführt. Die Stickstoffsorption (77 K) hat sich bei porösen Materialien als Standardmethode etabliert. Stickstoff hat dennoch einige Einschränkungen, insbesondere für die Charakterisierung mikroporöser Materialien oder Materialien mit geringen Oberflächen. Alternativen zur Analyse von mikroporösen Systemen sind die Argonsorption (87 K aber auch 77 K) bzw. die CO_2-Sorption (195 K, 273 K, 298 K) im Fall vom Ultramikroporen (Poren <0,7 nm). Die Charakterisierung von mikroporösen Materialien mit Stickstoff bei 77 K birgt einige Schwierigkeiten, da das Auffüllen von Poren mit 0,5 - 1,0 nm Durchmesser bei sehr niedrigen relativen Drücken von $p\ p_0^{-1} = 10^{-7} - 10^{-5}$ (p = gemessener Druck, p_0 = Sättigungsdruck) erfolgt. In diesem Niederdruckbereich sind die Diffusions- und Gleichgewichtsprozesse sehr langsam. Argon bei 87 K hingegen füllt Mikroporen mit gleicher Porengröße bei höheren relativen Drücken von $p\ p_0^{-1} = 10^{-5} - 10^{-3}$, woraus kürzere Gleichgewichtszeiten und Analysezeiten folgen. Zusätzlich ist bekannt, dass das Quadrupolmoment des Stickstoffmoleküls verantwortlich ist für die spezifische Wechselwirkung mit einer Vielzahl von funktionellen Oberflächengruppen und Ionen (vgl. Zeoltihe).[92] Dies beeinflusst nicht nur die Orientierung des adsorbierten Stickstoffmoleküls auf dem Adsorbens (was stark die Oberflächenberechnung beeinflussen kann, wie im IUPAC-Bericht beschrieben),[93] sondern beeinflusst auch stark den Mikroporenfülldruck und verschiebt den Porenfüllbereich auf sehr niedrige Drücke (typischerweise in einen Bereich unter $p\ p_0^{-1} = 10^{-5}$). Trotz der zuvor genannten Nachteile, wird die Stickstoffsorption zur Charakterisierung bevorzugt, da eine bessere Vergleichbarkeit mit Literaturwerten gegeben ist. Die Argonsorption ist vergleichsweise deutlich seltener zu sehen. Als beste Alternative für Materialien mit geringer Oberfläche hingegen gilt die Krypton-Sorption, welche in der Forschung eher selten zu finden ist.[94] Da die Oberfläche der hergestellten Materialien in dieser Arbeit hoch ist, hat die Krypton-Sorption keine Bedeutung.

Auswertemethoden der Stickstoffsorption

Eine Sorptionsisotherme stellt das adsorbierte Volumen V_{ads} (bzw. das desorbierte Volumen V_{des}) des Messgases (Adsorptiv) in Abhängigkeit vom Relativdruck $p\ p_0^{-1}$ bei einer konstanten

Temperatur dar. Die Adsorptionsisotherme wird Punkt für Punkt aufgenommen, indem das eingeleitete Gasvolumen zur festen Phase (Adsorbens) schrittweise gesteigert wird. Die wichtigsten Vergleichsmerkmale poröser Materialien und die zugehörigen Auswertemethoden, die zu ihrer Berechnung in dieser Arbeit verwendet werden, sind in Tabelle 2 aufgelistet.

Tabelle 2: Auswertemöglichkeiten aus der Stickstoffsorption.

Eigenschaft	**Kürzel**	**Auswertebereich[a]**	**Auswertemethoden**
Spezifische Oberfläche	S_{BET}	0,05-0,30	Multipoint-BET[95]
Totales Porenvolumen	V_{total}	0,90	Gurvich-Regel [96,97]
Mikro-/Mesoporenvolumen	V_{meso}/V_{mikro}	0,2-0,4	Gurvich-Regel, t-Plot [98,99,100]

[a] Relativdruck p p_0^{-1}

In den folgenden Abschnitten werden die theoretischen Grundlagen und die genutzten Auswertemethoden (BET, t-Plot) für die Stickstoff-Sorption näher erläutert.[100-103]

Spezifische Oberfläche nach der BET-Methode

Die Brunauer-Emmett-Teller-Methode (kurz BET-Methode) ist die am weitesten verbreitete Methode zur Beurteilung der Oberfläche poröser Materialien.[104,105] Die Formel zur Berechnung der BET-Oberfläche lässt sich wie folgt beschreiben:

$$\frac{1}{W((p_0/p)-1)} = \frac{1}{W_m C} + \frac{C-1}{W_m C}\left(\frac{p}{p_0}\right)$$

W = Gewicht des adsorbierten Gases bei einem bestimmten relativen Druck p p_0^{-1}; W_m = Gewicht des Adsorbats bei einer Monoschichtlage; C = BET-Konstante, Adsorptionsenergie bei Monolage (Hinweis auf Größe der Adsorbens-Adsorbat-Wechselwirkungen)

Die BET-Oberfläche kann unter bestimmten sorgfältig kontrollierten Bedingungen für nichtporöse, makroporöse oder mesoporöse Feststoffe mit definierten Isothermen vom Typ II oder Typ IVa im relativen Druckbereich p p_0^{-1} 0,05 - 0,30 angewendet werden. Eine Annahme der BET-Methode ist, dass sich an den Porenwänden eine Monoschicht bildet, wobei dieser

Wert für die Berechnung (vgl. W_m) genutzt wird. Bei Materialien mit Mikroporen jedoch ist es schwierig die Monoschichtadsorption von der Mikroporenfüllung zu unterscheiden, da die Monoschichtadsorption bei relativen Drücken unter 0,15 bereits abgeschlossen ist.[106] Auch im unteren Bereich der mesoporösen Materialien (Molekularsieb mit Porenweiten von weniger als 4 nm) ist teilweise eine klare Differenzierung nicht möglich, da die Porenkondensation und die Monoschicht-Multischicht-Bildung sich überlagern. Dies kann zu einer deutlichen Überschätzung der Monoschichtkapazität führen.[104] Zur besseren Vergleichbarkeit der Ergebnisse empfiehlt sich somit den BET-Auswertungsbereich anzugeben.

Zu Beginn ist es notwendig, eine Physisorptionsisotherme in das „BET-Diagramm" umzuwandeln, um daraus einen Wert für die BET-Monoschichtkapazität W_m abzuleiten. Dazu werden die Punkte aus dem zuvor genannten Druckbereich ausgewählt und umgerechnet. Das Volumen V, erhalten aus der Isotherme, wird mittels idealem Gasgesetz in die Masse W umgerechnet. W wird mit dem zugehörigen relativen Druck in 1/ (W((p_0/p)-1) umgeformt und anschließend gegen p p_0^{-1} aufgetragen. Die BET-Gerade wird typischerweise aus mindestens 5 Messwerten (5-Point-BET) dargestellt. Mittels der Steigung s und dem Ordinatenabschnitt i der Gerade lässt sich das Gewicht der Monolage W_m wie folgt berechnen:

$$W_m = \frac{1}{s+i}$$

Nun kann über die Gleichung die Gesamtoberfläche der Probe S_t berechnet werden, welche abschließend auf die eingewogene Probenmenge normiert werden muss.

$$S_t = \frac{W_m N A_{cs}}{M} \; ; \; SBET = \frac{S_t}{m}$$

SBET = Oberfläche normiert auf g; S_t = Gesamtoberfläche der Probe; N = Avogadrozahl; A_{CS} = Oberflächenbedarf eines Moleküls Stickstoff, 16,2 $Å^2$ = 16,2x10^{-20} m^2; M = molare Masse des Adsorptivs; m = Masse des Produktes

SBET setzt sich zusammen aus einer inneren und äußeren Oberfläche. Diese lässt sich mittels weiterer Methoden (z. B. t-Plot-Methode) auftrennen. Diese Methode wird anschließend näher erläutert.

Porenvolumen (Gurvich-Regel)

Eine weitere wichtige Kenngröße poröser Materialien ist das Porenvolumen, wobei bei mikro- und mesoporösen Systemen zwischen dem Gesamtporenvolumen V_{total}, dem Mikroporenvolumen V_{Mikro} und dem Mesoporenvolumen V_{Meso} unterschieden werden kann. Nach der Gurvich-Regel erreicht die Isotherme beim Relativdruck von p p_0^{-1} = 1,0 das Plateau, bei dem alle Poren mit flüssigem Adsorptiv gefüllt sind.[103] Unter realen Bedingungen jedoch treten Effekte wie die Adsorption außerhalb der Poren (z. B. in den Partikelzwischenräumen) auf, welche einen starken Anstieg der Kurve ab einem Relativdruck von p p_0^{-1} = 0,9 verursacht. Aus diesem Grund wird zur Berechnung des totalen Porenvolumens V_{total} der letzte Punkt des vorhandenen Plateaus herangezogen (in der vorliegenden Arbeit immer p p_0^{-1} = 0,9). Das totale Porenvolumen lässt sich mittels folgender Formel berechnen:

$$Vtotal = V1 = \frac{V(STP)\ M\ P}{\rho\ R\ T} = V(STP) * 1{,}547 * 0{,}001$$

M = Molmasse eines Stickstoffmoleküls; ρ = Dichte flüssliger Stickstoff; R = Gaskonstanten, T = Temperatur bei STP; P = Luftdruck bei Standardbedingungen.

Für Isothermen, bei denen kein Plateau gegen p p_0^{-1} = 1.0 erreicht wird (vgl. Typ II) eignet sich die Gurvich-Regel zur Berechnung des totalen Porenvolumens nicht. Auch hier sollte, analog zur BET-Oberflächenberechnung, der Relativdruck angegeben werden, an dem die Gurvich-Regel angewendet wurde.

Mikro- und Mesoporenanalyse (t-Plot-Methode)

Liegen in porösen Materialien unterschiedlich große Porensysteme nebeneinander vor, können diese durch Anwendung bestimmter Auswertemethoden genauer untersucht werden. Zur Berechnung des Mikro-/Mesoporenvolumens lässt sich der t-Plot-Methode nach J. de Boer *et al.* verwenden.[98,99] Das Verfahren nach de Boer *et al.* basiert auf der Auftragung des adsorbierten Volumens gegen die statistische Schichtdicke t. De Boer *et al.* erstellten t-Kurven für verschiedene Standardmaterialien (darunter Al_2O_3, TiO_2, MgO, ZrO_2 und $BaSO_4$), woraus jedem Relativdruck p p_0^{-1} eine Schichtdicke t zugeordnet werden kann. Der relative Druck lässt sich mittels folgender Formel in die statistische Schichtdicke umrechnen:

$$t = \left[\frac{13{,}99}{\log\left(\frac{p0}{p}\right) + 0{,}034}\right]^{1/2} \text{ Å}$$

Sorptionsisothermen können mittels dieser Formel in V-t-plots umgewandelt werden.

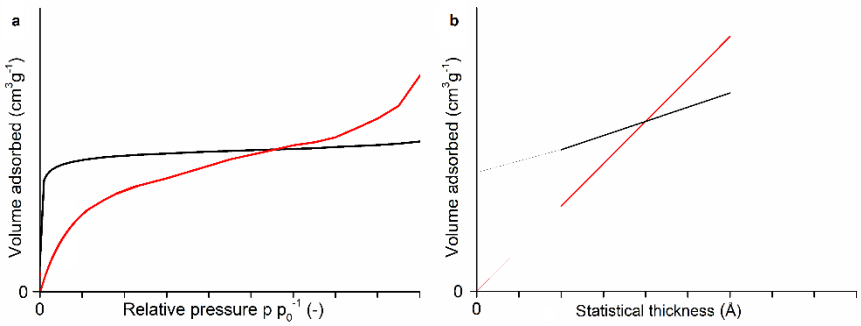

Abbildung 20: Schematische V-t-Plot-Auswertungen aus N_2 Sorptionsisothermen: Material ohne Mikroporen (rot) und mit Mikroporen (schwarz).

Wählt man nun den korrekten Auswertebereich (typischerweise Relativdruck von 0,2-0,4) aus, lässt sich eine Gerade erstellen. Mittels der Steigung s und dem Ordinatenabschnitt i lässt sich nun die Oberfläche und das Porenvolumen der Mikro-/Mesoporen berechnen. Dazu können folgende Formeln verwendet werden:

$$St = s * 15{,}47\frac{m2}{g};\ Vt = Vporen = i * 1{,}547 * 0{,}001\frac{cm3}{g}$$

1.5.3 Hochdrucksorption

In jüngster Zeit wird in der Forschung und Entwicklung ein großer Aufwand für die Gastrennung und Gasspeicherung von CO_2 (H_2, CH_4 und weiteren Gasen) betrieben, da eine Reduzierung der ausgestoßenen Treibhausgase erforderlich ist. Poröse Materialien, insbesondere MOFs, haben das Potential in der Gasspeicherung und –trennung eingesetzt zu werden.[4] Ein wichtiger Schritt zur Anwendung ist die Bestimmung der Adsorptionskapazitäten unter realen Bedingungen, welche mittels der Hochdruckadsorption durchgeführt werden können.

Hochdruckadsorptionsmessungen können, analog zu Niederdruckmessungen, sowohl volumetrisch als auch gravimetrisch durchgeführt werden. Die Rubotherm ISOSORP® HyGrA ist eine gravimetrische Hochdrucksorptionsanlage, die in dieser Arbeit genutzt wurde. Diese nutzt eine Magnetschwebewaage mit einer Auflösung von 0,01 mg ± 0,03 mg, die die Massenänderung einer Probe in Abhängigkeit von der Druckänderung vermisst.

Die Hochdrucksorptionsmessung setzt sich aus drei Einzelmessungen zusammen. Zuerst wird eine Leermessung mit dem zu adsorbierenden Gas durchgeführt. Die Leermessung (engl. *Blank Measurement*) dient zur Bestimmung der Masse (m^{SC}) und des Volumens (V^{SC}) des Probenbehälters (engl.: *Sample Container*, kurz SC). Hierbei wird die Masse gegen die Dichte des Messgases aufgetragen. Die Steigung s gibt das Volumen V^{SC}, der Ordinatenabschnitt i hingegen die Masse m^{SC} wieder.

Anschließend wird eine Auftriebskorrekturmessung (engl. *Bouyancy Measurement*) mit einer aktivierten Probe durchgeführt. Diese erfolgt mit einem Inertgas wie Helium, da es vom porösen Material nicht adsorbiert wird. Der Auftriebseffekt ist die Masse der Reaktionsgasatmosphäre und wirkt der Gravitationskraft entgegen, was zu einer scheinbaren Abnahme der Probenmasse führt. Der Auftriebseffekt muss korrigiert werden, um die korrekte Probenmasse zu ermitteln. Die Masse (m^S) und das Volumen (V^S) der Probe können wie folgt bestimmt werden:

Auftriebskorrekturmessung:	$(m^{SC} + m^S)$	und	$(V^{SC} + V^S)$
- Leermessung:	m^{SC}	und	V^{SC}
Differenz:	m^S	und	V^S

Die Dichte der Probe errechnet sich wie folgt:

$$\rho S = \frac{mS}{VS}$$

Der statische Auftrieb hat bei Hochdrucksorptionsmessungen einen hohen Einfluss. Diese ist eine der Schwerkraft entgegengesetzte Kraft auf einen Körper in Flüssigkeiten oder Gasen:

$$Fb = (Vsc + Vs + Va) * \rho\,(p,T,y) * g$$
$$Fg = (msc + ms + ma) * g$$

F = Kraft; b = buoyancy (Auftrieb); SC = Sample Container; V = Volumen; S = Sample; g = Erdbeschleunigung; A = Adsorbat; M = Masse; ρ = Dichte der Fluids in Abhängigkeit des Druckes p, der Temperatur T und der Gaszusammensetzung y

Aus der Differenz der Gravitationskraft und der Auftriebskraft, lässt sich die auf den Probenbehälter wirkende experimentelle Kraft ermitteln:

$$Fexp = Fg - Fb = g * (msc + ms + ma - (Vsc + Vs + Va) * \rho\,(p,T,y))$$

Durch Umformen der Gleichung kann die Masse des Adsorbats bestimmt werden (die Massendifferenz $\Delta m = m^{SC}+m^{S}$ wird experimentell bestimmt):

$$\Delta m = \frac{Fexp}{g} = msc + ms + ma - (Vsc + Vs + Va) * \rho\,(p,T,y)$$
$$ma = \Delta m - msc - ms + (Vsc + Vs + Va) * \rho\,(p,T,y)$$

Zur Bestimmung des Volumens des Adsorbats V^A wird angenommen, dass die Dichte der adsorbierten Phase näherungsweise der Flüssigkeitsdichte in einem Referenzzustand ($\rho_{ads} = \rho_{liq}$, Siedepunkt bei 101325 Pa) entspricht, ρ(p,T,y) wird aus der equtation of state (EOS) erhalten. Das Δm wird experimentell in der dritten Messung (mit Messgas) bestimmt, sodass die adsorbierte Masse m^A kalkuliert werden kann. Die Sorptionsisotherme wird durch Auftragung der adsorbierten Masse in Abhängigkeit vom Druck erhalten.

2. Aufgabenstellung

Die folgende Dissertation wurde im Rahmen des OPTIMAT-Projektes angefertigt. Das übergeordnete Ziel des Projekts OPTIMAT war die Entwicklung neuer mikroporöser Materialien und Komposite für den Einsatz in thermisch getriebenen Wärmepumpen und Klimaanlagen. Der Fokus der Dissertation lag hierbei auf der Syntheseoptimierung und Charakterisierung geeigneter Plattform-MOFs, der Herstellung von Polymer/MOF Kompositen zur Formgebung, sowie der Übertragung des Komposits in einen vorindustriellen Maßstab zur Anwendung in einer Kältemaschine.

Bei der Syntheseoptimierung sollte der Fokus auf UiO-MOFs gelegt werden, welche seit längerer Zeit im Mittelpunkt der Forschung stehen. Ziel der Optimierung war eine umweltfreundlichere Syntheseroute, welche ein hochkristallines Produkt mit hoher BET-Oberfläche liefert. Die hohe Synthesedauer der Solvothermalsynthese sollte mittels einer mikrowellenassister Trockengelumwandlung verkürzt werden.

Die Formgebung von MOFs soll durch Einsatz des organischen Polymers PVA durchführt werden, da sowohl die Hydrophilie als auch die Porenzugänglichkeit des Polymers vielversprechend erschienen. Hierbei sollten verschiedene Granulierungsmethoden wie Gefriergranulierung und Kompaktierung durchgeführt werden. Die hergestellten PVA/MOF Komposite sollten auf die Zyklenstabilität sowie die mechanische Stabilität überprüft, in einen vorindustriellen Maßstab gebracht und anschließend in einer sorptionsgetriebenen Kältemaschine eingesetzt werden. Dabei sollte das Ziel einer niedrigtemperatur-getriebenen Kältemaschine verfolgt werden.

3. Ergebnisse/Publikationen

In den Kapitel 3.1, 3.2 und 3.3. sind die Hauptergebnisse der Dissertation aufgeführt, die in internationalen Journalen publiziert bzw. zur Publikation eingereicht (3.3 submitted) wurden. Jede Publikation beinhaltet eine kurze Zusammenfassung und den Beitrag des Autors an der Veröffentlichung. Die Abbildungs-, Tabellen- und Quellennummerierungen im diesem Abschnitt folgen nicht der Nummerierung im Haupttext. Die Nummerierung erfolgt nach der ursprünglichen Reihenfolge der Veröffentlichungen. Weitere, unveröffentlichte Ergebnisse sind in den Kapiteln 4.1 bis 4.4. aufgeführt.

3.1 Environmentally benign dry-gel conversions of Zr-based UiO metal–organic frameworks with high yield and the possibility of solvent re-use

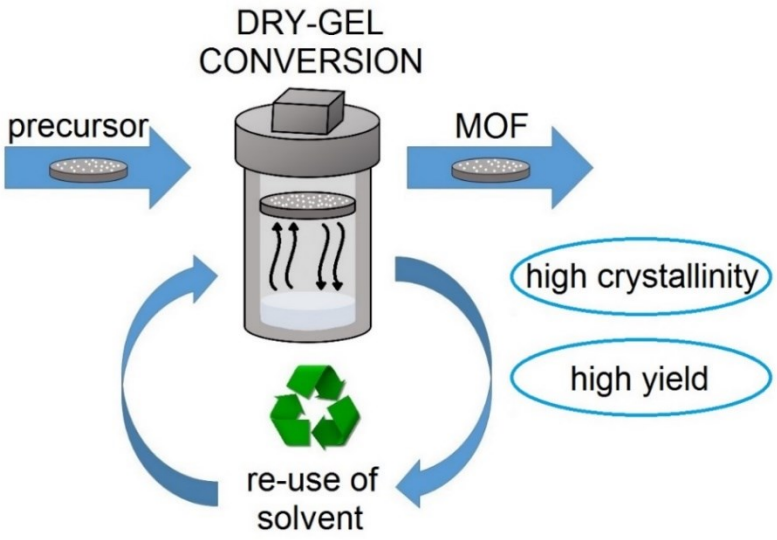

Zusammenfassung:
In dieser Arbeit wird eine alternative Synthesemethode für Zr-basierte Metall-organische Gerüstverbindungen (MOFs), die Trockengelumwandlung (engl.: *Dry-gel conversion*; kurz DGC), vorgestellt. Es konnten nano- bis mikroskaliges UiO-66, UiO-66-NH_2 und UiO-67 MOFs mit hoher Kristallinität, Oberfläche und Ausbeute hergestellt werden. Dabei wurde nur 1/6 oder weniger des Lösungsmittels, im Vergleich zur klassichen Solvothermalsynthese, verwendet. Darüber hinaus wird gezeigt, dass die Wiederverwendung des Lösungsmittels in mindestens fünf Synthesegängen möglich ist. Dies macht die DGC-Methode zu einem ökologischen und äußerst lösungsmittelökonomischen Weg, um UiO-MOFs zu erhalten.

Meine Beiträge:
- Experimentelle Arbeiten und Analytik (reproduziert von T. Diment; Ausnahme TGA und REM)
- Schreiben des Manuskripts, Erstellen der Abbildungen (Ausnahme: Figure S1) und Tabellen

- REM-Bilder wurden aufgenommen von Carsten Schlüsener, Sandra Nießing und Dennis Dietrich
- Alexa Schmitz führte die thermogravimetrischen Analysen durch
- Korrekturen erfolgten durch Herrn Prof. Christoph Janiak

Dieser Abschnitt basiert auf der Publikation:
S. Gökpinar, T. Diment and C. Janiak*, *Dalton Trans.*, 2017, **46**, 9895–9900.
Impact factor 2017: 4.099

Dalton Transactions

PAPER

View Article Online
View Journal | View Issue

Cite this: *Dalton Trans.*, 2017, **46**, 9895

Environmentally benign dry-gel conversions of Zr-based UiO metal–organic frameworks with high yield and the possibility of solvent re-use†

Serkan Gökpinar, Tatyana Diment and Christoph Janiak *

Received 11th May 2017,
Accepted 30th June 2017

DOI: 10.1039/c7dt01717k

rsc.li/dalton

Herein we report an alternative synthesis method for Zr-based UiO metal–organic frameworks (MOFs), namely dry-gel conversion (DGC). It was possible to synthesize nano- to microsized UiO-66, UiO-66-NH_2 and UiO-67 with high crystallinity, high surface area and increased yield using only one-sixth or less of the solvent volume compared to the solution synthesis on the same scale. Additionally, it is shown that solvent re-use is possible over at least five synthesis runs making the DGC method an ecological and extremely solvent-economical route to obtain Zr-based UiO-MOFs with reproducible results.

Introduction

Metal–organic frameworks (MOFs) are potentially porous materials consisting of metal ions or metal clusters connected by organic ligands[1,2] and are actively investigated towards various applications.[3–6]

Among the most intensively studied MOFs is the isoreticular UiO-series, especially UiO-66 (UiO = University in Oslo),[7–9] which was first synthesized by Lillerud and co-workers.[10] Zirconium(IV)-based UiO-MOFs have a $\{Zr_6O_4(OH)_4\}$- or $\{Zr_6O_4(OH)_4(-CO_2)_{12}\}$-SBU which is 12 coordinated by the linker molecules.[10] UiO-66 has benzene-1,4-dicarboxylate linkers (BDC), while UiO-67 contains biphenyl-4,4′-dicarboxylate (BPDC) linkers.[10] The SBU is an octahedral cluster of six edge-sharing ZrO_8 square-antiprisms, which is connected to 12 neighboring SBUs in a face-centered cubic (fcc) packing arrangement (see Fig. S1 in the ESI†). The properties of these UiO-MOFs are interesting for gas storage,[11] separation,[12] water sorption,[8,13] sensing[14] and catalysis.[15]

Much research is currently done to optimize the synthesis techniques of MOFs also in an environmentally and economically advantageous way.[16] Goals are to find synthesis routes to decrease the reaction time, temperature or solvent consumption and to avoid the use of HF or acidic fluoride solutions.[17,18] Ultrasound can be applied for rapid and low-temperature syntheses, for example for MIL-53(Fe),[19] HKUST-1[20] and MOF-5.[21] Mechanochemical methods can be realized without any solvent and are known, for example, for MIL-101 (Cr)[22] and UiO-66.[23] Alternatively, microwave heating-induced synthesis can be used to obtain UiO-66.[24] Advantages like fast crystallization and phase selectivity can be achieved. A recent alternative synthesis method for MOFs is dry-gel conversion (DGC). In Fig. 1, the working principle of the DGC method is illustrated. A small amount of solvent is placed at the bottom of a Teflon container and the solid starting materials are placed up in the head on a sieve or porous support.[25] Consequently, the physical separation of the solvent and reactant mixture is achieved. From this separation results one of the big advantages of DGC, namely after the reaction, the solvent can be recovered largely uncontaminated and can be used for further reaction runs. This possibility offers an easy solvent re-use and can be interesting for industrial applications. The advantages of DGC are strongly reduced consumption of the solvent with no production of the mother liquor which needs to be disposed,[26] high product yields,[27,28] reduced reactor size and the possibility of continuous production.[25]

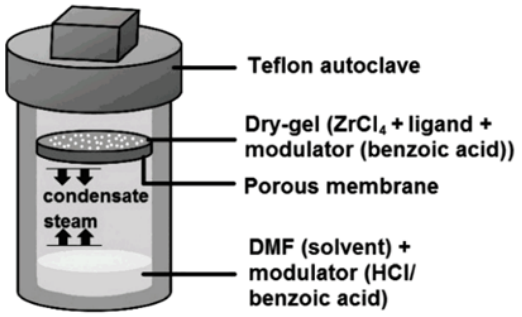

Fig. 1 Schematic drawing of the reactor setup for DGC with starting materials for the synthesis of UiOs.

Institut für Anorganische Chemie und Strukturchemie, Heinrich-Heine-Universität Düsseldorf, 40204 Düsseldorf, Germany. E-mail: janiak@uni-duesseldorf.de

† Electronic supplementary information (ESI) available: Synthesis and characterization details, TGA and defect calculations, PXRD patterns, pore size distributions, SEM images and reproducibility data. See DOI: 10.1039/c7dt01717k

For the synthesis of zeolites, steam-assisted DGC methods are used very often,[22,24] but so far there have been only a few reports about the DGC synthesis of MOFs.[29–31] Shi *et al.* synthesized zeolitic imidazolate framework (ZIF) materials (ZIF-8 and ZIF-67) through DGC by replacing dimethylformamide (DMF) with water as the solvent.[32] The DGC synthesis of MIL-100(Fe) without adding hydrofluoric acid (HF) to the reaction mixture was established by Ahmed *et al.*[33] Kim *et al.* reported the DGC synthesis of MIL-101(Cr) using water as the solvent and HF acid as an additive.[34] Recently, Tan *et al.* used DGC for the synthesis of magnetically responsive HKUST-1/Fe_3O_4 composites.[35]

Experimental

Materials

All reagents were used as received. Terephthalic acid H_2BDC, biphenyl-4,4′-dicarboxylic acid, H_2BPDC, ethanol and hydrochloric acid 37% (HCl) were purchased from Sigma Aldrich. *N*,*N*′-Dimethylformamide (DMF) was obtained from Fischer Chemicals. 2-Aminoterephthalic acid (NH_2-H_2BDC) and anhydrous $ZrCl_4$ were purchased from Alfa Aesar. Benzoic acid (BA) was purchased from Riedel de Haen. Alternatively, the use of benzoic acid in technical grade is possible.

Instrumentation

Powder X-ray diffraction (PXRD) patterns were obtained at ambient temperature on a Bruker D2 phaser (300 W, 30 kV, 10 mA) using Cu-Kα radiation (λ = 1.54182 Å) between 5° < 2Θ < 50° with a scanning rate of 0.0125° s^{-1}. The diffractograms were obtained on a flat "low background sample holder", in which at low angle the beam spot is strongly broadened so that only a fraction of the reflected radiation reaches the detector, hence the low relative intensities measured at 2Θ < 7°. The analyses of the diffractograms were carried out with "Match 3.11" software. Thermogravimetric analysis (TGA) was performed with a Netzsch TG209 F3 Tarsus instrument. Samples were placed in alumina pans and heated at a rate of 5 °C min^{-1} from 25 to 700 °C under a nitrogen atmosphere. Nitrogen (purity 99.9990%) physisorption isotherms were obtained on a Nova 4000e from Quantachrome at 77 K. Before obtaining the isotherms, the products were transferred into glass tubes capped with septa, which were weighed before. These tubes were attached to the corresponding degassing port of the sorption analyzer, degassed under vacuum at 120 °C for 3 h, weighed again and then transferred to the analysis port of the sorption analyzer. BET surface areas were calculated from the nitrogen adsorption isotherms in the p/p_0 range of 0.005–0.05. Total pore volumes were calculated from the nitrogen sorption isotherm at p/p_0 = 0.95. DFT calculations for the pore size distribution curves were carried out with the native 'NovaWin 11.03' software using the 'N_2 at 77 K on carbon, slit pore, NLDFT equilibrium' model. SEM images were recorded with a Jeol JSM-6510LV QSEM advanced electron microscope with a LaB_6 cathode at 5–20 keV. The microscope was equipped with a Bruker Xflash 410 silicon drift detector.

DGC synthesis of UiOs

For UiO-66-BA, $ZrCl_4$ (60 mg, 0.26 mmol), H_2BDC (44 mg, 0.26 mmol) and benzoic acid (0.2 g, 1.64 mmol) were mixed, ground and placed in a DGC sieve. A small amount (typically 2.5 mL) of DMF solvent was placed at the bottom of a 15 mL Teflon container and benzoic acid (1.4 g, 11.46 mmol) was added to the solvent. The DGC sieve was placed above the solvent mixture and the Teflon container was capped. The Teflon container was sealed in a stainless steel autoclave, and allowed to react at 120 °C for 24 h in a preheated oven. After cooling, the obtained as-synthesized product was left to soak in DMF (2 × 5 mL) and ethanol (5 mL) for 3 d. The solution was exchanged every 24 h. After 3 d of soaking, the solids were centrifuged and dried under vacuum. In the case of HCl modulation, only 0.5 mL of 37% aqueous HCl was added to the solvent. For the synthesis of UiO-66-NH_2, H_2BDC was replaced by NH_2-H_2BDC, and for UiO-67, H_2BPDC was used. More detailed information on the syntheses, workup procedure and characterization is given in the ESI (section S3†).

Results and discussion

Synthesis and characterisation

To the best of our knowledge, the synthesis of Zr-based UiO-MOFs by the DGC method has not been reported so far. Herein, we present a facile synthesis of UiO-MOFs using the DGC method. In the present study, UiO-66, UiO-66-NH_2 and UiO-67 were synthesized from $ZrCl_4$, H_2BDC, NH_2-H_2BDC or H_2BPDC, respectively, with DMF and a modulator (BA or HCl).

The modulator BA was chosen for several reasons: BA modulation delivers product advantages for UiOs which are discussed by Atzori *et al.*[36] They proved that monocarboxylic acid modulation supports the formation of "missing-cluster defects" whose charge and coordination deficiencies are compensated for by modulator ligands.[36] Important for DGC, BA modulation delivered products with stable and thick consistency. Also, BA in the solvent at the bottom of the container has an important role. If we do not use a solvent–modulator mixture a large part, if not all of the MOF product, is washed into the solvent (section S3 in the ESI†). Hence, the solvent cannot be re-used.

For batch sizes of 0.26 mmol of $ZrCl_4$ starting material, the DGC uses only 2.5 mL of DMF, while the standard solvothermal solution synthesis requires up to 15 mL of DMF solvent (see section S4 in the ESI†). Larger amounts of the solvent are also used in the washing procedure of the UiO products from solution synthesis.[37] In the case of benzoic acid modulated UiO, 112.5 mL of MeOH were used, while the DGC method used only 10 mL of DMF and 5 mL of EtOH for comparative yields of products. Both DGC and solution synthesis yield nearly the same amount of UiO products (83 mg from DGC and 80 mg from solution synthesis) for identical

amounts of the starting material (0.26 mmol of $ZrCl_4$) (see sections S3 and S4 in the ESI†). Several synthesis routes for UiO-66 are listed by Hu and Zhao.[38] A detailed comparison of UiO-66 through DGC and solution synthesis is given in Table S4 in the ESI.†

Fig. 2 shows the powder X-ray diffraction (PXRD) patterns of the obtained UiO products which verify their crystallinity and phase purity by positive matching with the simulated patterns. The experimental PXRD patterns contain a broad peak in the 2θ range of *ca.* 5–7°. This peak is not seen in the simulation of the UiO-66 phase, hence, it cannot be attributed to the UiO-66 phase. In the work of Shearer *et al.*, this "broad peak" was found in the 2θ range of 4–6° and assigned to **reo** nanoregions, where the **reo** phase can be thought of as UiO-66 with one-quarter of its clusters missing.[9] The slight shift in the 2θ range of this broad peak in the work of Shearer *et al.* may be due to the fact that their PXRD samples were activated (*i.e.*, desolvated) prior to the measurement, while our PXRD samples were measured only after a short activation time of 2 h at 120 °C. In our PXRD patterns, the broad peak is most prominent in the UiO-66-BA samples (see Fig. 2 and Fig. S6 and S8 in the ESI†).

Fig. 3 depicts the N_2 adsorption–desorption isotherms of the obtained UiO-MOFs with different modulators. The resulting BET surface areas and pore volumes are summarized in Table 1. The BET surface areas of UiOs from DGC are highly comparable to the results from the solution synthesis in the literature. The BET surface area of UiO-66 depends on the modulator such that HCl yielded a higher surface area than BA. On the other hand, BA modulated approaches deliver higher yields. The pore size distributions of selected UiOs are compared in the ESI (Fig. S7†). All obtained results are reproducible. Only weak fluctuations of the surface area and yield are observed in the first synthesis runs for different batches. This reproducibility of DGC for UiO-66-BA without the re-use of the solvent is shown in the ESI (Fig. S9†).

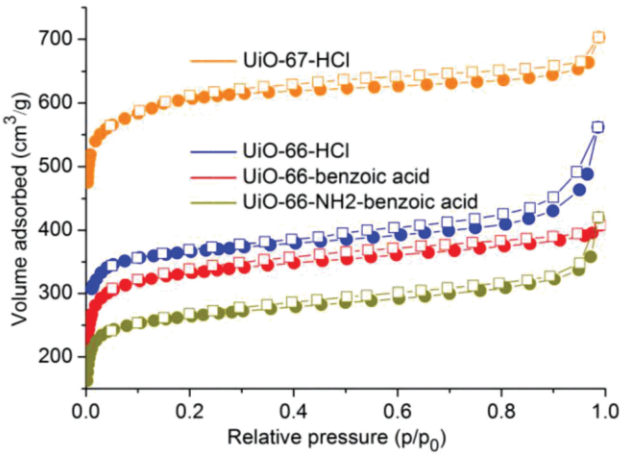

Fig. 3 N_2 sorption isotherms of UiO-66-NH_2-BA, UiO-66-BA, UiO-66-HCl and UiO-67-HCl synthesized through DGC. Filled symbols, adsorption; empty symbols, desorption.

Table 1 Results of DGC synthesis of UiO-66, UiO-66-NH_2 and UiO-67 with different modulators

MOF and modulator	BET surface area ($m^2\ g^{-1}$)	BET surface Lit.[a] ($m^2\ g^{-1}$)	Pore volume ($cm^3\ g^{-1}$)	Yield (mg)
UiO-66-BA	1242	1032 [8]–1450 [40]	0.550	83
UiO-66-HCl	1461		0.689	65
UiO-66-NH_2-BA	1023	1200 (HCl)[7]	0.485	93
UiO-67-HCl	2369	2500 [7]	0.911	82

[a] Results from standard solution synthesis in the literature.

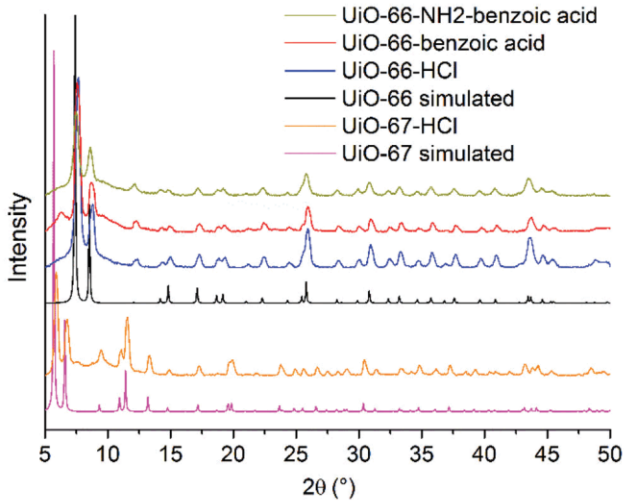

Fig. 2 PXRD patterns of simulated UiO-67, synthesized UiO-67-HCl, simulated UiO-66, synthesized UiO-66-HCl, UiO-66-BA and UiO-66-NH_2-BA from DGC. 'Benzoic acid' and 'HCl' refer to the used modulator. The simulated pattern of UiO-66 calculated from CSD-Refcode RUBTAK02,[39] and the simulated pattern of UiO-67 calculated from WIZMAV03.[40] For the four experimental PXRD patterns, we have also collected the diffractograms down to 2θ = 2° without observing additional peaks below 2θ = 5° (see Fig. S6 in the ESI†).

Nanocrystals were obtained for MFI type ferrisilicate zeolites through the DGC method.[41] No such observation on nanocrystals through DGC has yet been made for MOFs. Here we note that the primary particle size of UiO-66-HCl from DGC is between ~90 and 200 nm as illustrated by scanning electron microscopy images in Fig. 4. In comparison, Pullen *et al.* obtained UiO-66 crystals with a particle size ranging from ~200 to 500 nm through solution synthesis.[37] The DGC UiO-66-NH_2-BA particles vary from 200 to 500 nm. The primary particles of DGC UiO-67-HCl are around 500 nm, which are smaller than expected. Nik *et al.* obtained 1 μm-sized UiO-67 particles.[42] The selected SEM images are shown in Fig. 4. Further images are illustrated in Fig. S8 in the ESI.†

Characterization of defects

In TGA, three weight losses are observed. Firstly, solvent residues are removed in a temperature interval between 25 and 100 °C. Secondly, the removal of monocarboxylate ligands (BA)

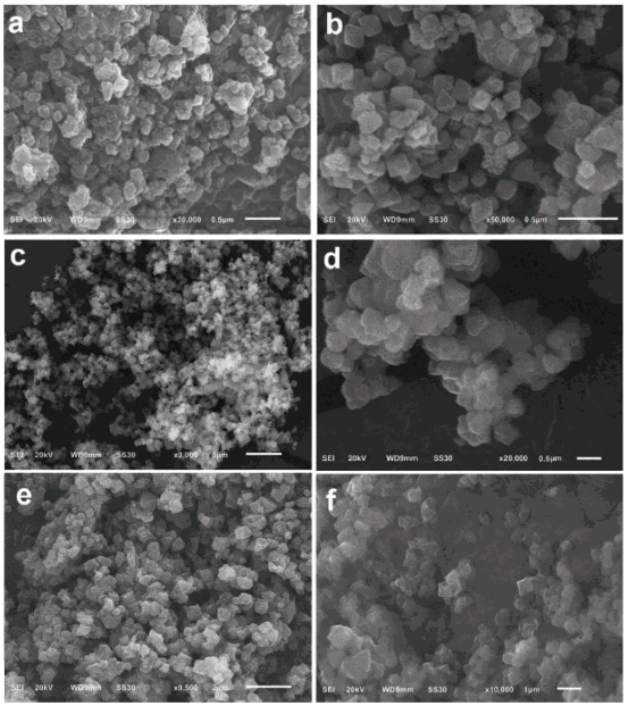

Fig. 4 SEM image of UiO-66-HCl (a and b), UiO-66-NH_2-BA (c and d) and UiO-67-HCl (e and f). Scale bar is 0.5 μm for a, b and d; 5 μm for c; 2 μm for e; 1 μm for f.

and the dehydroxylation of the $\{Zr_6O_4(OH)_4\}$ SBUs occur.[9] Both weight losses take place in a similar temperature range (*ca.* 180–300 °C),[39] followed by framework decomposition above *ca.* 350–550 °C.[39] Temperature ranges can be shifted depending on the used linker. The analysis of the weight losses allows the determination of linker defects as was shown by Shearer *et al.*[9] The calculation of defects was carried out according to this work.[9] The quantitative analysis of TGA data obtained on UiO MOFs was performed with the assumption that the residue in each TGA experiment is pure ZrO_2. Fig. 5 shows the TGA results of the obtained UiO products, with the residual mass set to 100%. A detailed determination of defects for selected UiO samples is outlined in the ESI (section S2†). The results of thermogravimetric analysis towards the number of defects are summarized in Table 2. The number of defects per SBU varies somewhat. The number of defects per SBU, that is per Zr_6 formula unit was in the range of 1.4 to 1.9 which is in the same range as the number of linker deficiencies reported by Shearer *et al.* for trifluoroacetic and difluoroacetic acid depending on the molar equivalents of the modulator used in the synthesis.[9]

Solvent re-use

The spatial separation of solvent and reaction products in DGC allows the solvent to be recovered largely uncontaminated. Therefore, we also tested the solvent re-use for further reaction runs. For the first run of the DGC synthesis of UiO-66, the solvent DMF was mixed with the modulator BA and placed at

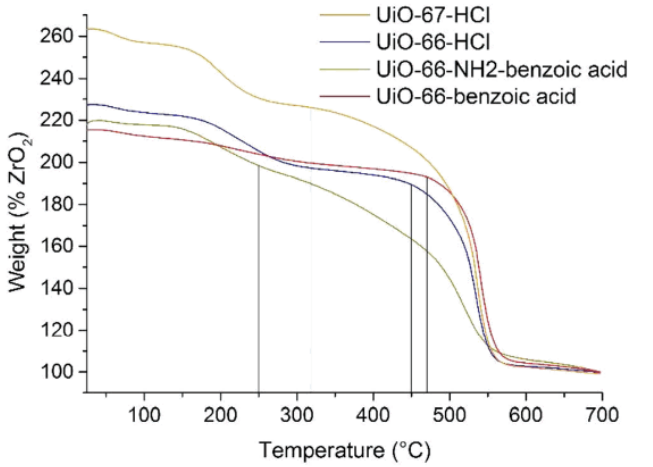

Fig. 5 TGA of UiO-66-NH_2-BA, UiO-66-BA, UiO-66-HCl and UiO-67-HCl synthesized through DGC (end weight normalized to 100%; the used area for $W_{Exp.Plat}$ is marked).

Table 2 Determination of defects from TGA

	Number of defects per SBU (x – *cf.* ESI)[a]	Molecular formula $Zr_6O_{6+x}(BDC)_{6-x}$[b]	Exp. molecular weight (g mol^{-1})
UiO-66-HCl	1.6	$Zr_6O_{7.6}(BDC)_{4.4}$	1397.48
UiO-66-BA	1.4	$Zr_6O_{7.4}(BDC)_{4.6}$	1427.10
UiO-66-NH_2-BA	1.6	$Zr_6O_{7.6}(NH_2\text{-}BDC)_{4.4}$	1463.81
UiO-67-HCl	1.9	$Zr_6O_{7.9}(BPDC)_{4.1}$	1663.39

[a] The used experimental weights $W_{Exp.Plat}$ and the mathematical calculations to derive at x are presented in the ESI (section S2). Values are rounded to one decimal digit, taking into account the experimental accuracy. [b] The determination of defects from TGA was performed according to the seminal work of Shearer *et al.*[9] where the molecular formula and experimental molecular weight derived therefrom were reported in the same way, that is, without modulator units in place of the missing BDC linkers.

the bottom of the Teflon container. The precursor mixture of $ZrCl_4$, H_2BDC and BA was placed on the porous support (*cf.* Fig. 1). When run 1 was completed, the porous support with the reaction products from the head of the container was carefully removed without contaminating the solvent. For run 2, another support containing the freshly prepared precursor mixture was placed in the Teflon container with the same solvent mixture from run 1. This synthesis and workup procedure was repeated at 120 °C for 24 hours over five runs. The results concerning the yield and BET surface area of the UiO-66 products with the re-use of the same 2.5 mL DMF solvent are shown in Fig. 6. BET surface areas vary between 1242 and 936 $m^2\ g^{-1}$. We obtained the yields between 68 and 83 mg per run, while solution synthesis delivered a yield of 80 mg per run. In comparison with the reproducibility of the first synthesis runs (*cf.* Fig. S9 in the ESI†), we observe that upon solvent recycling the surface area and yield vary strongly. Nonetheless, the surface area and yield remain in an acceptable range. Notably, the surface area and yield do not only

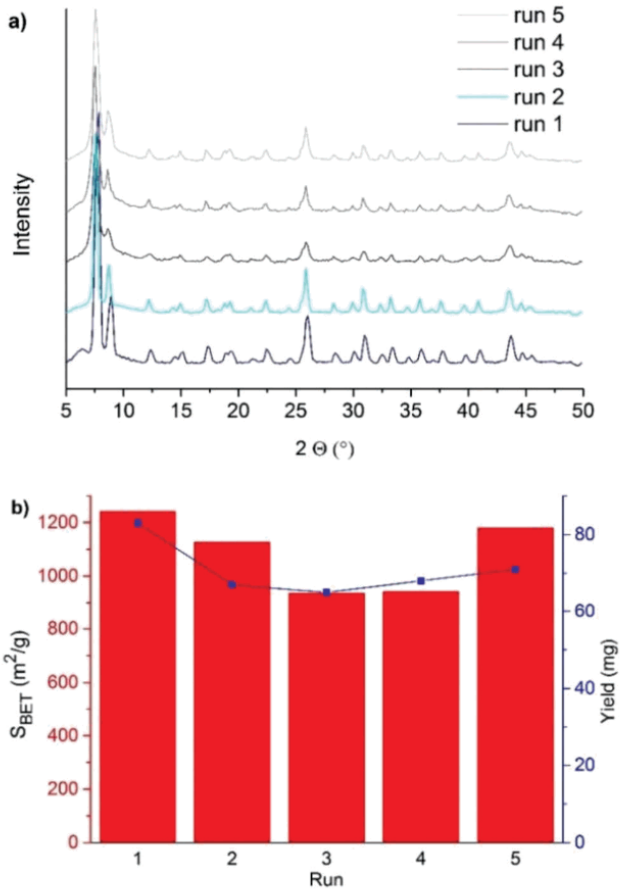

Fig. 6 Results of five DGC runs re-using the same solvent/modulator mixture for UiO-66-BA. (a) Surface area and yield of UiO-66-BA and (b) PXRD patterns of each run.

decrease but also recover from run 3 to run 5. The solvent re-use procedure over five runs was also successfully carried out for the synthesis of UiO-66-NH_2 (see section S9 in the ESI†). More detailed information on the syntheses, workup and characterization is given in the ESI.†

Conclusions

The dry-gel conversion (DGC) of the prototypical MOFs UiO-66, UiO-66-NH_2 and UiO-67 modulated with benzoic acid (BA) or hydrochloric acid (HCl/H_2O) was successful and highly reproducible. BA modulated UiOs were obtained in high yields and as highly stable dry gels; HCl modulated UiOs exhibited higher surface areas than their BA-modulated counterparts. Both modulators give rise to defects in the range of 1.4–1.9 defects per Zr_6-SBU. DGC uses only one-sixth or less of the solvent than the same scale solution synthesis. Additionally, it was proven that a re-use of the solvent over at least five synthesis runs is possible which reduces the needed DMF solvent volume for the total amount of the product even further to 1/30 or less of the solution synthesis.

Conflict of interest

There are no conflicts of interest to declare.

Acknowledgements

The work was supported by the Federal German Ministry of Education and Research (BMBF) under grant# 03SF0492C. We thank Carsten Schlüsener, Sandra Nießing and Dennis Dietrich for the SEM images and Alexa Schmitz for performing TGA.

References

1 H. C. Zhou, J. R. Long and O. M. Yaghi, *Chem. Rev.*, 2012, **112**, 673–674.
2 H. Furukawa, K. E. Cordova, M. O'Keeffe and O. M. Yaghi, *Science*, 2013, **341**, 1230444.
3 C. Janiak and J. K. Vieth, *New J. Chem.*, 2010, **34**, 2366–2388.
4 O. M. Yaghi, M. O'Keeffe, N. W. Ockwig, H. K. Chae, M. Eddaoudi and J. Kim, *Nature*, 2003, **423**, 705–714.
5 M. Eddaoudi, D. B. Moler, H. Li, B. Chen, T. M. Reineke, M. O'Keeffe and O. M. Yaghi, *Acc. Chem. Res.*, 2001, **34**, 319–330.
6 N. W. Ockwig, O. Delgado-Friedrichs, M. O'Keeffe and O. M. Yaghi, *Acc. Chem. Res.*, 2005, **38**, 176–182.
7 M. J. Katz, Z. J. Brown, Y. J. Colón, P. W. Siu, K. A. Scheidt, R. Q. Snurr, J. T. Hupp and O. K. Farha, *Chem. Commun.*, 2013, **49**, 9449–9451.
8 F. Jeremias, V. Lozan, S. K. Henninger and C. Janiak, *Dalton Trans.*, 2013, **42**, 15967–15973.
9 G. C. Shearer, S. Chavan, S. Bordiga, S. Svelle, U. Olsbye and K. P. Lillerud, *Chem. Mater.*, 2016, **28**, 3749–3761.
10 J. H. Cavka, S. Jakobsen, U. Olsbye, N. Guillou, C. Lamberti, S. Bordiga and K. P. Lillerud, *J. Am. Chem. Soc.*, 2008, **130**, 13850–13851.
11 H. Wu, Y. S. Chua, V. Krungleviciute, M. Tyagi, P. Chen, T. Yildirim and W. Zhou, *J. Am. Chem. Soc.*, 2013, **135**, 10525–10532.
12 M. W. Anjum, F. Vermoortele, A. L. Khan, B. Bueken, D. E. De Vos and I. F. J. Vankelecom, *ACS Appl. Mater. Interfaces*, 2015, **7**, 25193–25201.
13 F. Jeremias, D. Fröhlich, C. Janiak and S. Henninger, *New J. Chem.*, 2014, **38**, 1846–1852.
14 A. Shahat, H. M. A. Hassan and H. M. E. Azzazy, *Anal. Chim. Acta*, 2013, **793**, 90–98.
15 F. Vermoortele, B. Bueken, G. Le Bars, B. Van de Voorde, M. Vandichel, K. Houthoofd, A. Vimont, M. Daturi, M. Waroquier, V. Van Speybroeck, C. Kirschhock and D. E. De Vos, *J. Am. Chem. Soc.*, 2013, **135**, 11465–11468.
16 N. Stock and S. Biswas, *Chem. Rev.*, 2012, **112**, 933–969.
17 T. Zhao, F. Jeremias, I. Boldog, B. Nguyen, S. K. Henninger and C. Janiak, *Dalton Trans.*, 2015, **44**, 16791–16801.

18 F. Jeremias, S. K. Henninger and C. Janiak, *Dalton Trans.*, 2016, **45**, 8637–8644.
19 E. Haque, N. A. Khan, J. H. Park and S. H. Jhung, *Chem. – Eur. J.*, 2010, **16**, 1046–1052.
20 Z.-Q. Li, L.-G. Qiu, T. Xu, Y. Wu, W. Wang, Z.-Y. Wu and X. Jiang, *Mater. Lett.*, 2009, **63**, 78–80.
21 W.-J. Son, J. Kim, J. Kim and W.-S. Ahn, *Chem. Commun.*, 2008, **47**, 6336–6338.
22 K. Leng, Y. Sun, X. Li, S. Sun and W. Xu, *Cryst. Growth Des.*, 2016, **16**, 1168–1171.
23 K. Uzarevic, T. C. Wang, S.-Y. Moon, A. M. Fidelli, J. T. Hupp, O. K. Farha and T. Friscic, *Chem. Commun.*, 2016, **52**, 2133–2136.
24 Y. Li, Y. Liu, W. Gao, L. Zhang, W. Liu, J. Lu, Z. Wang and Y.-J. Deng, *CrystEngComm*, 2014, **16**, 7037–7042.
25 M. Matsukata, M. Ogura, T. Osaki, P. R. Hari Prasad Rao, M. Nomura and E. Kikuchi, *Top. Catal.*, 1999, **9**, 77–92.
26 N. Yang, M. Yue and Y. Wang, *Prog. Chem.*, 2012, **24**, 253–261.
27 C. S. Cundy and P. A. Cox, *Chem. Rev.*, 2003, **103**, 663–702.
28 S. Goergen, E. Guillon, J. Patarin and L. Rouleau, *Microporous Mesoporous Mater.*, 2009, **126**, 283–290.
29 X. Feng, C. Jia, J. Wang, X. Cao, P. Tang and W. Yuan, *Green Chem.*, 2015, **17**, 3740–3745.
30 C. M. Jia, J. Wang, X. Feng, Q. Lin and W. B. Yuan, *CrystEngComm*, 2014, **16**, 6552–6555.
31 N. D. McNamara and J. C. Hicks, *ACS Appl. Mater. Interfaces*, 2015, **7**, 5338–5346.
32 Q. Shi, Z. F. Chen, Z. W. Song, J. P. Li and J. X. Dong, *Angew. Chem., Int. Ed.*, 2011, **50**, 672–675.
33 I. Ahmed, J. Jeon, N. A. Khan and S. H. Jhung, *Cryst. Growth Des.*, 2012, **12**, 5878–5881.
34 J. Kim, Y. R. Lee and W. S. Ahn, *Chem. Commun.*, 2013, **49**, 7647–7649.
35 P. Tan, X.-Y. Xie, X.-Q. Liu, T. Pan, C. Gu, P.-F. Chen, J.-Y. Zhou, Y. Pan and L.-B. Sun, *J. Hazard. Mater.*, 2017, **321**, 344–352.
36 C. Atzori, G. C. Shearer, L. Maschio, B. Civalleri, F. Bonino, C. Lamberti, S. Svelle, K. P. Lillerud and S. Bordiga, *J. Phys. Chem. C*, 2017, **121**, 9312–9324.
37 S. Pullen, H. Fei, A. Orthaber, S. M. Cohen and S. Ott, *J. Am. Chem. Soc.*, 2013, **135**, 16997–17003.
38 Z. Hu and D. Zhao, *Dalton Trans.*, 2015, **44**, 19018–19040.
39 L. Valenzano, B. Civalleri, S. Chavan, S. Bordiga, M. H. Nilsen, S. Jakobsen, K. P. Lillerud and C. Lamberti, *Chem. Mater.*, 2011, **23**, 1700–1718.
40 O. V. Gutov, M. G. Hevia, E. C. Escudero-Adan and A. Shafir, *Inorg. Chem.*, 2015, **54**, 8396–8400.
41 K. Miyake, Y. Hirota, K. Ono, Y. Uchida, M. Miyamoto and N. Nishiyama, *New J. Chem.*, 2017, **41**, 2235–2240.
42 O. G. Nik, X. Y. Chen and S. Kaliaguine, *J. Membr. Sci.*, 2012, **413–414**, 48–61.

3.1.1 Electronic Supplementary Information

Environmentally benign dry-gel conversions of Zr-based UiO metal-organic frameworks with high yield and possibility of solvent re-use

Serkan Gökpinar, Tatyana Diment and Christoph Janiak*

Institut für Anorganische Chemie und Strukturchemie, Heinrich Heine Universität Düsseldorf, 40204 Düsseldorf. Germany
Emails: serkan.goekpinar@uni-duesseldorf.de; tatyana.diment@hhu.demailto:; janiak@uni-duesseldorf.de

Table of Contents

Section S1. Structure of UiO-66

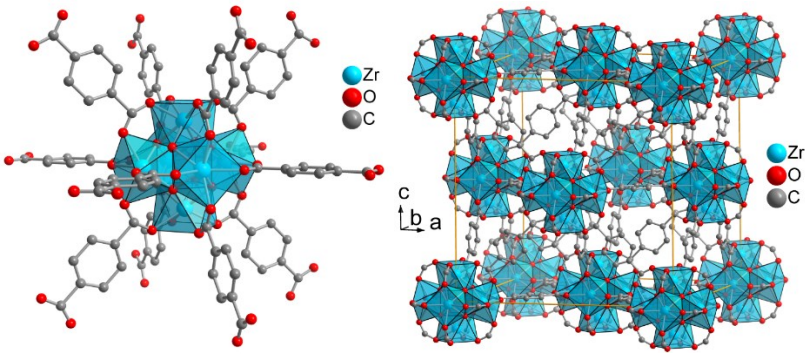

Figure S1 Crystal structure of zirconium terephthalate UiO-66.[1] The SBU is an octahedral cluster of six vertex-sharing ZrO_8 square-antiprism, which is connected to 12 neighboring SBUs in a face-centered cubic (fcc) packing arrangement. The Zr-MOF structures formed with linear ligands are therefore expanded versions of the cubic close packed (ccp) structure (= fcc). The Zr-MOF structures can be extended with increasing length of the linker from phenyl (in BDC with UiO-66) over biphenyl (in BPDC with UiO-67) to terphenyl (UiO-68) with retention of the framework topology (isoreticular structures). The UiO-66 structure is drawn from the deposited cif-files under CCDC 837796.[2]

Section S2. Determination of defects through thermogravimetric analysis (TGA)

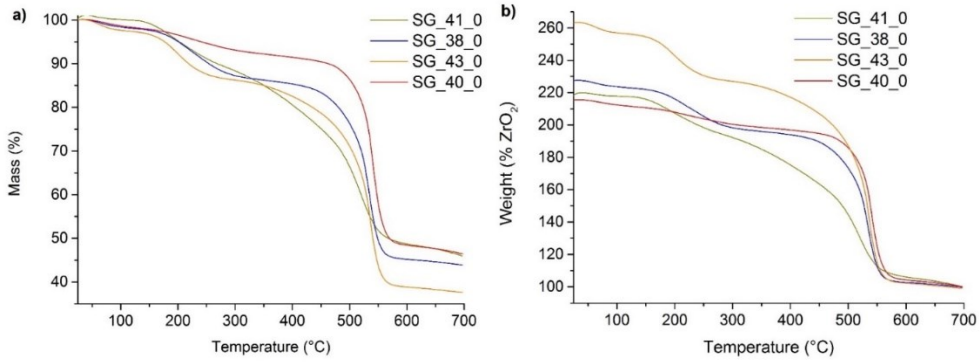

Figure S2 TGA of selected UiO-66 and UiO-67 materials: a) normalized such that initial weight = 100% and b) normalized such that end weight = 100%. The legend SG_xx_x refers to the experiment numbers in Table S1-S3.

Determination of defects per SBU was carried out similar to Shearer *et. al.*.[3] Evaluation of TGA data is made with an assumption: the residue in each TGA experiment is **ZrO_2**. The reaction for decomposition of ideal (defect-free), **dehydroxylated** UiO-66 (**$Zr_6O_6(BDC)_6$**) can be described as followed:

$$Zr_6O_6(BDC)_6 + 45\ O_2 \longrightarrow 6\ ZrO_2 + 48\ CO_2 + 12\ H_2O$$

First we have to determine theoretical TGA plateau weight $W_{Theo.Plat}$:

$W_{Theo.Plat} = (M_{Comp}/M_{6xZrO2})*W_{End}$

Where:

M_{Comp} is the molar mass of dehydroxylated, defect-free composition of interest:

M_W(UiO-66) = 1628,03 g/mol

M_W(UiO-66-NH_2) = 1724,04 g/mol
M_W(UiO-67) = 2084,57 g/mol
M_{6xZrO2} is the molar mass of 6 moles of zirconium oxide (**739.34** g/mol)
W_{End} is the end weight of the TGA run (= **100 %** if normalized as described above).

$W_{Theo.Plat}$ for dehydroxylated UiOs:
$W_{Theo.Plat}$ (UiO-66) = 220.20 %
$W_{Theo.Plat}$ (UiO-66-NH_2) = 233.19 %
$W_{Theo.Plat}$ (UiO-67) = 281.95 %

The weight contribution per BDC linker **$Wt.PL_{Theo}$** can be determined by following equation:
Where: **NL_{Ideal}** is the number of linkers (6) in the ***ideal*** Zr_6 formula unit
$Wt.PL_{Theo} = (W_{Theo.Plat} - W_{End})/NL_{Ideal}$
$Wt.PL_{Theo}$ (UiO-66) = (220.20−100)/6 = 20.03 %
$Wt.PL_{Theo}$ (UiO-66-NH_2) = (233.19 −100)/6 = 22.20 %
$Wt.PL_{Theo}$ (UiO-67) = (281.95 −100)/6 = 30.33 %
The experimental number of linkers per ***defective*** Zr_6-SBU, **NL_{Exp}** can be determined by following equation:
$NL_{Exp} = (6-x) = (W_{Exp.Plat} - W_{End})/ Wt.PL_{Theo}$

Where:
$W_{Exp.Plat}$ is the experimental TGA plateau and can be taken from Figure S2
x is the number of linker deficiencies per Zr_6 formula unit and can be determined by following equation:

$x = 6 - NL_{Exp} = 6-((W_{Exp.Plat} - W_{End})/Wt.PL_{Theo})$

x (UiO-66-HCl/SG_38_0) = 6−4.443 = 6−((**189**−100 %)/20.03 %) = **1.557**
x (UiO-66-BA/SG_40_0) = 6−4.643 = 6−((**193**−100 %)/20.03 %) = **1.357**
x (UiO-66-NH_2-BA/SG_41_0) = 6−4.414 = 6−((**198**−100 %)/22.20 %) = **1.586**
x (UiO-67-HCl/SG_43_0) = 6−4.121 = 6−((**225**−100 %)/30.33 %) = **1.879**

With x we obtain the experimental molecular weight Mw by using **$Zr_6O_{6+x}(BDC)_{6-x}$**

SG_38_0:	**x = 1.6**	**$Zr_6O_{7.6}(BDC)_{4.4}$**
SG_40_0:	**x = 1.4**	**$Zr_6O_{7.4}(BDC)_{4.6}$**
SG_41_0:	**x = 1.6**	**$Zr_6O_{7.6}(BDC\text{-}NH_2)_{4.4}$**
SG_43_0:	**x = 1.9**	**$Zr_6O_{7.9}(BPDC)_{4.1}$**

Experimental Mw:
Mw (UiO-66-HCl) =1397.48
Mw (UiO-66-BA) = 1427.10
Mw (UiO-66-NH_2-BA) = 1463.81
Mw (UiO-67-HCl) = 1663.39

Section S3. Synthesis of UiO-67, UiO-66-NH_2 and UiO-66 through DGC method

Preparation of DGC samples:

1. A small amount (typically 2.5 mL) of DMF solvent is placed at the bottom of a 15 mL Teflon container and modulator was added (Fig. S2a).
   In case of benzoic acid 1.4 g of modulator was dissolved.
   In case of HCl 0.5 mL of 37% aqueous HCl was used.
2. The solid starting materials are mixed and ground (Fig. S2b) ($ZrCl_4$, linker and optional benzoic acid) and placed in DGC head (Fig. S2c).
   In case of benzoic acid 0.2 g of modulator was used.
3. DGC sieve is placed above the solvent (Fig. S2d) and covered.
4. The Teflon container was capped in a stainless steel autoclave and the heating program was started (3 h ramp to heat up, 24 h at constant temperature, 3 h ramp for cooling down).
5. Pre-product was obtained (Fig. S2e) and washed with DMF (2 x 5 mL) and ethanol (5 mL).

The preparation of DGC samples and the used Teflon objects (sieve, rings and container) including their sizes are shown in Figure S3.

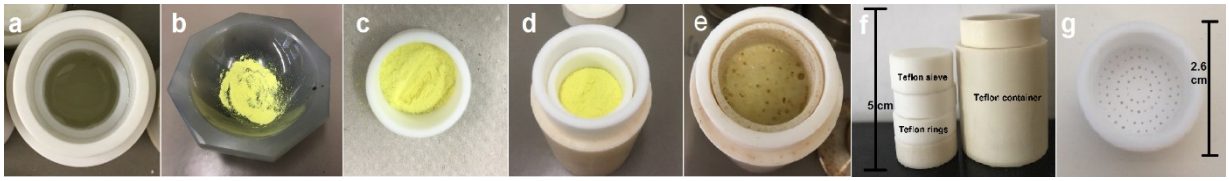

Figure S3 Pictures of sample preparation (a-e) and used Teflon objects for DGC (f and g).

Table S1 Dry gel conversion synthesis of UiO-67-HCl.

Experiment	$ZrCl_4$ [mmol]	BPDC [mmol]	DMF [mL]	HCl [mL]	Conditions (Time, Temp.)	Washing procedure (DMF, EtOH)	BET surface area [m^2/g]	Yield [mg]
SG_43_0	0.26	0.26	2.5	0.5	24 h, 150 °C	DMF (x2)	2369	82

Table S2 Dry gel conversion of UiO-66-NH_2-benzoic acid.

Experiment	$ZrCl_4$ [mmol]	NH_2-BDC [mmol]	DMF [mL]	Benzoic acid [mmol]	Conditions (Time, Temp.)	Washing procedure (DMF, EtOH)	BET surface area [m^2/g]	Yield [mg]
SG_29_0	0.26	0.26	5.0	13*	24 h, 120 °C	DMF (x2), EtOH (1x)	505	80
SG_33_0	0.26	0.26	3.5	13*	24 h, 120 °C	DMF (x2), EtOH (1x)	672	74
SG_30_2	0.26	0.26	2.5	13*	24 h, 120 °C	DMF (x2), EtOH (1x)	726	52
SG_30_3	0.26	0.26	2.5	13**	24 h, 120 °C	DMF (x2), EtOH (x1)	780	30
SG_36_0	0.26	0.26	2.5	13***	18 h, 120 °C	DMF (x2), EtOH (x1)	935	80
SG_41_0	0.26	0.26	2.5	13***	24 h, 120 °C	DMF (x2), EtOH (x1)	1023	93

*benzoic acid only at the bottom of the container in the DMF solvent, **benzoic acid only in DGC head, ***benzoic acid at the bottom of the container in the DMF solvent and in the DGC head,

Table S3 Dry gel conversion of UiO-66-benzoic acid and UiO-66-HCl.

Experiment	$ZrCl_4$ [mmol]	BDC [mmol]	DMF [mL]	Benzoic acid [mmol]/ HCl [mL]	Conditions (Time, Temp.)	Washing procedure (DMF, EtOH)	BET surface area [m^2/g]	Yield [mg]
SG_35_0	0.26	0.26	2.5	BA: 13***	18 h, 120 °C	DMF (x2), EtOH (1x)	860	40
SG_40_0	0.26	0.26	2.5	BA: 13***	24 h, 120 °C	DMF (x2), EtOH (1x)	1242	83
SG_38_0	0.26	0.26	2.5	HCl: 0.5	24 h, 120 °C	DMF (x2), EtOH (1x)	1461	65

***benzoic acid at the bottom of the container in the DMF solvent and in the DGC head

As an explanation for the effect of BA in the solvent we refer to the vapor pressure of BA of 5.8 hPa at 117 °C.[4]

In the following image we illustrate the influence of BA addition to solvent at the bottom of the Teflon container. If we do not use a solvent-modulator mixture (see a) and b)) a large part if not all of the MOF product is washed into the solvent (see c)). Hence, the solvent cannot be re-used. In case of a solvent-BA mixture the MOF will not be washed from the sieve (see a) and b)). We suggest that the amount of BA present in the solvent vapor will reduce the solubility of BA from the DGC head. Further, the BA-saturated DMF vapor may supply fresh BA which then also leads to a thicker and more stable dry gel.

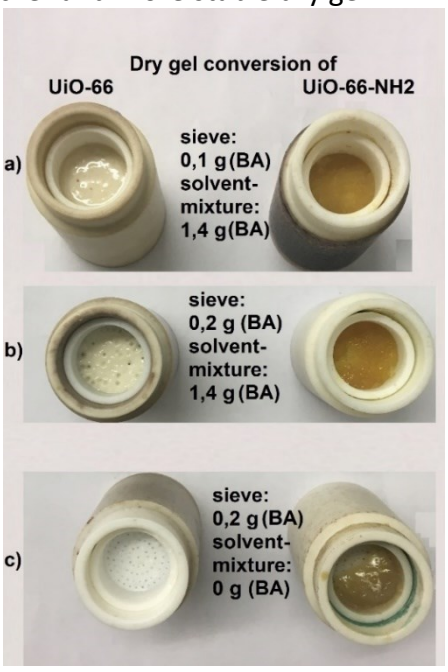

Figure S4 Influence of BA in solvent: a) and b) DMF/BA solvent-mixture c) only DMF.

Section S4. Comparison of UiO-66 through DGC and solution synthesis

Standard solvothermal synthesis of UiO-66

A standard solvothermal synthesis of benzoic acid modulated UiO-66 is performed by dissolving $ZrCl_4$ (60 mg, 0.26 mmol), BDC (44 mg, 0.26 mmol) and benzoic acid (1.6 g, 13.13 mmol) at room temperature in 15 mL of DMF. This solution was capped and sealed in a vial, and allowed to react solvothermally at 120 °C for 24 h. After cooling, the mixture was centrifuged, then the solids were left to soak in MeOH for 3 d. The solution was exchanged with fresh MeOH (37.5 mL) every 24 h. After 3 d of soaking, the solids were centrifuged and dried under vacuum.[5] The solution synthesis delivered a reproducible yield of 80 mg.

Table S4 Comparison of UiO-66 through DGC and solution synthesis; Table taken from literature 10 and supplemented by results of DGC method.

Items	UiO-66[1]	UiO-66[6]	UiO-66[7]	UiO-66[8]	UiO-66[9]	**UiO-66-HCl-DGC/ SG_38_ 0**	**UiO-66-BA-DGC/ SG_40_ 0**
$ZrCl_4$ (mg/mmol)	53/0.22 7	80/0.34 3	125/0.5 40	51300/2 20	116/0.5 00	**60/0.26**	**60/0.26**
BDC (mg/mmol)	37/0.22 7	57/0.34 3	123/0.7 5	35600/2 20	83/0.5	**44/0.26**	**44/0.26**
Modulators (mL/g)	N.A.	Acetic acid 0.5	HCl 1.0	Formic acid 0.83	Formic acid 1.89	**HCl 0.5**	**Benzoic acid 1.6**
DMF (mL)*	26	20	15	2000	18	**2.5**	**2.5**
Modulator/lig and molar ratio	N.A	30	15.5	100	100	**22.4**	**50**
Temperature (K)	393	393	353	393	393	**393**	**393**
Time (h)	24	24	12	24	24	**24**	**24**
Product types	Cubic (~100 nm)	Octah. (~200 nm)	Spheric. (~200 nm)	Octah. (~3 µm)	Octah. (~300 nm)	**Octah. (~150 nm)**	**Spheric. (~250 nm)**
BET/ Langmuir surface area (m^2/g)	N.A./11 87	1400/N. A.	1580/N. A.	1367/N. A.	1730/20 47	**1461/N. A.**	**1242/N. A.**

*used amount of DMF during synthesis (washing not included)

Section S5. Powder X-ray diffraction of UiO-66 and -67 materials

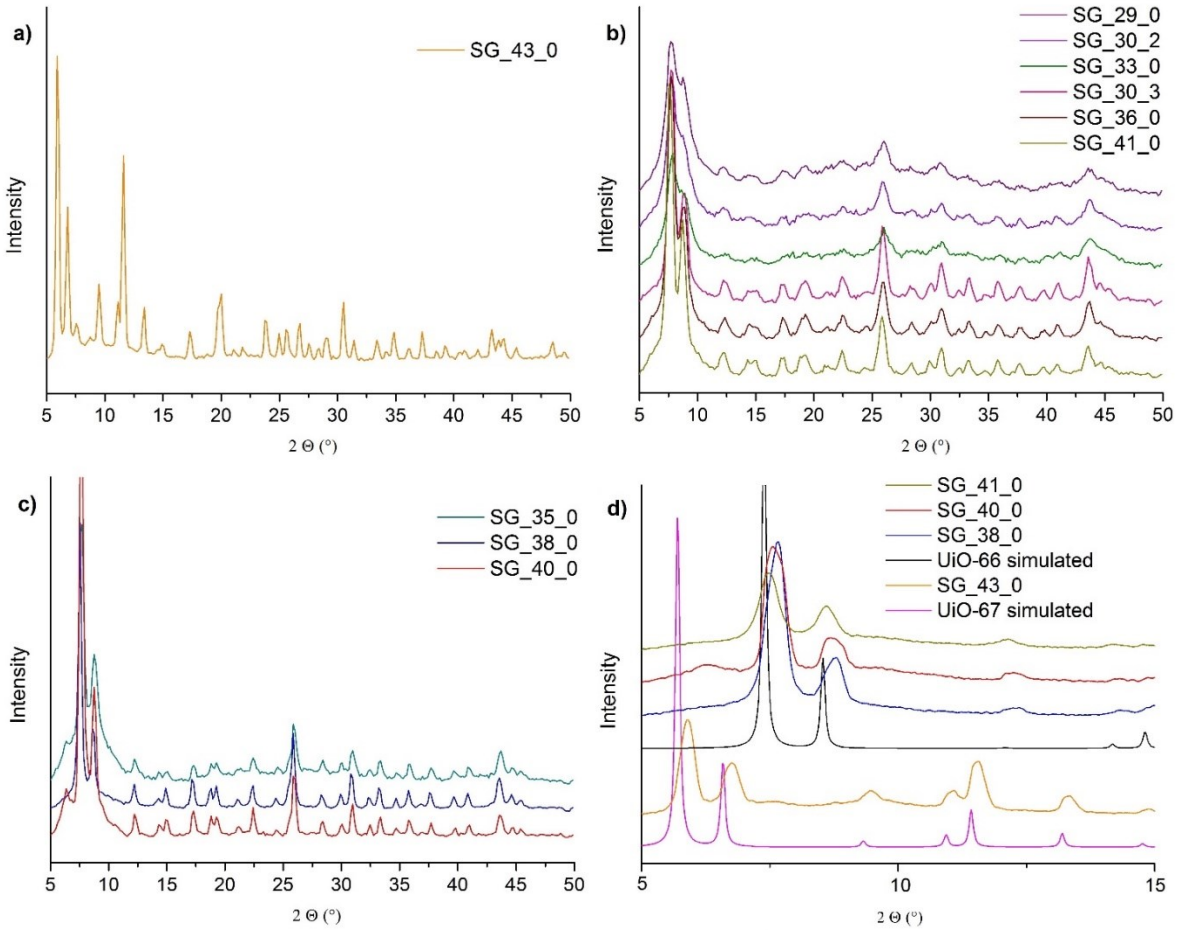

Figure S5 PXRD patterns of DGC products (a) UiO-67-HCl, (b) UiO-66-NH_2-benzoic acid, (c) UiO-66-BA or UiO-66-HCl materials and (d) enlarged low angle (2θ = 5-15°) region of Fig. 2 in the manuscript. The legend SG_xx_x refers to the experiment numbers in Table S1-S3.

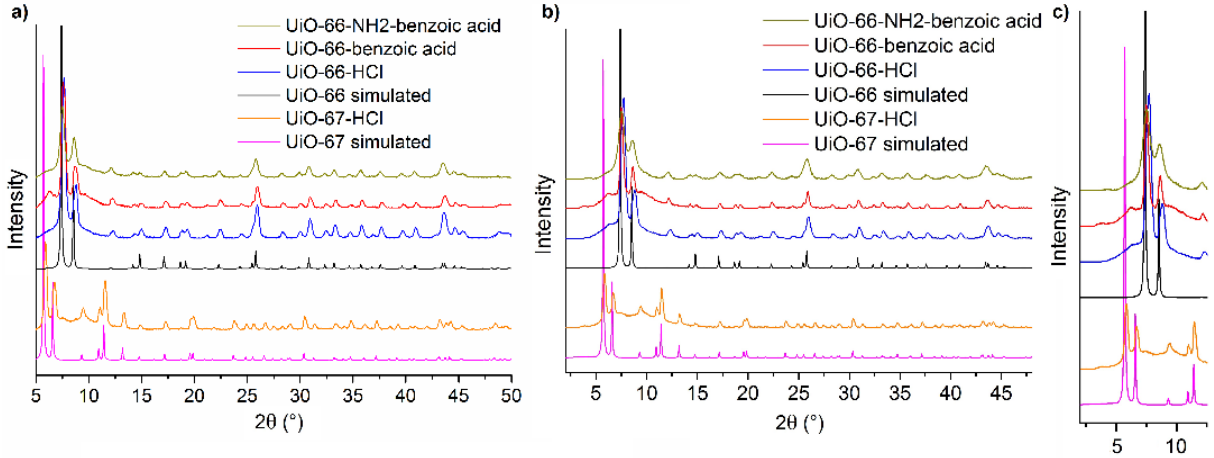

Figure S6 (a) PXRD-pattern in a 2θ range of ca. 5−50° (repeated from manuscript Fig. 2); (b) PXRD-pattern in a 2θ range of ca. 2−48°; (c) enlarged low angle of (b) in the range 2θ = 2-12.5°.

Section S6. Pore size distribution and elemental analysis of selected UiO-66 and -67 materials

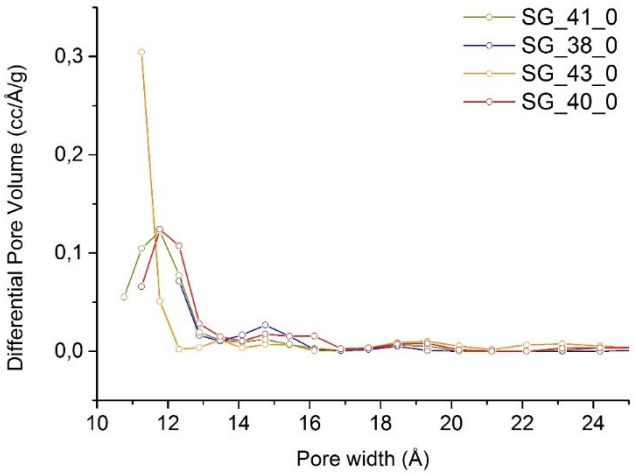

Figure S7 Pore size distribution of selected UiO-66 and UiO-67 materials. The legend SG_xx_x refers to the experiment numbers in Table S1-S3.

Table S5 CHN-Analysis of selected UiO-66 and UiO-67 materials. The legend SG_xx_x refers to the experiment numbers in Table S1-S3.

CHN analyses were performed with a Perkin Elmer CHN 2400 series 2 elemental analyzer.

MOF	% C	% H	% N
UiO-66 MOFs			
SG_38_0	32.22	3.61	/
SG_40_0	32.32	3.73	/
ideal UiO-66 $Zr_6O_4(OH)_4(BDC)_6$	theor. 34.61	theor. 1.68	theor. /
$Zr_6O_{7.6}(BDC)_{4.4}$	30.23		
$Zr_6O_{7.4}(BDC)_{4.6}$	30.94		
UiO-66-NH_2 MOF			
SG_41_0	31.76	3.72	5.01
ideal UiO-66-NH_2 $Zr_6O_4(OH)_4(BDC\text{-}NH_2)_6$	theor. 32.76	theor. 2.28	theor. 4.78
$Zr_6O_{7.6}(BDC\text{-}NH_2)_{4.4}$	28.86		
UiO-67 MOF			
SG_43_0	42.38	3.78	/
ideal UiO-67 $Zr_6O_4(OH)_4(BPDC)_6$	theor. 47.54	theor. 2.45	theor. /
$Zr_6O_{7.9}(BPDC)_{4.1}$	41.41		

The results of the elemental CH(N)-analysis are qualitatively in line with the found defects from thermogravimetic analysis in Section S2. The decrease of the % C compared to the theoretical value for the ideal UiO structure is dues to the presence defects, that is, missing

linkers in relation to the Zr_6 SBU. The increase of %H and the higher %C can be explained with small residues of DMF (%C 49.30, %H 9.65) and adsorbed water/moisture from air through the UiO hydrophilicity and capillary effects upon sample handling under air. In view of the difficult to assess solvent content in MOFs we refrain from further detailed analysis of the CH(N) data.

Section S7. Scanning electron microscopy (SEM) images of selected UiO-66 and -67 materials

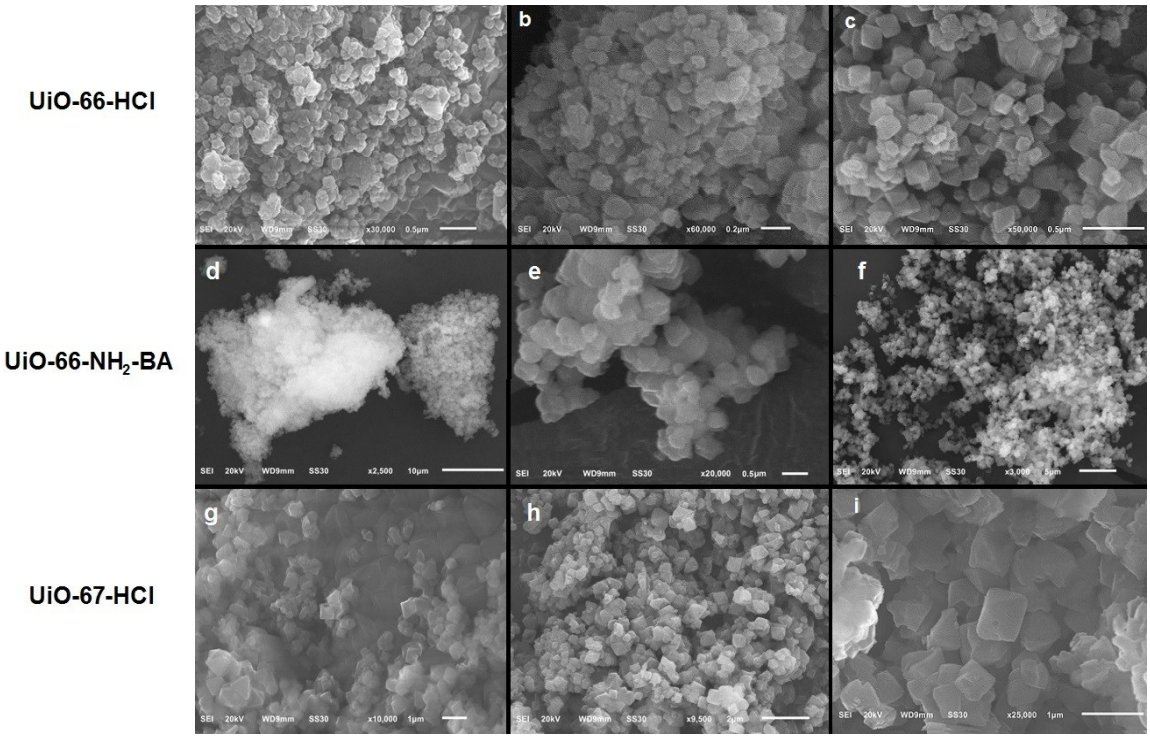

Figure S8 Scanning electron microscopy images of selected UiO-66 and -67 materials.

Section S8. Reproducibility of DGC for UiO-66-BA without re-use of solvent

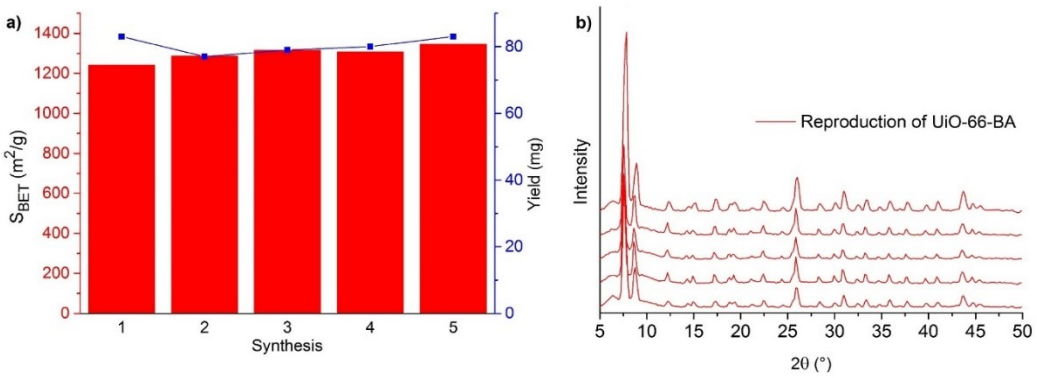

Figure S9 Reproducibility of UiO-66-BA without re-use of solvent. a) Surface area and yield; b) PXRDs of the product from each synthesis 1-5 (synthesis 1 at bottom).

Section S9. Results of five synthesis runs for UiO-66-NH_2

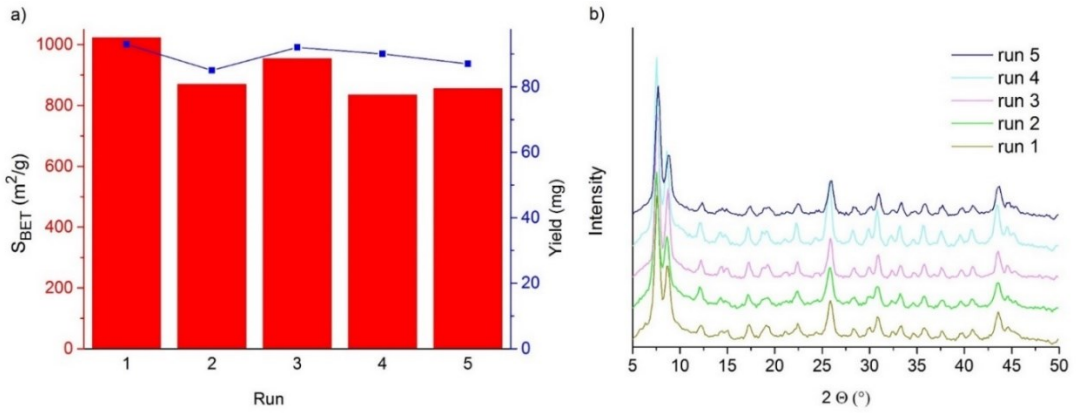

Figure S10 Results of five DGC runs re-using the same solvent/modulator mixture for UiO-66-NH_2-BA. a) Surface area and yield of UiO-66-NH_2-BA and b) PXRDs of each run.

Section S10. References

1 J. H. Cavka, S. Jakobsen, U. Olsbye, N. Guillou, C. Lamberti, S. Bordiga and K. P. Lillerud, *J. Am. Chem. Soc.*, 2008, **130**, 13850-13851.

2 L. Valenzano, B. Civalleri, S. Chavan, S. Bordiga, M. H. Nilsen, S. Jakobsen, K. P. Lillerud and C. Lamberti, *Chem. Mater.*, 2011, **23**, 1700-1718.

3 G. C. Shearer, S. Chavan, S. Bordiga, S. Svelle, U. Olsbye and K. P. Lillerud, *Chem. Mater.*, 2016, **28**, 3749−3761.

4 S. Pullen, H. Fei, A. Orthaber, S. M. Cohen and S. Ott, *J. Am. Chem. Soc.*, 2013, **135**, 16997−17003.

5 A. Schaate, P. Roy, A. Godt, J. Lippke, F. Waltz, M. Wiebcke and P. Behrens, *Chem. Eur. J.*, 2011, **17**, 6643–6651.

6 M. J. Katz, Z. J. Brown, Y. J. Colón, P. W. Siu, K. A. Scheidt, R. Q. Snurr, J. T. Hupp and O. K. Farha, *Chem. Commun.*, 2013, **49**, 9449–9451.

7 J. Ren, H. W. Langmi, B. C. North, M. Mathe and D. Bessarabov, *Int. J. Hydrogen Energy*, 2014, **39**, 890–895.

8 Z. Hu, S. Faucher, Y. Zhuo, Y. Sun, S. Wang and D. Zhao, *Chem. Eur. J.*, 2015, DOI: 10.1002/chem.201503078.

9 Z. Hu and D. Zhao, *Dalton Trans.*, 2015, **44**, 19018–19040.

3.2 Microwave-assisted dry-gel conversion-a new sustainable route for the rapid synthesis of metal–organic frameworks with solvent re-use

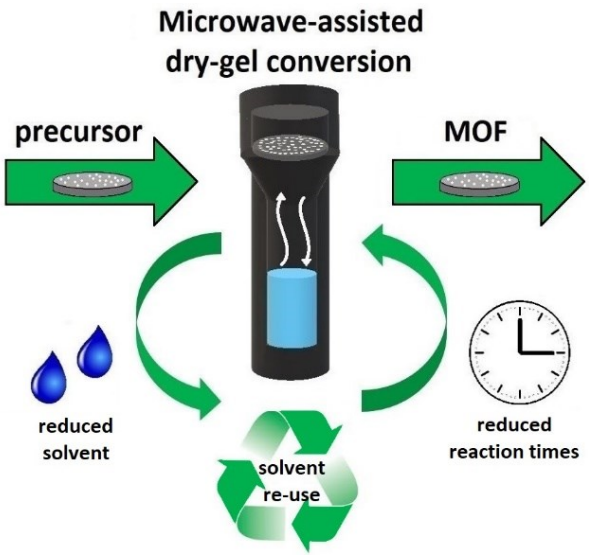

Zusammenfassung:
Die mikrowellenunterstützte Trockengelumwandlung (MW-DGC) kombiniert die Vorteile konzentrierter Reaktanten in DGC mit einer schnellen Erwärmung durch Mikrowellenbestrahlung. Diese Kombination ermöglicht, die Menge an Lösungsmittel, die für die Synthese benötigt wird, und die Reaktionszeiten drastisch zu reduzieren. Darüber hinaus ermöglicht MW-DGC die Rückgewinnung und Wiederverwendung des Reaktionslösungsmittels. Dadurch kann der gesamte Lösungsmittelabfall bei den Synthesen der vier wichtigen MOFs MIL-100 (Fe) (Basolite F300), UiO-66, MIL-140A und Aluminiumfumarat (Alfum, Basolite A520) signifikant reduziert werden. Alle von MOF-Produkte der MW-DGC zeigten im Vergleich zu den industriellen Benchmarks Basolite F300 und Basolite A520 zufriedenstellende Ausbeuten, Kristallinität und Porosität. Darüber hinaus führt MW-DGC auch vorteilhaft zu einem hierarchischen mikromeoporösen Alfum-Material, das sich von anderen Synthesemethoden unterscheidet.

Meine Beiträge:
- Experimentelle Arbeiten und Analytik zu Zr-MOFs UiO-66 und MIL-140 (Ausnahme: Ionische Flüssigkeit wurde von Alexa Schmitz zur Verfügung gestellt)
- Schreiben des Manuskripts und der ESI für UiO-66 und MIL-140A
- Erstellen der Tabellen und der Abbildungen für UiO-66 und MIL-140A (Ausnahme: Figure S4 von Herrn Prof. Christoph Janiak und Figure S11 von Sandra Nießing)
- Abschnitte Solvent re-use und Conclusion wurden gemeinsam mit Niels Tannert erstellt
- Erstellen des Grahpical Abstracts, Scheme 1 und Figure 9
- Korrekturen erfolgten durch Herrn Prof. Christoph Janiak

Dieser Abschnitt basiert auf der Publikation:
N. Tannert,[‡] S. Gökpinar,[‡] E. Hastürk, S. Nießing and C. Janiak*, *Dalton Trans.*, 2018, **47**, 9850 – 9860. [‡] contributed equally to the paper
Impact factor 2017: 4.099

Dalton Transactions

PAPER

Cite this: *Dalton Trans.*, 2018, **47**, 9850

Microwave-assisted dry-gel conversion-a new sustainable route for the rapid synthesis of metal–organic frameworks with solvent re-use†

Niels Tannert,‡ Serkan Gökpinar,‡ Emrah Hastürk, Sandra Nießing and Christoph Janiak *

Received 18th May 2018,
Accepted 29th June 2018

DOI: 10.1039/c8dt02029a

rsc.li/dalton

Microwave-assisted dry-gel conversion (MW-DGC) combines the advantages of concentrated reactants in DGC with fast heating by microwave irradiation. This novel combination allows drastically decreasing the amount of solvent needed for synthesis and reaction times with the energy needed. Furthermore, MW-DGC allows for the recovery and re-use of the reaction solvent and thereby can significantly reduce the overall solvent waste in the syntheses of the four important MOFs MIL-100(Fe) (*Basolite F300*), UiO-66, MIL-140A and aluminium fumarate (Alfum, *Basolite A520*). All the MOF products obtained from MW-DGC showed satisfying yields, crystallinity and porosity in comparison with the industrial benchmarks *Basolite F300* and *Basolite A520*. Moreover, MW-DGC also advantageously leads to a hierarchical micro-mesoporous Alfum material different to that from other synthesis methods.

Introduction

Metal–organic frameworks (MOFs) have gained considerable attention in recent years due to their high and designable inner surface as permanently porous, crystalline materials, built up by metal ions and bridging organic ligands ("linkers").[1] MOFs have been investigated for potential applications in the field of catalysis,[2,3] sensing,[4] gas separation[5,6] and storage,[7] drug delivery,[8] cyclic adsorption processes,[9] and many more. MOFs are ascribed to be easily tunable by the choice of metal[10] and linker[11] to modulate their properties.[12,13]

Still, some major challenges for the preparation of MOFs remain: faster, scaled-up syntheses and easier purification/activation procedures that are accompanied by sustainability.[14–21] Recently, Reinsch stated that the accessibility of MOFs will always be limited by the sustainability of the synthesis procedure.[22] The stated space–time yields in the literature do not take into account the economic and ecological aspects of the enormous amounts of mother liquor needed and solvent waste produced. Another recent contribution to optimized MOF synthesis claims that economic and sustainable strategies are imperative for promoting MOF materials for large-scale industrial use.[23]

The synthetic conditions often appear to be quite harsh (*i.e.* solvo/hydrothermal, use of hydrofluoric acid (HF) or other acidic modulators) and time- and energy-consuming. While mechano-chemical[24,25] or supercritical processing[26] as well as continuous-flow[17,27] methods can be considered as already established in the synthesis of MOFs, the research towards achieving optimized synthetic procedures is still growing rapidly. In order to improve the energy-related issues and further reduce the environmental impacts,[28] while obtaining materials with the maximized performance and minimized undesirable implications,[29] we chose dry-gel conversion (DGC) as an interesting solvent-saving synthesis method for MOFs.

Scheme 1 illustrates the working principle of DGC under microwave irradiation (MW-DGC). The starting materials were placed on a sieve or porous support at the top of an autoclave container, and a small amount of solvent is placed at the bottom of this vessel.[30] By separation of the solvent and reactant mixture, the solvent can be recovered with little contamination and then used again for further reaction runs.[31] Solvent re-use is a very important aspect, since industry generally prefers such environmental and economic improvements in product syntheses. Other advantages of DGC techniques are the reduced solvent amounts, high yields and minimized reactor size.[32]

Institut für Anorganische Chemie und Strukturchemie, Heinrich-Heine-Universität Düsseldorf, Universitätsstr. 1, 40204 Düsseldorf, Germany.
E-mail: janiak@uni-duesseldorf.de

†Electronic supplementary information (ESI) available: Details of materials and methods, syntheses, optimizations, work-up procedures, additional PXRDs, nitrogen sorption analyses, SEM, TGA. See DOI: 10.1039/c8dt02029a

‡These authors contributed equally.

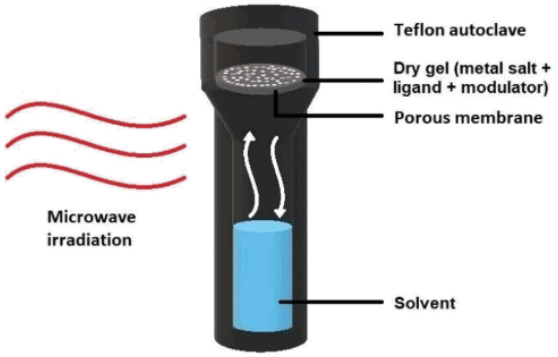

Scheme 1 Schematic drawing of the reactor set-up for microwave-assisted dry-gel conversion (MW-DGC).

To date, there are only a few reports for MOF synthesis using the DGC–concept.[31–38] These reports point to the advantages of DGC regarding the reduced reaction time[32] and solvent re-use,[31] compared to a conventionally heated solvothermal synthesis.

Microwave-assisted syntheses can further overcome time and energy issues and they are already well-established in synthetic chemistry but are still emerging for MOF syntheses.[39–41] In contrast to conductive heating, microwave radiation directly heats the reaction mixture and not primarily the vessel; hence, it is the reaction mixture that absorbs the microwave energy. This leads to localized superheating with very fast and efficient heating rates so that the desired temperatures are reached within seconds.[42–45] To the best of our knowledge, there has been no report yet on the production of MOFs using DGC in a microwave, with the original concept coming from zeolite synthesis.[14,46]

For the synthesis of MOFs in a microwave oven, the induction times are shortened and the rate constants are substantially increased.[20] In their 2012 review, Stock and Biswas list 25 MOFs prepared through microwave-assisted synthesis.[14] The combination of microfluidics with *e.g.* microwave synthesis may be an interesting efficient method for the large-scale production of MOFs.[47] HKUST-1, UiO-66 and MIL-53(Al) were already prepared in larger amounts and with a high space–time yield also through microwave-assisted heating.[48] Thereby, a continuous-flow microwave synthesis of MOFs as a potential highly efficient method for large-scale production was presented.[48] Furthermore, a recent review points out that microwave MOF synthesis can be considered extremely promising, as being associated with reduced reaction time and reduced process energy consumption, being also able to influence the MOF phase, crystal size, morphology and surface area, as well as being amenable to post-synthetic modifications of MOFs and scale up towards industrial-size microwave reactors.[49]

Besides extensive synthesis optimizations, one challenge was to ensure that microwave heating of the two compartments in the container (*i.e.* the reactants/dry-gel and solvent) occurs equally. However, the microwave absorption efficiency of organic solvents[50] is different from inorganic salts. As a consequence, overheating of the solid salt/linker reactants with decomposition occurred initially at higher pre-set temperatures in our hands, because the organic solvent was not heated to evaporation. We show here that this problem could be overcome by the addition of an ionic liquid (IL). ILs have a high absorption efficiency of microwave energy due to their ionic character, high polarity and high dielectric constant.[51]

In the following, we report the first syntheses of four MOFs by DGC under microwave irradiation with solvent re-use.

Experimental

Materials and instrumentation

All the chemicals were used as received by suppliers. For further information about all the materials see section S1 in the ESI†.

Powder X-ray diffractometry (PXRD) was performed at ambient temperature on a *D2 Phaser* (Bruker, Billerica, US) using Cu-K_α radiation (λ = 1.54182 Å) in the range 5° < 2Θ < 50° with a scanning rate of 0.0125° s^{-1} (300 W, 30 kV, 10 mA). Analyses of the diffractograms were carried out with *Match 3.11* software.

Thermogravimetric analysis (TGA) was carried out on a *Netzsch TG209 F3 Tarsus* (Netzsch, Selb, Germany) device under a synthetic air atmosphere, ramping at 5 K min^{-1} to 600 °C.

SEM images were acquired on a *JEOL JSM-6510 Advanced electron microscope* (Jeol, Akishima, Japan) with a LaB_6 cathode at 5–20 keV. The microscope was equipped with a *Xflash 410* (Bruker, Billerica, US) silicon drift detector.

Surface areas (BET) were determined by nitrogen (purity 99.999%, 5.0) sorption experiments at 77 K using liquid nitrogen and *ca.* 20–50 mg of the sample, performed on a *Quantachrome NOVA-4000e* (Quantachrome, Odelzhausen, Germany) instrument within a partial pressure range of pp_0^{-1} = 10^{-3}–1 bar. Each sample was degassed under vacuum (<10^{-2} mbar) at 150 °C for *ca.* 3 h prior to measurement. All the surface areas (BET) were calculated from five adsorption points applying Roquerol plots (r > 0.998). For the pressure ranges of each MOF, see chapter S7 (ESI†). Total pore volumes were calculated from the N_2 sorption isotherm at pp_0^{-1} = 0.95. NLDFT calculations for the pore size distributions were done with *NovaWin 11.03* software using the 'N_2 at 77 K on carbon, slit pore, as per the NLDFT equilibrium' model.

General

In a typical synthetic procedure, we prepared the reactant mixture of the metal salts and linker by pre-grinding them in the molar ratio according to the MOF formula. Microwave-assisted (MW) and, for comparison, conventional electric (CE)-heated DGC reactions were performed in a Teflon reactor using a *CEM MARS-5* microwave or a temperature programmable oven. Detailed information and pictures of the DGC reactors, synthesis information, work-up procedures and characterization are given in the ESI.† Product phase identity was veri-

fied by PXRD. For detailed information of the PXRD measurements with the suppression of X-ray fluorescence of iron, see section S6 (ESI†). Surface areas (*Brunauer*, *Emmett*, *Teller*, BET[52]) were determined by N_2 sorption at 77 K (*cf.* section S7 in the ESI†) and used as criteria for the porosity quality of the products.

MW-DGC of MIL-100(Fe)

$Fe(NO)_3{\cdot}9H_2O$ (77.2 mg, 0.19 mmol) or $FeCl_3{\cdot}6H_2O$ (52.0 mg, 0.19 mmol) and benzene-1,3,5-tricarboxylic acid (40.1 mg, 0.19 mmol) were placed on a MW-DGC sieve (*cf.* Fig. S1, ESI†) with water or an acidic solution (5 mL) at the bottom of the Teflon reactor, which was tightly closed and heated to 150 °C for 180 min by applying 800 W, using a *CEM MARS-5* microwave. The orange-brownish (from $Fe(NO)_3{\cdot}9H_2O$) or reddish (from $FeCl_3{\cdot}6H_2O$) solid products were washed with water and ethanol three times (10 mL each) and dried under vacuum (80 °C, 24 h). The amounts of starting materials for the repeat runs and the yields in the already optimized syntheses are given in Table S2 (ESI†).

MW-DGC of UiO-66

$ZrCl_4$ (88 mg, 0.38 mmol), terephthalic acid (H_2BDC) (63 mg, 0.38 mmol) and benzoic acid (BA) (100 mg, 0.82 mmol) were mixed, ground in a mortar and placed on the sieve. Dimethylformamide, DMF (10 mL) and HCl (1 mL, 37%) were placed at the bottom of the Teflon tube. The Teflon tube was capped and heated to 180 °C (10 min heating to 180 °C, 50 min, cooling) by applying 600 W, using a *CEM MARS-5* microwave. After the tube was cooled down to room temperature, the product was soaked in DMF (2 × 5 mL, 24 h each) and ethanol (5 mL, 24 h). The solvent was exchanged every 24 h. After a total time of 3 d of soaking, the solids were centrifuged and dried under vacuum (80 °C, 24 h).

MW-DGC of MIL-140A

$ZrCl_4$ (88 mg, 0.38 mmol), H_2BDC (63 mg, 0.38 mmol) and BA (100 mg, 0.82 mmol) were mixed, ground in a mortar and placed on the sieve. DMF solvent (10 mL) was placed at the bottom of the Teflon tube, which was capped and heated to 160 °C (10 min heating to 160 °C, 80 min, cooling) by applying 600 W, using a *CEM MARS-5* microwave. After the tube was cooled down to room temperature, the product was soaked in DMF (2 × 5 mL, 24 h each) and ethanol (5 mL, 24 h). The solvent was exchanged every 24 h. After 3 d of soaking, the solids were centrifuged and dried under vacuum (80 °C, 24 h).

MW-DGC of aluminium fumarate (Alfum)

$Al_2(SO_4)_3{\cdot}18H_2O$ (188 mg, 0.28 mmol), fumaric acid (65 mg, 0.56 mmol) and NaOH (44.8 mg, 1.12 mmol) were mixed and placed on a MW-DGC sieve with water (5 mL) at the bottom of a Teflon reactor. Conversion was carried out at 100 °C (60 min) by applying 800 W using a *CEM MARS-5* microwave. The white products were washed three times with water (10 mL each), and dried under vacuum (80 °C, 24 h).

Results and discussion

MIL-100(Fe)

In the case of MIL-100(Fe) (see section S2 in the ESI† for a brief description of this MOF, tradename *Basolite F300*), it was concluded that concentrated reactants may help achieve fast crystallization.[32,53] Hence, vapour-assisted methods, such as DGC and MW-DGC, should be advantageous.

For simplification, we do not list each experiment that was carried out within the synthesis optimizations. A lot of experiments yielded unsatisfying products, thereby, leading us to the eventually chosen – optimized – conditions. The synthesis optimization with the varying synthetic conditions for MIL-100(Fe) was done as follows: in a first approach towards MW-DGC of MIL-100(Fe), we optimized the DGC as described by Ahmed *et al.*[32] with respect to the reactants (using Fe^{III} salts instead of Fe^0 metal), a lower temperature (150 °C instead of 165 °C) and a significantly shorter reaction time (24 h instead of 4 d). So far in the literature report on the DGC of MIL-100(Fe), iron metal (Fe^0) was used in combination with HF.[32] Both for the CE-DGC and subsequent MW-DGC syntheses, the use HF or other fluoride sources, such as tetrabutylammonium fluoride (TBAF), as modulators did not increase the crystallinity or enhance the surface areas. Moreover, we found that the use of iron(III) salts with water only, *i.e.* without the use of HF or nitric acid, allowed reducing the reaction time from 96 h (ref. 32) to 24 h in the CE-DGC set-up and even further down to 3 h using MW-DGC. Water as a single solvent can help to overcome safety issues and environmental concerns, which are typically associated with strong acids in the synthesis of MIL-100(Fe).[19,32,54,55] Also, the use of iron(III) salts in CE-DGC seems to yield products with an increased porosity and enhanced BET areas compared to CE-DGC data from the literature (*cf.* Table 1).

MIL-100(Fe) was synthesized by MW-DGC and CE-DGC from a 1 : 1 mixture of $Fe(NO)_3{\cdot}9H_2O$ or $FeCl_3{\cdot}6H_2O$ and trimesic acid with water in good yields and in a significantly reduced time (*cf.* Table 1).

The crystallinity of all the obtained products by PXRD was at least equal, but often superior, to the commercially available, semi-amorphous product *Basolite F300* (*cf.* Fig. 1).

Fig. 2 shows the nitrogen sorption isotherms (from which the BET surface areas and pore volumes were derived) of the MIL-100(Fe) samples obtained *via* different synthetic approaches in comparison to *Basolite F300*.

MW-DGC yielded BET surface areas of MIL-100(Fe) ranging from 1000–1100 $m^2\ g^{-1}$, while CE-DGC syntheses formed products with values of *ca.* 1800–1900 $m^2\ g^{-1}$ (*cf.* Table 1).

Admittedly, MW-DGC yielded only MIL-100(Fe) products with a lower crystallinity and porosity than CE-DGC, albeit still comparable to the commercial *Basolite F300*. The lower crystallinity and porosity of MIL-100(Fe) can be traced to the xerogel-like or semi-amorphous formation of MIL-100(Fe),[19,59,73] when prepared in water only, *i.e.* without the use of strong mineral acids or other mineralizing agents. Also MW implies fast

Table 1 Comparison of BET surface areas and yields of MIL-100(Fe) from different synthesis routes

Synthesis route (reactant)	Time[a]	BET area[b] [$m^2 g^{-1}$]	Pore volume[c] [$cm^3 g^{-1}$]	Yield [%]
MW-DGC (Fe-chloride)	3 h	1002	0.43	78
MW-DGC (Fe-nitrate)		1105	0.48	81
CE-DGC (Fe-chloride)	24 h	1776	0.83	69
CE-DGC (Fe-nitrate)		1876	0.97	80
CE-DGC (Fe^0, ref. 32)	4 d	1340	0.63	Not specified
Solution-based (Fe^0 or Fe^{III})[d]	6 min,[41] 10 d(ref. 32)	356,[56] 2320[57]	0.39,[58] 1.30[59]	8,[60] 98[61]
Solvent-free(Fe^{III} and Fe^0)[e]	1 min–6 d	849–2492	0.69–0.96	17–99
Basolite F300(not specified)	Not specified	865–1252[f] 365–1001[g]	0.28–0.52[f] 0.15–0.60[g]	Not specified

[a] Reaction time includes any heating time needed to reach the set reaction temperature. [b] BET surface areas were obtained from five adsorption points in the pressure range pp_0^{-1} = 0.05–0.20. [c] Calculated using the NLDFT model for carbon (slit pore). [d] Lowest and highest values found in the literature.[32,41,53,55,57,59,62–65] A short synthesis correlates with a low BET surface area.[41] [e] Range of solvent-free approaches, which include MW, oven heating and grinding.[66,67] [f] Range of five individual measurements from the same batch (this work, *cf.* section S7 in the ESI). [g] Range in the literature,[53,56,58,59,68–70] where it is also noted that the BET given by the supplier (1300–1600 $m^2 g^{-1}$)[71] could not be verified. Values are rounded.

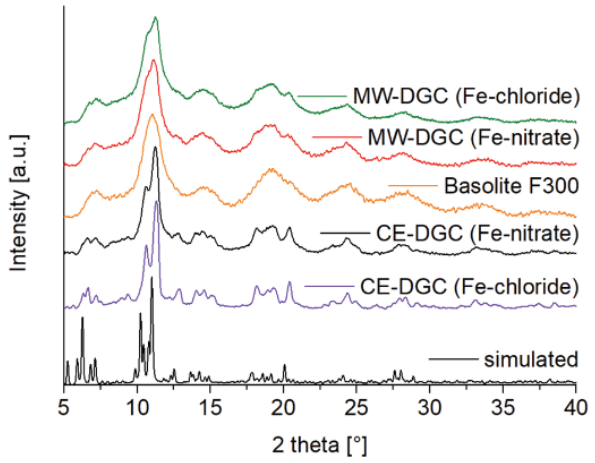

Fig. 1 PXRDs of CE- and MW-DGC products in comparison with the industrial benchmark *Basolite F300* and the simulated pattern. Simulated pattern was calculated using CSD-Refcode CIGXIA.[72]

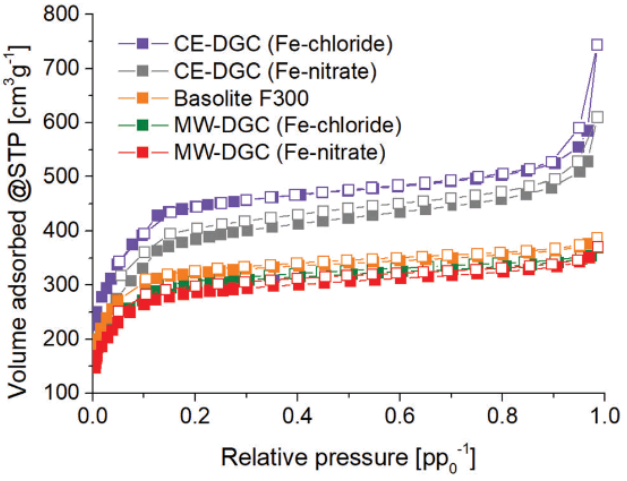

Fig. 2 Nitrogen sorption isotherms (77 K) of MIL-100(Fe) obtained *via* different synthetic routes in comparison to *Basolite F300*. Filled symbols: adsorption, empty symbols: desorption.

heating rates, which was found to be detrimental, particularly for highly porous MIL-100(Fe) products.[55,66]

The MIL-100(Fe) particle morphology, which was controlled *via* scanning electron microscopy (SEM), was similar for the DGC syntheses and commercial *Basolite F300*, with MW-DGC giving the largest particles (*cf.* section S8 in the ESI† for the SEM images).

UiO-66 and MIL-140A

We transferred our previously reported DGC procedure of UiO-66 into a microwave set-up.[31] Depending on the synthesis conditions we obtained two products, namely UiO-66 and MIL-140A (see section S2 in the ESI† for a brief description of these MOFs). In a typical MW-DGC synthesis of UiO-66, $ZrCl_4$ and H_2BDC were mixed in a 1 : 1 ratio and DMF was used as the reaction solvent at 180 °C with a 1 h reaction time. Additionally, two modulators (HCl/H_2O to DMF[74] and BA to $ZrCl_4/H_2BDC$[86]) were added. For synthesis of the polymorph MIL-140A, only BA was used and the temperature was set to 160 °C for 1.5 h (see section S4 in the ESI†). We noted that the reaction temperatures for the conventional solvothermal syntheses of the two polymorphs were reversed, in that UiO-66 was formed at only 120 °C in 24 h,[75] while for MIL-140A, 220 °C and 16 h were needed.[76] Fig. 3 shows the PXRD patterns of UiO-66 and MIL-140A products, verifying the crystallinity and phase purity by positive matching with the simulated patterns.

Fig. 4 shows the nitrogen sorption isotherms and Table 2 lists the porosity parameters derived therefrom. The obtained UiO-66 and MIL-140A product porosities were highly comparable with the results from the solution synthesis in the literature. The BET surface area of solvothermally synthesized UiO-66 varied between 769 (ref. 77) and 1777 $m^2 g^{-1}$.[78] Microwave-assisted synthesis delivered Langmuir surface areas of 888 up to 1661 $m^2 g^{-1}$.[79] The comparable BET surface areas obtained for UiO-66 *via* MW-DGC varied between 1194 $m^2 g^{-1}$ (HCl/BA modulated) and 1023 $m^2 g^{-1}$ (IL assisted). The BET surface area of MIL-140A from MW-DGC (354 $m^2 g^{-1}$) corresponds to the literature (335 $m^2 g^{-1}$).[80]

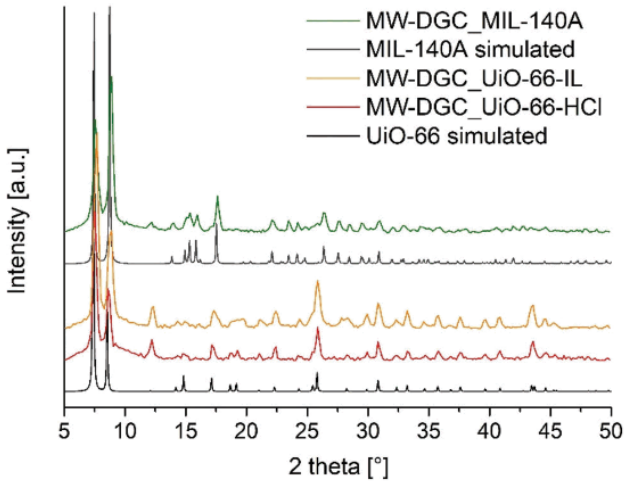

Fig. 3 PXRDs of simulated UiO-66, as-synthesized UiO-66-HCl (MW-DGC) and UiO-66-IL (MW-DGC), simulated MIL-140A and as-synthesized MIL-140A (MW-DGC). Simulated pattern of UiO-66 was calculated using CSD-Refcode RUBTAK02,[75] while the simulated pattern of MIL-140A was calculated using CSD-Refcode ZONBAH.[76]

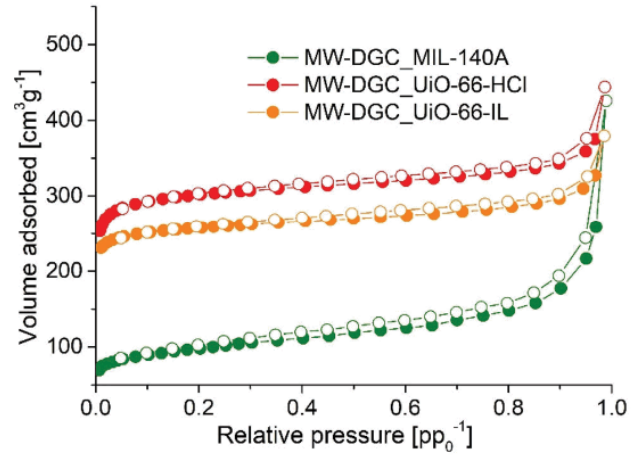

Fig. 4 Nitrogen sorption isotherms (77 K) of MW-DGC products of UiO-66 and MIL-140A. Filled symbols: adsorption, empty symbols: desorption.

The use of BA as a modulator in the reactant mixture ensured the formation of a dry-gel with a stable and thick consistency. $ZrOCl_2 \cdot 8H_2O$ was proven to allow gel-based morphological control, *e.g.* preparation as monolithic xerogels.[83] Without BA (but with HCl/H_2O) as a modulator, the reactants fell through the sieve. HCl as a modulator is often used to increase the defects in the framework to reach higher surface areas.[74] Here, the addition of aqueous HCl proved necessary to increase the microwave-energy absorption in DMF with the temperature set to 180 °C for sufficient evaporation to wet the reactants. Without HCl/H_2O, the reactants often decomposed partially due to the enhanced microwave irradiation needed to reach the set temperature of 180 °C. It has to be noted here that the IR temperature sensor of the microwave was placed below the bottom of the Teflon vessel, hence, it measured the temperature of the solvent part. Thus, reproducible preparation of UiO-66 at 180 °C was only successful when adding HCl/H_2O or an ionic liquid to DMF. For the synthesis of MIL-140A, the addition of HCl/H_2O proved not necessary as the set temperature of 160 °C did not induce decomposition in the reactants.

However, the use of aqueous HCl led to the decomposition of DMF to dimethylamine and formic acid,[84] which prevented the desired solvent re-use. This was the reason why HCl/H_2O was replaced by the ionic liquid to ensure the microwave absorption in the DMF akin to an IL-assisted synthesis.[85] As an IL, we used 1-*n*-butyl-3-methylimidazolium bis(trifluorosulfonyl)imide, $[BMIm]NTf_2$.

Recently we reported that CE-DGC delivers crystals of UiO-66 with a size range of 90–200 nm.[31] The MW-DGC of UiO-66-HCl led to relatively uniform-sized particles in a range of *ca.* 100 to 200 nm, which appear agglomerated. In comparison, solution synthesis delivered UiO-66 crystals with a particle size ranging from *ca.* 200 to 500 nm, as demonstrated by Pullen *et al.* (*cf.* section S8 in the ESI† for SEM images).[86] The MW-DGC of MIL-140A showed also agglomerated particles with a wide particle size ranging from 50 to 250 nm.

For Zr-based MOFs, it is recommended to perform thermogravimetric analysis (TGA) for defect analysis (*cf.* Fig. 5).[78] In the case of UiO-66, typically three weight losses were observed. At the beginning, solvent residues were degassed in a tempera-

Table 2 Results of MW-DGC synthesis of UiO-66 and MIL-140A with different modulators

Product(synthesis route)	Reaction time [a]	BET area[b] [$m^2\ g^{-1}$]	Pore volume[c] [$cm^3\ g^{-1}$]	Yield [%]
UiO-66-HCl (MW-DGC) [d]	1 h	1195	0.53	76
UiO-66-IL (MW-DGC) [d]	1 h	1023	0.46	68
UiO-66(CE-DGC, ref. 31)	27 h	1242–1461	0.55–0.69	65–83
UiO-66(solution-based) [e]	5 min,[48] 72 h (ref. 78)	769,[77] 1777[78]	0.44,[78] 0.69[78]	94[48]
UiO-66(solvent-free)	30 (ref. 81)–90 min (ref. 82)	730[82]–1217[81]	0.40[81]	
MIL-140A (MW-DGC) [d]	1.5 h	354	0.35	92
MIL-140A(solution-based) [f]	17 min,[80] 16 h (ref. 76)	337,[80] 415[76]	0.18[76]	91[76]

[a] Reaction time includes any heating time needed to reach the set reaction temperature. [b] BET surface areas were obtained from five adsorption points in the pressure range pp_0^{-1} = 0.01–0.05 for UiO-66 and pp_0^{-1} = 0.01–0.10 for MIL-140A. [c] Calculated using the NLDFT model for carbon (slit pore). [d] This work. [e] Lowest and highest values found in the literature on UiO-66.[48,77,78] [f] Lowest and highest values found in the literature on MIL-140A.[76,80] Values are rounded.

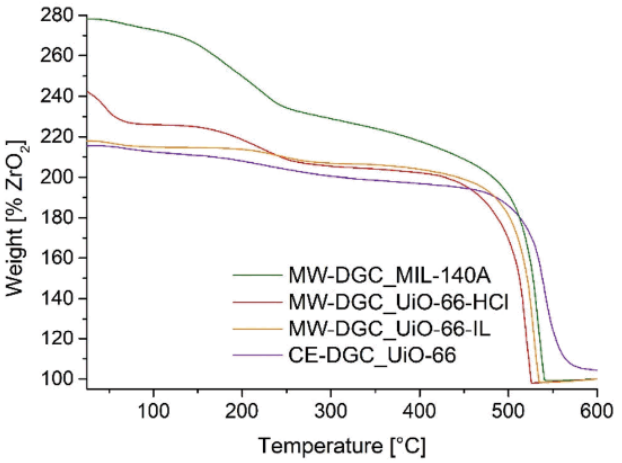

Fig. 5 TGA results of UiO-66-HCl (CE-DGC), UiO-66-IL (MW-DGC), UiO-66-HCl (MW-DGC) and MIL-140A (MW-DGC); end weights are normalized to 100%.

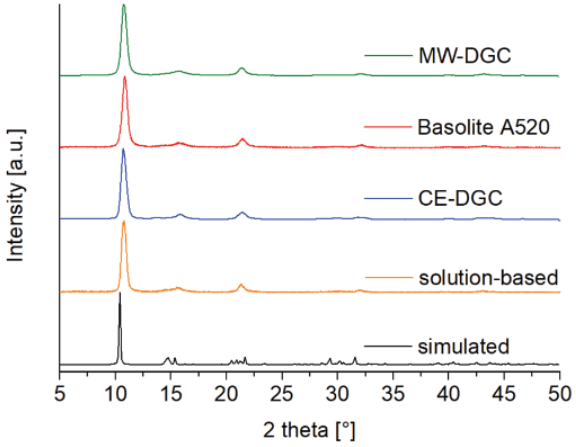

Fig. 6 PXRDs of CE- and MW-DGC products in comparison with solution-based synthesis, the industrial benchmark *Basolite A520* and the simulated pattern. Simulated pattern was calculated using CSD-Refcode DOYBEA.[89]

ture interval between 25 °C and 100 °C. Second, the decomposition of monocarboxylate ligands (*i.e.* BA) and the dihydroxylation of the $\{Zr_6O_4(OH)_4\}$ secondary building units (SBUs) occur in a similar temperature range of *ca.* 180–300 °C,[78] such that $\{Zr_6O_6\}$ SBUs are built.[75] Finally, the linker and framework decomposition occur above *ca.* 350–550 °C. In conclusion, we determined the linker defects per SBU unit according to Shearer *et al.*[78] An assumption for this method is that the residue in each TGA experiment is pure ZrO_2, which is set to 100% (*cf.* Fig. 5). A similar method to determine the defects was applied for MIL-140A.

The defect parameters for UiO-66 and MIL-140A calculated from thermogravimetric analyses are summarized in Table 3. For comparison, the TGA and defect analysis of UiO-66 obtained *via* CE-DGC is added. The number of defects per SBU were in the range of 1.16 to 1.36, which is in the same range of linker deficiencies reported by Shearer *et al.*[78] Detailed information about the calculation of defects is outlined in section S9 in the ESI.

Aluminium fumarate (Alfum)

We were able to transfer a solution-based synthesis of aluminium fumarate (see section S2 in the ESI† for a brief description of this MOF, tradename *Basolite A520*)[87,88] into a microwave autoclave for the first time. Alfum was obtained from a precursor mixture of $Al_2(SO_4)_3{\cdot}18H_2O$, fumaric acid and NaOH (molar ratio 1 : 2 : 4) with water. The MW-DGC products were compared to CE-DGC products and products from conventional solution-based synthesis. Detailed synthesis information is given in section S5 in the ESI.†

Since the stoichiometric ratio had already been optimized in the BASF patent,[87] we only varied the conversion times. The crystallinity of all the obtained products by PXRD was about equal, including the commercial *Basolite A520* product (*cf.* Fig. 6).

Therefore, the BET surface areas were again used as the main quality criterion for evaluation of all the obtained aluminium fumarate products and were found to be in good agreement with each other, independent of the synthesis method (*cf.* Table 4).

There was a significant difference in the shape of the nitrogen sorption isotherms between the MW-DGC and the other Alfum materials (*cf.* Fig. 7). At very low pp_0^{-1}, all the isotherms showed a steep increase in nitrogen uptake, characteristic of a Type I isotherm for microporous materials.[52] Different from a Type I isotherm, which has a limiting uptake governed by the

Table 3 Determination of defects from TGA under synthetic air atmosphere

Product(synthesis route)	No. of defects per SBU(x)[a].	Molecular formula $Zr_6O_{6+x}(BDC)_{6-x}$[b] and $ZrO_{1+x}(BDC)_{1-x}$	Exp. molecular weight [g mol^{-1}]
UiO-66 (CE-DGC, ref. 31)	1.36	$Zr_6O_{7.36}(BDC)_4$ [64]	1435.92
UiO-66-HCl (MW-DGC)	1.17	$Zr_6O_{7.17}(BDC)_4$ [73]	1447.83
UiO-66-IL (MW-DGC)	1.16	$Zr_6O_{7.16}(BDC)_4$ [74]	1449.34
MIL-140A (MW-DGC)	0.03	$ZrO_{1.03}(BDC)_0$ [97]	268.85

[a] Calculation of defect-numbers per SBU x are presented in the ESI (section S9). Values are rounded to one decimal digit. [b] Determination of defects from TGA are similar to those in the work of Shearer *et al.*,[78] where the molecular formula and experimental molecular weight were also given without modulator units in place of missing BDC linkers.

Table 4 Comparison of the porosity parameters and yields of Alfum from different aqueous synthesis routes

Synthesis route	Time [a]	BET area [b] [$m^2 g^{-1}$]	Pore volume [$cm^3 g^{-1}$] [c]	Yield [%]
MW-DGC[d]	1 h	1075–1150	0.72–0.94	76–89
CE-DGC[d]	6 h	1037–1188	0.43–0.61	58–71
Solution-based[d]	>3 h	780–1254	0.36–0.72	73–85
Solution-based[e]		925,[90] 1212[91]	0.44,[91] 0.65[90]	88,[90] 90[92]
Basolite A520	>5 h	723–1333[f,h]	0.47[89]	76–98[e]
		999–1040[g]	0.51–0.63[g]	

[a] Reaction time includes any heating time needed to reach the set reaction temperature. [b] BET surface areas were obtained from five adsorption points in the pressure range pp_0^{-1} = 0.001–0.05. [c] Calculated using the NLDFT model for carbon (slit pore); contributions from micropores are given in Table S7 (ESI). [d] This work, range of six samples. [e] Lowest and highest values found in the literature.[89–94] [f] Stated in the patent.[88] [g] Range of five individual measurements from the same batch (this work, *cf.* section S7 in the ESI) and in good agreement with ranges given in the literature.[87–89] [h] Langmuir surface area. Values are rounded.

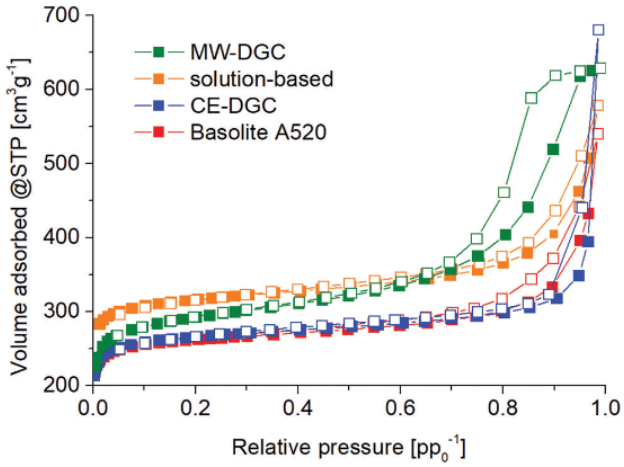

Fig. 7 Nitrogen sorption isotherms (77 K) of Alfum obtained *via* different synthetic routes in comparison to *Basolite A520*. Filled symbols: adsorption, empty symbols: desorption.

accessible microporous volume, the isotherms showed an increase in N_2 uptake at elevated partial pressure. For the Alfum materials from CE-DGC, solution synthesis and for *Basolite A520*, *this increase* corresponds to a Type II or III isotherm together with an H4 hysteresis. Thus, the overall adsorption isotherms of Alfum materials from CE-DGC, solution synthesis and for *Basolite A520* were a composite of Type I and II/III.

H4 loops go along with composite adsorption branches of Types I and II, and are often found with aggregated crystals of microporous materials. Thus, the microporous Alfum materials from CE-DGC, solution synthesis and *Basolite A520* featured macropores (>50 nm diameter) from the interparticle voids of aggregated microparticles (*cf.* Fig. S12 in the ESI† for the SEM images).[90] Interparticle condensation typically appears at pressures $pp_0^{-1} > 0.4$ for N_2 sorption (77 K).[95]

Alfum obtained by MW–DGC exhibited an adsorption isotherm with an increase at higher partial pressure to a final saturation plateau, which is typical for a Type IV isotherm. Type IV isotherms are given by mesoporous adsorbents. Also, H2(b) hysteresis is seen for mesoporous materials with complex pore structures and large size distribution of neck widths.[52] Overall, the adsorption isotherm for MW-DGC Alfum was bimodal as a combination of Type I (due to the known microporosity of Alfum) and Type IV. This bimodal Type I + IV feature is common and was highly reproducible for all the MW-DGC samples we prepared, as shown in Fig. S7 in the ESI.† Bimodal isotherms are in the literature described for the gel-like formation of MOFs.[96]

By principle, N_2 sorption isotherms and BET theory cannot probe macropores. Thus, the subsequent pore size distribution based on non-linear density functional theory (NLDFT) calculations showed only (micro- and) mesopores (2–50 nm). The pore size distributions for the different Alfum materials (*cf.* Fig. S8 and S9 and further porosity details in Table S7 in the ESI†) reflect the aforementioned differences in the sorption isotherms and hystereses between the MW-DGC and the three others. The highly reproducible pore width distribution for Alfum batches from MW-DGC (*cf.* Fig. 8) showed a pronounced and unique narrow mesopore contribution of 5–11 nm in comparison with Alfum obtained *via* other syntheses methods (*cf.* Fig. S8 and S9 in the ESI†). Porosity across the micro- and mesoporous regime is termed hierarchical porosity. We noted that the hierarchical porous Alfum material from MW-DGC

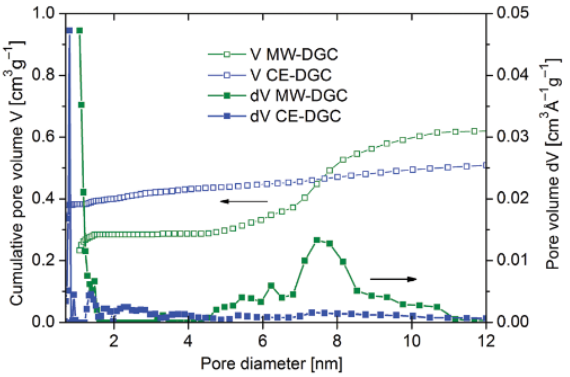

Fig. 8 Comparative pore size distributions as cumulative (left) and incremental pore volume (right) from N_2 sorption isotherms (77 K) of Alfum obtained *via* MW-DGC (green) and CE-DGC (blue). See ESI† for pore size distributions of solution-based Alfum and *Basolite A520*.

was achieved solely by the synthesis method, that is without the addition of surfactants or templates, as are typically used for the synthesis of hierarchical porous MOFs.[97–99]

It would not be reasonable to assume that particle aggregation leads to such a narrow mesopore range. Other gel-like micro-mesoporous MOFs exhibit much broader mesopore distribution over at least a 20 nm range, which is then interpreted as an interparticle void.[83] Instead we propose that the Alfum material made from MW-DGC features mesopores (together with micropores) within the framework due to defects. As such, MW-DGC advantageously leads to a different, namely, hierarchical micro–mesoporous Alfum material compared to the other synthesis methods (Table S7, ESI†).

Solvent re-use

The separation of the reaction products and solvent in DGC enables the solvent to be recovered largely uncontaminated and re-used, as was recently shown.[31] Hence, we performed repeated synthesis runs with re-use of the solvent and fresh precursors in the realm of sustainable MOF synthesis.[14,22,28] Thereby, we were able to prove that the re-use of solvent is generally possible in MW-DGC for at least three synthesis runs (*cf.* section S10 in the ESI†). The four MOFs MIL-100(Fe), UiO-66, MIL-140A and Alfum could be prepared by replacing the product with fresh precursor at the head of the container and then repeating the reaction with the same, unchanged solvent left in the bottom of the Teflon vessel. For UiO-66 the precursor also included the BA modulator. The quality criteria BET surface areas, crystallinity (PXRD, *cf.* Fig S14–S17 ESI† for 3 runs of each MOF) and yields varied, but within acceptable limits (*cf.* Fig. 9).

For MIL-100(Fe), the yield varied between 72% and 82%, the BET surface area between 935 and 1287 $m^2\ g^{-1}$.

For MIL-140A, the yields were in the range from 89% to 96% and the BET surface areas from 354 to 340 $m^2\ g^{-1}$.

For UiO-66, a solvent re-use was not possible in the presence of HCl/H_2O due to decomposition of DMF. Alternatively, the synthesis of UiO-66 with re-use of the solvent-mixture of DMF and IL was successful. Then, the UiO-66 yield varied between 68% and 73% and the BET surface areas between 717 and 1023 $m^2\ g^{-1}$.

For Alfum, we obtained yields between 76% and 89% and BET surface areas between 1075 and 1148 $m^2\ g^{-1}$.

When comparing DGC synthesis to seemingly simple and sometimes also fast solution synthesis routes, it should be noted that such solution syntheses involve large amounts of solvents. For example, in the patented and most effective aluminium fumarate synthesis, a space–time yield (STY) of 3615 kg m^{-3} day^{-1} goes along with the use of at least 84 555 L of mother liquor.[87] For a continuous-flow UiO-66 synthesis with an STY of 2053 kg m^{-3} day^{-1}, the amount of reaction mother liquor seems to be at least 59 000 L, and amounts to 289 000 L if washing solvents are included (*cf.* section S11 in the ESI† for details of the calculation).[48]

Conclusion

We demonstrated that the novel technique MW-DGC holds the potential to synthesize MOFs in a fast, safe, good-yield and energy-reduced procedure in qualities comparable to the literature or commercial MOF materials. The reaction times and therefore energy input could be drastically shortened, compared to conventional electric-heated dry-gel conversion or solvothermal synthesis. In addition, MW-DGC is a step towards sustainable MOF synthesis due to the ability of solvent re-use (*cf.* Fig. 10).

Noteworthy, MW-DGC can also give rise to a unique, hierarchical Alfum material with mesoporosity built into the otherwise microporous framework. This was shown through a comparative N_2 sorption and pore size analysis of Alfum materials from different synthesis methods. The prominent hysteresis

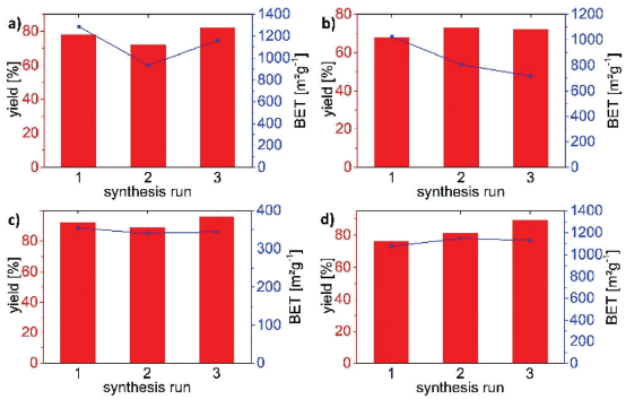

Fig. 9 Solvent re-use over three synthesis runs in the case of: (a) MIL-100(Fe), (b) UiO-66-IL, (c) MIL-140A and (d) Alfum. Data can be found in Tables S8–S11 in the ESI.†

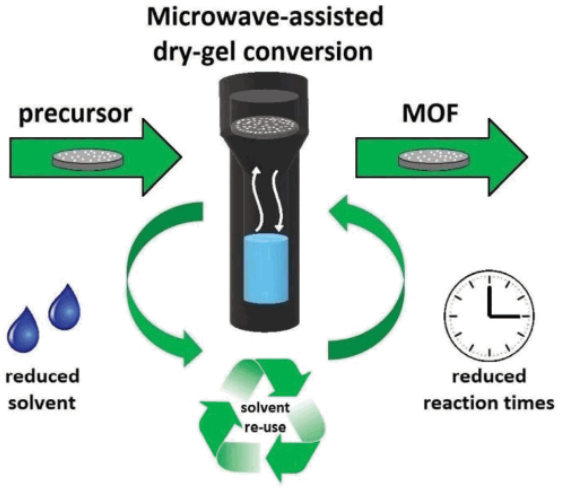

Fig. 10 Schematic summary of the advantages of MW-DGC with respect to reduced reaction times, reduced solvent amount and solvent re-use.

loop in the region $pp_0^{-1} > 0.7$ with mesopore characteristics was reproducibly obtained for the MW-DGC products of Alfum.

The recovery of solvent shown here for the MW-DGC technique allows reducing the solvent use in MOF synthesis drastically, as is otherwise only possible with mechano-chemistry. Accordingly, we hope that we can contribute to the environmentally and economically optimized syntheses of selected prototypical MOFs, since the technique should be clearly expandable to most MOF syntheses.

Conflicts of interest

There are no conflicts of interest to declare.

Acknowledgements

The authors gratefully acknowledge the financial support of the Federal German Ministry of Education and Research (BMBF) in the project Optimat under grant no. 03SF0492C.

References

1 G. Maurin, C. Serre, A. Cooper and G. Férey, *Chem. Soc. Rev.*, 2017, **46**, 3104–3107.
2 Y.-B. Huang, J. Liang, X.-S. Wang and R. Cao, *Chem. Soc. Rev.*, 2017, **46**, 126–157.
3 A. Herbst and C. Janiak, *CrystEngComm*, 2017, **19**, 4092–4117.
4 W. P. Lustig, S. Mukherjee, N. D. Rudd, A. V. Desai, J. Li and S. K. Ghosh, *Chem. Soc. Rev.*, 2017, **46**, 3242–3285.
5 J.-R. Li, R. J. Kuppler and H.-C. Zhou, *Chem. Soc. Rev.*, 2009, **38**, 1477–1504.
6 J. Dechnik, J. Gascon, C. J. Doonan, C. Janiak and C. J. Sumby, *Angew. Chem., Int. Ed.*, 2017, **56**, 9292–9310.
7 K. Adil, Y. Belmabkhout, R. S. Pillai, A. Cadiau, P. M. Bhatt, A. H. Assen, G. Maurin and M. Eddaoudi, *Chem. Soc. Rev.*, 2017, **46**, 3402–3430.
8 P. Horcajada, R. Gref, T. Baati, P. K. Allan, G. Maurin, P. Couvreur, G. Férey, R. E. Morris and C. Serre, *Chem. Rev.*, 2012, **112**, 1232–1268.
9 F. Jeremias, D. Fröhlich, C. Janiak and S. K. Henninger, *New J. Chem.*, 2014, **38**, 1846–1852.
10 J. Zhou, H. Li, H. Zhang, H. Li, W. Shi and P. Cheng, *Adv. Mater.*, 2015, **27**, 7072–7077.
11 F. A. Almeida Paz, J. Klinowski, S. M. F. Vilela, J. P. C. Tome, J. A. S. Cavaleiro and J. Rocha, *Chem. Soc. Rev.*, 2012, **41**, 1088–1110.
12 R. Haldar and T. K. Maji, *CrystEngComm*, 2013, **15**, 9276–9295.
13 C. R. Wade, T. Corrales-Sanchez, T. C. Narayan and M. Dincă, *Energy Environ. Sci.*, 2013, **6**, 2172–2177.
14 N. Stock and S. Biswas, *Chem. Rev.*, 2012, **112**, 933–969.
15 J. Chen, K. Shen and Y. Li, *ChemSusChem*, 2017, **10**, 3165–3187.
16 M. Gaab, N. Trukhan, S. Maurer, R. Gummaraju and U. Müller, *Microporous Mesoporous Mater.*, 2012, **157**, 131–136.
17 P. A. Bayliss, I. A. Ibarra, E. Pérez, S. Yang, C. C. Tang, M. Poliakoff and M. Schröder, *Green. Chem.*, 2014, **16**, 3796–3802; C. Avci-Camur, J. Troyano, J. Pérez-Carvajal, A. Legrand, D. Farrusseng, I. Imaz and D. Maspoch, *Green Chem.*, 2018, **20**, 873–878.
18 J. Ren, X. Dyosiba, N. M. Musyoka, H. W. Langmi, M. Mathe and S. Liao, *Coord. Chem. Rev.*, 2017, **352**, 187–219.
19 K. Guesh, C. A. D. Caiuby, Á. Mayoral, M. Díaz-García, I. Díaz and M. Sanchez-Sanchez, *Cryst. Growth Des.*, 2017, **17**, 1806–1813.
20 H. Reinsch and N. Stock, *Dalton Trans.*, 2017, **46**, 8339–8349.
21 Z. Hu and D. Zhao, *Dalton Trans.*, 2015, **44**, 19018–19040.
22 H. Reinsch, *Eur. J. Inorg. Chem.*, 2016, **27**, 4290–4299; H. Reinsch, S. Waitschat, S. M. Chavan, K. P. Lillerud and N. Stock, *Eur. J. Inorg. Chem.*, 2016, 4490–4498.
23 G. Zhan and H. C. Zheng, *Chem. Commun.*, 2017, **53**, 72–81.
24 T. Friščić, S. L. Childs, S. A. A. Rizvi and W. Jones, *CrystEngComm*, 2009, **11**, 418–426.
25 D. Crawford, J. Casaban, R. Haydon, N. Giri, T. McNally and S. L. James, *Chem. Sci.*, 2015, **6**, 1645–1649.
26 K. Matsuyama, *J. Supercrit. Fluid*, 2018, **134**, 197–203.
27 P. W. Dunne, E. Lester and R. I. Walton, *React. Chem. Eng.*, 2016, **1**, 352–360.
28 P. A. Julien, C. Mottillo and T. Friščić, *Green Chem.*, 2017, **19**, 2729–2747.
29 L. M. Gilbertson, J. B. Zimmermann, D. L. Plata, J. E. Hutchinson and P. T. Anastas, *Chem. Soc. Rev.*, 2015, **44**, 5758–5777.
30 M. Matsukata, M. Ogura, T. Osaki, P. R. H. P. Rao, M. Nomura and E. Kikuchi, *Top. Catal.*, 1999, **9**, 77–92.
31 S. Gökpinar, T. Diment and C. Janiak, *Dalton Trans.*, 2017, **46**, 9895–9900.
32 I. Ahmed, J. Jeon, N. A. Khan and S. H. Jhung, *Cryst. Growth Des.*, 2012, **12**, 5878–5881.
33 H. Zhang, J. Zhong, G. Zhou, J. Wu, Z. Yang and X. Shi, *J. Nanomater.*, 2016, 9648386.
34 Q. Shi, Z. Chen, Z. Song, J. Li and J. Dong, *Angew. Chem., Int. Ed.*, 2011, **50**, 672–675.
35 J. Kim, Y.-R. Lee and W.-S. Ahn, *Chem. Commun.*, 2013, **49**, 7647–7649.
36 N. D. McNamara and J. C. Hicks, *ACS Appl. Mater. Interfaces*, 2015, **7**, 5338–5346.
37 A. K. Das, R. S. Vemuri, I. Kutnyakov, B. P. McGrail and R. K. Motkuri, *Sci. Rep.*, 2016, **6**, 28050.
38 P. Tan, X.-Y. Xie, X.-Q. Liu, T. Pan, C. Gu, P.-F. Chen, J.-Y. Zhou, Y. Pan and L.-B. Sun, *J. Hazard. Mater.*, 2017, **321**, 344–352.
39 Z. Ni and R. I. Masel, *J. Am. Chem. Soc.*, 2006, **128**, 12394–12395.

40 S. H. Jhung, J.-H. Lee, J. W. Yoon, C. Serre, G. Férey and J.–S. Chang, *Adv. Mater.*, 2007, **19**, 121–124.

41 A. G. Márquez, A. Demessence, A. E. Platero-Prats, D. Heurtaux, P. Horcajada, C. Serre, J.-S. Chang, G. Férey, V. A. de la Peña-O'Shea, C. Boissière, D. Grosso and C. Sanchez, *Eur. J. Inorg. Chem.*, 2012, 5165–5174.

42 M. F. Groh, M. Heise, M. Kaiser and M. Ruck, *Nachr. Chem.*, 2013, **61**, 26–29.

43 A. L. Buchachenko and E. L. Frankevich, *Chemical Generation and Reception of Radio- and Microwaves*, Wiley-VCH, Weinheim, Germany 1993, pp. 41–56.

44 V. K. Ahluwulia, *Alternative Energy Processes in Chemical Synthesis*, Alpha Science International LTD, Oxford, United Kingdom, 2008.

45 I. Bilecka and M. Niederberger, *Nanoscale*, 2010, **2**, 1358–1374.

46 C. S. Cundy and P. A. Cox, *Chem. Rev.*, 2003, **103**, 663–702.

47 C. Echaide-Górriz, C. Clément, F. Cacho-Bailo, C. Téllez and J. Coronas, *J. Mater. Chem. A*, 2018, **6**, 5485–5506.

48 M. Taddei, D. A. Steitz, J. A. van Bokhoven and M. Ranocchiari, *Chem. – Eur. J.*, 2016, **22**, 3245–3249.

49 I. Thomas-Hillmann, A. Laybourn, C. Dodds and S. W. Kingman, *J. Mater. Chem. A*, 2018, **6**, 11564–11581.

50 A. de la Hoz, A. Diaz-Ortiz and A. Moreno, *Chem. Soc. Rev.*, 2005, **34**, 164–178.

51 M. Larhed, C. Moberg and A. Hallberg, *Acc. Chem. Res.*, 2002, **35**, 717–727.

52 M. Thommes, K. Kaneko, A. V. Neimark, J. P. Olivier, F. Rodriguez-Reinoso, J. Rouquerol and K. S. Sing, *Pure Appl. Chem.*, 2015, **87**, 1051–1069.

53 Y.-K. Seo, J. W. Yoon, J. S. Lee, U.-H. Lee, Y. K. Hwang, C.–H. Jun, P. Horcajada, C. Serre and J.-S. Chang, *Microporous Mesoporous Mater.*, 2012, **157**, 137–145.

54 G. Férey, C. Serre, C. Mellot-Draznieks, F. Millange, S. Surblé, J. Dutour and I. Margiolaki, *Angew. Chem.*, 2004, **116**, 6456–6461.

55 F. Jeremias, S. K. Henninger and C. Janiak, *Dalton Trans.*, 2016, **45**, 8637–8644.

56 G. Majano, O. Ingold, M. Yulikov, G. Jeschke and J. Pérez-Ramírez, *CrystEngComm*, 2013, **15**, 9885–9892.

57 J. W. Yoon, Y.-K. Seo, Y. K. Hwang, J.-S. Chang, H. Leclerc, S. Wuttke, P. Bazin, A. Vimont, M. Daturi, E. Bloch, P. L. Llewellyn, C. Serre, P. Horcajada, J. M. Grèneche, A. E. Rodrigues and G. Férey, *Angew. Chem.*, 2010, **122**, 6085–6088.

58 M. Pilloni, F. Padella, G. Ennas, S. Lai, M. Bellusci, E. Rombi, F. Sini, M. Pentimalli, C. Delitala, A. Scano, *et al.*, *Microporous Mesoporous Mater.*, 2015, **213**, 14–21.

59 M. Sanchez-Sanchez, I. de Asua, D. Ruano and K. Diaz, *Cryst. Growth Des.*, 2015, **15**, 4498–4506.

60 E. Bellido, M. Guillevic, T. Hidalgo, M. J. Santander-Ortega, C. Serre and P. Horcajada, *Langmuir*, 2014, **30**, 5911–5920.

61 A. García Márquez, A. Demessence, A. E. Platero-Prats, D. Heurtaux, P. Horcajada, C. Serre, J.–S. Chang, G. Férey, V. A. de la Peña-O'Shea, C. Boissière, D. Grosso and C. Sanchez, *Eur. J. Inorg. Chem.*, 2012, **30**, 5165–5174.

62 M. Wickenheisser, T. Paul and C. Janiak, *Microporous Mesoporous Mater.*, 2015, **215**, 258–269.

63 M. Wickenheisser, A. Herbst, R. Tannert, B. Milow and C. Janiak, *Microporous Mesoporous Mater.*, 2016, **220**, 143–153.

64 F. Jeremias, S. K. Henninger and C. Janiak, *J. Mater. Chem.*, 2012, **22**, 1014810151.

65 H. Tian, J. Peng, Q. Du, X. Hui and H. He, *Dalton Trans.*, 2018, **47**, 3417–3424.

66 M. Lanchas, S. Arcediano, A. T. Aguayo, G. Beobide, O. Castillo, J. Cepeda, D. Vallejo-Sánchez and A. Luque, *RSC Adv.*, 2014, **4**, 60409–60412.

67 L. Han, H. Qi, D. Zhang, G. Ye, W. Zhou, C. Hou, W. Xu and Y. Sun, *New J. Chem.*, 2017, **41**, 13504–13509.

68 A. Dhakshinamoorthy, M. Alvaro, P. Horcajada, E. Gibson, M. Vishnuvarthan, A. Vimont, J.-M. Grèneche, C. Serre, M. Daturi and H. Garcia, *ACS Catal.*, 2012, **2**, 2060–2065.

69 A. Dhakshinamoorthy, M. Alvaro, H. Chevreau, P. Horcajada, T. Devic, C. Serre and H. Garcia, *Catal. Sci. Technol.*, 2012, **2**, 324–330.

70 G. Blanco-Brieva, J. M. Campos-Martin, S. M. Al-Zahrani and J. L. G. Fierro, *Global NEST J.*, 2010, **12**, 296–304.

71 http://www.sigmaaldrich.com/catalog/product/aldrich/690872; 28.06.2017, 16:03 h.

72 P. Horcajada, S. Surble, C. Serre, D.-Y. Hong, Y.-K. Seo, J.–S. Chang, J.-M. Grèneche, I. Margiolaki and G. Férey, *Chem. Commun.*, 2007, **27**, 2820–2822.

73 S. Xiang, L. Li, J. Zhang, X. Tan, H. Cui, J. Shi, Y. Hu, L. Chen, C.–Y. Su and S. L. James, *J. Mater. Chem.*, 2012, **22**, 1862–1867.

74 M. J. Katz, Z. J. Brown, Y. J. Colón, P. W. Siu, K. A. Scheidt, R. Q. Snurr, J. T. Hupp and O. K. Farha, *Chem. Commun.*, 2013, **49**, 9449–9451.

75 L. Valenzano, B. Civalleri, S. Chavan, S. Bordiga, M. H. Nilsen, S. Jakobsen, K. P. Lillerud and C. Lamberti, *Chem. Mater.*, 2011, **23**, 1700–1718.

76 V. Guillerm, F. Ragon, M. Dan-Hardi, T. Devic, M. Vishnuvarthan, B. Campo, A. Vimont, G. Clet, Q. Yang, G. Maurin, G. Ferey, A. Vittadini, S. Gross and C. Serre, *Angew. Chem., Int. Ed.*, 2012, **51**, 9267–9271.

77 Z. Hu, Y. Peng, Z. Kang, Y. Qian and D. Zhao, *Inorg. Chem.*, 2015, **54**, 4862–4868.

78 G. C. Shearer, S. Chavan, S. Bordiga, S. Svelle, U. Olsbye and K. P. Lillerud, *Chem. Mater.*, 2016, **28**, 3749–3761.

79 Y. Li, Y. Liu, W. Gao, L. Zhang, W. Liu and J. Lu, *CrystEngComm*, 2014, **16**, 7037–7042.

80 W. Liang and D. M. D'Alessandro, *Chem. Commun.*, 2013, **49**, 3706–3708.

81 P. Hu, X. Liang, M. Yaseen, X. Sun, Z. Tong, Z. Zhao and Z. Zhao, *Chem. Eng. J.*, 2018, **332**, 608–618.

82 K. Užarević, T. C. Wang, S.-Y. Moon, A. M. Fidelli, J. T. Hupp, O. K. Farha and T. Friščić, *Chem. Commun.*, 2016, **52**, 2133–2136.

83 B. Bueken, N. Van Velthoven, T. Willhammar, T. Stassin, I. Stassen, D. A. Keen, G. V. Baron, J. F. M. Denayer, R. Ameloot, S. Bals, D. De Vos and T. D. Bennett, *Chem. Sci.*, 2017, **8**, 3939–3948.

84 H.-P. Kruse, Key word 'Dimethylformamide', in *Römpp Lexikon Chemie*, ed. J. Falbe and M. Regitz, Georg Thieme Verlag, Stuttgart, Germany, 10th edn, 1997.
85 B. Floris, F. Sabuzi, P. Galloni and V. Conte, *Catalysts*, 2017, 7, 261; A. K. Pathak, C. Ameta, R. Ameta and P. B. Punjabi, *J. Heterocycl. Chem.*, 2016, **53**, 1697–1705.
86 S. Pullen, H. Fei, A. Orthaber, S. M. Cohen and S. Ott, *J. Am. Chem. Soc.*, 2013, **135**, 16997–17003.
87 C. Kiener, U. Müller and M. Schubert, Method of using a metal organic frameworks based on aluminum fumarate, *U.S. Patent*, 8518264, BASF SE, 27 Aug. 2013.
88 E. Leung, U. Müller, N. Trukhan, H. Mattenheimer, G. Cox and S. Blei, Process for preparing porous metal-organic frameworks based on aluminum fumarate, *U.S. Patent*, 8524932, BASF SE, 3 Sep. 2013.
89 E. Alvarez, N. Guillou, C. Martineau, B. Bueken, B. Van de Voorde, C. Le Guillouzer, P. Fabry, F. Nouar, F. Taulelle, D. de Vos, J.-S. Chang, K. H. Cho, N. Ramsahye, T. Devic, M. Daturi, G. Maurin and C. Serre, *Angew. Chem., Int. Ed.*, 2015, **54**, 3664–3668.
90 L. Zhou, X. Zhang and Y. Chen, *Mater. Lett.*, 2017, **197**, 224–227.
91 E. Elsayed, R. AL-Dadah, S. Mahmoud, P. A. Anderson, A. Elsayed and P. G. Youssef, *Desalination*, 2017, **406**, 25–36.
92 F. Jeremias, D. Fröhlich, C. Janiak and S. K. Henninger, *RSC Adv.*, 2014, **4**, 24073–24082.
93 M. Rubio-Martinez, T. D. Hadley, M. P. Batten, K. Constanti-Carey, T. Barton, D. Marley, A. Mönch, K.-S. Lim and M. R. Hill, *ChemSusChem*, 2016, **9**, 938–941.
94 S. Karmakar, J. Dechnik, C. Janiak and S. De, *J. Hazard. Mater.*, 2016, **303**, 10–20.
95 S. J. Gregg and K. S. W. Sing, *Adsorption, Surface Area and Porosity*, Academic Press, London, 1982.
96 L. Li, S. Xiang, S. Cao, J. Zhang, G. Ouyang, L. Chen and C.-Y. Su, *Nat. Commun.*, 2013, **4**, 1774.
97 D. Bradshaw, S. El-Hankari and L. Lupica-Spagnolo, *Chem. Soc. Rev.*, 2014, **43**, 5431–5443.
98 M.-H. Pham, G.-T. Vuong, F.-G. Fontaine and T.-O. Do, *Cryst. Growth Des.*, 2012, **12**, 1008–1013.
99 B. Seoane, A. Dikhtiarenko, A. Mayoral, C. Tellez, J. Coronas, F. Kapteijn and J. Gascon, *CrystEngComm*, 2015, **17**, 1693–1700.

3.2.1 Electronic Supplementary Information

Microwave assisted dry-gel conversion - a new sustainable route for the rapid synthesis of metal-organic frameworks with solvent re-use

Niels Tannert,[a,b] Serkan Gökpinar,[a,b] Emrah Hastürk,[a] Sandra Nießing,[a] and Christoph Janiak[a]*

[a] Institut für Anorganische Chemie und Strukturchemie, Heinrich-Heine-Universität Düsseldorf, Universitätsstraße 1, 40225 Düsseldorf, Germany.
*E-mail: janiak@uni-duesseldorf.de
[b] These authors contributed equally.

Keywords
Metal-Organic Frameworks, MIL-100(Fe), UiO-66, MIL-140A, Aluminum fumarate, microwave, Dry-Gel Conversion, Synthesis Optimization, Sustainability, Solvent re-use

Emails: niels.tannert@hhu.de; serkan.goekpinar@hhu.de; emrah.hastuerk@hhu.de; sandra.niesssing@hhu.de

Table of Contents

S1. Materials and equipment

All chemicals were used as received from supplier (cf. Table S1).

Table S1 Used chemicals, supplier and purities.

Chemical	Supplier	Purity
$Al(SO)_4 \cdot 18H_2O$	AppliChem	not specified
Basolite™ A520	Sigma Aldrich	not specified
Basolite™ F300	Sigma Aldrich	not specified
Benzene-1,4-dicarboxylic acid	Sigma Aldrich	≥98.0%
Benzene-1,3,5-tricarboxylic acid	Sigma Aldrich	95%
Benzoic acid	Riedel de Haen	99.5%
Dimethylformamide	Fischer Chemicals	99.99%
Ethanol	Sigma Aldrich	>99.8%
$FeCl_3 \cdot 6H_2O$	Sigma Aldrich	97%
$Fe(NO)_3 \cdot 9H_2O$	Sigma Aldrich	98%
Fumaric acid	Alfa Aesar	99%
Hydrochloric acid, 37%	Sigma Aldrich	p.a.
Hydrofluoric acid, 48%	Sigma Aldrich	p.a.
NaOH (microgranulate)	Chem Solute	not specified
Nitric acid, 65%	VWR Chemicals	p.a.
Sodium fluoride	Sigma Aldrich	99.99%
Tetrabutylammonium fluoride, hydrate	Sigma Aldrich	96%
Zirconium chloride	Alfa Aesar	≥99.5%

Powder X-ray diffraction (PXRD) patterns were obtained out at ambient temperature on a *D2 phaser* (BRUKER, Billerica, US) using Cu-Kα radiation (λ = 1.54182 Å) between 5° < 2Θ < 50° with a scanning rate of 0.0125 °/s (300 W, 30 kV, 10 mA). The diffractograms were obtained on a flat "low background sample holder", in which at low angle the beam spot is strongly broadened so that only a fraction of the reflected radiation reaches the detector, hence the low relative intensities measured at 2Θ < 7°. Analyses of the diffractograms were carried out with *Match 3.11* software.

Thermogravimetric analysis (TGA) was performed with a *TG209 F3 Tarsus* (NETZSCH, Selb, Germany). Samples were placed in alumina pans and heated at a rate of 5 $Kmin^{-1}$ from 25-600 °C under synthetic air atmosphere.

Nitrogen (purity 99.9990%, 5.0) physisorption isotherms were carried out on a *Nova 4000e* (QUANTACHROME, Odelzhausen, Germany) at T = 77 K. Before measuring of the isotherms, the products were transferred into glass tubes capped with septa, which were weighted out before. These tubes were attached to the corresponding degassing port of the sorption analyzer, degassed under vacuum at 120 °C for 3 h, weighted out again and then transferred to the analysis port of the sorption analyzer. BET surface areas were calculated from the N_2 adsorption isotherms in an individual p/p_0 range for each MOF (cf. Section S7). Total pore volumes were calculated from the N_2 sorption isotherm at $p/p_0 = 0.95$. NLDFT calculations for the pore size distribution curves were done with the native *NovaWin 11.03* software using the 'N_2 at 77 K on carbon, slit pore, NLDFT equilibrium' model.

Scanning electron microscopy (SEM) images were recorded with a *JSM-6510LV QSEM Advanced electron microscope* (JEOL, Akishima, Japan) with a LaB_6 cathode at 5–20 keV. The microscope was equipped with a *Xflash 410* (BRUKER, Billerica, US) silicon drift detector.

The microwave for MW-DGC syntheses was a *MARS-5* (CEM, Matthews, US).

DGC inlays were self-built, made of Teflon. The holes in the DGC sieves had 0.5 mm diameter. The ring inlays, shown in Figure S1, can have various heights for adjustment. We thank the precision mechanics workshop of Heinrich-Heine-University.

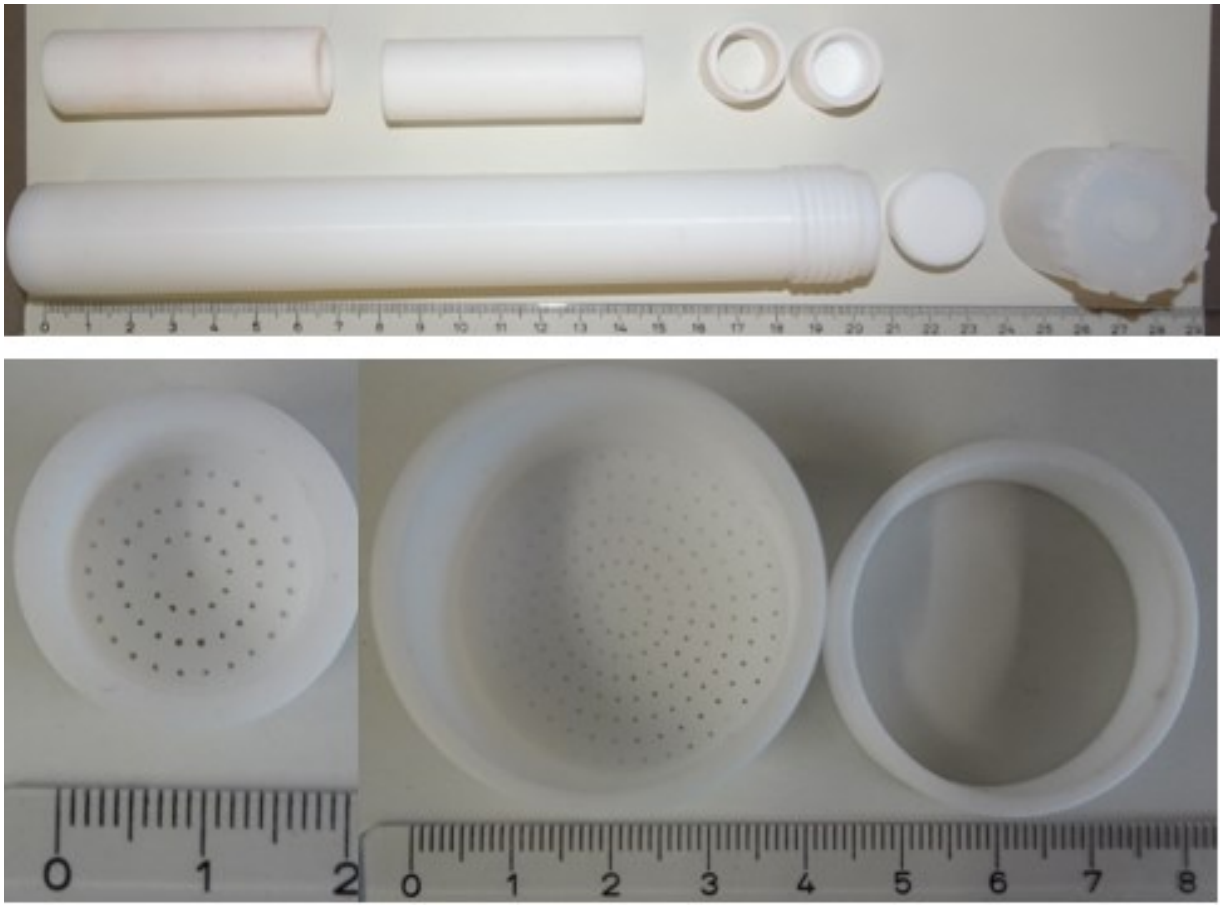

Figure S1 Top: Full autoclave set for MW-DGC with microwave tube, lid and screw-cap, three ring inlays for height-adjustment of sieve and DGC sieve, given also at bottom left in close-up view. Bottom right: Close-up view of a CE-DGC sieve with inlay ring for height adjustment.

S2. Brief description of synthesized metal-organic frameworks

S2.1. MIL-100(Fe)

Metal-organic frameworks with MIL-100 topology (*Matériaux de l'Institut Lavoisier*) were first described by the group of G. Férey in 2004.[1] Figure S2 shows the structural features of MIL-100(Fe) with respect to bonding situations and cavities.

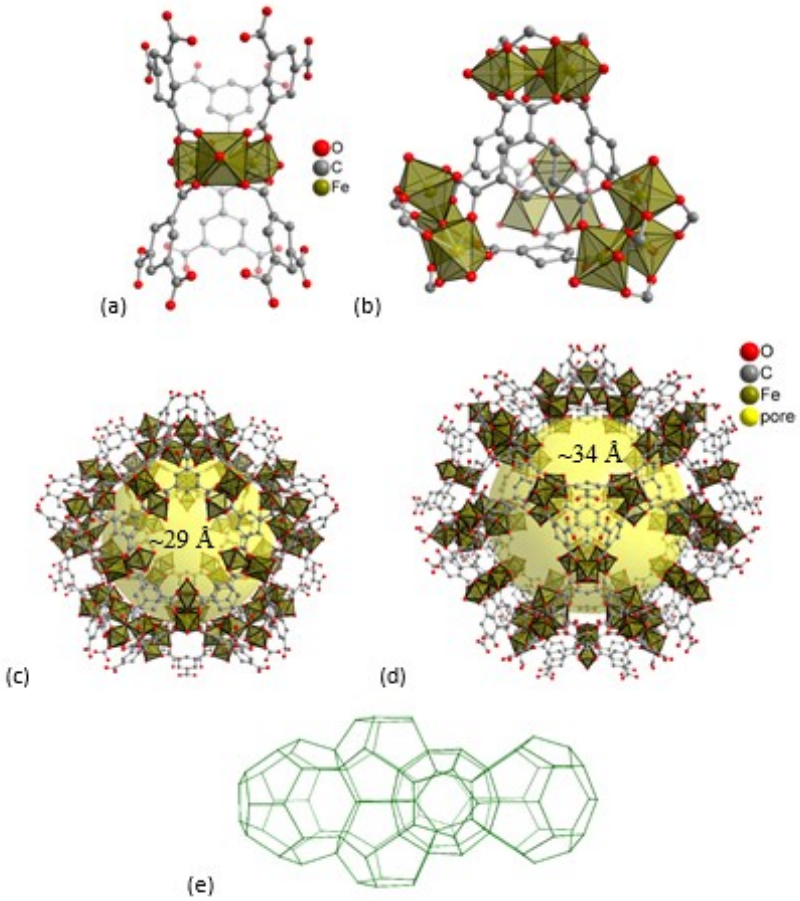

Figure S2 Structural features of MIL-100(Fe). (a) secondary building unit (SBU), (b) supertetrahedra, (c) small S cage, (d) large L cage and (e) topology of the mesoporous network (objects are not drawn to scale). Hydrogen atoms and solvent molecules are not shown. The yellow spheres in the mesoporous cages with the indicated diameters take into account the van-der-Waals radii of the framework walls. Hydrogen atoms and solvent molecules of crystallization are not shown. Graphics have been drawn with the software DIAMOND[2] from the deposited cif-file under CCDC no. 640536 for Fe.[3]

MIL-100(Fe) consists of hybrid supertetrahedra with oxocentered trimers of trivalent metal octahedra connected by trimesate anions (benzene-1,3,5-tricarboxylate – short: BTC).[1,4] MIL-100(Fe) with the chemical formula $[Fe^{III}_3(\mu_3\text{-}O)(X)(BTC)_2 \cdot nH_2O]m$ (with X = F, OH; depending on synthetic conditions) exhibit zeolite MTN topology, mesoporous cages of 25 and 29 Å with microporous (i.e. <2 nm) windows of 5.5 and 8.6 Å and an inner specific surface area of 356-2320 m^2g^{-1} (*Brunauer-Emmett-Teller*, BET area), highly depending on synthetic conditions.[5-6] MIL-100 is studied for gas storage and sequestration,[11-7] in composites,[8,9] as sorption material for heating/cooling applications,[10-13] mixed-matrix membranes,[14] many-sided synthesis optimizations,[5,8,10,15,16] drug delivery and more.[17-18] Notably, MIL-100 materials were shown

to be highly versatile and tunable in terms of crystallinity, morphology and particle size.[19-20] This in turn allows their preparation as xerogels and aerogels, what expands applicability even further.[21-22] Moreover, MIL-100 proved to be suitable as heterogeneous catalyst in several organic reactions.[3,20,22-24] Low toxicity, biocompatibility and abundancy of iron are key-factors for utilization of MIL-100(Fe) in application-oriented research.[3]
MIL-100(Fe) can as well be prepared continuously with a space-time yield (STY) of 20 kg m^{-3} day^{-1}.[25] STY is hereby defined as the amount of produced MOF (kg) per unit volume of reactor (m^3) per day of synthesis (alternatively: per unit volume of reaction mixture (m^3) per day of synthesis[26]).[27]
Exemplarily, Figure S3 depicts MIL-100(Fe) products, obtained by DGC.

Figure S3 Left: Autoclave with DGC sieve, with MIL-100(Fe) product on top. Right: Products obtained from $Fe(NO_3)_3 \cdot 9H_2O$ (left), $FeCl_3 \cdot 6H_2O$ (right).

S2.2. UiO-66 and MIL-140A

Zirconium MOFs represent a subclass of frameworks, which gets more and more attention, due to their excellent stability in thermal, aqueous and acid conditions.[28,29] Among these Zr-MOFs is UiO-66 (*Universitetet i Oslo*), which was first synthesized by Lillerud and co-workers[30] and MIL-140A synthesized by Serre and co-workers.[31] UiO-MOFs have a $\{Zr_6O_4(OH)_4\}$-SBU, which is an octahedral Zr_6-cluster of six edge-sharing ZrO_8 square-antiprism and which is 12 coordinated by the linker molecules to 12 neighboring SBUs in a face-centered cubic (fcc) packing arrangement.[44] Depending on used dicarboxylate linker it can be obtained UiO-66 (linker = 1,4-benzenedicarboxylic acid), UiO-67 (linker = 4,4'-biphenyldicarboxylic acid) or UiO-68 (4,4''-terphenyldicarboxylic acid) with an isoreticular framework. Figure S4 shows the crystal structure of zirconium terephthalate UiO-66.

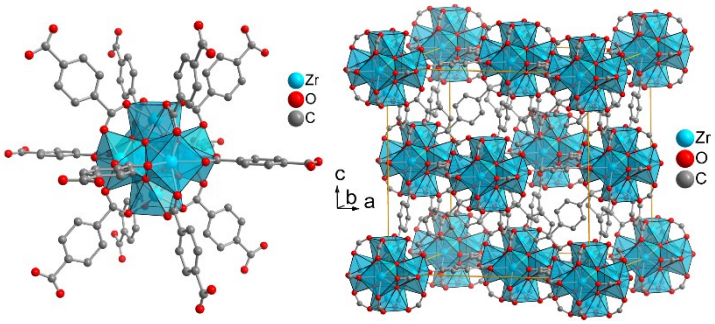

Figure S4 Crystal structure of zirconium terephthalate UiO-66.[44] Hydrogen atoms and solvent molecules are not shown. The UiO-66 structure is drawn with the software Diamond[2] from the deposited cif-file under CCDC no. 837796.[32]

The properties of these UiO-MOFs are interesting for gas storage,[33] separation,[34] water sorption,[35,36] sensing[37] and catalysis.[38,39] UiO-66 can be synthesized solvothermally, *via* mechanochemistry[40] or DGC[41] and also continuously with a space-time yield (STY) of 4,899 kg d^{-1} m^{-3}.[42]

Figure S5 shows the crystal structure of zirconium terephthalate MIL-140A. The MIL-140 series are polymorphs of the UiOs with the general formula [ZrO(linker)], while MIL-140A has a BDC linker. MIL-140s consist of one dimensional zirconium oxide chains (along the c-axis), which are linked to six other chains through dicarboxylate linkers, thereby obstructing one-dimensional channels.[45]

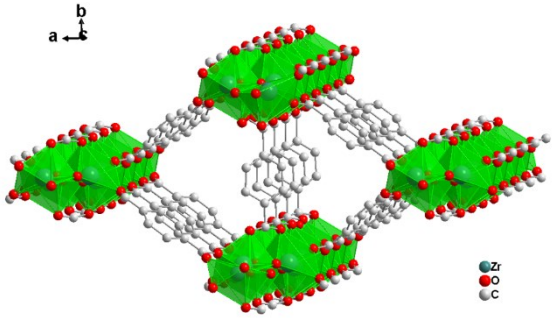

Figure S5 Crystal structure of zirconium terephthalate MIL-140A. The MIL-140A structure is drawn with the software Diamond[2] from the deposited cif-file under CCDC no. 905026.[45]

S2.3. Aluminum fumarate (Alfum)

Aluminum fumarate (Alfum) was first described in the patent literature.[43,44] Figure S6 shows the structural features of aluminum fumarate with respect to bonding situations and cavities.

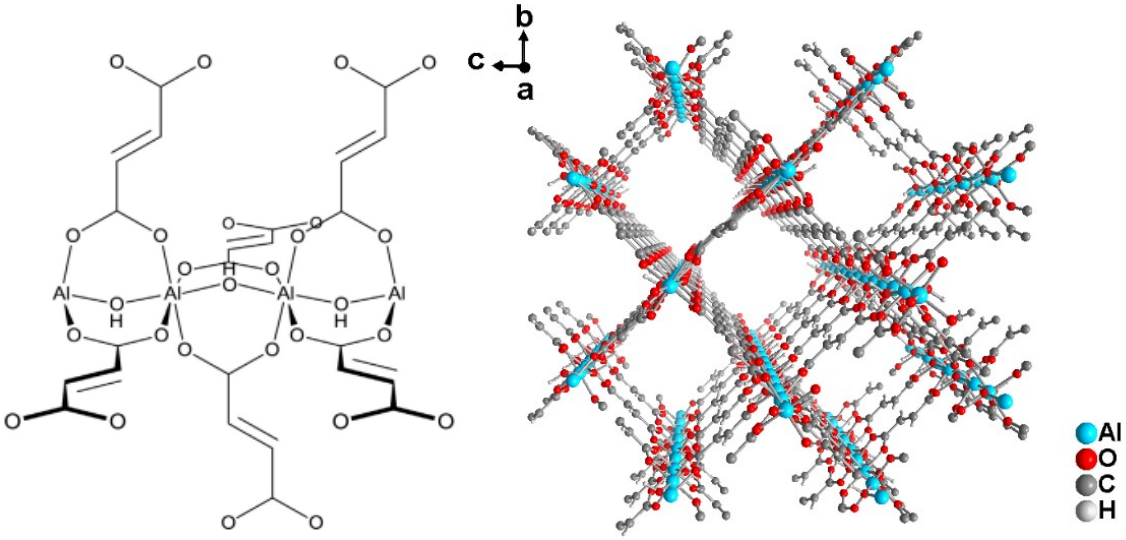

Figure S6 Left: Building block of Alfum, in analogy to the structure of MIL-53. The illustration was taken from ref. 45 Right: Crystal structure of aluminum fumarate. Graphic produced by software Diamond [2] from cif-file for Basolite A520 (CSD-Refcode DOYBEA, CCDC no. 1051975).[46]

Alfum resembles the monoclinic MIL-53(Al) structure (i.e. with benzene-1,4-dicarboxylate as linker) with infinite Al-OH-Al chains connected by fumarate linkers. It has the chemical formula $[Al(OH)(O_2C\text{-}CH{=}CH\text{-}CO_2)]_n$ and displays microporous, rhombohedral channels with circa 5.7 x 6.0 $Å^2$ free dimensions.[60,47]

Aluminum fumarate is one of the most promising MOFs for application,[59,60,48] due to its hydrothermal stability and an environmentally friendly synthesis route with water as single solvent, inexpensive and benign metal cation, moreover, a “green” linker from renewable biomass,[49] besides possible large scale production with a high STY of >3615 kg m^{-3} day^{-1}.[57,58,50] Gaab *et al.* proved its applicability as storage container for natural gas, used as fuel in a vehicle, by 40% increased cruising distance.[64] Moreover, Alfum was proven to represent suitable water sorption characteristics and cyclic stability for heat transformation application,[59] it is applicable as super adsorbent for removal of fluoride from water[51] and in desalination processes[52] and it was proposed to be the best porous solid for mechanical energy storage.[53] It can as well be prepared *via* (potentially continuously operable) mechanochemical techniques, such as extrusion.[54] Thereby, 27000 kg m^{-3} day^{-1} STY were calculated to be feasible.[55] Continuous flow methods achieved even STYs up to 97 159 kg m^{-3} day^{-1} at 5.6 kg h^{-1} and ca. 1000-1100 m^2g^{-1}.[40]

S3. Syntheses of MIL-100(Fe)

In a typical synthetic procedure, the metal salts $Fe(NO)_3 \cdot 9H_2O$ and $FeCl_3 \cdot 6H_2O$ were ground with H_3BTC in a molar ratio of 1:1 (2-4 mmol of each reactant) *via* ball-milling (20 Hz, 20 Min) using a *Retsch MM301* (RETSCH, Haan, Germany). However, simple grinding in a mortar yielded the desired phase too.

S3.1. Microwave-assisted dry-gel conversion (MW-DGC)

The precursor mixture of around 100 mg combined mass was placed on a MW-DGC sieve (cf. Fig. S1) with water or acidic solutions (5 mL) at the bottom of the Teflon-reactor, which was tightly closed and heated to 150 °C for 180 min by applying 800 W, using a *CEM MARS-5* microwave. The orange-brownish (from $Fe(NO)_3 \cdot 9H_2O$) or reddish (from $FeCl_3 \cdot 6H_2O$) solid products were washed with water and ethanol three times (10 mL each) and dried (80 °C, 24 h). Amounts of starting materials and yields in already optimized syntheses are given in Table S2.

Table S2 Synthesis details of different MIL-100(Fe) samples obtained *via* MW-DGC.

Fe source	Solvent (5 mL)	$m_{Fe\text{-}salt}$ [mg]	m_{H3BTC} [mg]	$n_{Fe} = n_{BTC}$ [mmol]	Yield [g]	Yield [%] [a]	BET [m^2g^{-1}]
Fe-chloride	neat H_2O	50.0	38.9	0.185	0.045	78	1002
	H_2O + HNO_3 (1:1)	49.5	38.4	0.183	0.046	81	460
	H_2O/EtOH (4:1)	53.0	41.2	0.196	0.037	61	922
Fe-nitrate	neat H_2O	77.2	40.1	0.191	0.047	81	1105
	H_2O + HNO_3 (1:1)	78.0	41.3	0.193	0.046	78	526
	H_2O/EtOH (4:1)	84.8	45.0	0.210	0.050	78	1180

[a] Based on the amount of Fe-salt and on the MIL-100(Fe) formula of $[Fe^{III}_3(\mu_3\text{-}O)(H_2O)_2(Cl)(BTC)_2 \cdot 14.5\ H_2O]_m$ and M_W= 930.47 $gmol^{-1}$ for MIL-100(Fe) products of Fe-chloride based synthesis, respectively $[Fe^{III}_3(\mu_3\text{-}O)(H_2O)_2(OH)(BTC)_2 \cdot 14.5\ H_2O]_m$ and M_W = 912.02 $gmol^{-1}$ for MIL-100(Fe) products of Fe-nitrate based synthesis. The amount of crystal water after drying was estimated to be x = 14.5 per formula unit in accordance to earlier reports.[9,11]

S3.2. Conventionally heated dry-gel conversion (CE-DGC)

Synthetic conversions of precursors were performed on top of a DGC sieve holder with water or acidic solutions (20 mL) on the bottom of a Teflon-lined steel autoclave at 150 °C (2 h heating to 150 °C, 24 h, 2 h cooling) using electrical heating ovens. The orange-brownish (from $Fe(NO)_3 \cdot 9H_2O$) or reddish (from $FeCl_3 \cdot 6H_2O$) solid products were washed with water and ethanol three times (each 40 mL), dried and finally activated (80 °C, 24 h). Initial weights of precursor mixtures and yields in already optimized syntheses are given in Table S3.

Table S3 Synthesis details of different MIL-100(Fe) samples obtained *via* CE-DGC.

Fe source	Solvent (20 mL)	$m_{Fe\text{-}salt}$ [mg]	m_{H3BTC} [mg]	$n_{Fe} = n_{BTC}$ [mmol]	Yield [g]	Yield [%] [a]	BET [m^2g^{-1}]
Fe-chloride	neat H_2O	205.4	159.7	0.760	0.162	69	1776
	H_2O + HNO_3 (1:1)	203.8	158.4	0.754	0.146	62	1469
	H_2O/EtOH (4:1)	197.0	153.2	0.729	0.101	45	1287
Fe-nitrate	neat H_2O	444.0	230.9	1.099	0.267	80	1876
	H_2O + HNO_3 (1:1)	248.0	129.0	0.614	0.166	89	1550
	H_2O/EtOH (4:1)	190.7	99.2	0.472	0.138	96	1561

[a] Based on the amount of Fe-salt and on the MIL-100(Fe) formula of $[Fe^{III}_3(\mu_3\text{-}O)(H_2O)_2(Cl)(BTC)_2 \cdot 14.5\ H_2O]_m$ and M_W= 930.47 $gmol^{-1}$ for MIL-100(Fe) products of Fe-chloride based synthesis, respectively $[Fe^{III}_3(\mu_3\text{-}O)(H_2O)_2(OH)(BTC)_2 \cdot 14.5\ H_2O]_m$ and M_W = 912.02 $gmol^{-1}$ for MIL-100(Fe) products of Fe-nitrate based synthesis. The amount of crystal water after drying was estimated to be x = 14.5 per formula unit in accordance to earlier reports.[9,11]

During our work we have carried out synthesis optimization for the MW-DGC approach for MIL-100(Fe): We varied the molar ratio of reactants, reaction time and temperature, respectively microwave irradiation power. Additionally, we performed syntheses with fluoride sources such as tetrabutylammonium fluoride (TBAF) and sodium fluoride, by adding 2 wt.% to the precursor mixture. Aqueous HF was added to the solvent (1: 10 by vol.). The addition of any fluoride source did not lead to improved products. Also other ratios of water/ethanol and water/HNO_3 were applied, but did not yield improved products. Thus, we describe only the optimized syntheses above.

S4. Syntheses of UiO-66 and MIL-140A

S4.1. UiO-66

S4.1.1. Microwave-assisted dry-gel conversion (MW-DGC)

For the synthesis of UiO-66-HCl *via* MW-DGC, $ZrCl_4$ (88 mg, 0.38 mmol, 1.0 eq), H_2BDC (63 mg, 0.38 mmol, 1.0 eq) and benzoic acid (BA) (100 mg, 0.82 mmol, 2.1 eq) were mixed, ground in a mortar and placed on the sieve. DMF solvent (10 mL) and 1 mL of HCl (37%) was placed at the bottom of the Teflon tube. The sieve, which was filled with precursor mixture was placed above the solvent-mixture and the Teflon tube was capped and heated to 180 °C (10 min heating to 180 °C, 50 min, cooling) by applying 600 W, using a *CEM MARS-5* microwave. After the tube was cooled down to room temperature, the obtained as-synthesized product was soaked in DMF (2 x 5 mL, 24 h each) and ethanol (5 mL, 24 h). The solvent was exchanged every 24 h. After a total time of 3 d of soaking, the solids were centrifuged and dried under vacuum. For UiO-66-IL a DMF/[BMIm]NTf_2 (9:1 by vol.) solvent mixture was used.

S4.1.2. Synthesis of ionic liquid (IL) [BMIm]NTf_2

The ionic liquid was synthesized according to a modified procedure of Deetlefs *et al.*[56] For microwave synthesis of [BMIm]Cl a mixture of 1-methylimidazole (150 mmol) and 1-chlorobutane (153 mmol) was placed in a Teflon vessel equipped with a magnetic stirrer. The temperature was raised to 160 °C over the course of 20 min, and microwave irradiation continued for a further 60 min. The anion of [BMIm]Cl was exchanged by reaction with $LiNTf_2$ (150 mmol) in H_2O to give the [BMIm]NTf_2 according to the procedure by Wegner *et al*.[57]

S4.2. MIL-140A

S4.2.1. Microwave-assisted dry-gel conversion (MW-DGC)

For the synthesis of MIL-140A *via* MW-DGC, $ZrCl_4$ (88 mg, 0.38 mmol, 1 eq), H_2BDC (63 mg, 0.38 mmol, 1 eq) and benzoic acid (100 mg, 0.82 mmol, 2.1 eq) were mixed, ground in a mortar and placed on the sieve. The DMF solvent (10 mL) was placed at the bottom of the Teflon tube and the sieve, filled with precursor mixture, was placed above the solvent. The Teflon tube was capped and heated to 160 °C (10 min heating to 160 °C, 80 min, cooling) by applying 600 W, using a *CEM MARS-5* microwave. After the tube was cooled down to room temperature, the obtained as-synthesized product was soaked in DMF (2 x 5 mL, 24 h each) and ethanol (5 mL, 24 h). The solvent was exchanged every 24 h. After 3 d of soaking, the solids were centrifuged and dried under vacuum.

Yields, BET areas and pore volumes for UiO-66 and MIL-140A from MW-DGC synthesis are given in Table 2 in the full manuscript, in comparison with literature values for CE-DGC and solution synthesis.

S5. Syntheses of aluminum fumarate

The compounds $Al_2(SO_4)_3 \cdot 18H_2O$, fumaric acid and NaOH were mixed at a molar ratio of 1:2:4 by rapid grinding in a mortar. Thereupon, the precursor mixture was quickly placed on top of a DGC sieve holder, quickly placed in the Teflon container for the reaction in the microwave or CE oven.

S5.1. Microwave-assisted dry-gel conversion (MW-DGC)

Synthetic conversions of precursors were performed on top of a MW-DGC sieve holder with water (5 mL) at the bottom of a Teflon-reactor at 100 °C (60 Min) by applying 800 W using a *CEM MARS-5* microwave. The white products were washed three times with water (10 mL each), and dried under vacuum (80 °C, 24 h). Initial weights of precursor mixtures and yields are given in Table S4.

Table S4 Synthesis details of different aluminum fumarate samples obtained via repeated MW-DGC.

Precursor [g]	$m_{Al\text{-}salt}$ [g]	$m_{fumaric\ acid}$ [g]	n_{Al} [mmol]	$n_{fumaric\ acid}$ [mmol]	Yield [g]	Yield [%] [a]	BET [m^2g^{-1}]
0.273	0.172	0.060	0.52	0.52	0.062	76	1075
0.252	0.159	0.055	0.48	0.48	0.060	81	1150
0.298	0.188	0.065	0.56	0.56	0.079	89	1128

[a] Based on the amount of Al-salt and on the product formula $[Al(OH)(O_2C\text{-}CH{=}CH\text{-}CO_2)]_n$ and M_W = 158.045 $gmol^{-1}$ for Alfum.

S5.2. Conventionally electric-heated dry-gel conversion (CE-DGC)

Synthetic conversions of precursors were performed on top of a DGC sieve holder with water (2 mL) at the bottom of a Teflon-reactor inside a stainless-steel autoclave at 100 °C (6-24 h) in an electrically heated oven. The white products were washed three times with water (50 mL each) and dried under vacuum (80 °C, 24 h). Initial weights of aluminum sulfate and yields are given in Table S5.

Table S5 Synthesis details of different aluminum fumarate samples obtained via CE-DGC.

$m_{Al\text{-}salt}$ [g]	$m_{fumaric\ acid}$ [g]	n_{Al} [mmol]	$n_{fumaric\ acid}$ [mmol]	Yield [g]	Yield [%] [a]	BET [m^2g^{-1}]	Time [h]
0.159	0.111	0.48	0.96	0.0435	58	1284	6
0.157	0.109	0.47	0.94	0.0500	67	1037	6
0.159	0.111	0.48	0.96	0.0532	71	1129	24

[a] Based on the amount of Al-salt and on the product formula $[Al(OH)(O_2C\text{-}CH{=}CH\text{-}CO_2)]_n$ and M_W = 158.045 $gmol^{-1}$ for Alfum.

S5.3. Conventional solution-based synthesis

According to the patent by BASF,[57,58] we performed solution-based syntheses at 60 °C under aqueous reflux conditions in a round-bottom flask. Aluminum sulfate-octadecahydrate (1.1710 g, 1.76 mmol, 1 eq), sodium hydroxide (0.2803 g, 7.01 mmol, 4 eq) and fumaric acid (0.3863 g, 3.33 mmol, 2 eq) yielded 74% of product (0.4104 g; after vacuum, 80 °C, 24 h).

S6. PXRD measurements

Crystallinity and phase purity was examined with powder X-ray diffractometry (PXRD), using a *D2 Phaser* (BRUKER, Billerica, US) diffractometer with a flat silicon, low background sample holder and Cu-K_α radiation (λ = 1.54184 Å) at 30 kV and 0.04 °s^{-1} in the 2θ = 5-50 ° range. In the case of MIL-100(Fe) samples detector limits were 0.18 and 0.25 V, in order to suppress the X-ray-fluorescence of iron. Analyses of the diffractograms were carried out with *Match 3.11* software.
Relevant PXRD plots are given in the full paper.

S7. Nitrogen sorption experiments (T = 77 K)

Surface areas (BET) were determined by nitrogen (purity 99.999%, 5.0) sorption experiments at T = 77 K using a *NOVA-4000e* (QUANTACHROME, Odelzhausen, Germany) instrument within a partial pressure range of $p/p_0 = 10^{-3}$-1 bar. Each sample (20-50 mg each) was degassed under vacuum (< 10^{2} mbar) at 100 °C (MIL-100(Fe)), 120 °C (UiO-66, MIL-140A) and 150 °C (Alfum) for ca. 3 h, prior to measurement.
All surface areas (BET) were calculated from five adsorption points in the pressure range p/p_0 = 0.05-0.2 for samples of MIL-100(Fe), p/p_0 = 0.01-0.05 for UiO-66, p/p_0 = 0.01-0.10 for MIL-140A and p/p_0 = 0.001-0.05 for Alfum. This range is suitable for microporous materials.[58]
Full isotherms were collected exemplarily and are given in the full paper in Fig. 2, Fig. 4 and Fig. 7.
Table S6 summarizes repeated N_2 sorption results of the industrial benchmarks *Basolite F300* and *Basolite A520* using the same batch, but not the same sample.

Table S6 Repeated determination of BET surface areas of Basolite F300 and Basolite A520 using nitrogen sorption (T = 77 K).

Benchmark	No. of measurement	BET [$m^2\ g^{-1}$]
Basolite F300	1	1140
	2	1252
	3	847
	4	1100
	5	1024
Basolite A520	1	1030
	2	1038
	3	999
	4	1040
	5	1026

All relevant nitrogen isotherm plots are given in the full paper.

Figure S7 exemplarily depicts four N_2 sorption isotherms of Alfum obtained *via* MW-DGC, proving reproducibility of the composite Type I + Type IV isotherm, caused by micro-mesoporous structure (cf. Fig. S8 and S9).

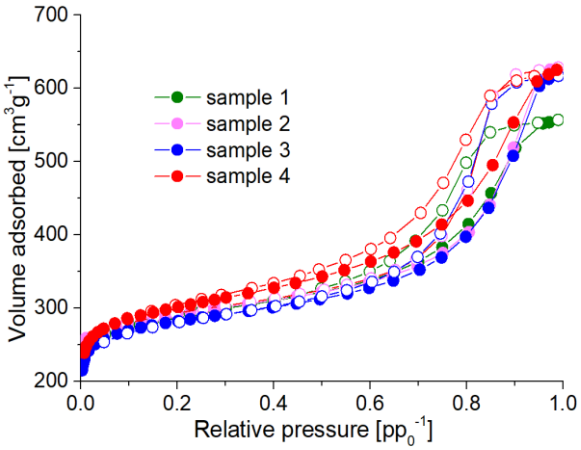

Figure S7 Examples of nitrogen sorption isotherms (77 K) of four Alfum samples obtained via MW-DGC, revealing reproducibility of adsorption behavior, i.e. composite Type I + Type IV isotherm.

S7.1. Pore size distributions of Alfum samples

Figures S8 and S9 depict the pore size distributions (NLDFT equilibrium model, carbon, slit pore, N_2 at 77 K) of Alfum samples obtained by different synthesis methods. All pore size distribution curves were calculated with the native *NovaWin 11.03* software using the 'N_2 at 77 K on carbon, slit pore, NLDFT equilibrium' model.
The images visualize the different porosity properties of Alfum samples obtained by different synthesis methods including *Basolite A520*.

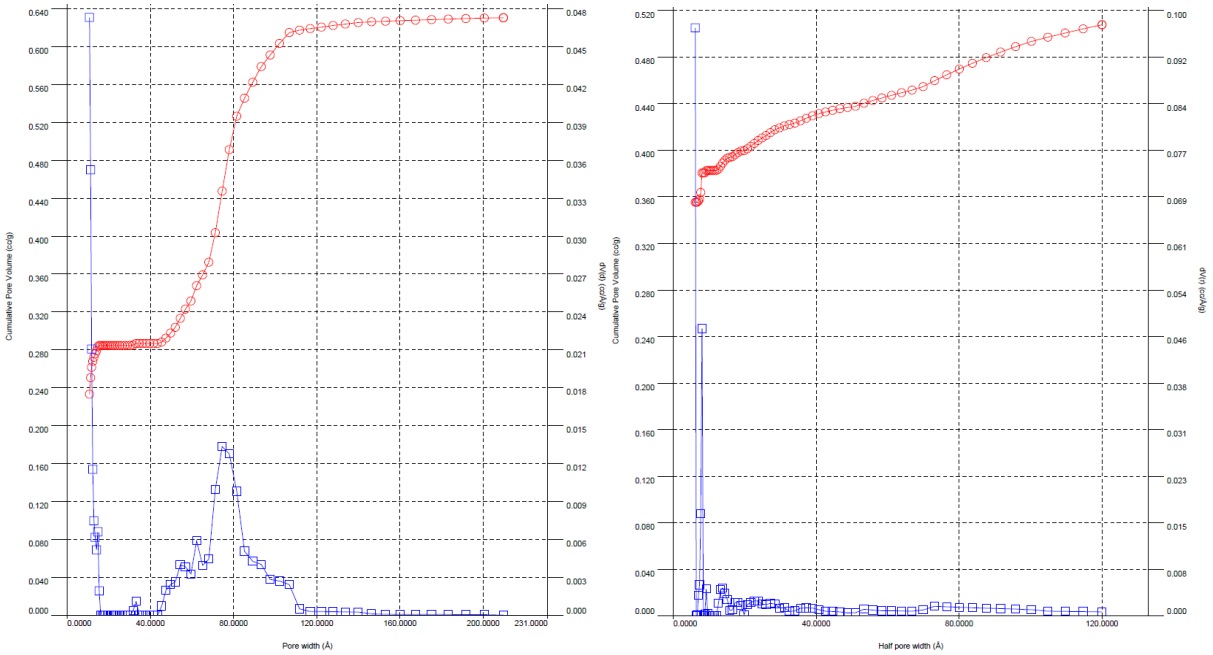

Figure S8 Pore size distributions (NLDFT equilibrium model, carbon, slit pore, N_2 sorption at 77 K) of Alfum samples obtained by MW-DGC (left) and CE-DGC (right). The images shown here are

representative examples out of more than 10 determined pore size distributions for the Alfum materials.

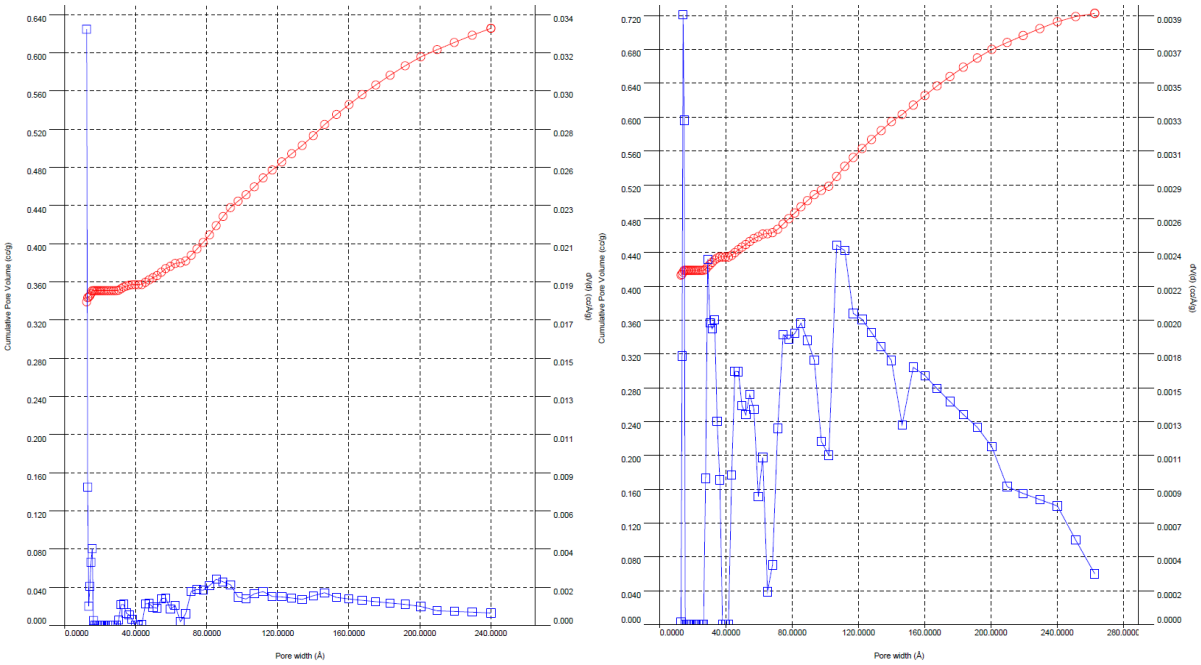

Figure S9 Pore size distributions (NLDFT equilibrium model, carbon, slit pore, N_2 sorption at 77 K) of Alfum samples obtained by solution-based synthesis (left) and Basolite A520 (right). The images shown here are representative examples out of 6 determined pore size distributions for the Alfum materials.

S7.2. Comparison of porosity parameters of Alfum samples

Table S7 summarizes the ranges from at least six samples from each synthesis method for Alfum within this work, described in Section S5. All values were derived from N_2 sorption isotherms using the native *NovaWin 11.03* software.

Table S7 Ranges of porosity parameters from different Alfum samples obtained via MW-DGC, CE-DGC and solution-based synthesis in comparison with Basolite A520. At least six samples of each synthesis method were measured and taken into account.

	S_{BET} $[m^2g^{-1}]$ [a]	$S_{micro\text{-}BET}$ $[m^2g^{-1}]$ [b]	S_{Ext} $[m^2g^{-1}]$ [c]	$V_{pore\ (total)}$ $[cm^3g^{-1}]$ [d]	$V_{pore\ (NLDFT)}$ $[cm^3g^{-1}]$ [e]	$V_{pore\ (micro)}$ $[cm^3g^{-1}]$ [f]
MW-DGC	1015-1148	781-912	216-307	0.67-0.96	0.72-0.94	0.27-0.36
CE-DGC	1037-1188	941-1089	86-118	0.43-0.72	0.43-0.61	0.37-0.42
Solution-based	780-1254	654-1120	126-134	0.49-0.72	0.36-0.72	0.26-0.43
Basolite A520	999-1040	885-930	109-114	0.58-0.63	0.51-0.63	0.31-0.36

[a] BET surface areas (S_{BET}) were obtained from five adsorption points in the pressure range pp_0^{-1}=0.001-0.05. [b] Micropore areas ($S_{micro\text{-}BET}$) were obtained by t-plot and V-t-method. [c] External area (S_{Ext}) refers to all area that does not originate from micropores and it includes meso- and macropores, i.e. pores > 2nm. Obtained by t-plot and V-t-method. [d] Total pore volumes ($V_{pore\ (total)}$) were derived at pp_0^{-1} = 0.95 for pores ≤20 nm. [e] Pore volumes from NLDFT ($V_{pore\ (NLDFT)}$) were calculated using 'N_2 at 77 K on carbon, slit pore, NLDFT equilibrium' model. [f] Micropore volume ($V_{pore\ (micro)}$) refers to volume that originates only from micropores, obtained by V-t-method with thickness method 'DeBoer'.

All correlation coefficients (r) within calculations were >0.999.

S8. Scanning electron microscopy (SEM)

The morphology was imaged by SEM using a *JSM-6510 advanced electron microscope* (JEOL, Akishima, Japan) with a LaB_6 cathode at 5-20 keV. Figures S10-S12 display obtained products at different scales.

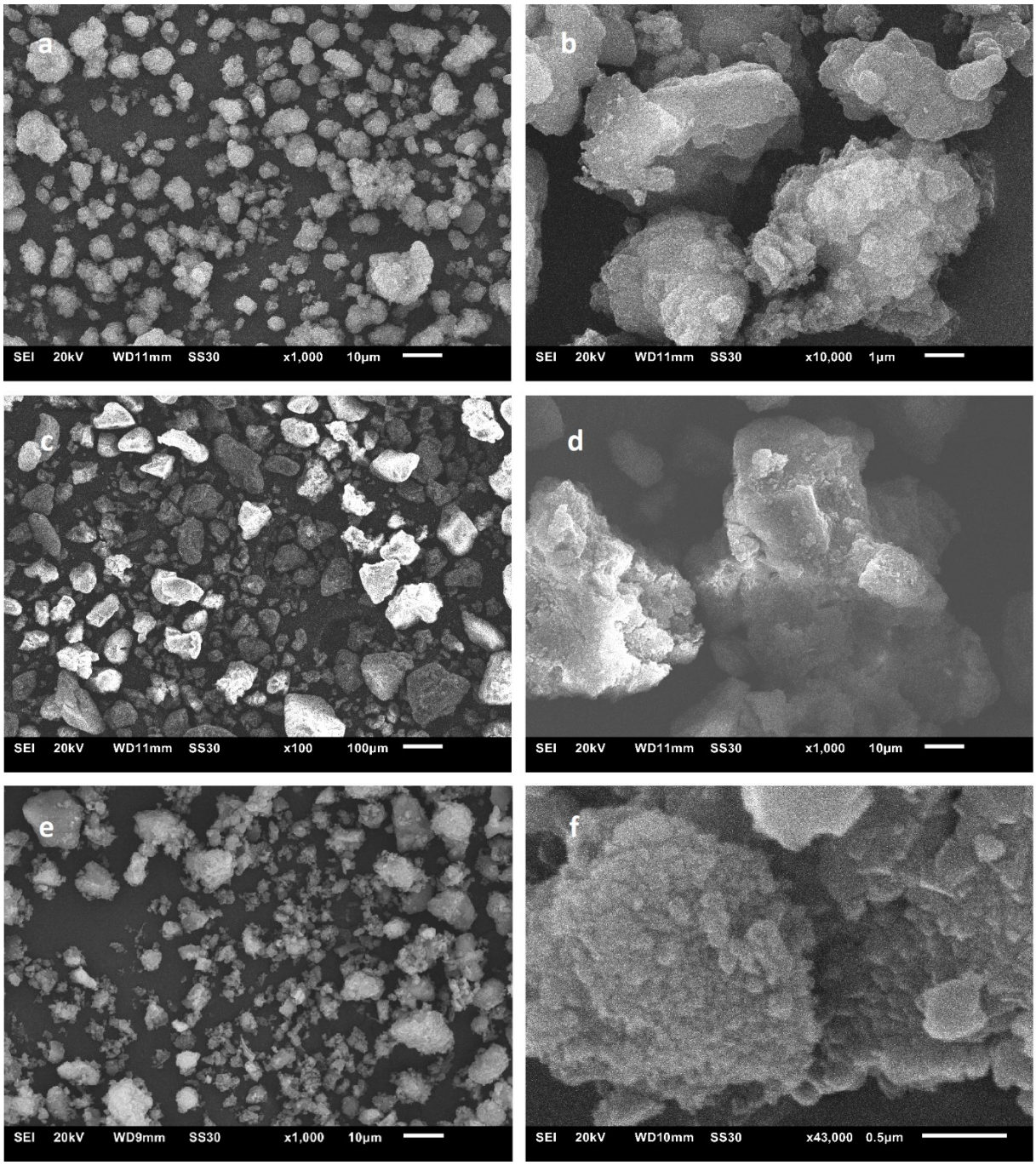

Figure S10 SEM images of MIL-100(Fe) (left: overview, right: close-up): Basolite F300 (a, b), MW-DGC product (c, d) and CE-DGC product (e, f).

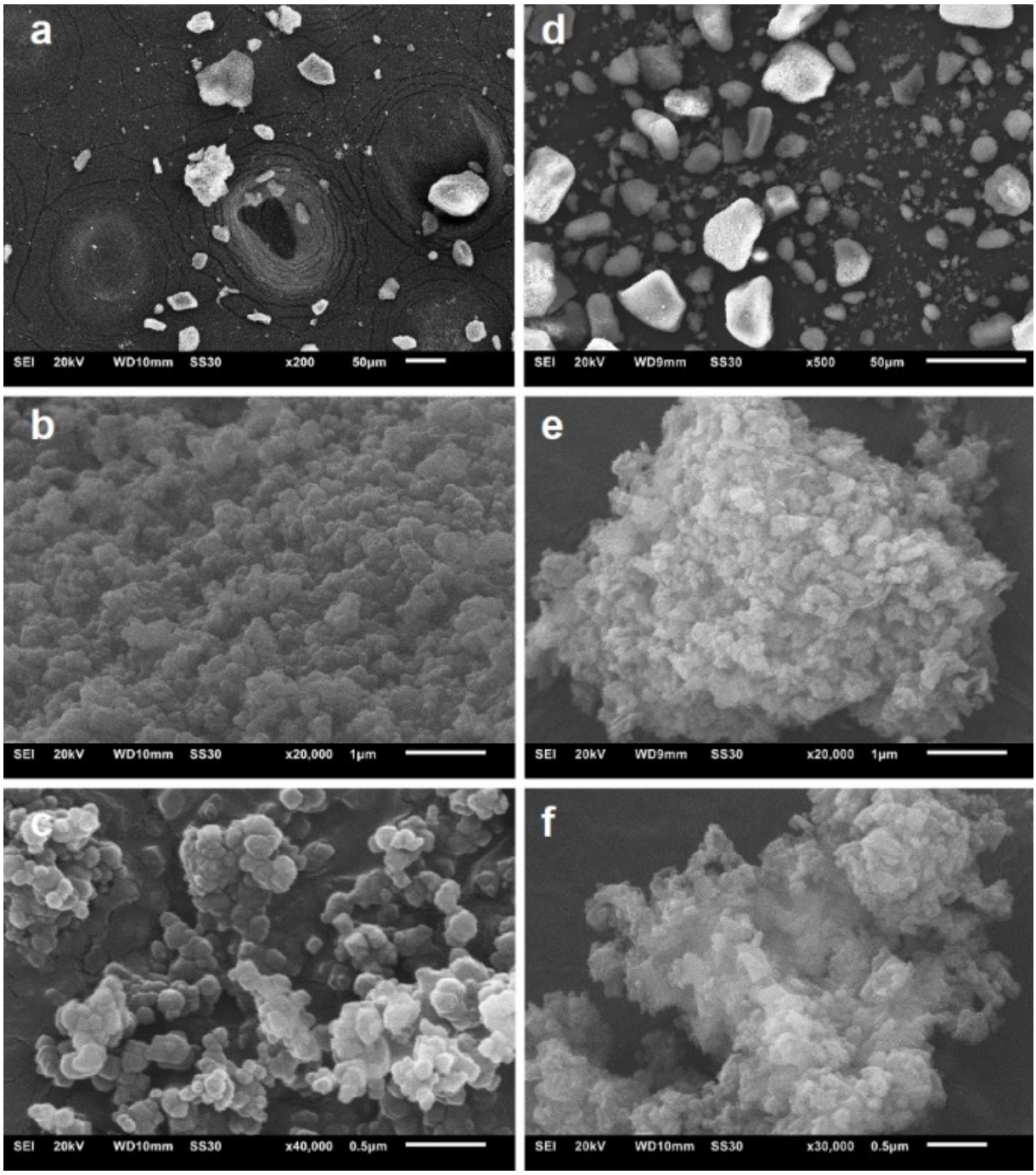

Figure S11 SEM images of UiO-66-HCl (a, b and c) and MIL-140A (d, e and f) obtained via MW-DGC.

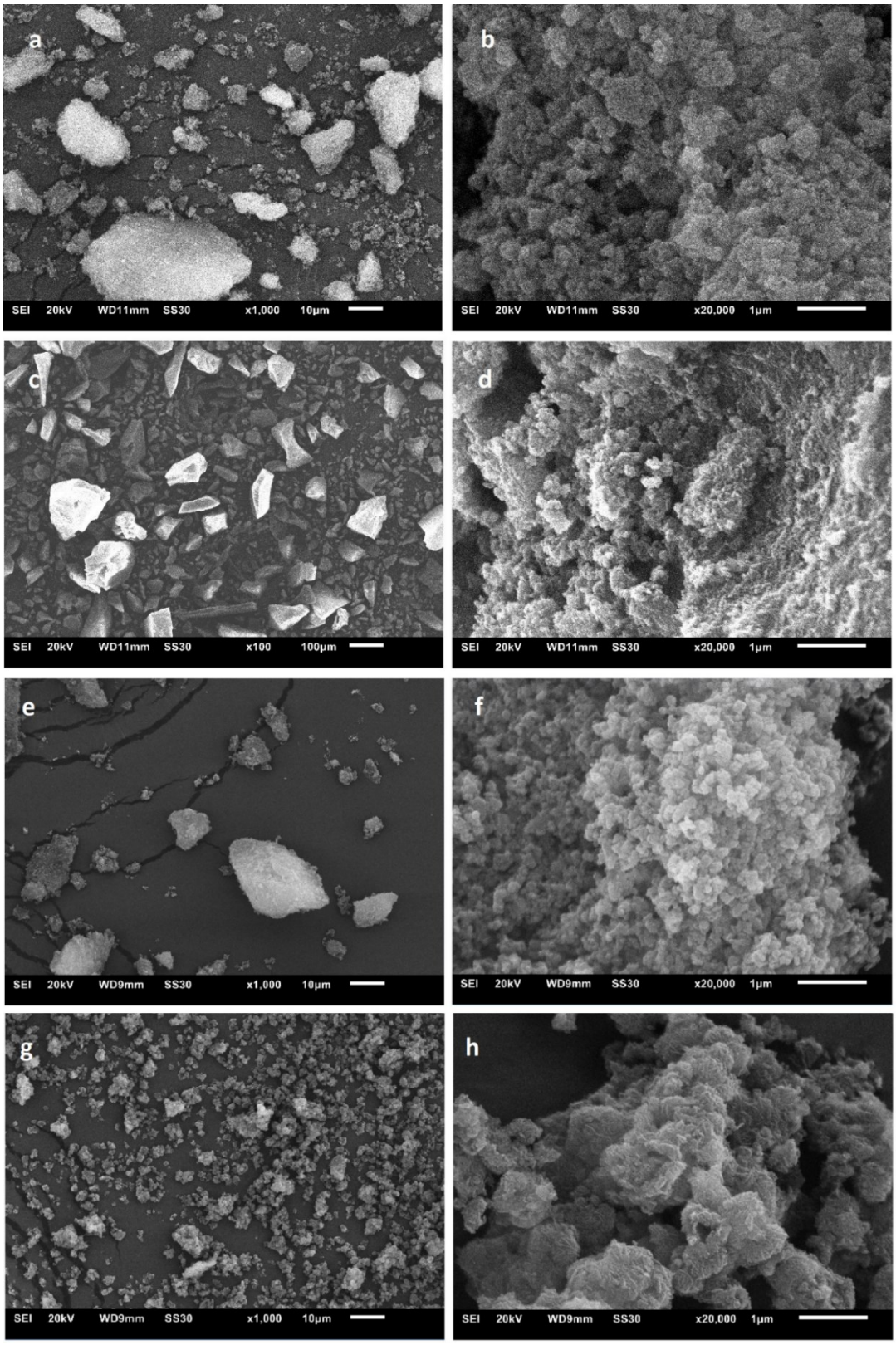

Figure S12 SEM images of aluminum fumarate (left: overview, right: close-up): Basolite A520 (a, b), MW-DGC product (c, d), CE-DGC product (e, f) and conventional solution-based product (g, h).

S9. Thermogravimetric Analysis (TGA)

TGA measurements were carried out on a *TG209 F3 Tarsus* (NETZSCH, Selb, Germany) device under synthetic air atmosphere, ramping with 5 $Kmin^{-1}$ to target temperature (600 °C). Figure S13 shows the TGA curves of MW-DGC products of UiO-66 and MIL-140A in comparison to the CE-DGC product of UiO-66 from ref. 55.

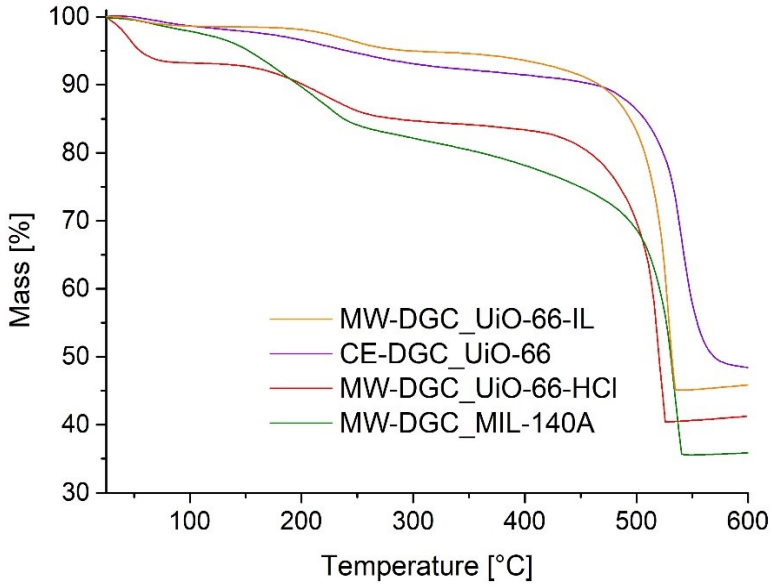

Figure S13 TGA results of MW-DGC products UiO-66 and MIL-140A.

Determination of defects per SBU was done similar to the procedure of Shearer *et al*..[43] An assumption of this method is that the residue in each TGA experiment is ZrO_2. The reaction of decomposition for both MOFs UiO-66 ($Zr_6O_6(BDC)_6$ (defect-free and dehydroxylated) and MIL-140A ZrO(BDC) can be described as follows:

$$Zr_6O_6(BDC)_6 + 45\ O_2 \longrightarrow 6\ ZrO_2 + 48\ CO_2 + 12\ H_2O$$

$$2\ ZrO(BDC) + 15\ O_2 \longrightarrow 2\ ZrO_2 + 16\ CO_2 + 4\ H_2O$$

The determination can be parted in three steps:

1) Determine the theoretical plateau weight $\mathbf{W_{Theo.Plat}}$:

$$W_{Theo.Plat} = (M_{Comp}/M_{6xZrO2}) \cdot W_{End}$$

$$W_{Theo.Plat} = (M_{Comp}/M_{ZrO2}) \cdot W_{End}$$

with M_{Comp} (UiO-66; dehydroxylated, defect-free) = 1628.03 g/mol, M_{Comp} (MIL-140A) = 271.22 g/mol, M_{6xZrO2} = 739.34 g/mol, M_{ZrO2} = 123.22 g/mol and W_{End} = 100%, which is the end weight of the TGA run (=normalized to 100%).

We obtain $W_{Theo.Plat}$ values of UiO-66 and MIL-140A:

$W_{Theo.Plat}$ (UiO-66) = 220.20%

$W_{Theo.Plat}$ (MIL-140A) = 220.20%

2) Determination of the weight contribution per BDC linker **$Wt.PL_{Theo}$**:

$$Wt.PL_{Theo} = (W_{Theo.Plat} - W_{End})/NL_{Ideal}$$

$$Wt.PL_{Theo}\ (UiO\text{-}66) = (220.20-100)/6 = 20.03\%$$

$$Wt.PL_{Theo}\ (MIL\text{-}140A) = (220.20-100)/1 = 120.20\%$$

, while NL_{Ideal} is the number of linkers (1 or 6) in *ideal* Zr/Zr_6-SBU.

3) Calculation of number of linkers per *defective* Zr/Zr_6 unit **NL_{Exp}**:

$$NL_{Exp} = (6\text{-}x) = (W_{Exp.Plat} - W_{End})/\ Wt.PL_{Theo} \text{ or } NL_{Exp} = (1\text{-}x) = (W_{Exp.Plat} - W_{End})/\ Wt.PL_{Theo}$$

, while $W_{Exp.Plat}$ is the experimental TGA plateau. The value can be taken from **Figure** . $\boldsymbol{x}$ is the number of linker deficiencies per Zr_6 SBU. We used following equations to calculate:

$$x = 6 - NL_{Exp} = 6\text{-}[(W_{Exp.Plat} - W_{End})/Wt.PL_{Theo}]$$

$$x = 1 - NL_{Exp} = 1\text{-}[(W_{Exp.Plat} - W_{End})/Wt.PL_{Theo}]$$

x (CE-DGC-UiO-66) = 6−4.643 = 6−((**193.0**−100%)/20.03%) = **1.357 ≅ 1.36** [55]

x (MW-DGC-UiO-66-HCl) = 6−4.833 = 6−((**196.8**−100%)/20.03%) = **1.167 ≅ 1.17**

x (MW-DGC-UiO-66-IL) = 6−4.843 = 6−((**197.0**−100%)/20.03%) = **1.157 ≅ 1.16**

x (MW-DGC-MIL-140A) = 1−0.970 = 1−((**216.5**−100%)/120.2%) ≅ **0.03**

S10. Results of three synthesis runs with solvent re-use

The MW-DGC synthesis procedures described in Section S3 were exemplarily performed with solvent re-use, that is, using the same solvent, but fresh precursor on top of the DGC sieve each time. Figures S14-S17 show PXRD patterns of all four presented MOFs, each proving maintaining crystallinity over three repeated synthesis runs with solvent re-use.
According to the data given in the Tables S8-S11 (cf. Fig. 8 in the full manuscript), we were able to prove the re-use of solvent with good yields and high specific surface areas (BET).

S10.1 MIL-100(Fe)

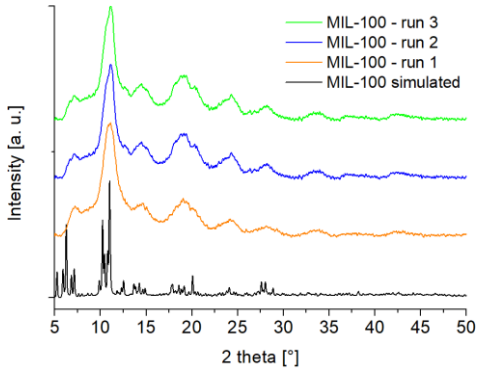

Figure S14 PXRD patterns of MIL-100(Fe) samples from repeated synthesis runs with solvent re-use.

Table S8 Results of three repeated synthesis runs with re-use of solvent for MIL-100(Fe).

Run	BET [m^2g^{-1}]	Yield [%]
1	1287	78
2	935	72
3	1158	82

S10.2. UiO-66-IL

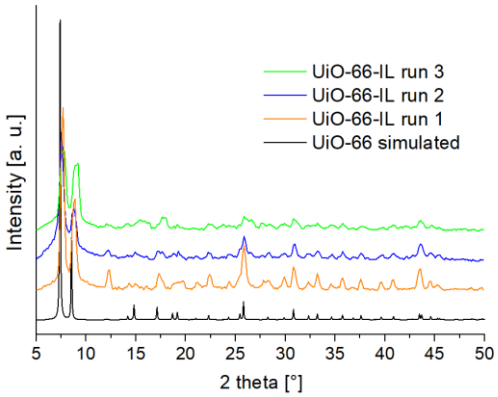

Figure S15 PXRD patterns of UiO-66-IL samples from repeated synthesis runs with solvent re-use.

Table S9 Results of three repeated synthesis runs with re-use of solvent for UiO-66-IL.

Run	BET [m^2g^{-1}]	Yield [%]
1	1023	68
2	807	73
3	717	72

S10.3. MIL-140A

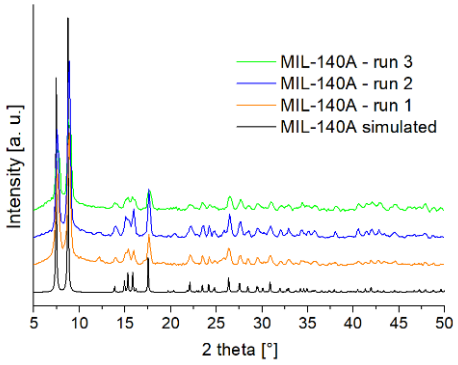

Figure S16 PXRD patterns of MIL-140A samples from repeated synthesis runs with solvent re-use.

Table S10 Results of three repeated synthesis runs with re-use of solvent for MIL-140A.

Run	BET [m^2g^{-1}]	Yield [%]
1	354	92
2	340	89
3	344	96

#

S10.4. Aluminum fumarate

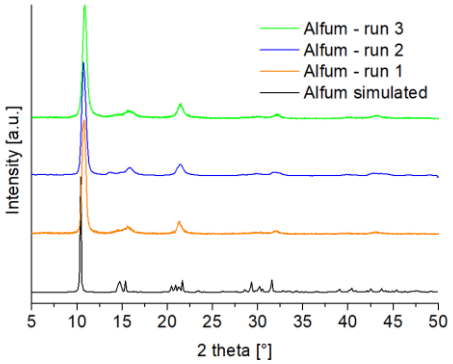

Figure S17 PXRD patterns of Alfum samples from repeated synthesis runs with solvent re-use.

Table S11 Results of three repeated synthesis runs with re-use of solvent for aluminum fumarate.

Run	BET [m^2g^{-1}]	Yield [%]
1	1075	76
2	1148	81
3	1128	89

S11. Calculation of solvent amounts

- for aluminum fumarate

The patented synthesis procedure for continuous production of Alfum demonstrates different methods with varying STYs from 2032-5339 kg m^{-3} day^{-1}. The most effective one (i.e. 3615 kg m^{-3} day^{-1}) yields 97.5 mol-% based on Al, achieving 4.1 wt.% product in solution.[57]

3615 kg m^{-3} day^{-1} = 4.1 wt.% of product in solution

→ 95.9 wt.% mother liquor = 84555.73 kg = 84.55 tons

- for UiO-66

The continuous flow synthesis procedure reports STY = 7163 kg m^{-3} day^{-1} with a concentration of 0.1 mol L^{-1} Zr in solution, 94% yield (i.e. 0.094 mol L^{-1} product in solution), a flow of 1.23 mL min^{-1}. Specifically it is stated that from 20 mL processed a yield of 0.696 g (94%)" of desolvated MOF in 24.4 min total run time was obtained.
This amounts to 0.696 g / [(0.020 L/10^{-3} L/m^3) x (24.4 min/1440 min/day)] = 2054 kg m^{-3} day^{-1}. There is an additional solvent amount of 8 mL + 10 mL and 60 mL for washing, that is in total apparently 98 mL for the STY of 2053 kg m^{-3} day^{-1}.

From only the 20 mL = 0.02 L and STY of 2054 kg m^{-3} day^{-1} the solvent volume per day is estimated as

$x = 2053 \cdot 10^3$ g / 0.696 g x 0.02 L = 59 000 L

From the total of 98 mL = 0.098 L and STY of 2054 kg m^{-3} day^{-1} the solvent volume per day is estimated:

$x = 2053 \cdot 10^3$ g / 0.696 g x 0.098 L = 289 000 L

S12. References

1 G. Férey, C. Serre, C. Mellot-Draznieks, F. Millange, S. Surblé, J. Dutour and I. Margiolaki, *Angew. Chem.*, 2004, **116**, 6456-6461.
2 K. Brandenburg, Diamond 4.3.1, Crystal and Molecular Structure Visualization, Crystal Impact - K. Brandenburg & H. Putz GbR, Bonn, Germany, 2009.
3 P. Horcajada, S. Surblé, C. Serre, D.-Y. Hong, Y.-K. Seo, J.-S. Chang, J.-M. Grèneche, I. Margiolaki and
G. Férey, *Chem. Commun.*, 2007, **27**, 2820-2822.
4 L. Sciortino, A. Alessi, F. Messina, G. Buscarino and F. M. Gelardi, *J. Phys. Chem. C*, 2015, **119**, 7826-7830.
5 F. Jeremias, S. K. Henninger and C. Janiak, *Dalton Trans.*, 2016, **45**, 8637-8644.
6 J. W. Yoon, Y.-K. Seo, Y. K. Hwang, J.-S. Chang, H. Leclerc, S. Wuttke, P. Bazin, A. Vimont, M. Daturi, E. Bloch P. L. Llewellyn, C. Serre, P. Horcajada, J.-M. Grenèche, A. E. Rodrigues and G. Férey, *Angew. Chem.*, 2010, **122**, 6085-6088.
7 P. L. Llewellyn, S. Bourrelly, C. Serre, A. Vimont, M. Daturi, L. Hamon, G. de Weireld, J.-S. Chang, D.-Y. Hong, Y. K. S. H. Jhung and G. Férey, *Langmuir*, 2008, **24**, 7245-7250.
8 I. Ahmed and S. H. Jhung, *Mater. Today*, 2014, **17,** 136-146.
9 C. Petit and T. J. Bandosz, *Adv. Funct. Mater.*, 2011, **21**, 2108-2117.

10 F. Jeremias, A. Khutia, S. K. Henninger and C. Janiak, *J. Mater. Chem.*, 2012, **22**, 10148-10151.
11 S. K. Henninger, F. Jeremias, H. Kummer, P. Schossig and H.-M. Henning, *Energy Proced.*, 2012, **30**, 279-288.
12 S. K. Henninger, F. Jeremias, H. Kummer and C. Janiak, *Eur. J. Inorg. Chem.*, 2012, **16**, 2625-634.
13 A. Rezk, R. Al-Dadah, S. Mahmoud and A. Elsayed, *Int. J. Heat Mass Tran.*, 2012, **55**, 7366-7374.
14 S. Kovačič, M. Mazaj, M. Ješelnik, D. Pahovnik, E. Žagar, C. Slugovc and N. Z. Logar, *Macromol. Rapid Comm.*, 2015, **36**, 1605-1611.
15 A. G. Márquez, A. Demessence, A. E. Platero-Prats, D. Heurtaux, P. Horcajada, C. Serre, J.-S. Chang, G. Férey, V. A. de la Peña-O'Shea, C. Boissière, D. Grosso and C. Sanchez, *Eur. J. Inorg. Chem.*, 2012, 5165-5174.
16 M. Pilloni, F. Padella, G. Ennas, S. Lai, M. Bellusci, E. Rombi, F. Sini, M. Pentimalli, C. Delitala, A. Scano, V. Cabras and I. Ferino, *Micropor. Mesopor. Mater.*, 2015, **213**, 14-21.
17 S. Rojas, F. J. Carmona, C. R. Maldonado, E. Barea and J. A. R. Navarro, *New J. Chem.*, 2016, **40**, 5690-5694.
18 E. Bellido, M. Guillevic, T. Hidalgo, M. J. Santander-Ortega, C. Serre and P. Horcajada, *Langmuir*, 2014, **30**, 5911-5920.
19 A. García Márquez, A. Demessence, A. E. Platero-Prats, D. Heurtaux, P. Horcajada, C. Serre, J.-S. Chang, G. Férey, de la Peña-O'Shea, Victor Antonio, C. Boissière, D. Grosso and C. Sanchez, *Eur. J. Inorg. Chem.*, 2012, 5165-5174.
20 F. Tan, M. Liu, K. Li, Y. Wang, J. Wang, X. Guo, G. Zhang and C. Song, *Chem. Eng. J.*, 2015, **281**, 360-367.
21 L. Li, S. Xiang, S. Cao, J. Zhang, G. Ouyang, L. Chen and C.-Y. Su, *Nat. Commun.*, 2013, **4**, article 25
number 1774.
22 B. Zhang, J. Zhang, C. Liu, L. Peng, X. Sang, B. Han, X. Ma, T. Luo, X. Tan and G. Yang, *Sci. Rep.*, 2016, **6**, article number 21401.
23 F. Vermoortele, R. Ameloot, L. Alaerts, R. Matthessen, B. Carlier, E. V. R. Fernandez, J. Gascon, F. Kapteijn and D. E. de Vos, *J. Mater. Chem.*, 2012, **22**, 10313-10321.
24 J.-W. Zhang, G.-P. Lu and C. Cai, *Green Chem.*, 2017, **19**, 4538-4543.
25 A. U. Czaja, N. Trukhan and U. Müller, *Chem. Soc. Rev.*, 2009, **38**, 1284-1293.
26 M. Rubio-Martinez, T. D. Hadley, M. P. Batten, K. Constanti-Carey, T. Barton, D. Marley, A. Mönch, K.-S. Lim and M. R. Hill, *ChemSusChem*, 2016, **9**, 938-941.
27 M. Rubio-Martinez, C. Avci-Camur, A. W. Thornton, I. Imaz, D. Maspoch and M. R. Hill, *Chem. Soc. Rev.*, 2017, **46**, 3453-3480.
28 M. J. Katz, Z. J. Brown, Y. J. Colón, P. W. Siu, K. A. Scheidt, R. Q. Snurr, J. T. Hupp and O. K. Farha, *Chem. Commun*., 2013, **49**, 9449-9451.
29 G. C. Shearer, S. Chavan, S. Bordiga, S. Svelle, U. Olsbye and K. P. Lillerud, *Chem. Mater.*, 2016, **28**, 3749-3761.
30 J. H. Cavka, S. Jakobsen, U. Olsbye, N. Guillou, C. Lamberti, S. Bordiga and K.P. Lillerud, *J. Am. Chem. Soc.*, 2008, **130**, 13850-13851.
31 V. Guillerm, F. Ragon, M. Dan-Hardi, T. Devic, M. Vishnuvarthan, B. Campo, A. Vimont, G. Clet, Q. Yang, G. Maurin, G. Férey, A. Vittadini, S. Gross and C. Serre, *Angew. Chem. Int. Ed.*, 2012, **51**, 9267-9271.
32 L. Valenzano, B. Civalleri, S. Chavan, S. Bordiga, M. H. Nilsen, S. Jakobsen, K. P. Lillerud and C. Lamberti, *Chem. Mater.*, 2011, **23**, 1700-1718.

33 H. Wu, Y. S. Chua, V. Krungleviciute, M. Tyagi, P. Chen, T. Yildirim and W. Zhou, *J. Am. Chem. Soc.*, 2013, **135**, 10525-10532.
34 M. W. Anjum, F. Vermoortele, A. L. Khan, B. Bueken, D. E. De Vos and I. F. J. Vankelecom, *ACS Appl. Mater. Interfaces*, 2015, **7**, 25193-25201.
35 F. Jeremias, V. Lozan, S. K. Henninger and C. Janiak, *Dalton Trans.,* 2013, **42**, 15967-15973.
36 F. Jeremias, D. Fröhlich, C. Janiak and S. Henninger, *New J. Chem.*, 2014, **38**, 1846-1852.
37 A. Shahat H. M. A. Hassan and H. M. E. Azzazy, *Analyt. Chim. Acta*, 2013, **793**, 90-98.
38 F. Vermoortele, B. Bueken, G. Le Bars, B. Van de Voorde, M. Vandichel, K. Houthoofd, A. Vimont, M. Daturi, M. Waroquier, V. Van Speybroeck, C. Kirschhock and D. E. De Vos, *J. Am. Chem. Soc.*, 2013, **135**, 11465-11468.
39 W. Cao, W. Luo, H. Ge, Y. Su, A. Wang and T. Zhang, *Green Chem.*, 2017, **19**, 2201-2211.
40 K. Užarević, T. C. Wang, S.-Y. Moon, A. M. Fidelli, J. T. Hupp, O. K. Farha and T. Friščić, *Chem. Commun.*, 2016, **52**, 2133-2136.
41 S. Gökpinar, T. Diment and C. Janiak, *Dalton Trans.*, 2017, **46**, 9895-9900.
42 M. Taddei, D. A. Steitz, J. A. van Bokhoven and M. Ranocchiari, *Chem. Eur. J.*, 2016, **22**, 3245-3249.
43 E. Leung, U. Müller, N. Trukhan, H. Mattenheimer, G. Cox and S. Blei, *Process for preparing porous metal-organic frameworks based on aluminum fumarate*, U.S. Patent No. 8,524,932, BASF SE, 3
Sep. 2013.
44 C. Kiener, U. Müller and M. Schubert, *Method of using a metal organic frameworks based on aluminum fumarate*, U.S. Patent No. 8,518,264, BASF SE, 27 Aug. 2013.
45 F. Jeremias, D. Fröhlich, C. Janiak and S. K. Henninger, *RSC Adv.*, 2014, **4**, 24073-24082.
46 E. Alvarez, N. Guillou, C. Martineau, B. Bueken, B. Van de Voorde, C. Le Guillouzer, P. Fabry, F. Nouar, F. Taulelle, D. de Vos, J.-S. Chang, K. H. Cho, N. Ramsahye, T. Devic, M. Daturi, G. Maurin and C. Serre, *Angew. Chem. Int. Ed.*, 2015, **54**, 3664-3668.
47 T. Loiseau, C. Volkringer, M. Haouas, F. Taulelle and G. Férey, *C. R. Chim.*, 2015, **18**, 1350-1369.
48 B. Yilmaz, N. Trukhan and U. Müller, *Chin. J. Catal.*, 2012, **33**, 3-10.
49 J. Chen, K. Shen and Y. Li, *ChemSusChem*, 2017, **10**, 3165-3187.
50 M. Gaab, N. Trukhan, S. Maurer, R. Gummaraju and U. Müller, *Micropor. Mesopor. Mater.*, 2012, **157**, 131-136.
51 S. Karmakar, J. Dechnik, C. Janiak and S. De, *J. Hazard. Mater.*, 2016, **303**, 10-20.
52 E. Elsayed, R. Al-Dadah, S. Mahmoud, P. A. Anderson, A. Elsayed and P. G. Youssef, *Desalination*, 2017, **406**, 25-36.
53 P. G. Yot, L. Vanduyfhuys, E. Alvarez, J. Rodriguez, J.-P. Itié, P. Fabry, N. Guillou, T. Devic, I. Beurroies, P. L. Llewellyn V. Van Speybroek, C. Serre and G. Maurin, *Chem. Sci.*, 2016, **7**, 446-450.
54 D. E. Crawford and J. Casaban, *Adv. Mater.*, 2016, **28**, 5747-5754.
55 D. Crawford, J. Casaban, R. Haydon, N. Giri, T. McNally and S. L. James, *Chem. Sci.*, 2015, **6**, 1645-1649.
56 M. Deetlefs and K. R. Seddon, *Green Chem.*, 2003, **5**, 181-186.
57 S. Wegner, C. Rutz, K. Schette, J. Barthel and A. Bushmelev, *Chem. Eur. J.*, 2017, **23**, 6330-6340.
58 M. Thommes, K. Kaneko, A. V. Neimark, J. P. Olivier, F. Rodriguez-Reinoso, J. Rouquerol and K. S. Sing, *Pure Appl. Chem.*, 2015, **87**, 1051-1069.

3.3 Engineering metal–organic frameworks in binder composites for water sorption driven chiller systems

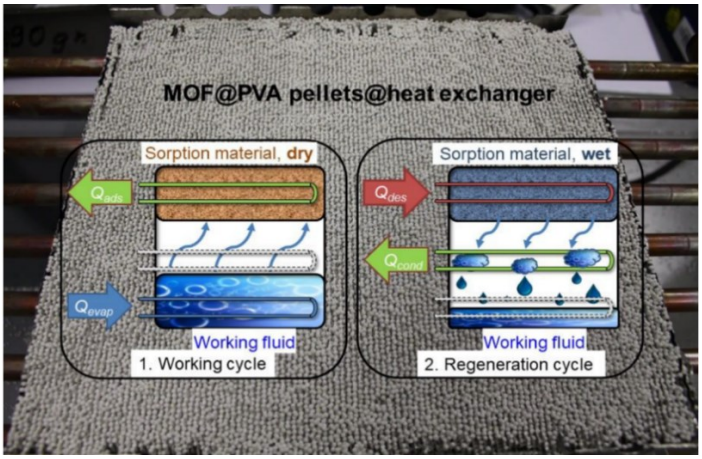

Zusammenfassung
Aufgrund der weltweit steigenden Temperaturen steigt auch die Anzahl der installierten Kältemaschinen. Die neue Materialklasse der metallorganischen Gerüste (MOFs) ermöglicht die Nutzung von Niedertemperatur-Abwärme und übertrifft gleichzeitig die Adsorptionskapazität moderner Werkstoffe. Sie haben daher das Potenzial, den Erfolg der Adsorptionstechnologie weiter voranzutreiben. Für den praktischen Einsatz in Adsorptionswärmepumpen (AHPs) müssen die mikrokristallinen Pulver geformt werden, sodass ihre hohe Porosität und Porenzugänglichkeit erhalten bleibt. In dieser Arbeit wird die Herstellung von millimetergroßen Pellets aus MIL-160 (Al), Al-Fumarat (Basolite A520), UiO-66 (Zr) und Zr-Fumarat (MOF-801) unter Anwendung der Gefriergranulationsmethode vorgestellt. Die Verwendung von Polyvinylalkohol (PVA) als Bindemittel führte reproduzierbar zu hochstabilen, gleichmäßig geformten PVA/MOF-Pellets mit einer MOF-Beladung von 80 wt% mit annähernd unveränderter MOF-Porosität. Die geformten Pellets wurden durch Wasseradsorptionsisothermen, Wassersorptionszyklen sowie thermische und mechanische Stabilitätstests auf ihre Anwendung in AHPs analysiert. Ferner wurden die PVA/Al-fum pellets in einem Festbett-Wärmeaustauscher aufgebracht, der spezifische Kühlleistungen (SCP) von 349 bis zu 431 W/kg(Adsorbens) erbrachte, die die derzeit kommerziell verwendeten Kieselgele in AHPs unter vergleichbaren Betriebsbedingungen übertreffen.

Meine Beiträge:

- Konzeptentwicklung, Herstellung der PVA/MOF-pellets (small-scale Produkt + large-scale Vorprodukt) und Durchführung der Grundcharakterisierung (XRD, N_2- und Wassersorption)
- Schreiben des Manuskripts-Entwurfs, Erstellen der Tabellen und Abbildungen (Ausgenommen: Fig. 3, 5-7; Fig. S2, S3, S6-9, S13, S17, S18 und Graphical Abstract)
- Korrekturen erfolgten durch Herrn Prof. Christoph Janiak

Dieser Abschnitt basiert auf der Publikation:
S. Gökpinar,[a] S.-J. Ernst,[b] E. Hastürk,[a] M. Möllers,[b] I. E. Aita,[c] R. Wiedey,[c] N. Tannert,[a] S. Nießing,[a] S. Abdpour,[a] A. Schmitz,[a] J. Quodbach,[c] G. Füldner,[c] S. K. Henninger,[b] and C. Janiak*, *Journal of XX*, 2019, **XX**, XXX–XXX.

Engineering metal–organic frameworks in binder composites for water adsorption heat transformation systems

Serkan Gökpinar,[†] Sebastian-Johannes Ernst,[‡] Emrah Hastürk[†] Marc Möllers,[‡] Ilias El Aita[‖] Raphael Wiedey,[‖] Niels Tannert[†] Sandra Nießing,[†] Soheil Abdpour,[†] Alexa Schmitz,[†] Julian Quodbach,[‖] Gerrit Füldner,[‡] Stefan K. Henninger,[‡] and Christoph Janiak[†]*

† Institut für Anorganische Chemie und Strukturchemie and ‖ Institut für Pharmazeutische Technologie und Biopharmazie, Heinrich-Heine-Universität Düsseldorf, 40204 Düsseldorf, Germany
‡ Fraunhofer Institut für Solare Energie Systeme (ISE), Heidenhofstr. 2, 79110 Freiburg, Germany.
*Corresponding author: janiak@uni-duesseldorf.de

KEYWORDS
Aluminum fumarate, Shaping, Adsorption heat transformation, Metal-organic framework.

ABSTRACT

Metal–organic frameworks (MOFs) currently receive high interest for cycling water adsorption applications like adsorption heat transformation (AHT). For practical use in adsorption heat pumps (AHPs) the microcrystalline powders must be formulated such that their high porosity and pore accessibility is retained. In this work, the preparation of millimeter-scaled pellets of MIL-160(Al), Al-fumarate (Basolite A520), UiO-66(Zr) and Zr-fumarate (MOF-801) is reported applying the freeze granulation method. The use of poly(vinyl alcohol) (PVA) as binder reproducibly resulted in highly stable, uniformly shaped PVA/MOF pellets with 80 wt% MOF loading, with essentially unchanged MOF porosity properties after shaping. The shaped pellets were analyzed for the application in AHPs by water adsorption isotherms, over 1000 water adsorption/desorption cycles and thermal and mechanical stability tests. Further, the Al-fum pellets were applied in a fixed-bed, full-scale heat exchanger, yielding specific cooling powers (SCP) from 349 up to 431 W/kg(adsorbent), which outperforms current commercially used silica gel grains in AHPs under comparable operating conditions.

Introduction

The worldwide energy consumption is increasing and a significant proportion of this energy consumption is caused by heating and cooling. In the EU, the heating of buildings presents 52% of the energy demand for the residential sector.[1] In countries with warmer climates similar values are needed for cooling and dehumidification processes. This amounts to around 20% of the electrical energy worldwide which is currently used for refrigeration and air-conditioning.[2] The need for refrigeration and air conditioning in private and non-private households is expected to increase.[3,4] Traditional air conditioners are based on vapor compression technology using refrigerants being increasingly restricted due to their high global warming potential (GWP) and have a high electricity consumption. At the same time, there is an agreement in society and politics that emissions of greenhouse gases must be reduced. This can be achieved by using technologies with a lower carbon footprint. The use of cooling technologies like adsorption heat transformation can contribute significantly to a greener, but better air-conditioned future.

Adsorption heat transformation (AHT) is a heating and cooling technology, which is commercially available and is based on an energy-saving and eco-friendly process, however, requires further improvement for wider acceptance. The process consists of two steps: An adsorption step during which the working fluid is evaporated consuming heat from a heat source and then adsorbed by the adsorbent releasing the heat of adsorption. As soon as the adsorbent reaches a certain capacity, desorption is initiated by heating the adsorbent collecting the desorbed working fluid in the condenser.

AHT is eco-friendly by advantageously avoiding halogenated refrigerants, operates silently by not using a compressor and regeneration is achieved through the use of low temperature driving heat sources such as solar, geothermal, industrial waste heat, etc.[5,6,7] Environmentally friendly organic vapors like water[8] or alcohols[9] can be used as working fluids, while water is preferred in this work. Commonly, porous silica gels or zeolites are applied as adsorbents in such sorption driven chillers, because of their inexpensive synthesis and easy availability.[6]

The integration of sorption materials in AHT devices using heat exchangers can be done using a bulk of loose grains, fixed/glued monolayers of grains, binder coatings or direct crystallization e.g. by partial support transformation, the latter often with poor mechanical stability.[10,11] Although alternatives to fixed bed heat exchangers are more [4] efficient, this technique is common because of its simplicity and its long-term mechanical stability.

A promising class of porous adsorbent materials for AHT is the class of metal–organic frameworks (MOFs), consisting of metal ions or metal clusters connected by organic ligands,12 which are actively investigated towards various applications.[13,14] MOFs get more and more attention due to their ability to achieve high vapor uptakes at configurable relative pressures.[15,16] However, MOFs are usually obtained as powders, which are unpractical for direct applications where shaping is needed. Different shaping of MOF leading to granules, pellets, thin films, foams, gels, paper sheets and hollow structures can be found in the literature (see ESI† for examples).[17,18,19]

MOF powders can readily be combined with the hydrophilic commodity polymer PVA for example by freeze granulation which involves dropping a slurry or suspension into liquid nitrogen followed by freeze-drying of the frozen droplets. The slurry can be obtained by dissolving the PVA in water and adding MOF powder under stirring. Instead of freeze-drying, a solvent exchange in acetone can be carried out to avoid melting and deformation of obtained pellets during the drying process. In this work, the isoreticular Zr-based MOFs UiO-66,20 and MOF-801/Zr-fumarate (Zr-fum)[21] together with the MOFs Al-fumarate22,23 and MIL-160(Al) are used (detailed description and structures are presented in Section S2 in the ESI†).[16, 24] The latter two MOFs could be obtained through an environmentally benign, water based synthesis.

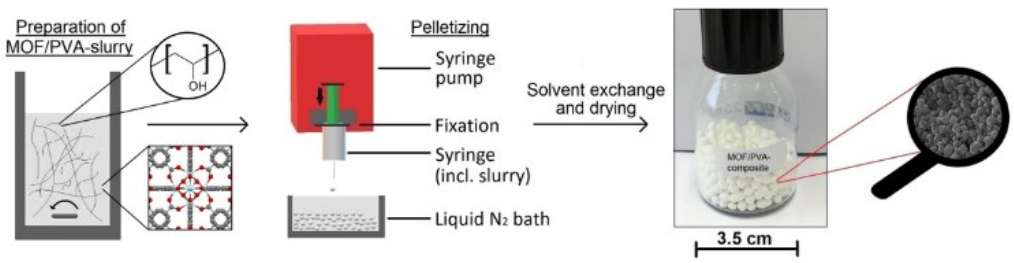

Figure 1 Fabrication process of pellets including preparation of PVA/MOF-slurry (exemplary MOF-structure and PVA; left), schematic drawing of the setup (middle) and picture of product with SEM-image exemplary shown for PVA/UiO-66 pellet (right).

Here we present the fabrication and characterization of PVA/MOF pellets being highly porous and stable as a ready-to-use drop-in solution for such AHT applications using a modified freeze granulation method.[25] Figure 1 shows a schematic drawing of the reactor setup and a picture of obtained pellets. In order to proof the potential of the presented method and materials, the characterization includes measurements with a full-scale heat exchanger filled with these grains.

Experimental procedure

Materials: All reagents were used as received. Terephthalic acid, ethanol, formic acid and hydrochloric acid 37% (HCl) were purchased from Sigma Aldrich. Acetone and N,N'-dimethylformamide (DMF) were obtained from Fischer Chemicals, fumaric acid from Tokyo Chemical Industry. Anhydrous $ZrCl_4$ and basic aluminum acetate, Al(OH)(CH3COO)2 were purchased from Alfa Aesar. Basolite A520 was supplied from BASF SE, benzoic acid (BA) from Riedel-de Haën and furan-2,5-dicarboxylic acid from Oxchem. Poly(vinyl alcohol) (Mowiol® 20-98) average molecular weight, Mw of 125 kDa, 98 % hydrolyzed was obtained from Sigma Aldrich. Water was de-ionized (DI). *Instrumentation:* Powder X-ray diffraction (PXRD) patterns were measured at ambient temperature by Bruker D2 Phaser (300 W, 30 kV, 10 mA) using Cu-Kα radiation (λ = 1.54182 6Å) from 5° to 50° 2Θ and a scanning rate of 0.0125 °/s. The diffractograms were carried out on a flat "low background sample holder". For analysis of the diffractograms, Match 3.11 software was used. PXRD of pellets after 1000 water sorption cycles were obtained using a Rigaku MiniFlex 600 powder diffractometer with Cu-Kα radiation (40 kV, 15 mA), 0.02° step size and 4 s step time. The most intense reflection was normalized to 1 for all diffractograms. Thermogravimetric analysis (TGA) were done with a Netzsch TG209 F3 Tarsus instrument. Samples were heated in alumina pans from 25-600°C with a rate of 5 °C/min under synthetic air. Differential scanning calorimetry (DSC) was measured using a Mettler Toledo DSC 3 with a temperature gradient of 15 K/min in the temperature range of -50 °C to 250 °C for the determination of the glass temperatures. The results were analyzed with the STARe SW 16.00 software. Nitrogen (purity 99.999 %) physisorption isotherms were executed on an Autosorb-6iSA from Quantachrome at 77 K (except pellets after 1000 cycles which were measured on a QuadraSorb evo at 77 K). Water sorption isotherms were collected on a vapor sorption analyzer (VSTAR™) from Quantachrome. Prior to the measurements, the samples were filled into glass tubes capped with septa for initial weighing. The tubes including the samples were degassed under vacuum at 100 °C for 3 h and weighed again. The samples were attached to the analysis port and measurements were started. BET surface areas were calculated using Rouquerol plots.[26] Gravimetric vapor sorption analysis was carried out on a SPS-11 from ProUmid GmbH & CoKG at relative humidity of 74.5% and 40 °C. Scanning electron microscopy (SEM) images were taken with a Jeol JSM-6510LV QSEM Advanced electron microscope equipped with a LaB6 cathode at 5–20 keV. The microscope was equipped with a Bruker Xflash 410 silicon drift detector for energy-dispersive X-ray spectrometric (EDX) elemental analysis. The resistance against deformation of the pellets up to 63 N was determined with a texture analyzer TA-XT2i 7 from Stable Micro Systems with constant speed of 0.35 mm/s. Alternatively, mechanical stabilities were measured by an Erweka TBH210 with a force capacity of 300 N. All values are referred to an average from a measurement of 10 pellets. X-ray micro-computed tomographic imaging was performed on a CT alpha (Proxon X-Ray, D) with a voxel size of 3 µm. The data was reconstructed using VG Studio 3.0 software (Volume Graphics, D). Data visualization and separation was conducted with Avizo Fire 9.0 (FEI, USA). Binarization was performed by applying a watershed algorithm.

The necessary starting points were defined by thresholding. Hg-porosimetry of at least 10 pellets was performed with a Hg-intrusion PASCAL 140-440 porosimeter from Thermo Scientific. The data was analyzed with the Solid 1.6.3 software. For the granulation process, a spheronizer Schlüter RM 300 with a 2 mm sieve and 6000 rpm was used. Pellets from large scale production were compressed on a rotary die press IMA Pressima from Kilian equipped with a pelleting tool with the following parameters: filling depth 4.08 mm, precompression 7.04 mm, compression 0.63 mm.

Synthesis of MOF powder, small-scale pellets and large-scale pellets: The synthesis of UiO-66 is adapted from Pullen et al.[27] $ZrCl_4$ (3.24 g, 13.9 mmol), H_2BDC (2.31 g, 13.9 mmol) and benzoic acid (51.24 g, 420 mmol) were dissolved in DMF (400 mL) under stirring in a round bottom flask and transferred into a vial. The vial was closed and allowed to react at 120 °C for 24 h in a preheated oven. After cooling, the as-synthesized product was washed by soaking in DMF (2 x 50 mL for 24 h each) and then the solvent was exchanged by soaking in ethanol (50 mL, 24 h). After altogether 3 d of soaking in DMF and ethanol, the solid was centrifuged and dried under vacuum.

The synthesis of Zr-fum was carried out following the procedure of Wißmann et al.[21] $ZrCl_4$ (2.4 g, 10.3 mmol) and fumaric acid (3.6 g, 30.9 mmol) were dissolved in a glass 8 flask at room temperature in DMF (400 mL). Then, formic acid (38 mL, 100 eq) was added. The glass flask was capped and heated in an oven at 120 °C for 24 h. After cooling, the white precipitate was washed with DMF (2 x 50 mL) and ethanol (50 mL), with each of the solvent aliquots exchanged every 24 h.

Al-fum was supplied from BASF SE, synthesized following the procedure of Gaab et al.[28]

MIL-160 was synthesized following the procedure of Permyakova et al.[24] $Al(OH)(CH_3COO)_2$ (5.86 g, 37.5 mmol) and 2,5-furandicarboxylic acid (6.08 g, 37.5 mmol) were added to a round-bottomed flask (250 mL) containing distilled water (37.5 mL). Then, the mixture was stirred under reflux for 24 h. The resulting white solid was recovered by filtration, washed with ethanol, and dried in the oven at 100 °C.

For the small-scale production of pellets 3 g of poly(vinyl alcohol) (PVA) were dissolved in 50 mL of DI water at 90 °C in a closed vial (ratio 60 mg PVA/1 mL water). Then, the MOF powder was added in a mass ratio of 4 (MOF):1 (PVA) and stirred for at least 3 h until a homogenous suspension was obtained. The suspension was drawn up in a syringe and added dropwise into liquid nitrogen using a diffuser (dropping rate 6 mL/min) to achieve freeze granulation. The pellets were collected and a solvent exchange in acetone was carried out over a time of 24 h, followed by drying in air. The air-dried pellets were further dried in vacuum at 80 °C for 3 h.

For the large-scale production of pellets the slurry was prepared similar to the above pelletizing process but with 30 g of PVA in a 500 mL of DI water. The PVA/MOF/water slurry was directly poured into liquid nitrogen (alternatively frozen at -20 °C in a freezer). The obtained larger PVA/Al-fum pieces of 5 cm diameter and more were collected and a solvent exchange in acetone was carried out with a duration time of 24 h. The pieces were dried in vacuum at 80 °C over night and crushed in a spheronizer (6000 rot/min with a 200 µm sieve). The obtained powder was then compressed to 2 x 1.8 mm sized pellets using a rotary die press.

Results and Discussion

Sample characterization

Figure 2 shows the powder X-ray diffraction (PXRD) patterns of the obtained MOF powders and pellets along with the simulated patterns verifying their high crystallinity and phase purity

by positive matching with the literature data. The amorphous PVA binder causes neither extra peaks, nor a significant background. The pellets have slightly broadened peaks in comparison to the pure MOF powder, which is caused by dilution through the added PVA binder, resulting in reduced peak intensity.

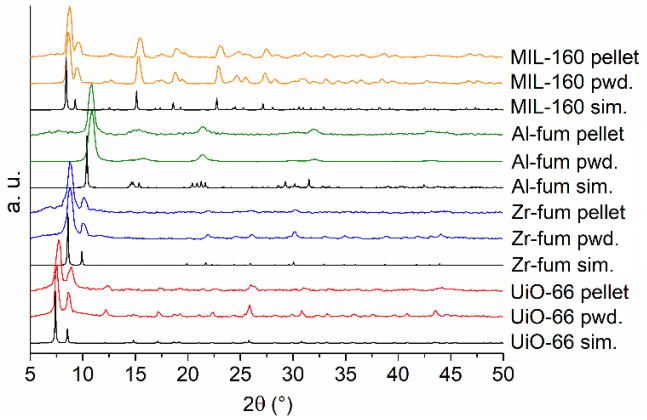

Figure 2 PXRDs of MIL-160, Al-fum, Zr-fum and UiO-66 powder (pwd.), pellets and their simulated (sim.) diffractograms from deposited crystal structure files. Simulated patterns were calculated from CSD-Refcode RUBTAK02 for UiO-66,[29] from BOHKAM for Zr-fum,[30] from DOYBEA for Al-fum[23] and from PIBZOS for MIL-160.[31]

The N_2-adsorption isotherms (Fig. S1, ESI†) yielded BET surface areas (SBET) and pore volumes of the pure MOF powder in the range of their literature values. The MOF pellets retained in most cases over 90% of the calculated SBET from the sum of the mass-weighted surface areas of the MOF and the PVA (Table 1).

Table 1 N_2 adsorption of Zr-fum, Al-fum, MIL-160 and UiO-66 pellets.

MOF	SBET of MOF powder [$m^2\ g^{-1}$]	SBET of pellets [$m^2\ g^{-1}$] (% of calc. SBET) [a]	Total pore volume of MOF powder [$cm^3\ g^{-1}$] [b]	Total pore volume of pellets [b] [$cm^3\ g^{-1}$] (% of calc. vol) [c]	SBET in Lit. [$m^2\ g^{-1}$]
MIL-160	1122	866 (96)	0.46	0.32 (83)	968 – 1180[32]
Al-fum	988	595 (74)	0.51	0.30 (73)	1080[23]
Zr-fum	643	479 (91)	0.31	0.22 (85)	408[33] – 856[21]
UiO-66	1295	1031 (99)	0.57	0.44 (93)	1032[8]-1461[34]

a expected BET surface area with 80 % MOF-loading calculated as the sum of the mass-weighted areas of the MOF (0.8) and freeze-granulated pure PVA (0.2) from the following formula, respectively: SBETcalc. = $SBET_{MOF}$ x 0.8 + $SBET_{PVA}$ x 0.2; with $SBET_{PVA}$ = 46 $m2g^{-1}$; b total pore volume is calculated at p p_0^{-1} = 0.90 by using Gurvich-rule for pores ≤ 21 nm. c expected total pore volume, with 80 % MOF-loading calculated as the sum of the mass-weighted pore volumes of the MOF and freeze-granulated neat PVA from the following formula: Vcalc. = V_{MOF} x 0.8 + VPVA x 0.2; with V_{PVA} = 0.05 $cm3g^{-1}$.

A comparison between SBET of synthesized PVA/MOF pellets and calculated SBET for 80 wt% MOF content shows an almost quantitative pore accessibility, varying between 74 to 99 % of

the mass-weighted areas. We already note that for the decisive water uptake the PVA/Al-fum composite will features near 100% water uptake when compared to the constituents. Also, total pore volumes of pellets are varying in a similar range between 73 and 93 % as compared to calculated total pore volume considering the mass ratio of PVA/MOF (for a detailed comparison of porous properties of MOFs before and after shaping by various shaping methods see ESI†, Section S1 and S3).

Differential scanning calorimetry and thermogravimetric analysis (DSCs and TGAs, see ESI†, Section S8) indicate no significant effect of the MOF content on the glass transition and decomposition temperature of the polymer.

For analysis of the macropore structure, X-ray micro-computed tomography (micro-CT) was performed. With a resolution of 3 µm/voxel, only pores with a diameter > 9 µm can be detected, as the accepted limit to reliably identify a feature is 3 x 3 voxels. In Figure 3, micro-CT cross-sections (left), SEM pictures of the pellets surface (middle) and macropores of a single pellet particle (3D micro-CT rendering, right) are presented. Even with the detection limitation of 9 µm remarkable differences can be observed between the samples. Al-fum and UiO-66 pellets show larger numbers of distinct void spaces that are clearly separated from each other (Figure 3a and c). MIL-160 and Zr-fum pellets also have some separated pores, but the majority of void volume is clustered in one or few large pore(s) in the center of the pellets. The shape of pores cannot be attributed to sample morphology: SEM reveals that Al-fum and MIL-160 have a similar microscopic appearance but the pore system is vastly different. The SEM pictures (Fig. S6-S9, ESI†) show the particles of the MOF powder before embedding in PVA and the surface and cross-section morphology of the prepared pellets. The two Al-MOFs Al-fum and MIL-160 show already a strong agglomeration of primary particles in the powder, whereas the Zr-MOF powders Zr-fum and UiO-66 feature separate, octahedrally-shaped particles.

These individual Zr-MOF particles can still be identified on the surface of the PVA/Zr-MOF pellets. In all cases, surface macropores, which allow for the pore accessibility of the embedded MOFs, are visible.

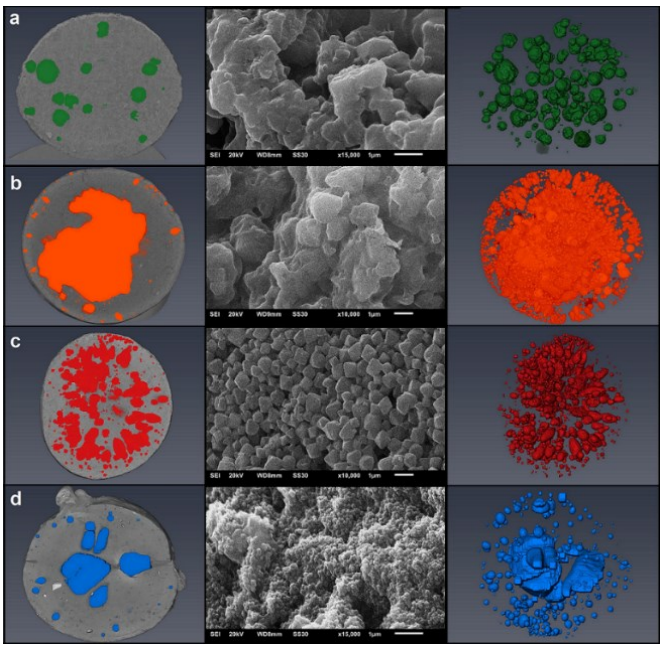

Figure 3 Micro-CT cross-section (left), SEM pictures of surface structure (middle) and macropores (right) of a representative PVA/MOF pellet with the MOF a) Al-fum b) MIL-160, c) UiO-66 and d) Zr-fum.

Hg-porosimetry further confirms the micro-CT observations (intrusion data is shown in Section S9 in the ESI†). At least 10 pellets were investigated per sample via Hg-porosimetry to characterize the bulk properties of the material complementing the micro-CT imaging. Fig. S14 displays the intrusion of large quantities of Hg at large pore sizes for MIL-160 and Zr-fum. Steps in the intrusion data can be attributed to large bottleneck pores as they are expected from the micro-CT data especially for MIL-160. These steps are also visible as sharp peaks in Fig. S14. Bottleneck pores are large pores with a narrow access point that prevents Hg from intruding at the assumed pressure. Only above the necessary pressure to pass the accessing pore, Hg will intrude the larger cavity. Numerous pores between 0.3 and 3 µm are found for the pellets fabricated of MIL-160, Zr-fum and UiO-66. The one fabricated of Al-fum show no pores > 0.3 µm and the majority of pores at 0.15 µm.

The different pore systems are also reflected in the mechanical stability of pellets. Even though the mechanical resistance is high in all cases (lowest crushing strength 14 ± 2 N for Zr-fum, Table 2), the observed differences are pronounced. Micro-CT images show that the larger and more isodiametric pores of Al-fum are of comparable size and evenly distributed throughout the pellet. This favors the distribution of force within the pellets, which leads to the highest crushing strength of 79 ± 11 N. Compared to the other Al-MOF MIL-160, the large central pore reduces the mechanical resistance, displayed in a lower crushing strength of 34 ± 7 N. The irregularly shaped pores of UiO-66 and Zr-fum promote crack propagation, leading to crushing strengths of 22 ± 3 N and 14 ± 2 N. The deformation behavior of all samples is similar. The pellets display comparable elastic and elastic-plastic deformation (Force–Displacement curves are presented in Section S5 in the ESI†) before reaching a critical crushing force Fc. Force higher than Fc lead to brittle fragmentation.[35] Only a few values can be found in the literature for shaped MOFs and show reduced mechanical stabilities as compared to the pellets presented here. The typical average crushing strength of robust silica gel pellets is about 57 N,[36] while zeolite shaped bodies are around 40-50 N.[37] Noteworthy, scratch tests of zeolite coatings give typically stabilities around 2–3 N.[11]

Table 2 Diameter and hardness (mechanical stability) of PVA/MOF pellets.[a]

MOF	Average diameter [mm][b]	Crushing strength F_c (Lit.) [N] [b,c]
MIL-160	2.6 ± 0.1	34 ± 7
Al-fum	2.7 ± 0.2	79 ± 11 [d] (24-80[37])
Zr-fum	2.9 ± 0.3	14 ± 2
UiO-66	3.1 ± 0.3	22 ± 3 (5[38])

[a] from small-scale production; [b] average diameter and standard deviation from 10 pellets; [c] rounded off to whole numbers; [d] value with Erweka TBH210 (higher than 63 N).

Water sorption isotherms and long-time stability tests

An adsorbent material for heat transformation should have a sorption isotherm with an S-shape (IUPAC classification Type V)[39] giving the steep rise in the relative pressure range of $p\,p0^{-1} \approx 0.10–0.30$[40,41], depending on the aimed application. There should be no or only little hysteresis which reduces the usable part of the loading and causes loss of sensible heat.[42,43] The S-shape is advantageous as it provides a large sorption lift within a narrow relative pressure range.[41] The uptake or working capacity should be higher than 0.20 g g^{-1}.[42] The shape of the isotherm depends on chemical interactions between the water molecules and the surface of the material. The hydrophobicity/hydrophilicity of the ligand, pore size, defects (missing linkers and missing clusters), open-metal site of clusters and hydrogen-bonding

capabilities of functional linker groups can be important for the water sorption process.[43-48] Based on the above prerequisites we had selected the already mentioned MOFs for shaping towards a close to realistic use in AHTs.

Characteristics of shaped materials strongly depend on the used binder. Herein, we show that the hydrophilic polymer PVA as binder material has no negative effect on the underlying MOF porosity and uptake capacities. The water sorption isotherms of the Zr- and Al-MOF powders and pellets measured volumetrically at 20 °C are shown in Figure 4.

The water adsorption of MOF powders and comparison between PVA/MOF pellets at rH of 0.76 is given in Table 3. The water uptake of the neat MOFs is in good agreement with reported results in literature (see Table 3). Al-fum- and MIL-160 pellets show a water uptake close to the calculated values within the measurement error. In case of Zr-MOFs we noticed an increased water uptake to 113%.

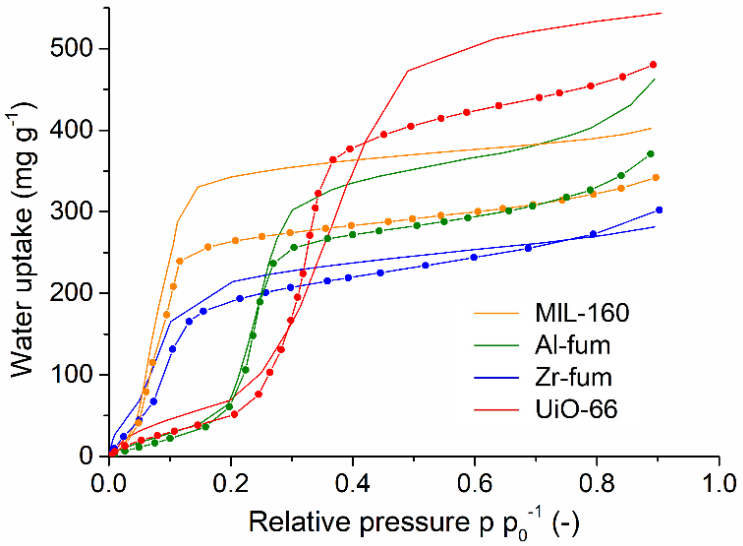

Figure 4 Water adsorption isotherms of UiO-66, Zr-fum, Al-fum and MIL-160 powder and pellets. Water uptake of pellets are not corrected to 100% MOF loading. Lines with data points (filled circles) are PVA/MOF pellets; lines without data points are neat MOF powders. Water adsorption isotherms are measured at 20 °C (water sorption isotherms of MOF pellets at different temperatures are in given in ESI†, Section S4).

Table 3 Comparison of water uptake between MOF powders and PVA/MOF pellets.

	Water uptake of MOF at rH of 0.76 [g g^{-1}][a]	Water uptake of pellets at rH of 0.76 [g g^{-1}][a] (% of calc. water uptake)[d]	Water uptake MOF in Lit. at rH of 0.76 [g g^{-1}]
MIL-160	0.39	0.32 (96)	0.37[16,c]
Al-fum	0.39	0.32 (96)	0.36[49,b]
Zr-fum	0.27	0.27 (113)	0.27 - 0.34[30,b]
UiO-66	0.52	0.45 (103)	0.38[8] - 0.56[50,b]

a water sorption isotherm is measured at 20 °C, b at 25 °C and c at 30 °C. d expected water uptake, with 80 wt% MOF-loading calculated as the sum of the mass-weighted water uptake of the MOF and neat, freeze-granulated PVA from the following formula: water uptakecalc. = water uptakeMOF x 0.8 + water uptakePVA x 0.2; with water uptakePVA = 0.11 g g^{-1}.

The possibly higher than 100% water uptake in PVA/Zr-MOF pellets compared to calculated values can be explained by two effects. First, defects can influence the water sorption isotherms. Not only the uptake amount, also the relative pressure can be shifted depending on the type of defects.[51]
SEM images reveal that the freeze-drying process has led to fracturing of the Zr-fum particles with smaller particles in the PVA/Zr-fum composite than in the neat MOF. The smaller particles have a larger outside surface area and will also have a higher particle-polymer interface volume which can rationalize the relative increase of the water uptake of the PVA/Zr-fum pellets over neat Zr-fum.
We also note that the pretreatment and the microstructure of hydrophilic polymer PVA has an influence. More separated polymer strands which become available through freeze-drying have their C-OH groups more readily accessible for water hydrogen bonding. This results in higher water uptakes compared to strongly agglomerated random coils in native PVA (for a comparison of water sorption isotherms of freeze-granulated and untreated PVA see ESI†, Figure S15 top, left).[52]
For application of these PVA/MOF composites under real conditions it is important to prove their long-term hydrothermal stability. For this reason, 1000 water ad- and desorption cycles in a custom-made cycle test have been performed. This setup does not allow an in-situ determination of the water uptake. Therefore, the characterization of pellets is repeated after running 1000 water sorption cycles between 25 °C adsorption and 130 °C desorption for water vapor of 12 mbar. The stability for Al-fum and MIL-160 after 1000 cycles of water ad- and desorption is verified by PXRD and N_2-sorption measurements through an unchanged structure and porosity. No loss of porosity, within the measurement error, was observed for Al-fum and MIL-160 pellets, such that SBET and pore volume was fully retained. Zr-fum shows a slight reduction of SBET and pore about 9 %, while UiO-66 is decreased about 19% (all values are given in ESI†, Section S7). This verifies the results of Jeremias et al. for amino-functionalized UiO-66.[8] It is assumed that hydrolysis occurs between metal and linker such that the bond is broken by addition of hydroxyl groups on metal, and a free, protonated linker is released.[53]
After the initial 1000 cycles water sorption was continued to be followed for another 20 cycles with the ad- and desorption temperature of the sample chamber set to 40 °C and 140 °C with a cycle time of 200 min. Water sorption was measured in-situ under a humidified argon flow (pH2O = 5.6 kPa) on a thermogravimetric balance (Fig. 5). The water uptake at each cycle (green dots in Fig. 5) seems to have stabilized for all MOFs. In this setup, thermodynamic analysis cycles were performed over 10 h at the 1001st and 1020th (last) cycling experiment to determine the total H_2O uptake capacity of the material (following the 1000 water sorption cycles). The total water loading lift under thermodynamic uptake conditions after 1000 cycles is around 0.28 g g^{-1} for PVA/UiO-66 and 0.20 g g^{-1} for PVA/Zr-fum pellets, to be compared with 0.38 and 0.25 g g^{-1} from the volumetric measurement at 40 °C before cycling (Table S3, ESI†), respectively. Thus, both PVA/Zr-MOF pellets have strongly decreased their water uptake during cycling.
PVA/MIL-160 pellets have an uptake of 0.30 g g^{-1}, PVA/Al-fum pellets of about 0.28 g g^{-1} after 1000 cycles. The obtained results are comparable with volumetrically determined water uptake capacities in case of the Al-MOF composites before cycling (Table S3, ESI†). It is remarkable that there is no significant performance loss after 1000 cycles for the PVA/Al-MOF pellets, which renders them as promising candidates for an adsorption-based cycling heat transformation application.

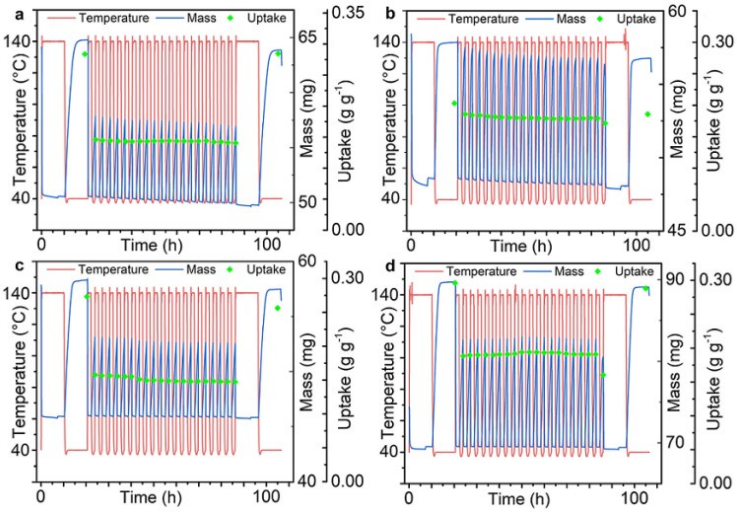

Figure 5 Cycle 1001 to 1020 of water sorption measured on thermogravimetric balance for a) UiO-66, b) Zr-fum, c) Al-fum and d) MIL-160 pellets. The green dots illustrate the specific water uptake.

As mentioned above, a hydrolysis between metal and linker occurs and the Zr-MOFs get more and more instable. This Zr-MOF decomposition is confirmed by a decrease in N_2 uptake in the N_2-sorption isotherms after 1000 cycles (Figure S11).
Care must be taken not to cycle at too high temperatures so as to avoid a loss of OH-groups from the PVA polymer chains. It is known that the degradation of side groups (-OH) to polyen and elimination of residual acetate groups can occur in PVA.[54,55] Furthermore, a thermally induced chain scission to aldehydes can occure.[54] It requires, however, temperatures above 200 °C to induce the decomposition of the polymer. The glass transition temperature of the PVA/MOF composites is shifted to lower temperatures by heating to 250 °C in the DSC. Hence, it is desirable to be able to work at low driving temperatures of less than 100 °C in the regeneration process of AHPs to avoid any organic polymer decomposition.

Adsorption heat transformation

From the above-determined hydrothermal stability and its commercial availability, Al-fum was chosen as the best MOF to be tested within a real heat exchanger (HX). Radu et al. described water sorption dynamics for various particle sizes and packing configurations for sorption driven chillers. In summary, pellets with smaller diameters and less layers of particles on the metal heat exchanger show the highest specific sorption rate.[56] We considered pellets with a diameter size around 2.5 mm still too large for the AHP application. Therefore, pellets with diameter size of 2 x 1.8 mm were shaped using the large-scale production method. Within 1 h, it was possible to produce more than 300 g of uniformly shaped PVA/Al-fum pellets with very high mechanical stability. For the pelleting process, spheronized PVA/Al-fum fragments were prepared, the solid material was compressed and ejected by a pelleting device (a detailed description of the production process is given in the ESI†, Section S11). A pipe-lamella heat exchanger was filled with the pelletized PVA/Al-fum adsorbent (denoted as ads-HX) (Figure 6). A home built adsorber element test setup (short «AdElTest«) was used for the adsorption measurements under pure water vapor conditions. The setup performs pressure jumps at quasi-isothermal adsorption temperatures (a scheme of the setup is given in Fig. S18 in the ESI†, for a detailed description of the method see ref. 57).

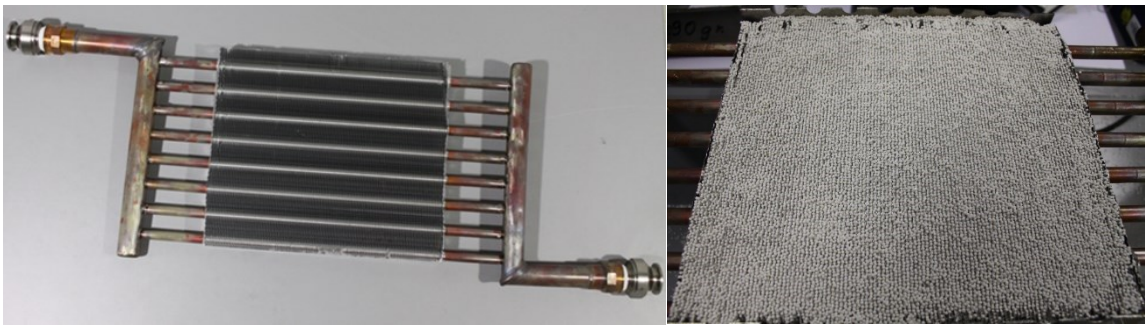

Figure 6 Pipe-lamella heat exchanger unfilled (left) and filled (right) with pellets.

Two types of measurements were conducted at two different temperature sets. Prior to all measurements, the ads-HX was degassed at a temperature of 90 °C under vacuum for 6 h. It is noteworthy, that a statement regarding the full cycle can therefore not be made based on this data. After letting the ads-HX cool to the set adsorption temperature, the adsorber was either preloaded according to the assumed desorption conditions (referred to as preloaded) or used fully desorbed (referred to as desVac). The measurement is started by opening a valve to the evaporator.

The temperatures of desorption, adsorption/condensation and evaporation ($T_{des}/T_{ads}/T_{evap}$) are set to 90/30/18 °C representing a standard cooling application[49] and to 60/22/18 representing a more advanced cooling scenario, e.g. data center cooling.

Table 4 summarizes the key parameters of measurement and results of the PVA/Al-fum pellet filled heat exchanger. Figure 7 shows the mass signal of the ads-HX over time. The maximum water uptake achieved was around 70 g during cycle 1 and around 85 g for cycle 2 resulting in a water exchange of 0.20 g g^{-1} and 0.25 g g^{-1} being slightly lower than expected from equilibrium adsorption experiments (0.25 and 0.28 g g^{-1}). However, as can be seen the adsorption equilibrium state has not been reached in the experiment, explaining the deviation. Further, it is noteworthy, that it is of minor influence for the uptake capacity if the adsorber was desorbed under vacuum or under realistic conditions. The higher uptake during cycle 2 is mainly caused by the higher relative pressure in the adsorption stage.

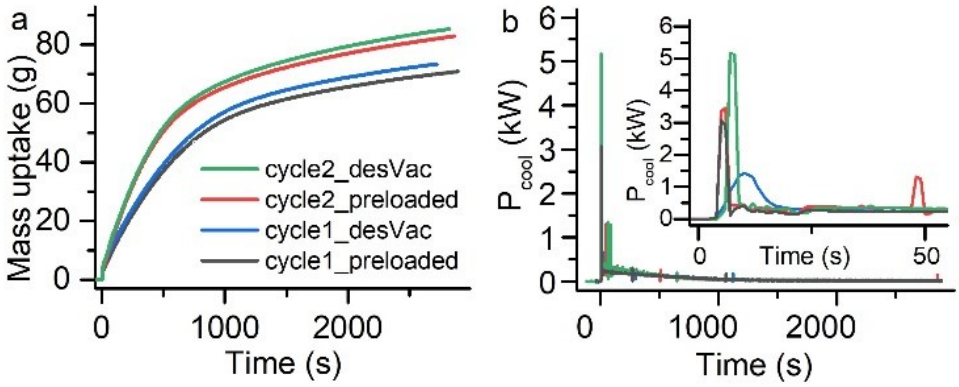

Figure 7 a) Mass of heat exchangers over time and b) cooling power of adsorber over time (including enlarged view).

As shown in Figure 7, the mass increase of the heat exchanger through water adsorption is near to 90 g (around 90% of maximal adsorption reached in 32 min) for pellets. A more pronounced effect of the desorption conditions can be seen in the peak of the adsorption

power that is much higher for the vacuum desorbed samples (457 W vs. 336 W and 535 W vs. 426 W, respectively) and further in the position of the peaks of cooling power calculated from the derivative of the mass uptake.

Table 4 Key parameters, values and results of measurement with PVA/Al-fum pellet-filled heat exchanger.

	Unit	Pellets			
		Cycle 1		Cycle 2	
		desVac	preloaded	desVac	preloaded
Specific temperatures [b]	[°C]	90/30/18	90/30/18	60/22/18	60/22/18
$Mass_{pellet}$	[g]	334	334	334	334
Δm (H_2O)	[g]	69	67	85	82
t of Δm_{90} (H_2O)	[s]	1587	1693	1650	1660
Loading change Δx (90%) [b]	[kg/kg_{ADS}]	0.24	0.24	0.28	0.28
Adsorption power	[W]	118	107	143	137
Integral cooling power P_{90}	[W]	103	93	115	111
Mean specific cooling power $MSCP_{90}$ [b]	[W/kg_{ADS}]	386	349	431	416
Peak adsorption power	[W]	457	336	535	426

[a] PVA/Al-fum pellets from large-scale production; [b] temperatures of desorption, adsorption/condensation and evaporation ($T_{des}/T_{ads}/T_{evap}$) [c] referred to mass of adsorbents ($Mass_{pellet}$*$wt\%_{MOF}$)

The pellet-filled HX (Figure 6) delivers specific cooling powers of 386 W/kg_{ADS} for standard conditions of 90/30/18, while 431 W/kg_{ADS} is reached for 60/22/18 (Table 4). For a better comparison of obtained specific cooling powers with literature values we refer to Table 5. As can be seen, the specific cooling powers of the pellet filled heat exchanger are higher than compared to other loose grain filled heat exchanger with comparable configurations. While silica gel typically reaches values from 50 to 230 W/kg_{ADS} under time optimized conditions, Al-fum pellets reach about 386 W/kg_{ADS}.[64,58] Further, we want to underline that the Al-fum material allows a desorption temperature down to 60 °C with SCP of 431 W/kg_{ADS}, seldomly seen in the literature especially for loose grains. None of the reported data have been collected at the more advanced temperature triplet of 60/22/18. At this triplet, the Al-fum shows a very promising performance that can further be optimized. An increase of SCP can be realized by optimization of cycle time, S/m ratio (ratio between surface of HX fins to the adsorbent mass) and grain size as presented by Aristov et al.[59,60,61]

Table 5 Comparison of different adsorbent heat exchanger configurations.

Material, [a] Literature	Loading time [min] [x]	Temperature set [°C] [x]	SCP [W/kg_{ADS}] [x]
Zeolite 13X [62,b]	132	310/25/10	26
Silica gel [63,c]	80	80/30/15	68

Silica gel [64]	13	86/30/15	120
Silica gel [64]	10	62/30/15	50
AQSOA-FAM-Z02 [65,d]	7	90/28/13	260
Al-fum [e] (this work)	26	90/30/18	386
Al-fum [e] (this work)	28	60/22/18	431

[a] materials are used as loose grains (packed bed); water is used as adsorbate; grain size: [b] 2–3 mm [c] ~2 mm [d] 0.25–0.45 mm [e] 1.8 x 2.0 mm [x] values are rounded to whole numbers.

Summary and Outlook

Herein, we present a simple method for the shaping of MOFs into pellets by freeze granulation. The use of poly(vinyl alcohol) (PVA) as binder resulted in highly mechanically stable, uniformly shaped PVA/MOF pellets with 80 wt% MOF loading which show excellent resistance against mechanical stress from 14 N up to 79 N. All MOFs maintain their porous properties after shaping with PVA. UiO-66, Zr-fum, Al-fum and MIL-160 pellets are produced and characterized for application in sorption driven chiller systems. While Zr-MOF pellets show decreased water uptakes after cycling processes, Al-fum and MIL-160 pellets exhibit unchanged water uptakes without performance loss over more than 1000 water ad- and desorption cycles. Finally, a full-scale heat exchanger was equipped with PVA/Al-fum pellets showing comparably good results to other loose-grain packed beds at standard driving temperature of 90 °C. Following the aim of smaller temperature differences between the ad- and desorption step, the driving temperature can be reduced to 60 °C[3,7] successfully obtaining specific cooling powers (SCPs) up to 431 W/kg_{ADS}. In summary, the ease of handling, possibility of low regeneration temperature, high mechanical and chemical stability, environmentally benign production and long-term resistance to repeated cycles are interesting features of the presented composite material. Further investigation will address the production of smaller granules and the optimization of the contact between granule and heat exchanger to speed up the sorption process.

ASSOCIATED CONTENT

Supporting Information
The Supporting Information is available free of charge on the ACS Publications website at DOI: 10.1021/acs.iecr.XXXX.
Sorption isotherms, structures of MOF, heat of adsorption, SEM images, mechanical stability tests, water sorption cycling, thermogravimetric analysis, Hg-porosimetry, role of polymer, detailed characterization of Al-fum pellets and their adsorption heat transformation (PDF).

AUTHOR INFORMATION

Corresponding Author: *E-mail: janiak@uni-duesseldorf.de
Author Contributions: The manuscript was written through contributions of all authors. All authors have given approval to the final version of the manuscript.
Funding Sources: This work was supported by the Federal German Ministry of Education and Research (BMBF) under grant OPTIMAT 03SF0492A/C.
Notes: The authors declare no competing financial interest.

ACKNOWLEDGMENTS

We thank Prof. Dr. Laura Hartmann and Stephanie Scheelen for DSC measurements. Also, we are thankful to Mr. Ard Lura for help during the pelleting process, Mr. Simon Millan for helpful discussions and Mr. Tobie Matemb Ma Ntep for providing MOF-sample for pre-tests. Further, special thanks go to FläktGroup for providing a heat exchanger.

ABBREVIATIONS

AHT = adsorption heat transformation; HX = heat-exchanger; MOF = metal-organic framework SCP = specific cooling power

REFERENCES

(1) European Comission. Communication from the Commission to the European Parliament, the Council, the European Economic and Social Committee and the Committee of the Regions on an EU Strategy for Heating and Cooling **2016**.
(2) Dean, B.; Dulac, J.; Morgan, T.; Remme, U.; Motherway; B. The future of cooling: opportunities for energy- efficient air conditioning. *Int. Energy Agency* **2018**. https://www.iea.org/futureofcooling/.
(3) Wang, S.; Lee, J. S.; Wahiduzzaman, M.; Park, J.; Muschi, M.; Martineau-Corcos, C.; Tissot, A.; Cho, K. H.; Marrot, J.; Shepard, W.; Maurin, G.; Chang, J.-S.; Serre, C. A robust large-pore zirconium carboxylate metal–organic framework for energy-efficient water-sorption-driven refrigeration. *Nat. Energy* **2018**, 3, 985−993.
(4) De Lange, M. F.; Verouden, K. J. F. M.; Vlugt, T. J. H., Gascon, J.; Kapteijn, F. Adsorption-Driven Heat Pumps: The Potential of Metal−Organic Frameworks. *Chemical Reviews* **2015**, 115, 12205−12250.
(5) Henninger, S. K.; Habib, H. A.; Janiak, C. MOFs as Adsorbents for Low Temperature Heating and Cooling Applications. *J. Am. Chem. Soc.* **2009**, 131 (8), 2776–2777.
(6) Hastürk, E.; Ernst, S.-J.; Janiak, C. Recent advances in adsorption heat transformation focusing on the development of adsorbent materials. *Curr. Opin. Chem. Eng.* **2019**, 24, 26–36.
(7) Lenzen, D.; Zhao, J.; Ernst, S.-J.; Wahiduzzaman, M.; Inge, A. K.; Fröhlich, D.; Xu, H.; Bart, H.-J.; Janiak, C.; Henninger, S.; Maurin, G.; Zou, X.; Stock, N. A metal–organic framework for efficient water-based ultra-low-temperature-driven cooling. *Nat. Comm.* **2019**, 10, 3025.
(8) Jeremias, F.; Lozan, V.; Henninger, S. K.; Janiak, C. Programming MOFs for water sorption: amino-functionalized MIL-125 and UiO-66 for heat transformation and heat storage applications. *Dalton Trans., 2013, 42, 15967−15973.*
(9) De Lange, M. F.; Van Velzen, B. L.; Ottevanger, C. P.; Verouden, K. J. F. M.; Lin, L.-C.; Vlugt, T. J. H.; Gascon, J.; Kapteijn, F. Metal−Organic Frameworks in Adsorption-Driven Heat Pumps: The Potential of Alcohols as Working Fluids. *Langmuir* **2015**, 31, 12783−12796.
(10) Freni, A.; Bonaccorsi, L.; Calabrese, L.; Caprì, A.; Frazzica, A.; Sapienza, A. SAPO-34 coated adsorbent heat exchanger for adsorption chillers. *Appl. Therm. Eng.* **2015**, 82, 1−7.
(11) Freni, A.; Dawoud, B.; Bonaccorsi, L.; Chmielewski, S.; Frazzica, A.; Calabrese, L.; Restuccia, G. Characterization of Zeolite-Based Coatings for Adsorption Heat Pumps; SpringerBriefs in Applied Sciences and Technology (Chapter 4); Springer, 2015.
(12) Zhou, H. C.; Long, J. R.; Yaghi, O.M. Introduction to Metal–Organic Frameworks. *Chem. Rev.* **2012**, 112, 673−674.

(13) Ockwig, N. W.; Delgado-Friedrichs, O.; O'Keeffe, M.; Yaghi, O. M. Reticular chemistry: occurrence and taxonomy of nets and grammar for the design of frameworks. *Acc. Chem. Res.* **2005**, 38 (3), 176–182.
(14) Janiak, C.; Vieth, J. K. MOFs, MILs and more: concepts, properties and applications for porous coordination networks (PCNs). *New J. Chem.* **2010**, 34, 2366–2388.
(15) Jeremias, F.; Fröhlich, D.; Janiak, C.; Henninger, S. K. Advancement of sorption-based heat transformation by a metal coating of highly-stable, hydrophilic aluminium fumarate MOF. *RSC Advances* **2014**, 4, 24073–24082.
(16) Cadiau, A.; Lee, J. S.; Borges, D. D.; Fabry, P.; Devic, T.; Wharmby, M. T.; Martineau, C.; Foucher, D.; Taulelle, F.; Jun, C.-H.; Hwang, Y. K.; Stock, N.; De Lange, M. F.; Kapteijn, F.; Gascon, J.; Maurin, G.; Chang J.-S.; Serre, C. Design of Hydrophilic Metal Organic Framework Water Adsorbents for Heat Reallocation. *Adv. Mater.* **2015**, 27, 4775–4780.
(17) Khabzina, Y.; Dhainaut, J.; Ahlhelm, M.; Richter, H.-J.; Reinsch, H.; Stock, N.; Farrusseng, D. Synthesis and shaping scale-up study of functionalized UiO-66 MOF for ammonia air purification filters. *Ind. Eng. Chem. Res.* **2018**, 57 (24), 8200–8208.
(18) Valizadeh, B.; Nguyen T. N.; Stylianou, K. C. Shape engineering of metal–organic frameworks. *Polyhedron* **2018**, 145, 1–15.
(19) Bradshaw, D.; Garai, A.; Huo, J. Metal–organic framework growth at functional interfaces: thin films and composites for diverse applications. *Chem. Soc. Rev*. **2012**, 41, 2344–2381.
(20) Cavka, J. H.; Jakobsen, S.; Olsbye, U.; Guillou, N.; Lamberti, C.; Bordiga, S.; Lillerud, K. P. A New Zirconium Inorganic Building Brick Forming Metal Organic Frameworks with Exceptional Stability. *J. Am. Chem. Soc.* **2008**, 130 (42), 13850–13851.
(21) Wißmann, G.; Schaate, A.; Lilienthal, S.; Bremer, I.; Schneider A. M.; Behrens, P. Modulated synthesis of Zr-fumarate MOF. *Microporous and Mesoporous Mater.* **2012**, 152, 64–70.
(22) Leung, E.; Müller, U.; Trukhan, N.; Mattenheimer, H.; Cox, G.; Blei, S. Process for preparing porous metal-organic frameworks based on aluminum fumarate. *US8524932B2, US20120082864* **2013**.
(23) Alvarez, E.; Guillou, N.; Martineau, C.; Bueken, B.; Van de Voorde, B.; Le Guillouzer, C.; Fabry, P.; Nouar, F.; Taulelle, F.; de Vos, D.; Chang, J.-S.; Cho, K. H.; Ramsahye, N.; Devic, T.; Daturi, M.; Maurin, G.; Serre, C. The Structure of the Aluminum Fumarate Metal–Organic Framework A520. *Angew. Chem.*, **2015**, 54 (12), 3664–3668.
(24) Permyakova, A.; Skrylnyk, O.; Courbon, E.; Affram, M.; Wang, S.; Lee, U-H.; Valekar, A. H.; Nouar, F.; Mouchaham, G.; Devic, T.; Weireld, G. D.; Chang, J.-S.; Steunou, N.; Frere, M.; Serre, C. Synthesis Optimization, Shaping, and Heat Reallocation Evaluation of the Hydrophilic Metal–Organic Framework MIL-160(Al). *ChemSusChem* **2017**, 10, 1419–1426.
(25) Shanmugam, S. Granulation techniques and technologies: recent progresses. *BioImpacts* **2015**, 5, 55–63.
(26) Rouquerol, J.; Llewellyn, P.; Rouquerol, F. Is the bet equation applicable to microporous adsorbents?. *Stud. Surf. Sci. Catal.* **2007**, 160, 49–56.
(27) Pullen, S.; Fei, H.; Orthaber, A.; Cohen, S. M.; Ott, S. Enhanced Photochemical Hydrogen Production by a Molecular Diiron Catalyst Incorporated into a Metal–Organic Framework. *J. Am. Chem. Soc.* **2013**, 135 (45), 16997−17003.
(28) Gaab, M.; Kostur, M.; Müller, U. Stable Spherical, Porous Metal-Organic Framework Shaped Bodies for Gas Storage and Gas Separation. U.S. Patent 20140213832, 2014.
(29) Valenzano, L.; Civalleri, B.; Chavan, S.; Bordiga, S.; Nilsen, M. H.; Jakobsen, S.; Lillerud, K. P.; Lamberti, C. Disclosing the Complex Structure of UiO-66 Metal Organic Framework: A Synergic Combination of Experiment and Theory. *Chem. Mater.* **2011**, 23 (7), 1700–1718.

(30) Furukawa, H.; Gándara, F.; Zhang, Y.-B.; Jiang, J.; Queen, W. L.; Hudson, M. R.; Yaghi, O. M. Water adsorption in porous metal–organic frameworks and related materials. *J. Am. Chem. Soc.* **2014**, 136 (11), 4369–4381.
(31) Wahiduzzaman, M.; Lenzen, D.; Maurin, G.; Stock, N.; Wharmby, M. T. Rietveld Refinement of MIL-160 and its Structural Flexibility upon H2O and N2 Adsorption. *Eur. J. Inorg. Chem.* **2018**, 3626–3632.
(32) Tannert, N.; Jansen, C.; Nießing, S.; Janiak, C. Robust synthesis routes and porosity of the Al-based metal–organic frameworks Al-fumarate, CAU-10-H and MIL-160. *Dalton Trans.* **2019**, 48, 2967–2976.
(33) Hirschle, P.; Preis, T.; Auras, F.; Pick, A.; Völkner, J.; Valdepérez, D.; Witte, G.; Parak, W. J.; Rädler, J. O.; Wuttke, S. Exploration of MOF nanoparticle sizes using various physical characterization methods – is what you measure what you get?. *CrystEngComm*, **2016**, 18, 4359–4368.
(34) Gökpinar, S.; Diment, T.; Janiak, C. Environmentally benign dry-gel conversions of Zr-based UiO metal–organic frameworks with high yield and the possibility of solvent re-use. *Dalton Trans.* **2017**, 46, 9895-9900.
(35) Antonyuk, S.; Tomas, J.; Heinrich, S.; Morl, L. Breakage behaviour of spherical granulates by compression. *Chem. Engng. Sci.* **2005**, 60, 4031–4044.
(36) Denton, D. A. Method of preparing silica gel pellets U.S. Patent 4,256,682, 1981**.**
(37) Gaab, M.; Kostur, M.; Müller, U. Stable Spherical, Porous Metal-Organic Framework Shaped Bodies for Gas Storage and Gas Separation. U.S. Patent 20140213832, 2014.
(38) Valekar, A. H.; Cho, K.-H.; Lee, U.-H.; Lee, J. S.; Yoon, J. W.; Hwang, Y. K.; Lee, S. G.; Cho S. J.; Chang, J.-S. Shaping of porous metal–organic framework granules using mesoporous ρ-alumina as a binder. *RSC Adv.* **2017**, 7, 55767–55777.
(39) Thommes, M.; Kaneko, K.; Neimark, A. V.; Olivier, J. P.; Rodriguez-Reinoso, F.; Rouquerol, J.; Sing, K. S. W. Physisorption of gases, with special reference to the evaluation of surface area and pore size distribution. *Pure Appl. Chem.* **2015**, 87, 1051–1069.
(40) Aristov, Y. I. Challenging offers of material science for adsorption heat transformation: A review. *Appl. Therm. Eng.* **2013**, 50, 1610–1618.
(41) Henninger, S. K.; Jeremias, F.; Kummer, H.; Janiak, C. MOFs for use in adsorption heat pump processes. *Eur. J. Inorg. Chem.* **2012**, 2625–2634.
(42) Fröhlich, D.; Pantatosaki, E.; Kolokathis, P. D.; Markey, K.; Reinsch, H.; Baumgartner, M.; van der Veen, M. A.; De Vos, D. E.; Stock, N.; Papadopoulos, G. K.; Henninger, S. K.; Janiak, C. Water adsorption behaviour of CAU-10-H: a thorough investigation of its structure–property relationships. *J. Mater. Chem. A* **2016**, 4, 11859–11869.
(43) Khutia, A.; Rammelberg, H. U.; Schmidt, T.; Henninger, S.; Janiak, C. Water sorption cycle measurements on functionalized MIL-101Cr for heat transformation application. *Chem. Mater.* **2013**, 25, 790−798.
(44) Wade, C. R.; Corrales-Sanchez, T.; Narayan, T. C.; Dincă, M. Postsynthetic tuning of hydrophilicity in pyrazolate MOFs to modulate water adsorption properties. *Energy Environ. Sci.* **2013**, 6, 2172–2177.
(45) MaNtep, T. J. M.; Reinsch, H.; Moll, B.; Hastürk, E.; Gökpinar, S.; Breitzke, H.; Schlüsener, C.; Schmolke, L.; Buntkowsky G.; Janiak, C. Realizing the Potential of Acetylenedicarboxylate by Functionalization to Halofumarate in ZrIV Metal–Organic Frameworks. *Chem. Eur. J.*, **2018**, 24, 14048 –14053.
(46) Cmarik, G. E.; Kim, M.; Cohen, S. M.; Walton, K. S. Tuning the adsorption properties of UiO-66 via ligand functionalization. *Langmuir* **2012**, 28, 15606–15613.

(47) Ghosh, P.; Colón, Y. J.; Snurr, R. Q. Water adsorption in UiO-66: the importance of defects. *Chem. Commun.* **2014**, 50, 11329–11331.
(48) Schoenecker, P. M.; Carson, C. G.; Jasuja, H.; Flemming, C. J. J.; Walton, K. S. Effect of Water Adsorption on Retention of Structure and Surface Area of Metal–Organic Frameworks. *Ind. Eng. Chem. Res.* **2012**, 51 (18), 6513–6519.
(49) Kummer, H.; Jeremias, F.; Warlo, A.; Füldner, G.; Fröhlich, D.; Janiak, C.; Gläser, R.; Henninger, S. K. A. Functional Full-Scale Heat Exchanger Coated with Aluminum Fumarate Metal–Organic Framework for Adsorption Heat Transformation. *Ind. Eng. Chem. Res.* **2017**, 56 (29), 8393–8398.
(50) Dissegna, S.; Hardian, R.; Epp, K.; Kieslich, G.; Coulet, M.-V.; Llewellyn, P.; Fischer, R. Using water adsorption measurements to access the chemistry of defects in the metal–organic framework UiO-66. *CrystEngComm* **2017**, *19*, 4137−4141.
(51) Hossain, M. I.; Cunningham, J. D.; Becker, T. M.; Grabicka, B. E.; Walton, K. S.; Rabideau, B. D.; Glover, T. G. Impact of MOF defects on the binary adsorption of CO2 and water in UiO-66. *Chem. Eng. Sci*. **2019**, 203, 346–357.
(52) Salleh, M. S. N.; Nor, N. N. M.; Mohd, N.; Syed Draman, S. F. *AIP Conference Proceedings* **2017**, 1809, 020045.
(53) Kalmutzki, M. J.; Diercks, C. S.; Yaghi, O. M. Metal–Organic Frameworks for Water Harvesting from Air. *Adv. Mater.* **2018**, 1704304**.**
(54) Tsuchiya, Y.; Sumi, K. Thermal Decomposition Products of Poly(vinyl Alcohol). *J. Polym. Sci., Part A-1: Polym. Chem.* **1969**, 7, 3151−3158.
(55) Peng, Z.; Kong, L. X. A thermal degradation mechanism of polyvinyl alcohol/silica nanocomposites, *Polymer Degradation and Stability* **2007**, 92, 1061−1071.
(56) Radu, A. I.; Defraeye, T.; Ruch, P.; Carmeliet, J.; Derome, D. Insights from modeling dynamics of water sorption in spherical particles for adsorption heat pumps. *Int. J. Heat Mass Transfer* **2017**, 105, 326–337.
(57) Wittstadt, U.; Füldner, G.; Andersen, O.; Herrmann, R.; Schmidt, F. A New Adsorbent Composite Material Based on Metal Fiber Technology and Its Application in Adsorption Heat Exchangers. *Energies* **2015**, *8*, 8431−8446.
(58) Aristov, Y. I.; Sapienza, A.; Ovoshchnikov, D. S.; Freni, A.; Restuccia, G. Reallocation of adsorption and desorption times for optimisation of cooling cycles. Int. J. of Refrig. 2012, 35, 525-531.
(59) Sapienza, A.; Glaznev, I. S.; Santamaria, S.; Freni, A.; Aristov, Y. I. Adsorption chilling driven by low temperature heat: New adsorbent and cycle optimization. *Applied Thermal Engineering* **2012**, *32*, 141−146.
(60) Aristov, Y. I. Concept of adsorbent optimal for adsorptive cooling/heating. *Applied Thermal Engineering* **2014**, *72*, 166−175.
(61) Aristov, Y. I.; Glaznev, I. S.; Girnik, I. S. Optimization of adsorption dynamics in adsorptive chillers: Loose grains configuration. *Energy* **2012**, *46*, 484-492.
(62) Zhang, L.Z.; Design and testing of an automobile waste heat adsorption cooling system. *Appl. Therm. Eng.* **2000**, *20*, 103–114.
(63) Vodianitskaiaa, P. J.; Soaresb, J. J.; Herbert, M.; Gurgela, J. M. Experimental chiller with silica gel: Adsorption kinetics analysis and performance evaluation. *Energy Convers. Manage.* **2017**, *132*, 172−179.
(64) Wang, R. Z.; Pan, Q. W.; Xu, Z. Y. Solar-powered adsorption cooling systems, *Advances in Solar Heating and Cooling. Woodhead Publishing.* **2016**, 299-328.
(65) Vasta, S.; Freni, A.; Sapienza, A.; Costa, F.; Restuccia, G. Development and lab-test of a mobile adsorption air-conditioner. *Int. J. Refrig.* **2012**, *35*, 701-708.

3.3.1 Supporting Information

Engineering metal–organic frameworks in binder composites for water sorption driven chiller systems

Serkan Gökpinar,[†] Sebastian-Johannes Ernst,[‡] Emrah Hastürk,[†] Marc Möllers,[‡] Ilias El Aita,[‖] Raphael Wiedey,[‖] Niels Tannert,[†] Sandra Nießing,[†] Soheil Abdpour,[†] Alexa Schmitz,[†] Julian Quodbach,[‖] Gerrit Füldner,[‡] Stefan K. Henninger,[‡] and Christoph Janiak*[†]

[†] Institut für Anorganische Chemie und Strukturchemie and [‖] Institut für Pharmazeutische Technologie und Biopharmazie, Heinrich-Heine-Universität Düsseldorf, 40204 Düsseldorf, Germany
[‡] Fraunhofer Institut für Solare Energie Systeme (ISE), Heidenhofstr. 2, 79110 Freiburg, Germany.
*Email: serkan.goekpinar@uni-duesseldorf.de; sebastian-johannes.ernst@ise.fraunhofer.de; emrah.hastuerk@uni-duesseldorf.de; marc_moellers@web.de; elaita@uni-duesseldorf.de; raphael.wiedey@uni-duesseldorf.de; niels.tannert@hhu.de; Sandra.Niessing@uni-duesseldorf.de; abdpoursohail@gmail.com; alexa.schmitz@uni-duesseldorf.de; julian.quodbach@uni-duesseldorf.de; gerrit.fueldner@ise.fraunhofer.de; stefan.henninger@ise.fraunhofer.de; janiak@uni-duesseldorf.de

---

Contents

Section S1. N_2-Sorption Isotherms of MOF Powder and MOF Pellet

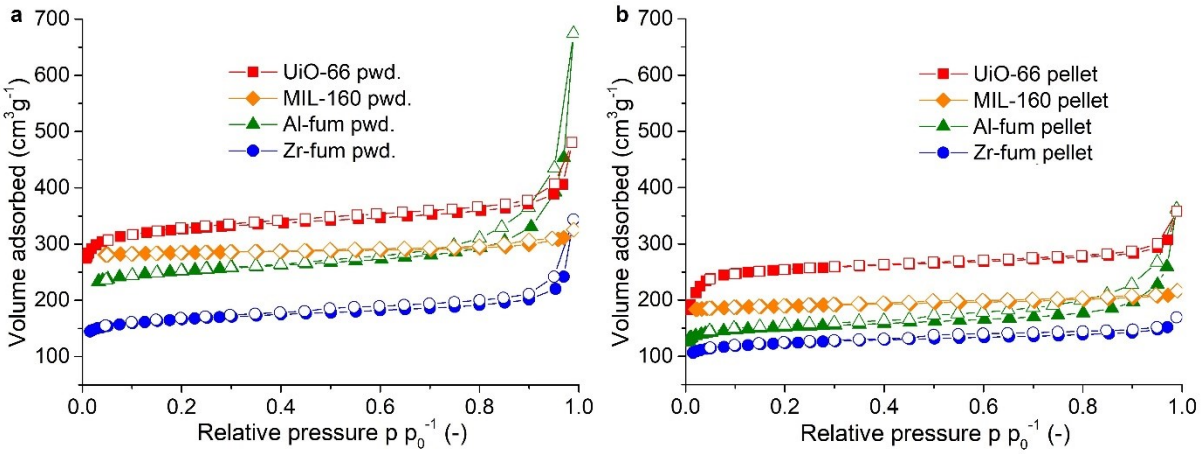

Figure S1 N_2 sorption isotherms of MIL-160, Al-fum, Zr-fum and UiO-66 a) powder and b) pellets. Filled symbols adsorption; empty symbols desorption.

Table S1. Micropore analysis of samples according to the V-t method.

Sample	Micropore SA [m^2/g] (% of calc. SA) [a]	External SA [m^2/g] (% of calc. SA) [a]	Micropore volume [$cm^3 \cdot g^{-1}$] (% of calc. micropore volume)
Al-fum	870	118	0.338
Al-fum pellet	517 (74)	78 (79)	0.201 (71)
MIL-160(Al)	1095	28	0.428
MIL-160(Al) pellet	825 (94)	41 (156)	0.276 (78)
Zr-fum	544	100	0.214
Zr-fum pellet	410 (93)	69 (82)	0.162 (88)
UiO-66(Zr)	1166	128	0.450
UiO-66(Zr) pellet	941 (100)	91 (86)	0.354 (95)

[a] expected surface area with 80 % MOF loading calculated as the sum of the mass-weighted areas of the MOF and PVA from the following formula, respectively: $SA_{calc.} = SA_{MOF}$ x wt% MOF + SA_{PVA} x wt% PVA with wt% MOF = 0.8, wt% MOF= 0.2, $SA_{micropore}$ = 27 m^2/g, $SA_{external}$ = 19 m^2/g [b] expected micropore volume with 80 % MOF loading calculated as the sum of the mass-weighted micropore volume of the MOF and PVA from the following formula, respectively: $V_{micropore\ calc.} = V_{MOF,\ micropore}$ x wt% MOF + $V_{PVA,\ micropore}$ x wt% PVA with $V_{PVA,\ micropore}$ = 0.06 cm^3/g.

Section S2. Structure of Used MOFs

UiO-66 (UiO = University in Oslo), firstly synthesized by Lillerud and co-workers, is consisted of a $\{Zr_6O_4(OH)_4\}$-SBU, twelvefold coordinated by the linker molecule benzene-1,4-dicarboxylate linkers (BDC) resulting in a face-centered cubic (fcc) packing arrangement (see Fig. S2).[1] While UiO-66 has BDC as linker, the isoreticular MOF-801/**Zr-fumarate** is coordinated by fumaric acid.[2] The properties of these Zr-MOFs are interesting for gas storage,[3] separation,[4] water sorption,[5,6] sensing[7] and catalysis.[8]

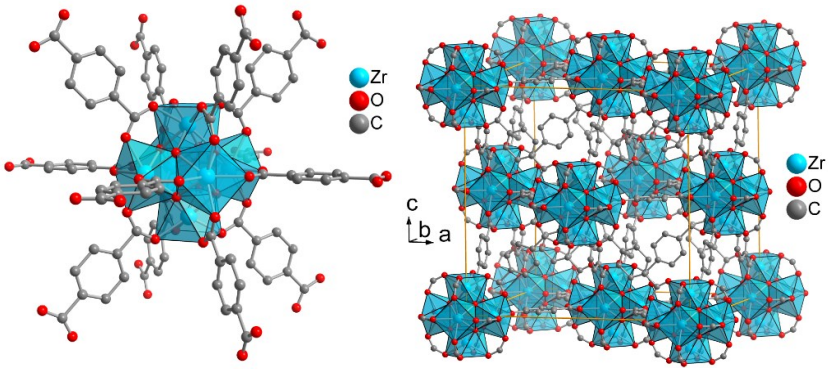

Figure S2 Crystal structure of zirconium terephthalate UiO-66. Hydrogen atoms and solvent molecules are not shown. The UiO-66 structure is drawn with the software Diamond from the deposited cif-file under CCDC no. 837796.[9] Zr-fum has an isoreticular structure, while linker terephthalate is replaced by fumarate.

Al-fumarate, described in the patent literature,[10] is one of the most promising MOFs for cooling applications due to its water based synthesis, inexpensive and benign metal cation and high stability.[6] The framework with the chemical formula $\{Al(OH)(fum) \cdot n\ H_2O\}_m$ is built up from Al-OH-Al chains connected by fumarate linkers resulting in lozenge-shaped 1D pores (see Fig. S3 left).[11] Further, a novel and very promising candidate is **MIL-160**, firstly synthesized by Cadiau *et al.*[12] It consists of helical cis corner-sharing chains of $AlO_4(OH)_2$ octahedra connected by 2,5-furandicarboxylate groups, building one dimensional square-shaped sinusoidal channels (see Fig. S3 right).[13]

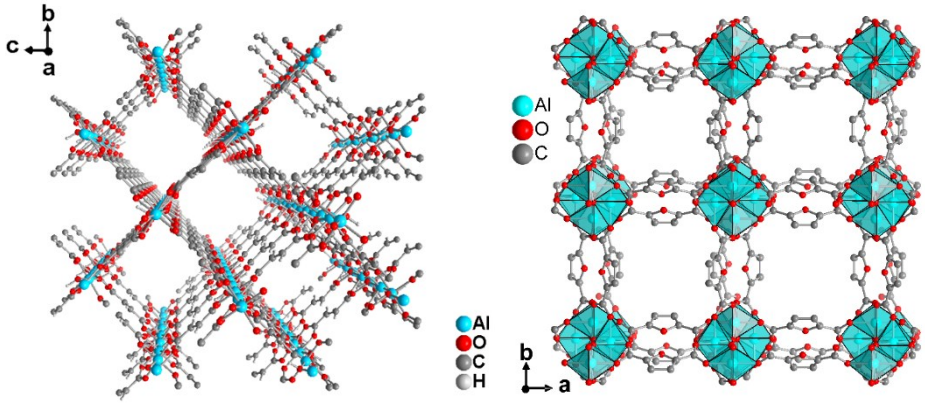

Figure S3 left: Crystal structure of aluminum fumarate. Graphic produced by software Diamond from cif-file for Basolite A520 (CCDC no. 1051975).[11]; right: Crystal structure of MIL-160. Graphic produced by software Diamond from cif-file under CCDC no. 1828695.[14]

Section S3. Summary of MOFs Before and After Shaping by Various Shaping Methods

MOF composite bodies using poly(vinylalcohol) (PVA) as a binder are known. Kim et al. produced PVA based granules of UiO-66 with a MOF-loading of ~78 wt% by using an extruder, synthesized for catalytic and gas storage application.[15] Khabzina et al. produced PVA and polysiloxane based UiO-66-COOH bodies for NH_3 air purification filters by using extrusion and freeze granulation technique.[16] Just to mention a few more shaping examples, Valekar et al. synthesized MIL-100(Fe), MIL-101(Cr), UiO-66(Zr) and UiO 66(Zr)-NH_2 MOF granules using the wet granulation method with 5 wt% mesoporous r alumina (MRA) as binder.[17] The calculated BET surface areas varied from 92 to 98 % of the dry powders' value (calculation in Electronic Supplementary Information Section S3) and the average crushing strengths varied between 2.5 and 6.7 N. These MOF bodies were also tested for NH3 adsorption and gas separation applications. Recently, Permyakova et al. produced MIL-160(Al) granules through wet granulation method using silica sol as binder (10 wt%), with a size distribution of 0.5 1.8 mm.[13] This MOF, including the granules are very promising for water sorption application. Further, Lenzen et al. reported coatings and monoliths based on CAU-10-H MOF using the water based SilRes MP50E binder for use in adsorption-driven chiller systems. The pore accessibility for water molecules are fully retained, while the water uptake is reduced in equivalent to the amount of binder.[18]

Table S2. Summary of porous properties of MOFs before and after shaping by various shaping methods. Table taken from Valekar *et al.*, modified and supplemented with own results.[15]

MOF	Additives	Shaped body	BET Surface area (m^2/g)			Ref.
			Powder	Shaped body	% of calc. SA[e]	
MIL-100(Fe)	5% mesoporous r-alumina (MRA)	Granules	2088	1831	92	17
MIL-101(Cr)	5% MRA	Granules	4066	3685	95	17
UiO-66(Zr)	5% MRA	Granules	1050	911	90	17
UiO-66(Zr)-NH_2	5% MRA	Granules	875	823	98	17
UiO-66(Zr)	10% Sucrose	Spheres	1367	674	≤55	19
UiO-66(Zr)	1% Graphite[b]	Pellet	1140	885	≤78	20
UiO-66(Zr)	23-33% Polyurethane[d]	Foam	1175	511-427	≤56-≤54	21
ZIF-8	20-50 Polysulfone[d]	Spheres	1023	761-128	≤93- ≤25	22
MIL-160	**20 % PVA**	**Pellets**	**1122**	**866**	**96**	o. w.
Al-fum	**20 % PVA**	**Pellets**	**988**	**595**	**74**	o. w.
Zr-fum	**20 % PVA**	**Pellets**	**643**	**479**	**91**	o. w.
UiO-66(Zr)	**20 % PVA**	**Pellets**	**1295**	**1031**	**99**	o. w.

a -granulation, b-pressing, c-spray drying and d-composite mixture shaping methods were used to shape the respective MOF, e– expected surface area calculated as the sum of the mass-weighted areas of the MOF and PVA from the following formula, respectively: $SBET_{calc.} = SBET_{MOF}$ x wt% MOF + $SBET_{PVA}$ x wt% PVA with $SBET_{PVA}$ = 48 m^2/g, $SBET_{MRA}$ = 218 m^2/g, [g] SBET of binder is not given and is set to 0 m^2/g to calculate the maximum.

Section S4. Heat of Adsorption Calculations for Pellets

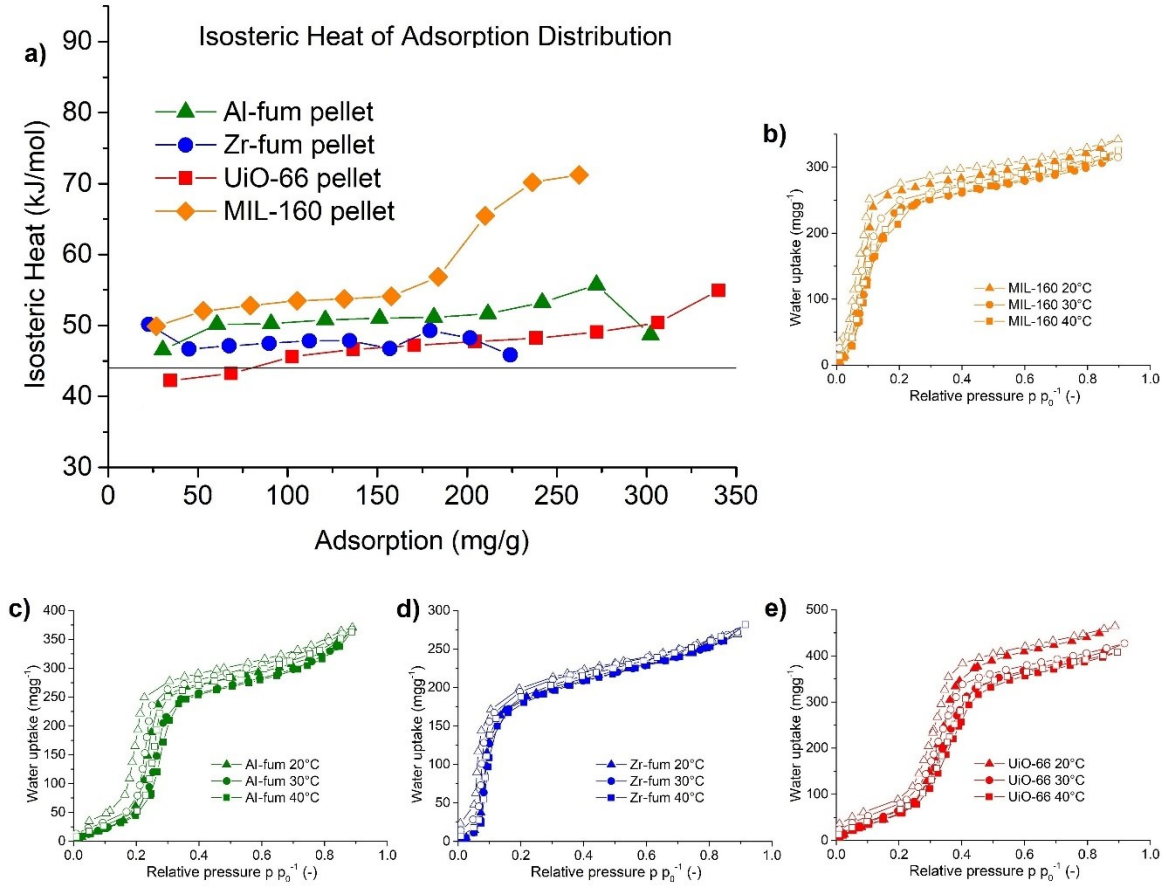

Figure S4 a) Heat of adsorption calculations of MIL-160, Al-fum, Zr-fum and UiO-66 pellets and volumetrically measured water sorption isotherms at different temperatures (20 °C, 30 °C and 40 °C) of b) MIL-160, c) Al-fum, d) Zr-fum and e) d) UiO-66 pellets.

Section S5. Mechanical stability Tests

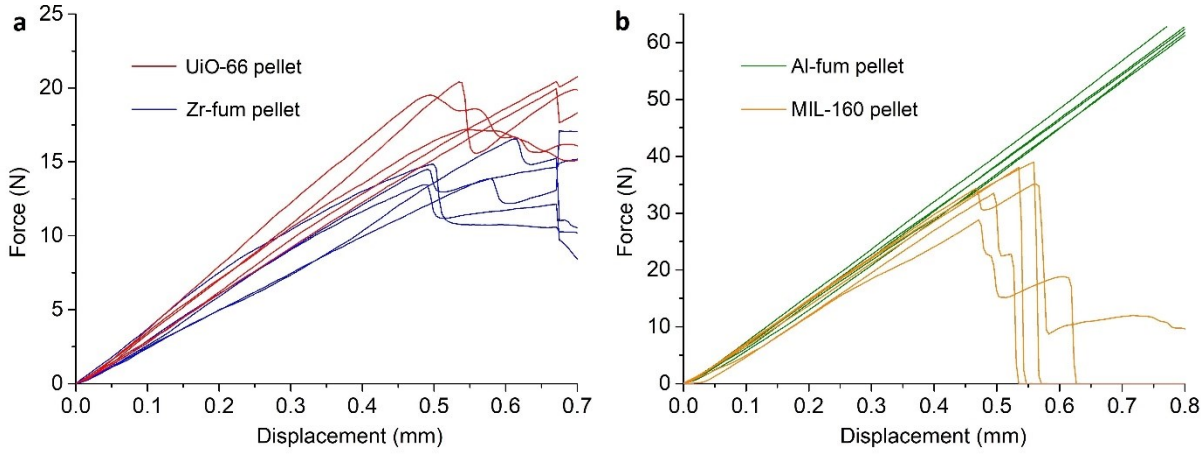

Figure S5 Mechanical stability tests of a) Zr-fum and UiO-66, b) MIL-160 and Al-fum pellets. All values higher than 63 N are measured by Erweka TBH210. For a better overview only 5 curves are shown.

Section S5. SEM Images

Al-fum

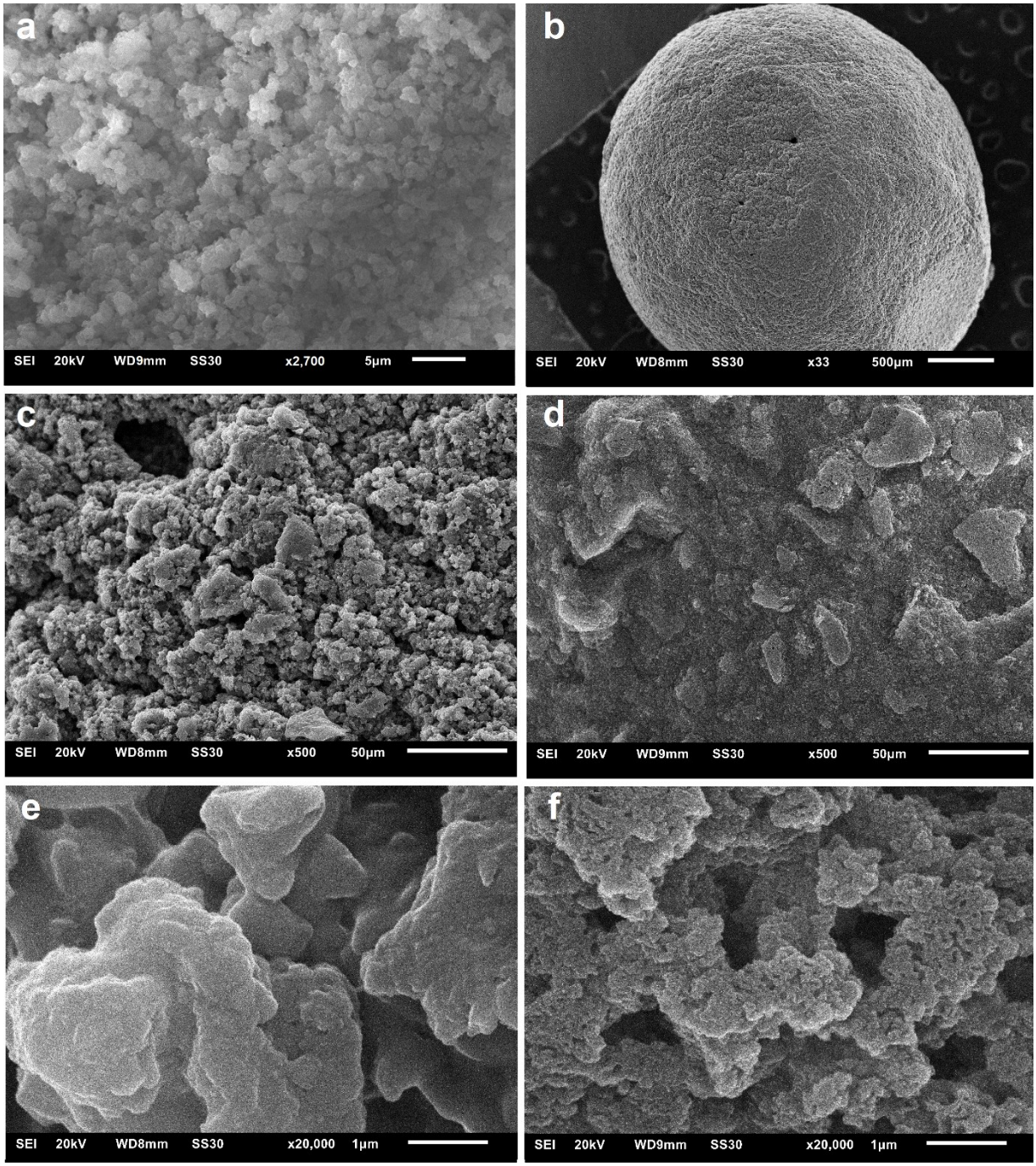

Figure S6 SEM pictures of Al-fum powder (a), overview of Al-fum pellet (b) surface of Al-fum pellet (c, e) and cross section of Al-fum pellet (d, f).

MIL-160

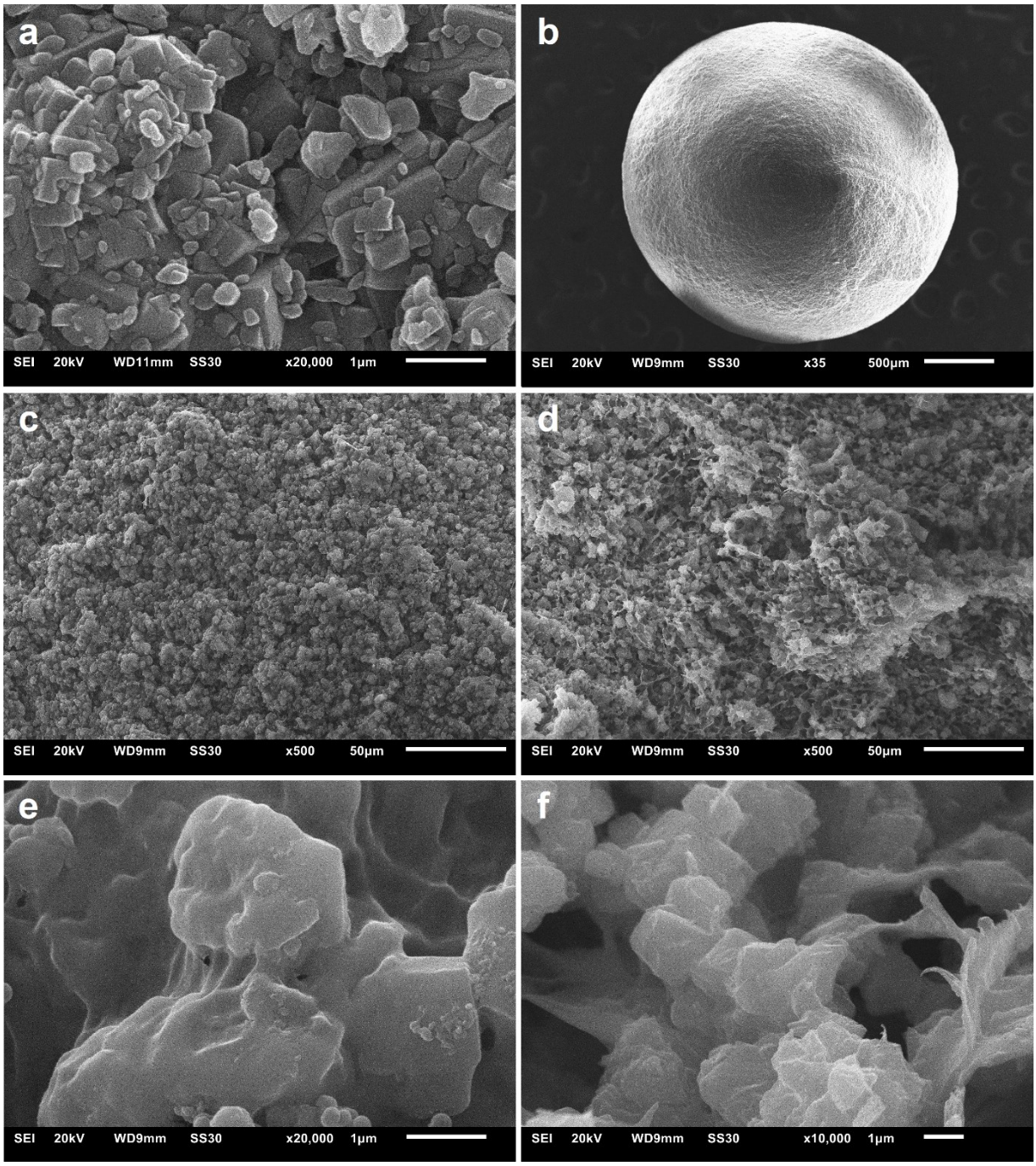

Figure S7 SEM pictures of MIL-160 powder (a), overview of MIL-160 pellet (b), surface of MIL-160 pellet (c, e) and cross section of MIL-160 pellet (d, f).

Zr-fum

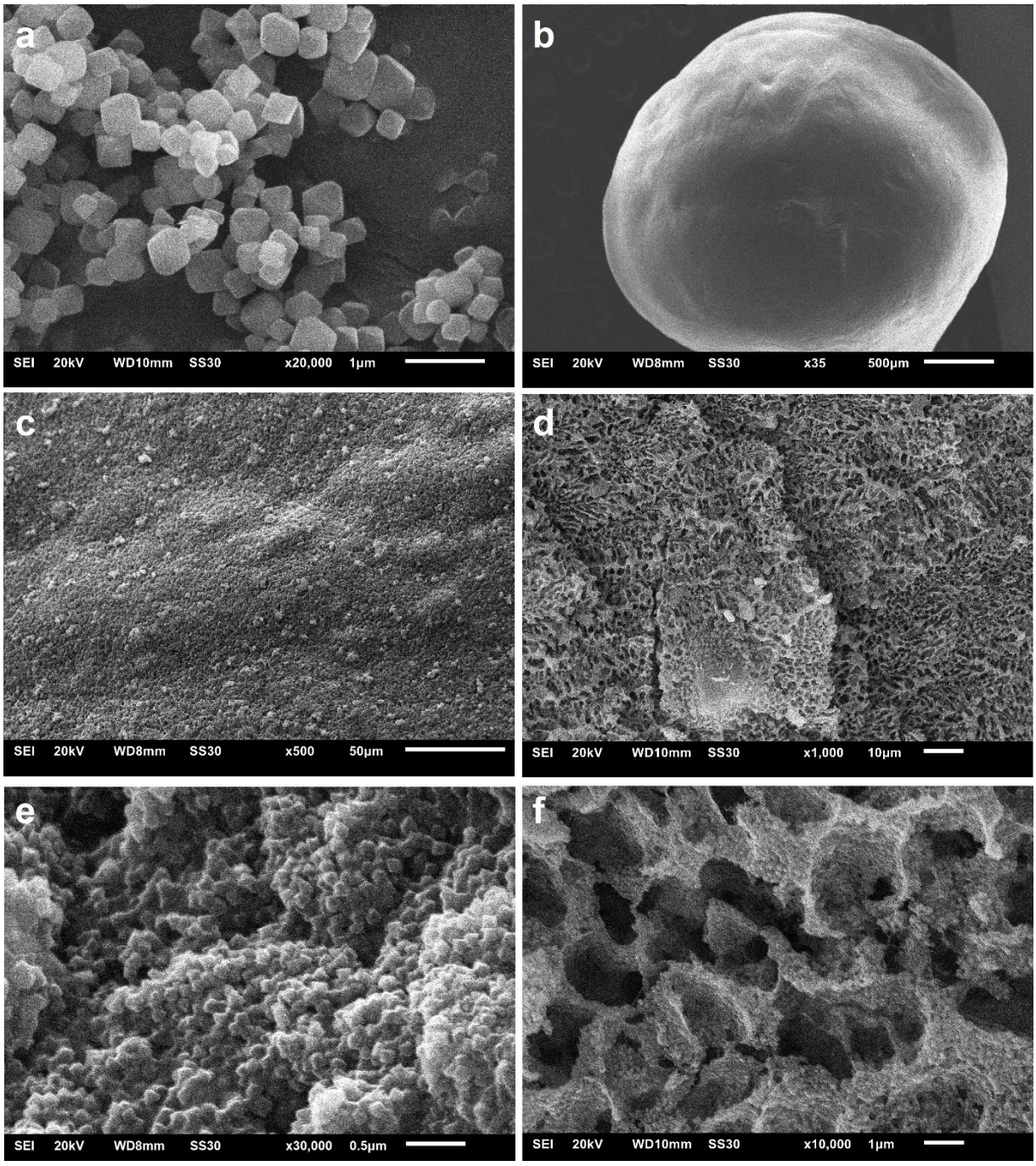

Figure S8 SEM pictures of Zr-fum powder (a), overview of Zr-fum pellet (b), surface of Zr-fum pellet (c, e) and cross section of Zr-fum pellet (d, f). (e) is an enlarged view of SEM-picture of manuscript.

UiO-66

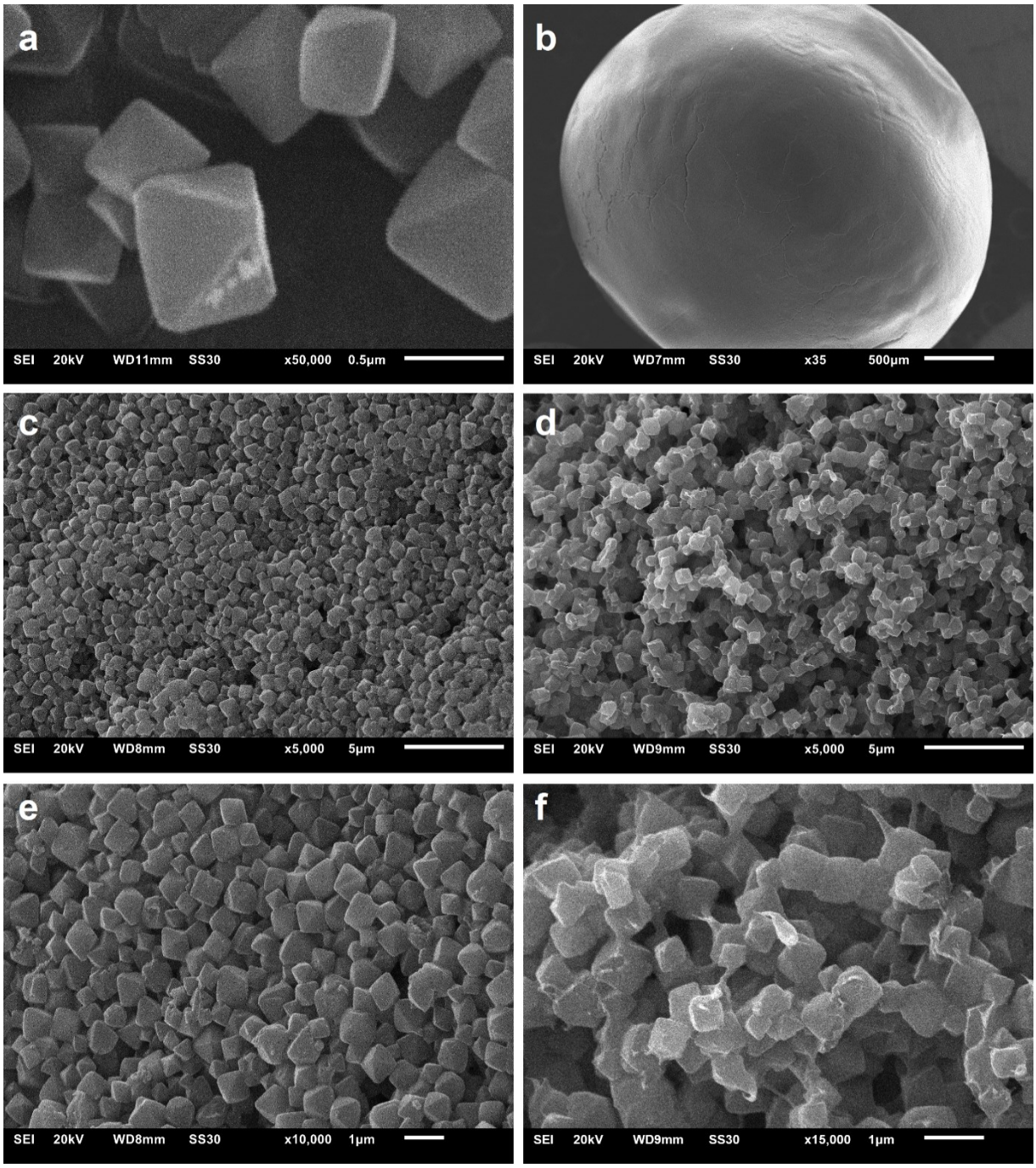

Figure S9 SEM pictures of UiO-66 powder (a), overview of UiO-66 pellet (b), surface of UiO-66 pellet (c, e) and cross section of UiO-66 pellet (d, f). (e) is also given in the manuscript.

Section S7. Water Sorption Cycling: PXRD After 1000 Cycles and N_2 Sorption Before and After 1000 Water Sorption Cycles

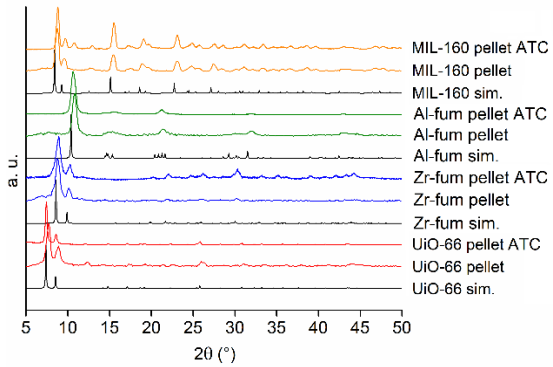

Figure S10 PXRD of MIL-160, Al-fum, Zr-fum and UiO-66 pellets after 1000 ad- and desorption cycles (ATC) of water.

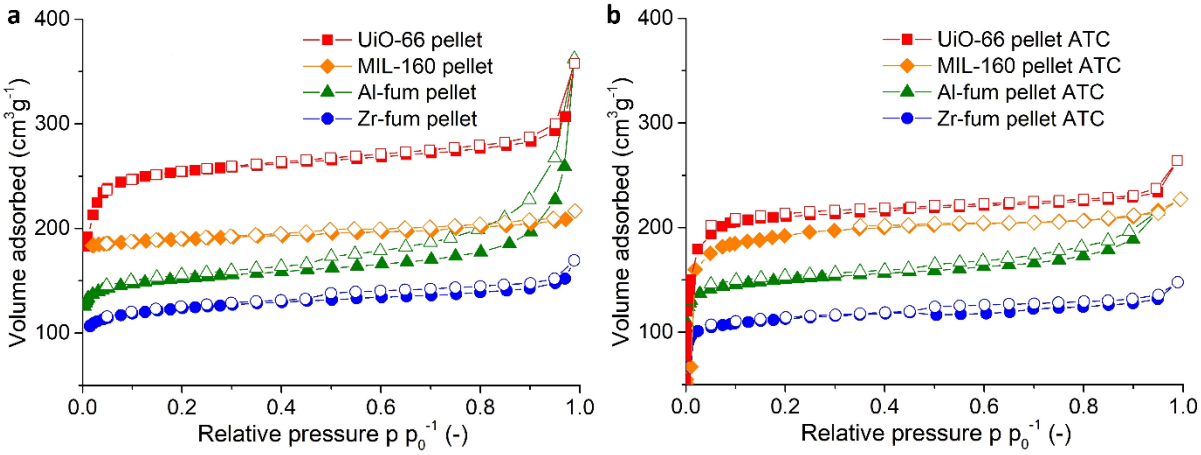

Figure S11 N_2-sorption isotherms of MIL-160, Al-fum, Zr-fum and UiO-66 pellets a) before and b) after 1000 water ad- and desorption cycles.

Table S3 N_2 and water sorption of MIL-160, Al-fum, Zr-fum and UiO-66 pellets before and after 1000 water ad- and desorption cycles.

	N_2 Sorption				Water sorption	
	before 1000 water ad- and desorption cycles		after 1000 water ad- and desorption cycles		before 1000 water ad- and desorption cycles	after 1000 water ad- and desorption cycles
MOF	SBET of pellets [$m^2 g^{-1}$]	Total pore volume of pellets [b] [$cm^3 g^{-1}$]	SBET of pellets [$m^2 g^{-1}$] (% of before cycling)	Total pore volume of pellets [b] [$cm^3 g^{-1}$] (% of before cycling)	Water upts at rH of 0.76 [$g g^{-1}$]; before cycl. (40°C)	Water uptake of pellets at rH of 0.76 [$g g^{-1}$]; after cycl. (40°C)
MIL-160	866	0.32	880 (102)	0.32 (100)	0.30	0.30
Al-fum	595	0.30	593 (100)	0.30 (100)	0.30	0.28
Zr-fum	479	0.22	437 (91)	0.20 (91)	0.25	0.20
UiO-66	1031	0.44	835 (81)	0.35 (80)	0.38	0.28

[b] total pore volume is calculated at p p_0^{-1} = 0.90 by using Gurvich-rule for pores ≤ 21 nm.

Section S8. Thermogravimetric Analysis (TGA) and Differential Scanning Calorimetry (DSC) of Pellets

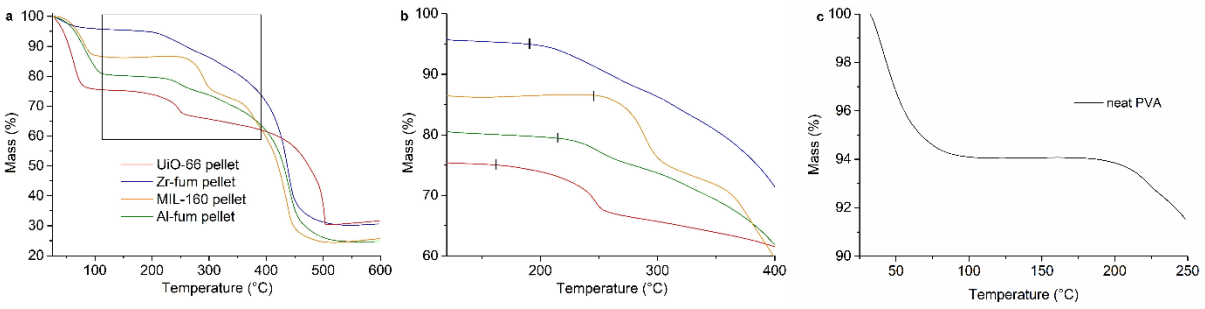

Figure S12 a) Thermogravimetric analysis of MIL-160, Al-fum, Zr-fum and UiO-66 pellets, b) enlarged view of TGA from 120 °C to 400 °C with marked starting points of weight loss debt by PVA and c) thermogravimetric analysis of neat PVA.

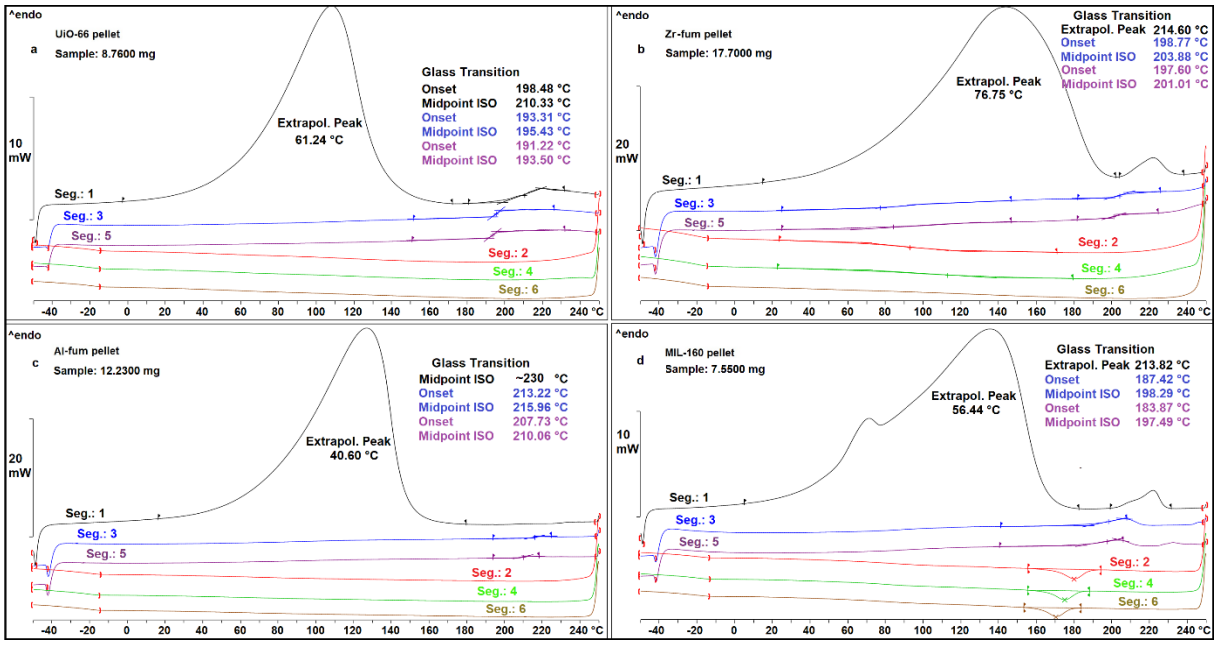

Figure S13 Differential scanning calorimetry of a) UiO-66, b) Zr-fum, c) Al-fum and d) MIL-160 pellets.

Section S9. Hg-Porosimetry

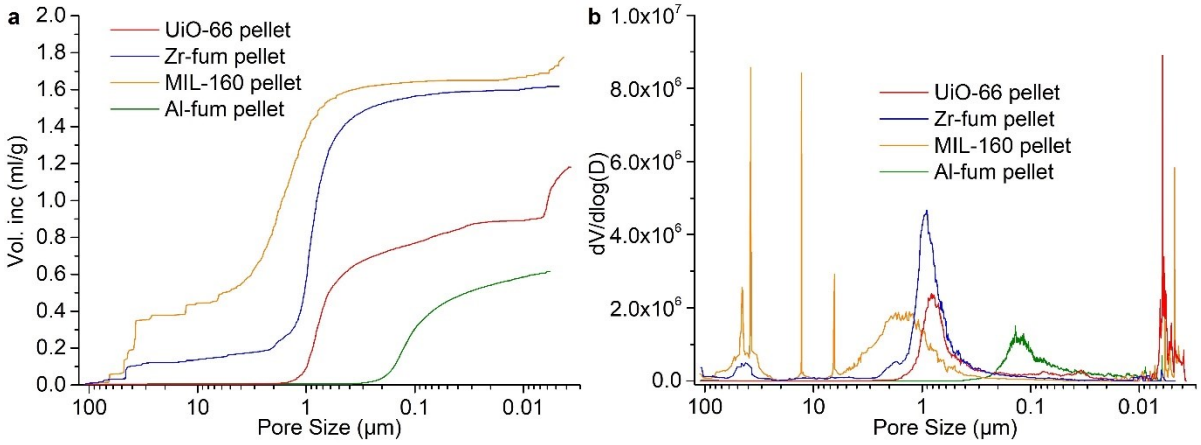

Figure S14 a) Cumulative pore volume and b) pore size distribution resulting from Hg-porosimetry MIL-160, Al-fum, Zr-fum and UiO-66 pellets.

Section S10. The Role of Random Coils During Water Sorption in PVA/MOF Composites and Pellet-Fabrication Set-up

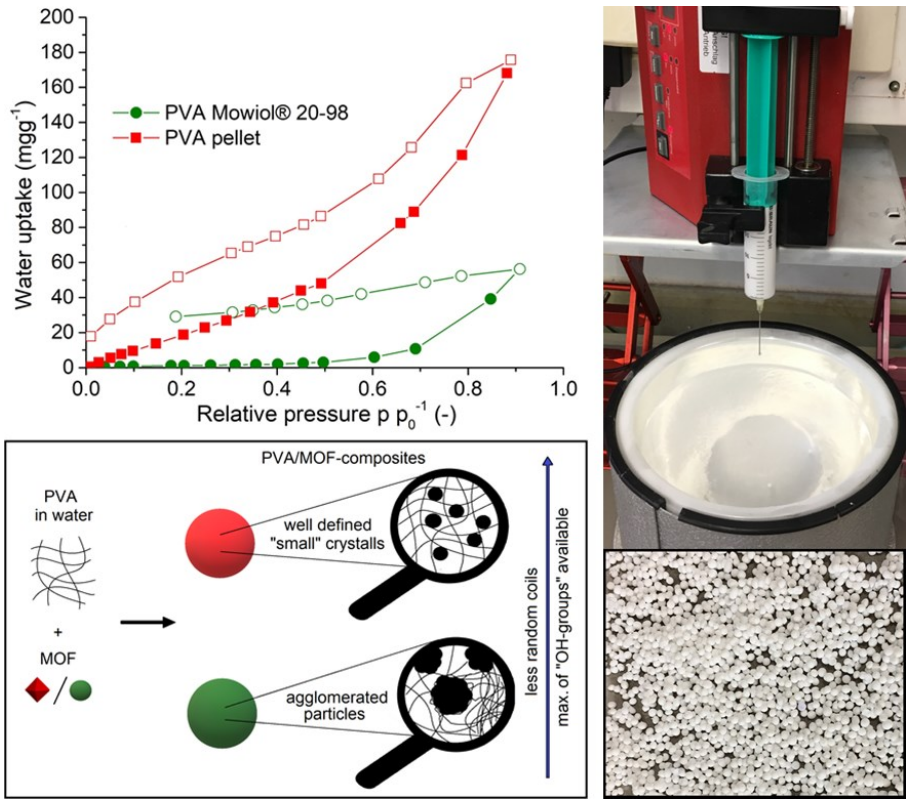

Figure S15 Left: Water sorption of untreated PVA (PVA Mowiol® 20-98) and pure, "freeze granulated"-PVA (PVA pellet) (top) and schematic presentation of availability of OH-groups of PVA depending on particle size of MOF (bottom). Filled symbols adsorption; empty symbols desorption. Water sorption isotherms are measured at 20 °C. Right: Picture of pellet-fabrication process (top) and obtained product (bottom).

Section S11 Characterization of Al-fum Pellets (Large-Scale Synthesis)

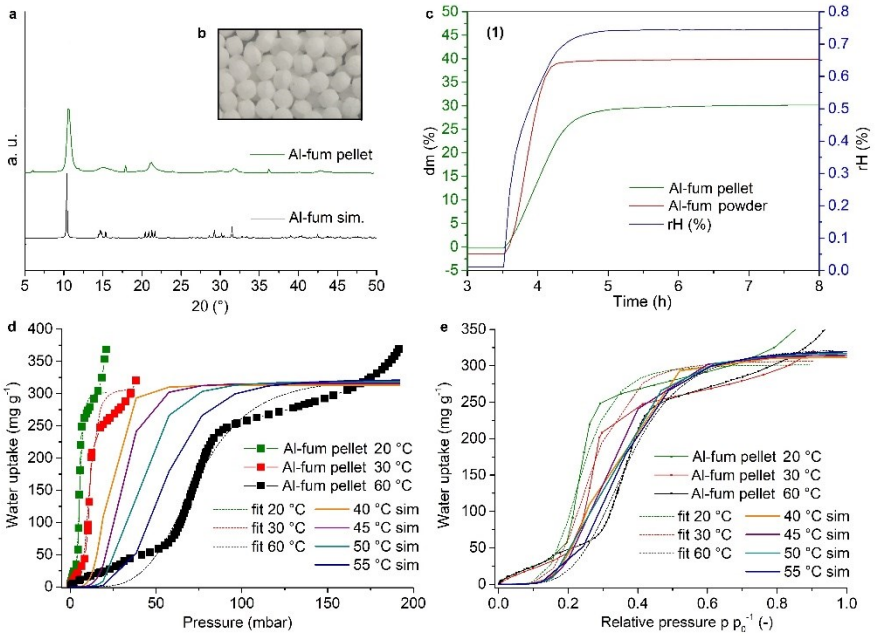

Figure S16 a) XRD of Al-fum pellet compared to simulated data, b) picture of fabricated pellets, c) Gravimetric water sorption measurements at 40 °C and rH of 74.5% and d) and e) water sorption isotherms of Al-fum pellets at 20 °C, 30 °C and 60 °C and their simulations at 40 °C, 45 °C, 50 °C and 55 °C using SIPS simulations giving calculated heat of adsorption of 52 KJ/mol.

Section S12. Characterization Adsorption Heat Transformation

A home built adsorber element test setup (short «AdElTest«) was used for the measurements under closed conditions. The setup performs pressure jumps at quasi-isothermal adsorption temperatures. Figure S17 shows a schematic representation of the setup. In the test setup the samples (3) are positioned inside a measurement chamber (1) suspended by a scale (2) and connected to the distributor circuit through flexible tubes. The working fluid is provided by a second heat exchanger partially submerged in water (6) working as either evaporator or condenser. It is placed in a second chamber (5) that is connected to the first chamber via two corrugated tubes.

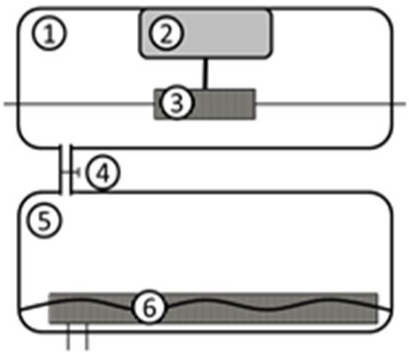

Figure S17 Schematic representation of the test setup used to characterise the full scale adsorber with (1) primary chamber, (2) scale, (3) adsorber with hydraulic connections, (4) valve, (5) secondary chamber, (6) evaporator partially submerged in water.[23]

The measurement procedure is presented in Figure S18. Prior to measurements, the adsorbent was desorbed at elevated temperature and vacuum (90°C, 6 h) and let cool down to adsorption temperature T_M (step A). The evaporator was then set to evaporation temperature T_{evap}. The adsorber was preloaded to a target loading via incremental dosage of small amounts of water vapor from the evaporator to the primary chamber (step B). When the conditioning of the adsorber is completed and the starting pressure (p_{init}) is reached in the primary chamber, the adsorption phase was started by completely opening the valve between chamber 1 and 2 (step C). In a variation, the experiment was conducted by initiating the adsorption directly from the evacuated state (step B').

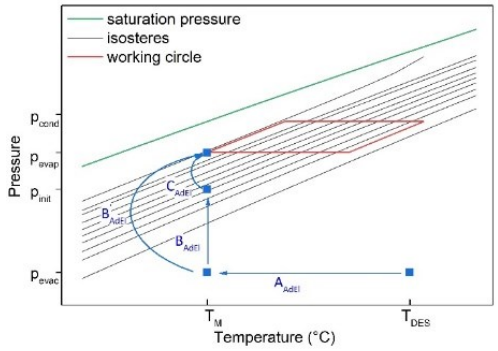

Figure S18 Schematic description of measuring procedure for the full scale AdsHX. First, the sample is desorbed at 90°C under vacuum, then let cool down to measurement temperature (A). Afterwards it was either preloaded (B) before the pressure jump for the measurement (C) was performed or a pressure jump was performed directly from the evacuated state (B').

Methods: The change in loading over time is the central parameter to evaluate adsorption kinetics. A central key data is the adsorption speed v_{ads}. It is calculated by dividing the loading difference ΔX by time. Different characteristic times are used in literature. Herein used is the time t_{90}, representing the time, in which 90% of the end loading is reached.
Different characteristic values for the power evaluation can be determined by means of energy balance in the adsorption circuit, time and geometric dimensions. It is important to notice that the experiment is a pressure jump method, where the sorber is quasi-isothermal. Therefore, the sensible heat of the sorber has little effect to the power output. This is a big difference to cycle measurements, where the adsorption power output is always higher due to the sensible heat released.
The mean cooling power is calculated from the scale signal and a constant evaporation enthalpy for the characteristic time t_{90}.

$$\overline{\dot{Q}_{cool}} = \frac{m_{uptake}}{t} \cdot 2500 \frac{kJ}{kg} \quad (1)$$

The cooling power is calculated from the derivative of the integral heat of evaporation:

$$P_{Cool} = \frac{d}{dt}\left[m_{Ads}(t) \cdot 2500 \frac{kJ}{kg}\right] \quad (2)$$

For better comparison volume-specific values are presented for power. The main key data is listed in Table S3. The test parameters and different weights are listed in Table S4 and Table S5.

Table S3. Main key data.

Item	Unit	Description
m_{sorb}	kg	dry mass of sorbent on HX
v_{ads}	$\cdot 10^{-4} \frac{g}{g \cdot s}$	adsorption speed
$\dot{Q}_{ads}$	W	mean specific adsorption power from energy balance
h_{ads}	$\frac{kJ}{kg}$	adsorption enthalpy
$\dot{Q}_{cool}$	W	mean specific cooling power via water uptake and enthalpy

Table S4. Parameter for AdEl tests.

Item	Unit	Data set real(target) – 1	Data set real(target) – 2
Desorption temperature	°C	90°C	60
Adsorption temperature	°C	30°C	22
Evaporation temperature	°C	18°C	18
Volume flow adsorber circuit	l/min	10	
Volume flow evaporator circuit	l/min	10	
Initial pressure p_{mc}	mbar	2.14	3.18

Table S5. Weights and volume of module.

	Weight /Volume
Heat exchanger	2388 g
Copper mesh	1289 g
Stainless steel frame	1421 g
Mass of adsorbent (desorbed)	334 g
Heat exchanger volume	2.34 L

Section S13. References

(1) Cavka, J. H.; Jakobsen, S.; Olsbye, U.; Guillou, N.; Lamberti, C.; Bordiga, S.; Lillerud, K. P. A New Zirconium Inorganic Building Brick Forming Metal Organic Frameworks with Exceptional Stability. *J. Am. Chem. Soc.* **2008**, 130 (42), 13850–13851.
(2) G. Wißmann, A. Schaate, S. Lilienthal, I. Bremer, A. M. Schneider and P. Behrens, *Microporous and Mesoporous Mater.*, 2012, **152**, 64–70.
(3) Wu, H.; Chua, Y. S.; Krungleviciute, V.; Tyagi, M.; Chen, P.; Yildirim, T.; Zhou, W. Unusual and highly tunable missing-linker defects in zirconium metal–organic framework UiO-66 and their important effects on gas adsorption. *J. Am. Chem. Soc.* **2013**, 135 (28), 10525−10532.
(4) Anjum, M. W.; Vermoortele, F.; Khan, A. L.; Bueken, B.; De Vos, D. E.; Vankelecom, I. F. J. Modulated UiO-66-Based Mixed-Matrix Membranes for CO_2 Separation. *ACS Appl. Mater. Interfaces* **2015**, 7 (45), 25193–25201.
(5) Jeremias, F.; Lozan, V.; Henninger, S. K.; Janiak, C. Programming MOFs for water sorption: amino-functionalized MIL-125 and UiO-66 for heat transformation and heat storage applications. *Dalton Trans.* **2013**, 42, 15967−15973.
(6) Jeremias, F.; Fröhlich, D.; Janiak, C.; Henninger, S. Water and methanol adsorption on MOFs for cycling heat transformation processes. *New J. Chem.* **2014**, 38, 1846–1852.
(7) Shahat, A.; Hassan, H. M. A.; Azzazy, H. M. E. Optical metal-organic framework sensor for selective discrimination of some toxic metal ions in water. *Analyt. Chim. Acta* **2013**, 793, 90–98.
(8) Vermoortele, F.; Bueken, B.; Le Bars, G.; Van de Voorde, B.; Vandichel, M.; Houthoofd, K.; Vimont, A.; Daturi, M.; Waroquier, M.; Van Speybroeck, V.; Kirschhock, C.; De Vos, D. E. Synthesis modulation as a tool to increase the catalytic activity of metal–organic frameworks: the unique case of UiO-66 (Zr). *J. Am. Chem. Soc.* **2013**, 135 (31), 11465–11468.
(9) Valenzano, L.; Civalleri, B.; Chavan, S.; Bordiga, S.; Nilsen, M. H.; Jakobsen, S.; Lillerud, K. P.; Lamberti, C.; Disclosing the Complex Structure of UiO-66 Metal Organic Framework: A Synergic Combination of Experiment and Theory. *Chem. Mater.* **2011**, 23 (7), 1700–1718.
(10) Leung, E.; Müller, U.; Trukhan, N.; Mattenheimer, H.; Cox, G.; Blei, S. Process for preparing porous metal-organic frameworks based on aluminum fumarate. *US8524932B2, US20120082864* **2013**.
(11) Alvarez, E.; Guillou, N.; Martineau, C.; Bueken, B.; Van de Voorde, B.; Le Guillouzer, C.; Fabry, P.; Nouar, F.; Taulelle, F.; de Vos, D.; Chang, J.-S.; Cho, K. H.; Ramsahye, N.; Devic, T.; Daturi, M.; Maurin, G.; Serre, C. The Structure of the Aluminum Fumarate Metal–Organic Framework A520. *Angew. Chem.* **2015**, 54 (12), 3664–3668.
(12) Cadiau, A.; Lee, J. S.; Borges, D. D.; Fabry, P.; Devic, T.; Wharmby, M. T.; Martineau, C.; Foucher, D.; Taulelle, F.; Jun, C.-H.; Hwang, Y. K.; Stock, N.; De Lange, M. F.; Kapteijn, F.; Gascon, J.; Maurin, G.; Chang J.-S.; Serre, C. Design of Hydrophilic Metal Organic Framework Water Adsorbents for Heat Reallocation. *Adv. Mater.* **2015**, 27, 4775–4780.
(13) Permyakova, A.; Skrylnyk, O.; Courbon, E.; Affram, M.; Wang, S.; Lee, U-H.; Valekar, A. H.; Nouar, F.; Mouchaham, G.; Devic, T.; Weireld, G. D.; Chang, J.-S.; Steunou, N.; Frere, M.; Serre, C. Synthesis Optimization, Shaping, and Heat Reallocation Evaluation of the Hydrophilic Metal–Organic Framework MIL-160(Al). *ChemSusChem* **2017**, 10, 1419–1426.
(14) Wahiduzzaman, M.; Lenzen, D.; Maurin, G.; Stock, N.; Wharmby, M. T. Rietveld Refinement of MIL-160 and its Structural Flexibility upon H_2O and N_2 Adsorption. *Eur. J. Inorg. Chem.* **2018**, 3626–3632.

(15) Kim, S.-N.; Lee, Y.-R.; Hong, S.-H.; Jang M.-S.; Ahn, W.-S; Pilot-scale synthesis of a zirconium-benzenedicarboxylate UiO-66 for CO_2 adsorption and catalysis. *Catal. Today* **2015**, 245, 54–60.
(16) Khabzina, Y.; Dhainaut, J.; Ahlhelm, M.; Richter, H.-J.; Reinsch, H.; Stock, N.; Farrusseng, D. Synthesis and Shaping Scale-up Study of Functionalized UiO-66 MOF for Ammonia Air Purification Filters. *Ind. Eng. Chem. Res.* **2018**, 57, 8200–8208.
(17) Valekar, A. H.; Cho, K.-H.; Lee, U.-H.; Lee, J. S.; Yoon, J. W.; Hwang, Y. K.; Lee, S. G.; Cho S. J.; Chang, J.-S.; Shaping of porous metal–organic framework granules using mesoporous ρ-alumina as a binder. *RSC Adv.* **2017**, 7, 55767–55777.
(18) Lenzen, D.; Bendix, P.; Reinsch, H.; Fröhlich, D.; Kummer, H.; Möllers, M.; Hügenell, P. P. C.; Gläser, R.; Henninger, S. K.; Stock, N. Scalable Green Synthesis and Full-Scale Test of the Metal–Organic Framework CAU-10-H for Use in Adsorption-Driven Chillers. *Adv. Mater.* **2017**, 6, 1705869
(19) Ren, J.; Musyoka, N. M.; Langmi, H. W.; Swartbooi, A.; North, B. C.; Mathe, M.; A more efficient way to shape metal-organic framework (MOF) powder materials for hydrogen storage applications. *Int. J. Hydrogen Energ.* **2015**, 40, 4617–4622.
(20) Moreira, M. A.; Santos, J. C.; Ferreira, A. F. P.; Loureiro, J. M.; Ragon, F.; Horcajada, P.; Shim, K.-E.; Hwang, Y.-K.; Lee, U.-H.; Chang, J.-S.; Serre, C.; Rodrigues, A. E.*;* Reverse shape selectivity in the liquid-phase adsorption of xylene isomers in zirconium terephthalate MOF UiO-66. *Langmuir* **2012**, 28 (13), 5715−5723.
(21) Pinto, M. L.; Dias, S.; Pires, J.; Composite MOF Foams: The Example of UiO-66/Polyurethane. *ACS Appl. Mater. Interfaces* **2013**, 5 (7), 2360–2363.
(22) Li, L.; Yao, J.; Xiao, P.; Shang, J.; Feng, Y.; Webley, P. A.; Wang, H.; One-step fabrication of ZIF-8/polymer composite spheres by a phase inversion method for gas adsorption. *Colloid and Polymer Science* **2013**, 291, 2711–2717.
(23) Bendix, P.; Füldner, G.; Möllers, M.; Kummer, H.; Schnabel, L.; Henninger, S.; Henning, H.-M.; Optimization of power density and metal-to-adsorbent weight ratio in coated adsorbers for adsorptive heat transformation applications. *Appl. Therm. Eng.* **2017**, 124, 83–90.

4 Unpublished Part

4.1 Shaping of MOF-granules for AHTs

Serkan Gökpinar, Ilias el Aita, Raphael Wiedey and Christoph Janiak → This topic is followed by Christian Jansen

Introduction

Two differently prepared PVA/Al-fum composites were produced successfully, namely pellets and granules. The pellets were successfully applied in AHT as presented in the paper "Engineering metal–organic frameworks in binder composites for water sorption driven chiller systems". As an alternative, the downsized monoliths (called granules) were produced. The particle size of granules is varying from 0.5 mm up to 1.5 mm (size distribution is given Figure 2). An important advantage of this method is the easiness of production and the possibility of producing smaller particles compared to the pellets. In the following chapter the results of granulation process are presented by verifying the crystallinity, measuring N_2 sorption, volumetric water sorption (20, 30, 40 °C) and gravimetric water sorption (40 °C, rH ~0.76).

Experimental Section/ Synthesis

For **production of granules** the slurry was prepared similar to the above pelletizing process (see paper) in a 500 mL large scale. Poly(vinyl alcohol) (PVA) were dissolved in DI water at 90 °C in a closed vial (ratio 60 mg PVA/1 mL water). Then, the MOF powder was added in a mass ratio of 4 (MOF):1 (PVA) and stirred for at least 3 h until a homogenous suspension was obtained. The slurry was directly poured in liquid nitrogen. The obtained larger PVA/Alfum pieces of 5 cm diameter and more were collected and a solvent exchange in acetone was carried out with a duration time of 24 h. The pieces were dried in vacuum at 80 °C over night (see Figure 2, left) and down sized in a Retsch mill (6000 rot/min and 2 mm sieve). The obtained mixture of differently sized particles was sieved and particles from 0.5 up to 1.5 mm were collected (see Figure 2, middle).

Results

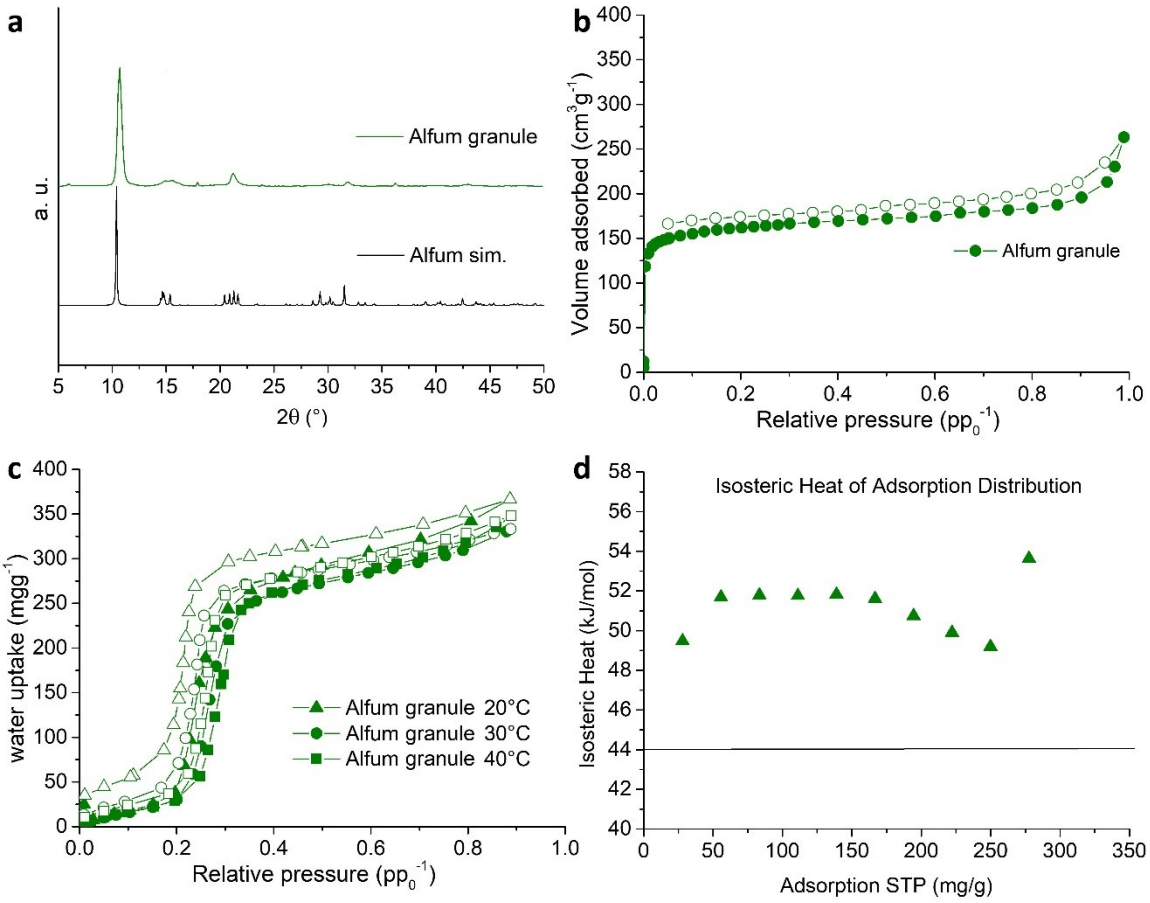

Figure 1: Characterization of PVA/MOF-granules: a) PXRD of granule and simulated pattern from DOYBEA[50] b) N_2 Sorption c) water sorption isotherms at 20, 30 and 40 °C and d) Heat of adsorption distribution of PVA/Alfum-granule.

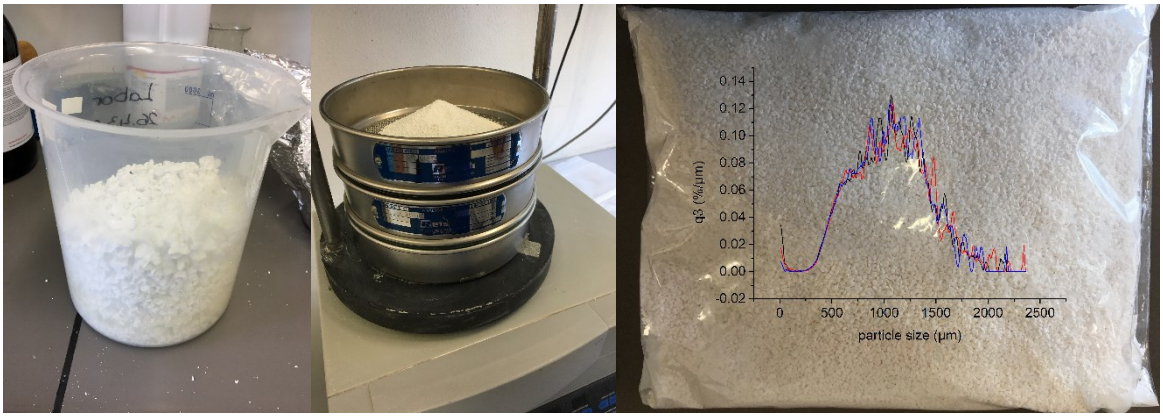

Figure 2: Picture of PVA/Alfum pieces (left) granules on sieve stack (middle) particle size distribution with product in background (right; 3 measurements of granule size distribution was determined by digital image analysis using a Retsch Camsizer XT).

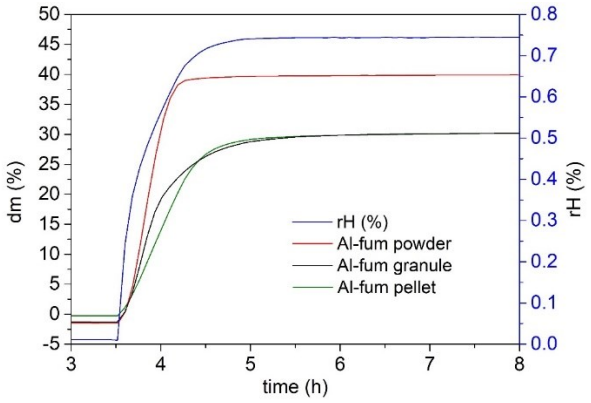

Figure 3: a) (1) Gravimetric water sorption measurements at 40 °C and rH of 74.5% of Alfum powder, granule and pellet. Figure is taken and from S16a of publication 3.3 and supplemented by result of PVA/Alfum granule.

The gravimetric water sorptions (presented in Figure 3) show a comparison to the already submitted work (Publication 3, Supporting Information, Figure S16a). In summary, we can achieve faster kinetics by using granules instead of the pellets (large-scale) to increase the performance of a fixed-bed based sorption driven chiller. Further investigations will be absolved by C. Jansen.

4.2 Sponge-like materials: Shaping of MOFs for CO_2 capture

Serkan Gökpinar, Tatyana Diment, Emrah Hastürk, and Cristoph Janiak → This topic is followed by Saskia Menzel

Introduction

Carbon capture and storage have received extensive attention in recent years. Currently, the chemical absorption using aqueous organic amines like monoethanolamine as absorbent is the most important method for CO_2 capture from industrial waste gases.

Alternatively, MOFs have shown enormous potential for CO_2 capture due to large specific surface area, tunable chemical structure, and pore properties. However, it remains a challenge to design MOFs with high CO_2 adsorption capacity as well as high selectivity. The resulting PEI modified MOFs, abbreviated as PEI/UiO-66-NH_2, were characterized with PXRD, water sorption, N_2 sorption, ^{1}H-NMR, and should evaluated as CO_2 adsorbents. Despite the low BET-surface areas of composites compared to pristine UiO-66-NH_2, the PEI/UiO-66-NH_2 composite can deliver increased CO_2 captures.

Experimental Section/ Synthesis

Polyethyleneimine (PEI)/ MOF (UiO-66-NH_2) composites were cryopolymerized at -18 °C. The crosslinking of amine groups of branched PEI and UiO-66-NH_2 was accomplished via ethylene glycol diglycidyl ether (EGDE). The crosslinking reaction is presented in Figure 4. In this work, the relation between polymer and MOF is varied from 1:9 to 7:3 MOF : polymer to analyze the influence on CO_2 capture. The synthesis details are presented in Table 3.

Table 3 Synthesis details of PEI/MOF composites.

	PEI, High M_w [g]	EGDE [µL]	H_2O [mL]	UiO-66-NH_2 [g; wt%]
SG_TD_5a	0.0908	33	1.91	0.0104; 7
SG_TD_5b	0.0804	33	1.93	0.0207; 15
SG_TD_5d	0.0707	33	1.92	0.0303; 23
SG_TD_5e	0.0606	33	1.91	0.0406; 30
SG_TD_5f	0.0304	66	1.91	0.0708; 53

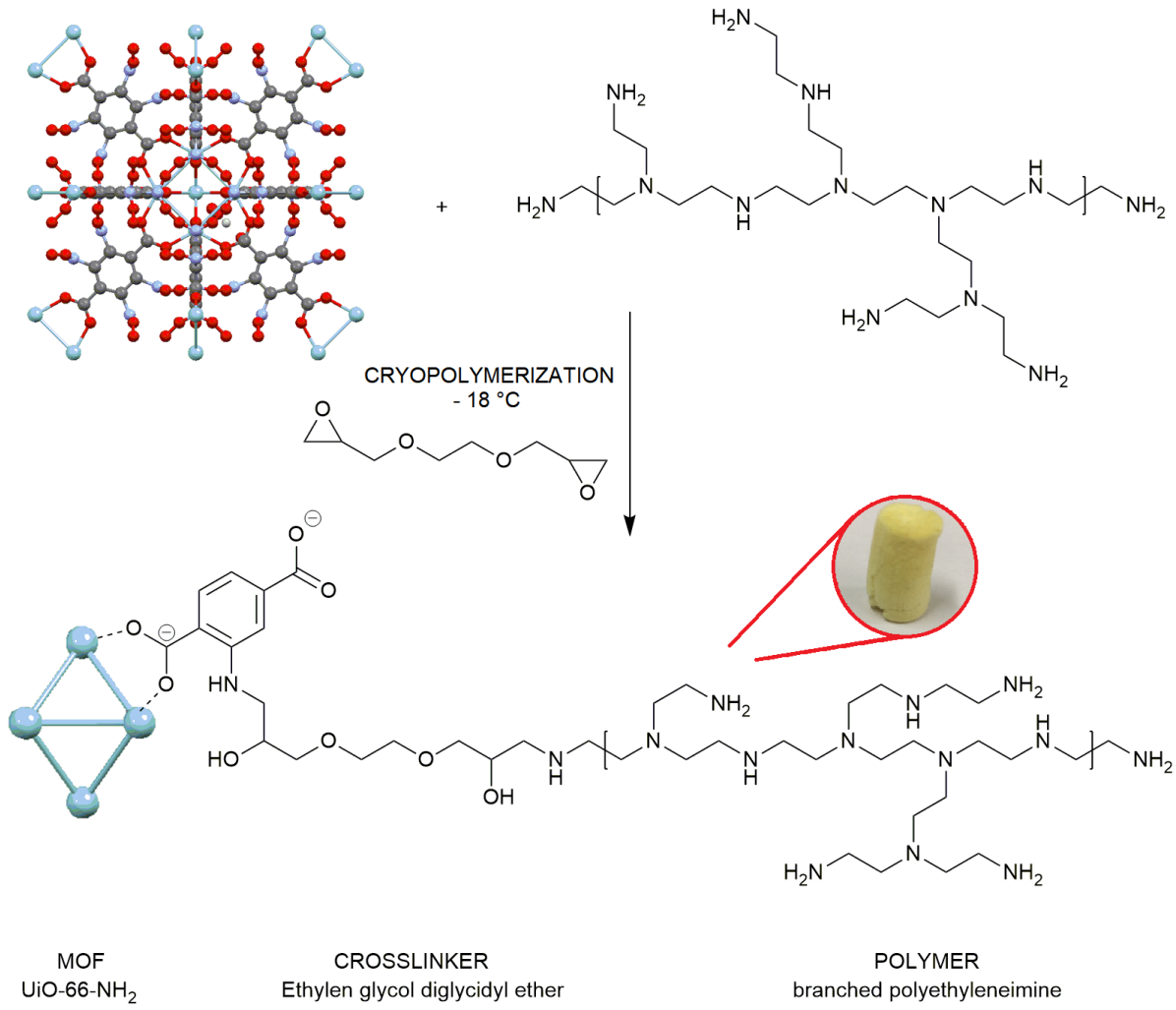

Figure 4: The schematic presentation of cryogel-synthesis of composite materials consisting of UiO-66-NH_2, Ethylene glycol diglycidyl ether (EGDE) and Polyethyleneimine and picture of monolith.

Results

Firstly, powder X-ray diffraction (PXRD) patterns of the obtained composites were measured to verify the crystallinity. Figure 5 shows these patterns along with the simulated pattern confirming their crystallinity by positive matching with the literature data. The reflexes are clear in case of composites with high amount of MOF and the MOF maintained the crystal structure. The higher the polymer part, the lower are the intensity of reflexes. The amorphous PEI binder causes a strong background and an extra reflex around 20° 2θ.

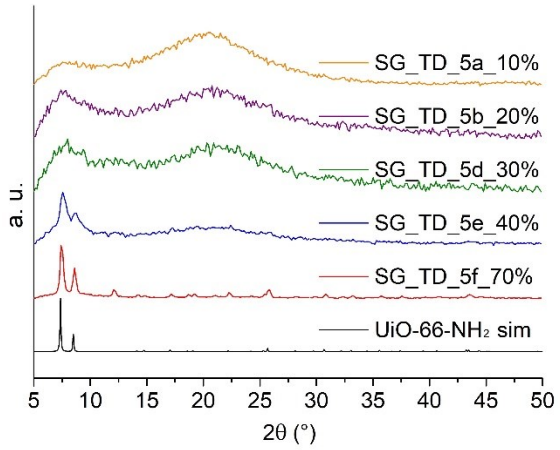

Figure 5: PXRDs of UiO-66-NH_2 monoliths with different MOF-loadings and the simulated (sim.) diffractogram of UiO-66-NH_2 from deposited crystal structure files. Simulated pattern was calculated from CSD-Refcode SURKAT[107].

Further, PEI is known for his hydrophilic character. Therefore, volumetric water sorption isotherms were measured. The sorption isotherm shows a maximal water uptake between 0.30 and 0.65 g g^{-1} at relative pressure of 0.9. The higher the amount of MOF, the lower is the water uptake as presented in Figure 6. The water uptake of these composite materials are high but not useful for application in a heat exchanger. An ideal adsorbent material should have a sorption isotherm with an S-shape giving the steep rise in the relative pressure range of p p_0^{-1} ≈ 0.10–0.30.[108,109] These requirement is not fulfilled.

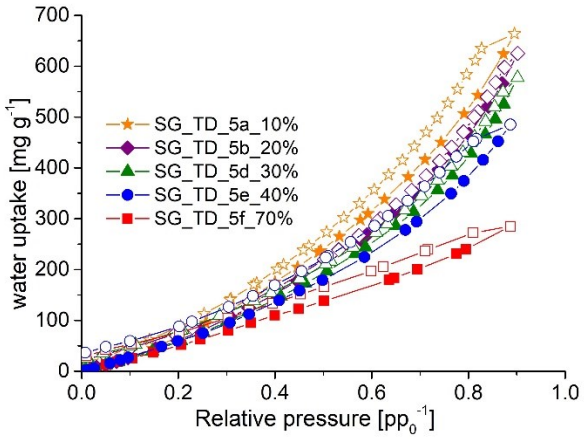

Figure 6: Water sorption isotherms of synthesized composites at 20 °C.

For CO_2 storage the uptake under high pressure is relevant. In case of CO_2 capture an antiproportional behavior compared to water sorption is observed. The higher the amount of MOF, the higher is the CO_2 uptake. As reference materials the pure MOF is given. SG_TD_5f and SG_TD_5e as shaped composites deliver higher uptakes than the pure materials (see Figure 7).

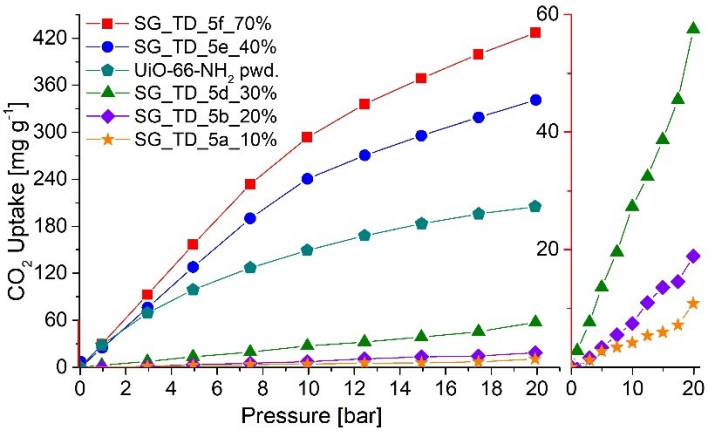

Figure 7: High pressure CO_2 uptake of synthesized composite material and neat UiO-66-NH_2 powder at 25 °C.

For calculation of CO_2 capture, the selectivity of the materials must be calculated for example CO_2/N_2, CO_2/CH_4 and several other combinations. To determine/proof the ratio of MOF and polymer ^{1}H-NMR is absolved. The composite material is treated in 1M NaOD/DMSO solution to digest the MOF structure and dissolve the polymer. As presented in Figure 8 no signals for polymer PEI is obtained. The high M_w of the polymer is resulting in insolubility.

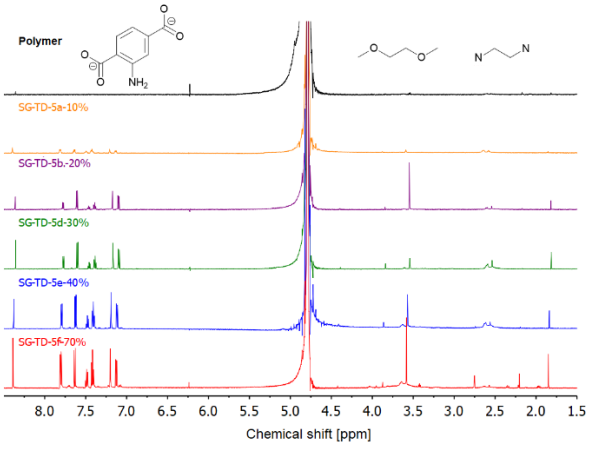

Figure 8: ^{1}H-NMR spectra of synthesized composites.

4.3 Calculation of defects by thermogravimetric analysis

Serkan Gökpinar (calculations), Niels Tannert (measurements) and Christoph Janiak → This topic is followed by Moritz Steinert

The measured TGAs of several Al-MOfs and Ti-MOFs are presented in Figure 9 and Figure 10.

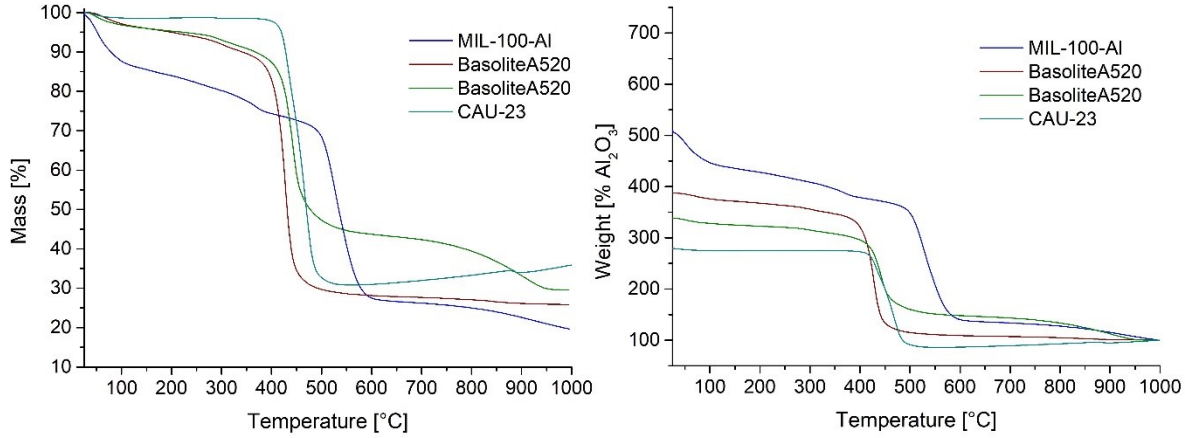

Figure 9: TGAs of several Al-MOFs: a) Starting weight is et to 100% and b) end weight of Al_2O_3 is set to 100%.

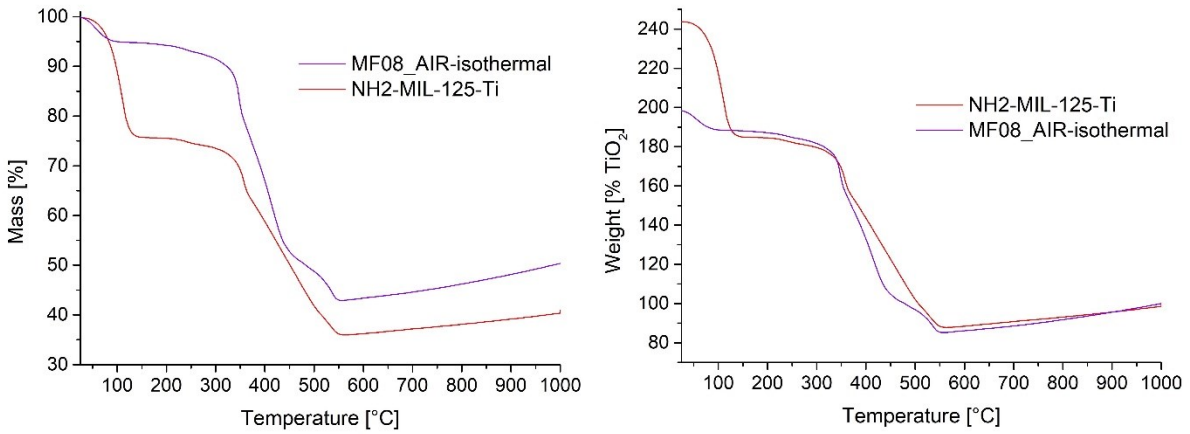

Figure 10: TGAs of several Ti-MOFs: a) Starting weight is et to 100% and b) end weight of TiO_2 is set to 100%.

Defect calculation per SBU was similar calculated to Shearer *et. al.* for Zr-MOFs.[23] Evaluation of TGA was done with assumption of getting pure Al_2O_3 or TiO_2 at 1000 °C. The chemical reactions can be described as follows:

Al-fum: $AlC_4O_5H_3 + 3\ O_2 \longrightarrow 1/2\ Al_2O_3 + 4\ CO_2 + 3/2\ H_2O$

CAU-10: $AlC_8O_5H_5 + 15/2\ O_2 \longrightarrow 1/2\ Al_2O_3 + 8\ CO_2 + 5/2\ H_2O$

MIL-160: $AlC_6O_6H_3 + 9/2\ O_2 \longrightarrow 1/2\ Al_2O_3 + 6\ CO_2 + 3/2\ H_2O$

CAU-23: $AlC_6SO_5H_3 + 6\ O_2 \longrightarrow 1/2\ Al_2O_3 + 6\ CO_2 + 3/2\ H_2O + SO_2$

MIL-100: $Al_3C_{18}O_{15}H_{10}Cl + 91/4\ O_2 \longrightarrow 3/2\ Al_2O_3 + 18\ CO_2 + 5\ H_2O + 1/2\ Cl_2$

NH_2-MIL-125: $Ti_8O_{36}H_{34}N_6C_{48} + 105/2\ O_2 \longrightarrow 8\ TiO_2 + 48\ CO_2 + 17\ H_2O + 6\ NO_2$

First we have to determine theoretical TGA plateau weight $W_{Theo.Plat}$:

$\mathbf{W_{Theo.Plat} = (M_{Comp}/M_{1/2xAl2O3})*W_{End}}$

$\mathbf{W_{Theo.Plat} = (M_{Comp}/M_{3/2xAl2O3})*W_{End}}$

$\mathbf{W_{Theo.Plat} = (M_{Comp}/M_{8xTiO2})*W_{End}}$

Where:

$\mathbf{M_{Comp}}$ is the molar mass of composition of interest:

M_W(Al-fum) = 158.04 g/mol

M_W(CAU-10) = 208.10 g/mol

M_W(MIL-160) = 198.07 g/mol

M_W(CAU-23) = 214.13 g/mol

M_W(MIL-100) = 518.52 g/mol

M_W(NH_2-MIL-125) = 1653.74 g/mol

$\mathbf{M_{1/2\ Al2O3}}$ is the molar weight of 1/2 Al_2O_3 (**50.98** g/mol)

$\mathbf{M_{3/2\ Al2O3}}$ is the molar weight of 3/2 Al_2O_3 (**152.94** g/mol)

$\mathbf{M_{8xTiO2}}$ is the molar weight of 8 TiO_2 (**638.93** g/mol)

$\mathbf{W_{End}}$ is the end weight of the TGA run (= **100 %** if normalized as described above).

$\mathbf{W_{Theo.Plat}}$ for MOFs:

$\mathbf{W_{Theo.Plat}}$ (Al-fum) = 310 %

$\mathbf{W_{Theo.Plat}}$ (CAU-10) = 408 %

$\mathbf{W_{Theo.Plat}}$ (MIL-160) = 389 %

$\mathbf{W_{Theo.Plat}}$ (CAU-23) = 420 %

$\mathbf{W_{Theo.Plat}}$ (MIL-100) = 339 %

$\mathbf{W_{Theo.Plat}}$ (NH_2-MIL-125) = 259 %

The weight contribution per BDC linker $\mathbf{Wt.PL_{Theo}}$ can be determined by following equation:

Where: $\mathbf{NL_{Ideal}}$ is the number of linkers (1) for Al-fum, CAU-10, MIL-160, CAU-23 and (2) for MIL-100 and (6) for NH_2-MIL-125-(Ti) in formula unit

$\mathbf{Wt.PL_{Theo}} = (\mathbf{W_{Theo.Plat}} - \mathbf{W_{End}})/\mathbf{NL_{Ideal}}$

$\mathbf{Wt.PL_{Theo}}$ (Al-fum) = (310−100)/1 = 210 %

$\mathbf{Wt.PL_{Theo}}$ (CAU-10) = (408 −100)/1 = 308 %

$\mathbf{Wt.PL_{Theo}}$ (MIL-160) = (389 −100)/1 = 289 %

$\mathbf{Wt.PL_{Theo}}$ (CAU-23) = (420−100)/1 = 320 %

$\mathbf{Wt.PL_{Theo}}$ (MIL-100) = (339 −100)/2 = 120 %

$\mathbf{Wt.PL_{Theo}}$ (NH_2-MIL-125) = (259 −100)/6 = 26.47 %

The experimental number of linkers per SBU, $\mathbf{NL_{Exp}}$ can be determined by following equation:

$\mathbf{NL_{Exp}} = \mathbf{(1-x)} = (\mathbf{W_{Exp.Plat}} - \mathbf{W_{End}})/\mathbf{Wt.PL_{Theo}}$

$\mathbf{NL_{Exp}} = \mathbf{(2-x)} = (\mathbf{W_{Exp.Plat}} - \mathbf{W_{End}})/\mathbf{Wt.PL_{Theo}}$

$\mathbf{NL_{Exp}} = \mathbf{(6-x)} = (\mathbf{W_{Exp.Plat}} - \mathbf{W_{End}})/\mathbf{Wt.PL_{Theo}}$

Where:

$\mathbf{W_{Exp.Plat}}$ is the experimental TGA plateau and can be taken from Figure 9 and Figure 10.

$\boldsymbol{x}$ is the number of linker deficiencies per cluster unit and can be determined by following equation:

$x = 1 - NL_{Exp} = 1-((W_{Exp.Plat} - W_{End})/Wt.PL_{Theo})$

$x = 2 - NL_{Exp} = 2-((W_{Exp.Plat} - W_{End})/Wt.PL_{Theo})$

$x = 6 - NL_{Exp} = 6-((W_{Exp.Plat} - W_{End})/Wt.PL_{Theo})$

x(Al-fum) = 1−0.938 = 1−((**297**−100 %)/210 %) = **0.062**

x(Al-fum) = 1−1.105= 1−((**332**−100 %)/210 %) = **-0.105**

x(CAU-23) = 1−0.540 = 1−((**270**−100 %)/320 %) = **0.460**

x(MIL-100) = 2−2.52 = 2−((**400**−100 %)/120 %) = **-0.520**

x(NH_2-MIL-125) = 6−3.21 = 6−((**185**−100 %)/26.47 %) = **2.790**

With $\boldsymbol{x}$ we obtain the experimental sum formula:

Al-fum:	**x = 0.06**	**$Al(OH)x(fum)_{0.94}$**
Al-fum:	**x = -0.10**	**$Al(OH)x(fum)_{1.10}$**
CAU-23:	**x = 0.46**	**$Al(OH)x(TDC)_{0.54}$**
MIL-100:	**x = -0.52**	**$Al_3(OH)x(H_2O)_2(BTC)_{2.52}$**
NH_2-MIL-125:	**x = 2.79**	**$Ti_8O_8(OH)_{4+x}(BDC\text{-}NH_2)_{3.21}$**

4.4 Spray coating of PVA/MIL-160 composite on Alumina-plates for water sorption applications

Serkan Gökpinar, Dieter Reenaers, Irina Gruber, Carsten Schlüssener, Wim Deferme and Christoph Janiak

Introduction

Metal–organic frameworks (MOFs) are potentially porous materials consisting of metal ions or metal clusters connected by organic ligands. In the last years, there is a growing interest on several applications, especially on sorption driven chillers. Firstly, Cadiau *et al.* synthesized MIL-160(Al), a novel and very promising candidate. It consists of helical cis corner-sharing chains of $AlO_4(OH)_2$ octahedra connected by 2,5-furandicarboxylate, building one dimensional square-shaped sinusoidal channels.[41] Recently, Permyakova *et al.* evaluated the features of MIL-160(Al) in a heat-reallocation open-system reactor prototype and pointed out the importance of this porous material.[46] Also, shaping of MIL-160(Al) was performed using the conventional wet-granulation method. Herein, we present an alternative shaping method as a binder coating, which is possibly more advantageous towards application, considering the increased heat transfer and adsorption rate to a fixed bed or a fixed monolayer (see Figure 11).

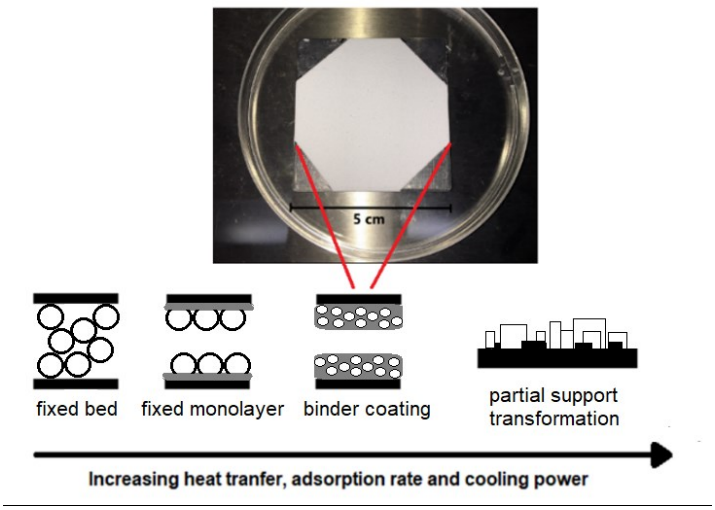

Figure 11: Schematic drawing of different shaping methods.

Experimental Section/ Synthesis

Plates with different amounts of PVA/MOF composite were spray coated (binder coatings) to analyse the kinetic effects of layer thickness on sorption properties. Further, we wanted to compare the kinetics of spray coatings (binder coatings) with granules, which is comparable with fixed bed or fixed monolayer heat exchanger (see Figure 1).

Table 1 Information about spray coated plates and their layer thickness.

No. of plate	Details	Layer thickness [µm]
15	24 layers, 3 % PVA+MOF	~70
25	30 layers, 3 % PVA+MOF	~80
35	38 layers, 3 % PVA+MOF	~130
39	54 layers, 3 % PVA+MOF	~170

Results

Firstly, powder X-ray diffraction (PXRD) patterns of the obtained MOF powders and composite were measured. Figure 12 shows these patterns along with the simulated pattern verifying their high crystallinity and phase purity by positive matching with the literature data. The amorphous PVA binder causes neither extra peaks, nor a significant background.

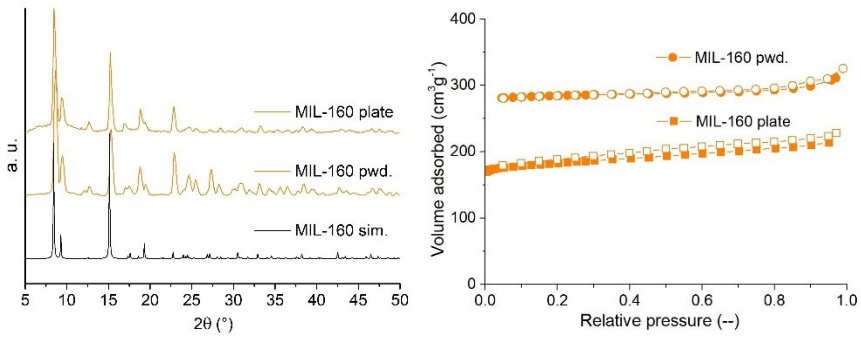

Figure 12: PXRDs and N_2 sorption isotherms of MIL-160-powder and -granules and their simulation data. Simulated pattern of MIL-160 calculated from PIBZOS.[49]

The composite have slightly broadened peaks in comparison to the pure MOF powder, which is caused by dilution through the added PVA binder, resulting in reduced peak intensity. Secondly, a nitrogen sorption measurement was absolved to analyze the quantitative pore accessibility of PVA/MIL-160 plate compared to neat MOF powder.

Table 2 Results of N_2 sorption isotherm.

MOF	SBET of MOF powder [$m^2\ g^{-1}$]	SBET of composite [$m^2\ g^{-1}$] (% of calc. SBET) [a]	Total pore volume of MOF powder [$cm^3\ g^{-1}$] [b]	Total pore volume of composite [b] [$cm^3\ g^{-1}$] (% of calc. vol) [c]	SBET in Lit. [$m^2\ g^{-1}$]
MIL-160	1122	744 (82)	0.46	0.33 (87)	968 -1180[110]

[a] expected BET surface area with 80 % MOF-loading calculated as the sum of the mass-weighted areas of the MOF (0.8) and freeze-granulated pure PVA (0.2) from the following formula, respectively: $SBET_{calc.} = SBET_{MOF} \times 0.8 + SBET_{PVA} \times 0.2$; with $SBET_{PVA} = 46\ m^2g^{-1}$; [b] total pore volume is calculated at $p\ p_0^{-1} = 0.90$ by using Gurvich-rule for pores ≤ 21 nm. [c] expected total pore volume, with 80 % MOF-loading calculated as the sum of the mass-weighted pore volumes of the MOF and freeze-granulated neat PVA from the following formula: $V_{calc.} = V_{MOF} \times 0.8 + V_{PVA} \times 0.2$; with $V_{PVA} = 0.05\ cm^3g^{-1}$.

A comparison between SBET of synthesized PVA/MOF composite and calculated SBET for 80 wt% MOF content shows an almost quantitative pore accessibility about 82 % of the mass-weighted areas. Also, total pore volumes of composite are in a similar range of 87 % as compared to calculated total pore volume considering the mass ratio of PVA/MOF. After confirming the pore accessibility for nitrogen molecules, the water sorption isotherm was absolved. The result is presented in Figure 13.

The pore accessibility for water molecules are given, while the water uptake of composite is about 100 % considering the mass ratios of MOF and PVA. The water cycle stability of PVA/MIL-160 composite is already analyzed in a pre-work, recently submitted (see Figure 13, right).

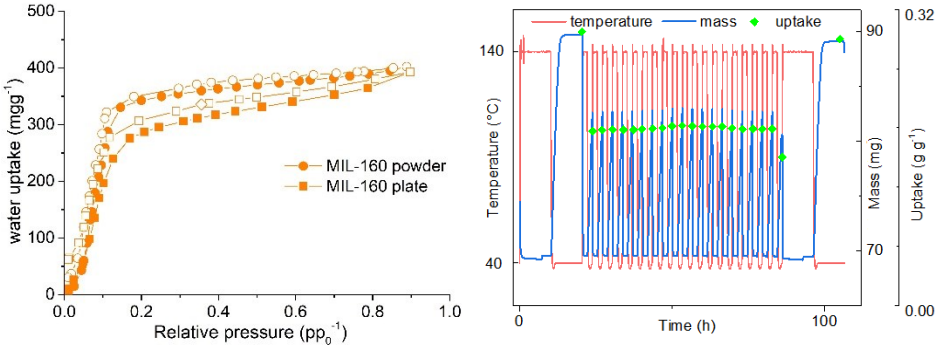

Figure 13: Water sorption isotherm of MIL-160 powder and plate (left) and water cycling experiment for similar synthesized PVA/MIL-160 pellets at 1001st to 1020th cycle (right, cycling experiment is taken from S. Gökpinar […] C. Janiak, **2019**, *submitted*).

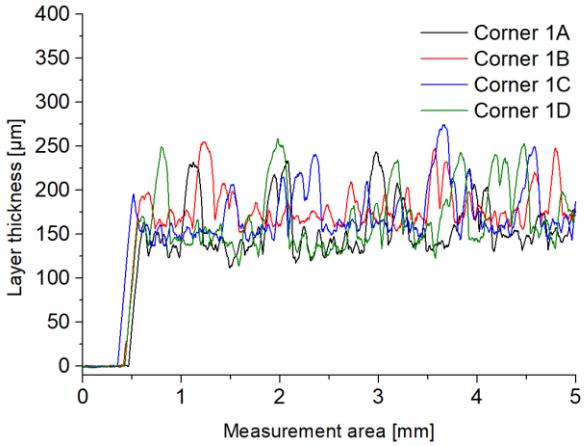

Figure 14: Exemplary shown layer thickness determination of plate 18. Layer thickness of aach sample is measured on four corners to proof their homogenous distribution.

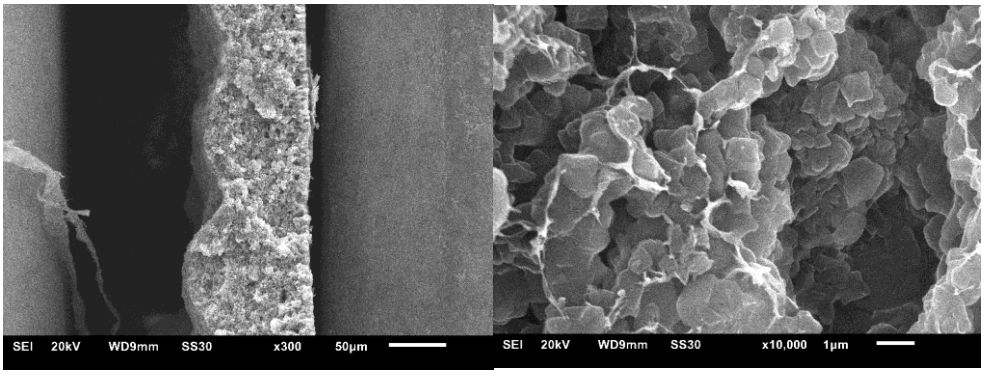

Figure 15: Scanning electron microscopy images of cross-section overview (left) and enlarged view (right).

5. Zusammenfassung und Ausblick

Die Synthese Zr-basierter MOF-Systeme wie UiO-66, UiO-66-NH_2 und UiO-67 wurde in einer konventiellen Trockengelumwandlung erfolgreich durchführt. In einer weiteren Arbeit konnten UiO-66 und das Polymorph MIL-140A in einer mikrowellenassistierten Trockengelumwandlung mit deutlich verringerten Reaktionszeiten erfolgreich umgesetzt werden. In beiden Arbeiten konnte eine vollständige Lösungsmittelwiederverwendung über mehrere Zyklen nachgewiesen werden.

Vier potentielle Kandidaten wurden für eine Anwendung in einer sorptionsgetriebenen Kältemaschine als PVA/MOF-Komposite in feste Form gebracht und anschließend hinsichtlich der Stabilität untersucht. Die PVA/Al-MOF-Komposite, genauer Alfum und MIL-160, erwiesen sich über 1000 Wassersorptionszyklen als stabil und weisen eine hohe mechanische Stabilität auf. Exemplarisch wurden die Alfum-pellets in einem „Full-scale“-Wärmeaustauscher angebracht, bei der die kommerziell verwendeten Kieselgele unter vergleichbaren Betriebsbedingungen übertroffen wurden.

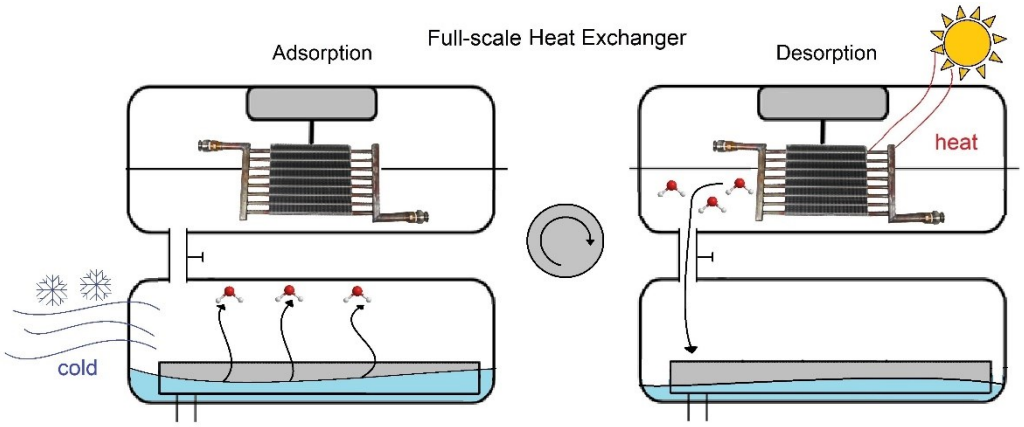

Abbildung 21: Arbeitszyklus einer sorptionsgetriebenen Kältemaschine.

Aus den unveröffentlichten Arbeiten geht hervor, dass die Geschwindigkeit der Wasseraufnahme im Fall der Granulate (vgl. Figure 3) höher ist als die der PVA/Al-fum Pellets, was eine Steigerung der Leistungsfähigkeit einer sorptionsgetriebenen Kältemaschine einbringen kann.

6. Experimenteller Teil

6.1 Materialien und Instrumente

6.1.1 Allgemeine Arbeitsmethoden

Alle Versuche wurden unter atmosphärischen Bedingungen durchgeführt. Verwendete Glasgeräte wurden durch Aufbewahrung in einem KOH/Isopropanol-Bad für mindestens 24 h gereinigt und anschließend einem verd. HCl-Bad neutralisiert. Die Glasgeräte wurden mit entionisiertem Wasser gewaschen und anschließend über Nacht im Trockenofen bei mindestens 80 °C getrocknet.

6.1.2 Chemikalienliste

Chemikalien, welche für die Arbeiten in den Publikationen verwendetet wurden, sind in diesen aufgelistet. Weitere Chemikalien sind in Tabelle 4 aufgelistet.

Tabelle 4: Chemikalienliste.

Chemikalienname	**Firma**	**Reinheit [%]**
Methanol	Fischer-Chemical	**≥** 99.99
Ethanol	Sigma-Aldrich	**≥** 99.80
Aceton	Sigma-Aldrich	**≥** 99.00
Dimethylformamid	Fisher-Chemical	**≥** 99.99
Salzsäure, 37%	Fischer-Chemical	p. a.
Terephthalsäure	Sigma Aldrich	≥98.0%
2-Aminoterephthalsäure	Alfa Aesar	**≥** 99.00
2,5-Furandicarbonsäure	Oxchem	**≥** 98.00
Zirkoniumchlorid	Riedel de Haen/ Alfa Aesar	99.5%
Zirkonylchlorid Octahydrat	Schuchardt München	ca. 99.00
Aluminiumacetat $Al(OH)(CH_3COO)_2$	Alfa Aesar	-
Ethylenglykoldiglycidylether	Tokyo Chemical Industry	-
Polyvinylalkohol - Mowiol® 20-98	Sigma Aldrich	-

6.1.3 Geräte

Pulverröntgendiffraktometrie (PXRD)

Pulverröntgendiffraktogramme (PXRD) wurden bei Umgebungstemperatur an einem Bruker D2 Phaser (300 W, 30 kV, 10 mA) unter Cu-Kα-Strahlung (λ = 1,54182 6 Å) von 5 bis 50 2θ und einer Abtastrate gemessen von 0,0125 °/s. Die Diffraktogramme wurden auf einem "Low Background Sample Holder" durchgeführt. Zur Analyse der Diffraktogramme wurde Match 3.11-Software verwendet. Die PXRD der Pellets nach 1000 Wassersorptionszyklen wurde unter Verwendung eines Rigaku MiniFlex 600-Pulverdiffraktometers mit Cu-Kα-Strahlung (40 kV, 15 mA), einer Schrittgröße von 0,02 ° und einer Schrittzeit von 4 s erhalten. Der intensivste Reflex wurde für alle Diffraktogramme auf 1 normiert.

Stickstoff-Sorptionsmessung/ Volumetrische Wassersorption

Stickstoff-Physisorptionsisothermen (Reinheit 99,999%) wurden auf einem Autosorb-6iSA von Quantachrome bei 77 K durchgeführt (Ausnahme: Pellets nach 1000 Zyklen am QuadraSorb evo bei 77 K). Wassersorptionsisothermen wurden an einem Vapor Sorption Analyzer (VSTAR) von Quantachrome gemessen. Vor den Messungen wurden die Proben zum anfänglichen Wiegen in mit Septen verschlossene Glasröhrchen gefüllt. Die Röhrchen einschließlich der Proben wurden unter Vakuum 3 Stunden lang bei 100 °C entgast und erneut gewogen. Die Proben wurden am Gerät angeschlossen und die Messungen gestartet. Die BET-Oberflächen wurden mit Rouquerol-Plots berechnet.

Thermogravimetrische Analyse (TGA)/ dynamische Differenzkalorimetrie (DSC)

Die thermogravimetrische Analyse (TGA) wurde mit einem Netzsch TG209 F3 Tarsus-Instrument durchgeführt. Die Proben wurden in Aluminiumoxidpfannen mit einer Geschwindigkeit von 5 °C/min unter synthetischer Luft oder Stickstoff von 25 bis 600 °C (teilweise bis 1000 °C) erhitzt. Die Differential Scanning Calorimetry (DSC) wurde einem Mettler Toledo DSC 3 mit einem Temperaturgradienten von 15 °C/min im Temperaturbereich von -50 ° C bis 250 ° C gemessen. Die Ergebnisse wurden mit der Software STARe SW 16.00 analysiert.

Gravimetrische Wassersorption

Die gravimetrische Wassersorption wurde an einem SPS-11 von ProUmid GmbH & CoKG bei einer relativen Luftfeuchtigkeit von 74,5% und einer Temperatur von 40 ° C durchgeführt.

Rasterelektronenmikroskopie

Rasterelektronenmikroskopische Aufnahmen (REM) wurden mit einem Jeol JSM-6510LV QSEM Advanced-Elektronenmikroskop aufgenommen, welches mit einer LaB_6-Kathode (5–20 keV) ausgestattet war.

Mechanische Stabilitätstests

Die mechanische Stabilität der Pellets bis zu 63 N wurde mit einem Texturanalyzer TA-XT2i 7 von Stable Micro Systems mit einer konstanten Geschwindigkeit von 0,35 mm/s bestimmt. Alternativ wurden mechanische Stabilitäten mit einem Erweka TBH210 mit einer Kraftkapazität von 300 N gemessen.

Hg-Porosimetrie

Eine Hg-Porosimetrie wurde mit einem PASCAL 140-440-Porosimeter mit Hg-Intrusion von Thermo Scientific durchgeführt. Die Daten wurden mit der Solid 1.6.3-Software analysiert.

Hochdruck-Adsorption

Die Hochdruck-Adsorptionsisothermen wurden gravimetrisch an einer IsoSORP® Static (G-HP) der Firma Rubotherm aufgenommen.

Labor-Mikrowellensystem

Für die Mikrowellenreaktionen wurde eine Labormikrowelle der Firma CEM des Modelltyps Discover verwendet.

7. Literaturverzeichnis

1 M. E. Davis, *Nature*, 2002, **417**, 813–821.

2 D. Braga, *Chem. Commun.*, 2003, 2751–2754.

3 R. A. Fischer and I. Schwedler, Angew. Chem., 2014, **126**, 7209–7214.

4 C. Janiak and J. K. Vieth, *New J. Chem.*, 2010, **34**, 2366–2388.

5 O. M. Yaghi and H. Li, *J. Am. Chem. Soc.*, 1995**, 117**, 10401–10402.

6 O. M. Yaghi, G. Li and H. Li, *Nature*, 1995, **378**, 703–706.

7 M. Kondo, T. Yoshitomi, H. Matsuzaka, S. Kitagawa and K. Seki, *Angew. Chem. Int. Ed.*, 1997, **36**, 1725–1727.

8 H. Li, M. Eddaoudi, T. L. Groy and O. M. Yaghi, *J. Am. Chem. Soc.*, 1998, **120**, 8571–8572.

9 M. Eddaoudi, J. Kim, N. Rosi, D. Vodak, J. Wachter, M. O'Keeffe and O.M. Yaghi, *Science*, 2002, **295**, 469–472.

10 V. Guillerm, F. Ragon, M. Dan-Hardi, T. Devic, M. Vishnuvarthan, B. Campo, A. Vimont, G. Clet, Q. Yang, G. Maurin, G. Férey, A. Vittadini, S. Gross and C. Serre*, Angew. Chem. Int. Ed.*, 2012, **51**, 9267−9271.

11 L. Valenzano, B. Civalleri, S. Chavan, S. Bordiga, M. H. Nilsen, S. Jakobsen, K. P. Lillerud and C. Lamberti, *Chem. Mater.*, 2011, **23**, 1700–1718.

12 G. Wißmann, A. Schaate, S. Lilienthal, I. Bremer, A. M. Schneider and P. Behrens, *Microporous and Mesoporous Mater.*, 2012, **152**, 64–70.

13 M. Taddei, *Coord. Chem. Rev.*, 2017, **343**, 1–24.

14 M. J. Katz, Z. J. Brown, Y. J. Colón, P. W. Siu, K. A. Scheidt, R. Q. Snurr, J. T. Hupp and O. K. Farha, *Chem. Commun.*, 2013, **49**, 9449–9451.

15 H. Wu, Y.S. Chua, V. Krungleviciute, M. Tyagi, P. Chen, T. Yildirim and W. Zhou*, J. Am. Chem. Soc.*, 2013, **135**, 10525–10532.

16 C.A. Trickett, K.J. Gagnon, S. Lee, F. Gandara, H.B. Burgi and O.M. Yaghi, Angew. *Chem. Int. Ed.*, 2015, **54**, 11162–11167.

17 G. C. Shearer, S. Chavan, J. Ethiraj, J.G. Vitillo, S. Svelle, U. Olsbye, C. Lamberti, S. Bordiga and K. P. Lillerud, *Chem. Mater.*, 2014, **26**, 4068–4071.

18 S. K. Henninger, F. Jeremias, H. Kummer and C. Janiak, *Eur. J. Inorg. Chem.*, 2012, 2625–2634.

19 D. Fröhlich, E. Pantatosaki, P. D. Kolokathis, K. Markey, H. Reinsch, M. Baumgartner, M. A. van der Veen, D. E. De Vos, N. Stock, G. K. Papadopoulos, S. K. Henninger and C. Janiak, *J. Mater. Chem. A*, 2016, **4**, 11859–11869.

20 H. Furukawa, F. Gándara, Y.-B. Zhang, J. Jiang, W. L. Queen, M. R. Hudson and O. M. Yaghi, *J. Am. Chem. Soc.*, 2014, **136**, 4369−4381.

21 J. H. Cavka, S. Jakobsen, U. Olsbye, N. Guillou, C. Lamberti, S. Bordiga and K. P. Lillerud, *J. Am. Chem. Soc.*, 2008, **130**, 13850–13851.

22 M. Kim and S. M. Cohen, *CrystEngComm,* 2012, **14**, 4096–4104.

23 G. C. Shearer, S. Chavan, S. Bordiga, S. Svelle, U. Olsbye and K. P. Lillerud, *Chem. Mater.*, 2016, **28**, 3749–3761.

24 A. W. Thornton, R. Babarao, A. Jain, F. Trousselet and F. X. Coudert, *Dalton Trans.*, 2016, **45**, 4352–4359.

25 R. C. Klet, Y. Liu, T.C. Wang, J. T. Hupp and O. K. Farha, *J. Mater. Chem. A*, 2016, **4**, 1479–1485.

26 J. Ethiraj, E. Albanese, B. Civalleri, J.G. Vitillo, F. Bonino, S. Chavan, G.C. Shearer, K.P. Lillerud and S. Bordiga, *ChemSusChem*, 2014, **7**, 3382–3388.

27 M. W. Anjum, F. Vermoortele, A. L. Khan, B. Bueken, D. E. De Vos and I. F. J. Vankelecom, *ACS Appl. Mater. Interfaces*, 2015, **745**, 25193–25201.

28 H. Fei and S. M. Cohen, *Chem. Commun.*, 2014, 50, 4810–4812.

29 K. A. Mocniak, I. Kubajewska, D. E. M. Spinalle, G. R. Williams and R. E. Morris, *RSC Adv.*, 2015, **5**, 83648–83656.

30 H. Wu, Y. S. Chua, V. Krungleviciute, M. Tyagi, P. Chen, T. Yildirim and W. Zhou, *J. Am. Chem. Soc.*, 2013, **135**, 10525−10532.

31 F. Jeremias, V. Lozan, S. K. Henninger and C. Janiak, *Dalton Trans.*, 2013, **42**, 15967−15973.

32 F. Jeremias, D. Fröhlich, C. Janiak and S. Henninger, *New J. Chem.*, 2014, **38**, 1846–1852.

33 A. Shahat, H. M. A. Hassan and H. M. E. Azzazy, *Analyt. Chim. Acta*, 2013, **793**, 90–98.

34 F. Vermoortele, B. Bueken, G. Le Bars, B. Van de Voorde, M. Vandichel, K. Houthoofd, A. Vimont, M. Daturi, M. Waroquier, V. Van Speybroeck, C. Kirschhock and D. E. De Vos, *J. Am. Chem. Soc.*, 2013, **135**, 11465–11468.

35 H. Kim, S. Yang, S. R. Rao, S. Narayanan, E. A. Kapustin, H. Furukawa, A. S. Umans, O. M. Yaghi and E. N. Wang, *Science*, 2017, **356**, 430−434.

36 M. Krüger, A. K. Inge, H. Reinsch, Y.-H. Li, M. Wahiduzzaman, C.-H. Lin, S.-L. Wang, G. Maurin and N. Stock, *Inorg. Chem.*, 2017, **56**, 5851−5862.

37 C. Schlüsener, M. Xhinovci, S.-J. Ernst, A. Schmitz, N. Tannert and C. Janiak, *Chem. Mater.*, 2019, **31**, 4051−4062.

38 N. Tannert, S.-J. Ernst, C. Jansen, H.-J. Bart, S. K. Henninger, and C. Janiak, *J. Mater. Chem. A*, 2018, **6**, 17706−17712.

39 D. Lenzen, J. Zhao, S.-J. Ernst, M. Wahiduzzaman, A. K. Inge, D. Fröhlich, H. Xu, H.-J. Bart, C. Janiak, S. Henninger, G. Maurin, X. Zou and N. Stock, *Nat. Comm.*, 2019, **10**, 3025, 1−9.

40 E. Leung, U. Müller, N. Trukhan, H. Mattenheimer, G. Cox, S. Blei, *US8524932B2, US20120082864*, 2013.

41 A. Cadiau, J. S. Lee, D. D. Borges, P. Farby, T. Devic, M. T. Wharmby, C. Martineau, D. Foucher, F. Taulelle, C.-H. Jun, Y. K. Hwang, N. Stock, M. F. De Lange, F. Kapteijn, J. Gascon, G. Maurin, J.-S. Chang and C. Serre, *Adv. Mat.*, 2015, **27**, 4775–4780.

42 H. Reinsch, M. A. van der Veen, B. Gil, B. Marszalek, T. Verbiest, D. E. De Vos and N. Stock, *Chem. Mater.*, 2013, **25**, 17−26.

43 M. Gaab, M. Kostur and U. Müller, U.S. Patent 20140213832, 2014.

44 P. Serra-Crespo, E. V. Ramos-Fernandez, J. Gascon and F. Kapteijn, Chem. Mater., 2011, **23**, 2565–2572.

45 G. Férey, M. Latroche, C. Serre, F. Millange, T. Loiseau and A. Percheron-Guégan, *Chem. Commun.*, 2003, 2976–2977.

46 A. Permyakova, O. Skrylnyk, E. Courbon, M. Affram, S. Wang, U.-H. Lee, A. H. Valekar, F. Nouar, G. Mouchaham, T. Devic, G. De Weireld, J.-S. Chang, N. Steunou, M. Frère, and C. Serre, *ChemSusChem*, 2017, **10**, 1419–1426.

47 D. Fröhlich, E. Pantatosaki, P. D. Kolokathis, K. Markey, H. Reinsch, M. Baumgartner, M. A. van der Veen, D. E. De Vos, N. Stock, G. K. Papadopoulos, S. K. Henninger and C. Janiak, *J. Mater. Chem. A*, 2016, **4**, 11859–11869.

48 H. Kummer, F. Jeremias, A. Warlo, G. Füldner, D. Fröhlich, C. Janiak, R. Gläser and S. K. Henninger, *Ind. Eng. Chem. Res.*, 2017, **56**, 8393–8398.

49 M. Wahiduzzaman, D. Lenzen, G. Maurin, N. Stock, M. T. Wharmby, *Eur. J. Inorg. Chem.*, 2018, 3626–3632.

50 E. Alvarez, N. Guillou, C. Martineau, B. Bueken, B. Van de Voorde, C. Le Guillouzer, P. Fabry, F. Nouar, F. Taulelle, D. de Vos, J.-S. Chang, K. H. Cho, N. Ramsahye, T. Devic, M. Daturi, G. Maurin, C. Serre, *Angew. Chem.*, 2015, **54**, 3664–3668.

51 M. F. De Lange, B. L. Van Velzen, C. P. Ottevanger, K. J. F. M. Verouden, L.-C. Lin, T. H. J. Vlugt, J. Gascon and F. Kapteijn, *Langmuir*, 2015, **31**, 12783−12796.

52 F. Jeremias, A. Khutia, S. K. Henninger and C. Janiak, *J. Mater. Chem.*, 2012, **22**, 10148–10151.

53 J. Klinowski, F. A. A. Paz, P. Silva and J. Rocha, *Dalton Trans.*, 2011, **40**, 321–330.

54 A. Rabenau, *Angew. Chem., Int. Ed. Engl.*, 1985, **24**, 1026.

55 N. Stock and S. Biswas, *Chem. Rev.*, 2012, **112**, 933–969.

56 U. Mueller, H. Puetter, M. Hesse and H. Wessel, PCT Patent, 2005, 049,892.

57 R. Ameloot, L. Stappers, J. Fransaer, L. Alaerts, B. F. Sels and D. E. De Vos, *Chem. Mater.*, 2009, **21**, 2580–2582.

58 A. M. Joaristi, J. Juan-Alcañiz, P. Serra-Crespo, F. Kapteijn and J. Gascon*, Crystal Growth & Design*, 2012, **127**, 3489–3498.

59 J. F. Fernandez-Bertran, *Pure Appl. Chem.*, 1999, **71**, 581–586.

60 M. Klimakow, P. Klobes, A. F. Thünemann, K. Rademann and F. Emmerling, *Chem. Mater.*, 2010, **22**, 5216–5221.

61 M. Rubio-Martinez, C. Avci-Camur, A. W. Thornton, I. Imaz, D. Maspoch and M. R. Hill, *Chem. Soc. Rev.*, 2017, **46**, 3453–3480.

62 D. Crawford, J. Casaban, R. Haydon, N. Giri, T. McNally and S. L. James, *Chem. Sci.*, 2015, **6**, 1645–1649.

63 B. Karadeniz, A. J. Howarth, T. Stolar, T. Islamoglu, I. Dejanović, M. Tilerli, M. C. Wasson, S.-Y. Moon, O. K. Farha, T. Friščić and K. Užarević, *ACS Sustainable Chem. Eng.*, 2018, **6**, 15841−15849.

64 K. S. Suslick, D. A. Hammerton and R. E. Cline, *J. Am. Chem. Soc.*, 1986, **108**, 5641–5642.

65 Y.-R. Lee, J. Kim and W.-S. Ahn, *Korean J. Chem. Eng.*, 2013, **30**, 1667–1680.

66 A. Lew, P. O Krutzik, M. E. Hart and A. R. Chamberlin, *J. Comb. Chem.*, 2002, **4**, 95–105.

67 S. Chandrasekhar and P. N. Pramada, *Microporous and Mesoporous Mater.*, 2008, **108**, 152–161.

68 P. Maniam and N. Stock, *Inorg. Chem.*, 2011, **50**, 5085–5097.

69 S. H. Jhung, J. H. Lee and J. S. Chang, *Bull. Korean Chem. Soc.*, 2005, **26**, 880–881.

70 D. M. Bibby and M. P. Dale, *Nature,* 1985, **317**, 157−158.

71 W. Xu, J. Dong, J. Li, J. Li and F. Wu., *J. Chem. Soc., Chem. Commun*., 1990, **10**, 755–756.

72 S. Gökpinar, T. Diment and C. Janiak, *Dalton Trans.*, 2017, **46**, 9895–9900.

73 Q. Shi, Z. F. Chen, Z. W. Song, J. P. Li and J. X. Dong, *Angew. Chem. Int. Ed.*, 2011, **50**, 672675.

74 I. Ahmed, J. Jeon, N. A. Khan and S. H. Jhung, *Cryst. Growth Des.*, 2012, **12**, 5878–5881.

75 J. Kim, Y. R. Lee and W. S. Ahn, *Chem. Commun.*, 2013, **49**, 7647–7649.

76 P. Tan, X.-Y. Xie, X.-Q. Liu, T. Pan, C. Gu, P.-F. Chen, J.-Y. Zhou, Y. Pan and L.-B. Sun, *J. Hazardous Mater.*, 2017, **321**, 344–352.

77 Y. Yan, M. E. Davis and G. R. Gavalas, *Ind. Eng. Chem. Res.*, 1995, **34**, 1652–1661.

78 P.B. Bendix, S.K. Henninger and H.-M. Henning, *Ind. Eng. Chem. Res.*, 2016, **55**, 4942–4947.

79 T. Qian and J. Li, *Adv. Powder Technol.*, 2015, **26**, 98–104.

80 E. Hastürk, C. Schlüsener, J. Quodbach, A. Schmitz and C. Janiak, *Microporous and Mesoporous Mater.*, 2019, **280**, 277–287.

81 J. Zhu, L. Wu, Z. Bu, S. Jie and B.-G. Li, *Ind. Eng. Chem. Res.*, 2019, **58**, 4257–4266.

82 B. Valizadeh, T. N. Nguyen and K. C. Stylianou, *Polyhedron*, 2018, **145**, 1–15.

83 Z. Luo, H. Chen, S. Wu, C. Yang and J. Cheng, *Chemosphere*, 2019, **237**, 124493.

84 A. N. Valekar, K.-H. Cho, U.-H. Lee, J. S. Lee, J. W. Yoon, Y. K. Hwang, S. G. Lee, S. J. Cho and J.-S. Chang, *RSC Adv.*, 2017, **7**, 55767–55777.

85 Y. Chen, X. Huang, S. Zhang, S. Li, S. Cao, X. Pei, J. Zhou, X. Feng and B. Wang, *J. Am. Chem. Soc.*, 2016, **138**, 10810−10813.

86 S. Hindocha, and S. Poulston, *Faraday Discuss.*, 2017, **201**, 113–125.

87 J. Dhainaut, C. Avci-Camur, J. Troyano, A. Legrand, J. Canivet, I. Imaz, D. Maspoch, H. Reinsch and D. Farrusseng, *CrystEngComm*, 2017, **19**, 4211–4218.

88 D. Bazer-Bachi, L. Assié, V. Lecoq, B. Harbuzaru and V. Falk, *Powder Technol.*, 2014, **255**, 52–59.

89 V. Finsy, L. Maa, L. Alaerts, D. E. De Vos, G. V. Baron and J. F. M. Denayer, *Microporous and Mesoporous Mater.,* 2009, **120**, 221–227.

90 M. A. Moreira, J. C. Santos, A. F. P. Farreira, J. M. Loureiro, F. Ragon, P. Horcajada, K.-E. Shim, Y.-K. Hwang, U.-H. Lee, J.-S. Chang, C. Serre and A. E. Rodrigues, *Langmuir*, 2012, **28**, 5715–5723.

91 Y. Khabzina, J. Dhainaut, M. Ahlhelm, H.-J. Richter, H. Reinsch, N. Stock and D. Farrusseng, *Ind. Eng. Chem. Res.*, 2018, **57**, 8200−8208.

92 Quantachrome Instruments, Powder TechNote 69, Aspects of the 2015 IUPAC Recommendations for Physical Adsorption Characterization [1].

93 M. Thommes, K. Kaneko, A. V. Neimark, J. P. Olivier, F. Rodriguez-Reinoso, J. Rouquerol and K. S. W. Sing, *Pure Appl. Chem.*, 2015, **87**, 1051–1069.

94 Quantachrome Instruments, Powder TechNote 52, Adsorptives for Physisorption Experiments: Selection and Their Physical Properties.

95 M. Thommes, K. Kaneko, A. V. Neimark, J. P. Olivier, F. Rodriguez-Reinoso, J. Rouquerol and K. S. Sing, *Pure Appl. Chem.*, 2015, **87**, 1051-1069.

96 L. Gurvich, *J. Phys. Chem. Soc. Russ.* 1915, **47**, 805.

97 J. Möllmer, M. Lange, A. Möller, C. Patzschke, K. Stein, D. Lässig, J. Lincke, R. Gläser, H. Krautscheid and R. Staudt, *J. Mater. Chem.*, 2012, **22**, 10274-10286.

98 J. H. de Boer, B. C. Lippens, B. G. Linsen, J. C. P. Broekhoff, A. van den Heuvel and T. J. Osinga, *J. Colloid Interface Sci.*, 1966, **21**, 405–414.

99 B. C. Lippens, B. G. Linsen and J. H. de Boer, *J. Catal.*, 1964, **3**, 32–37.

100 S. Lowell, J. E. Shields, M. A. Thomas and M. Thommes, *Characterization of porous solids and powders: surface area, pore size and density*, Kluwer Academic Publisher, Dordrecht **2004**.

101 S. Brunauer, P. H. Emmett and E. Teller, *J. Am. Chem. Soc.*,1938, **60**, 309–319.

102 M. Thommes, *Chem. Ing. Tech.*, 2010, **82**, 1059–1073.

103 J. Rouquerol, F. Rouquerol and K. Sing, *Adsorption by powders and porous solids*, Academic Press, London 1999.

104 Quantachrome Instruments, Powder TechNote 54, Automated Software Assistant for the Proper Calculation of BET Area of Microporous Materials.

105 J. Rouquerol, F. Rouquerol, K. S. W. Sing, P. Llewellyn and G. Maurin. *Adsorption by Powders and Porous Solids: Principles, Methodology and Applications*, Academic Press (2014).

106 ISO FDIS 9277, Determination of the Specific Surface Area of Solids by Gas Adsorption BET Method, 2009.

107 C. A. Trickett, K. J. Gagnon, S. Lee, F. Gándara, H.-B. Bürgi and O. M. Yaghi, *Angew. Chem. Int. Ed.*, 2015, **54**, 11162–11167.

108 S. K Henninger, F. Jeremias, H. Kummer and C. Janiak, *Eur. J. Inorg. Chem.*, 2012, 2625–2634.

109 Y. I. Aristov, *Appl. Therm. Eng.,* 2013, **50**, 1610–1618.

110 N. Tannert, C. Jansen. S. Nießing and C. Janiak, *Dalton Trans.*, 2019, **48**, 2967–2976.